

**CODING AND LEARNING OF CHEMOSENSOR ARRAY  
PATTERNS IN A NEURODYNAMIC MODEL OF THE  
OLFACTORY SYSTEM**

A Dissertation

by

AGUSTIN GUTIERREZ GALVEZ

Submitted to the Office of Graduate Studies of  
Texas A&M University  
in partial fulfillment of the requirements for the degree of  
DOCTOR OF PHILOSOPHY

May 2006

Major Subject: Computer Science

**CODING AND LEARNING OF CHEMOSENSOR ARRAY  
PATTERNS IN A NEURODYNAMIC MODEL OF THE  
OLFACTORY SYSTEM**

A Dissertation

by

AGUSTIN GUTIERREZ GALVEZ

Submitted to the Office of Graduate Studies of  
Texas A&M University  
in partial fulfillment of the requirements for the degree of

DOCTOR OF PHILOSOPHY

Approved by:

Chair of Committee,  
Committee Members,

Head of Department,

Ricardo Gutierrez-Osuna  
Yoonsuck Choe  
Santiago Marco Colas  
Bruce McCormick  
Michael S. Pilant  
Valerie E. Taylor

May 2006

Major Subject: Computer Science

## **ABSTRACT**

Coding and Learning of Chemosensor Array Patterns in a Neurodynamic Model of the  
Olfactory System.

(May 2006)

Agustin Gutierrez Galvez, B.S.; B.En., Universitat de Barcelona, Spain

Chair of Advisory Committee: Dr. Ricardo Gutierrez-Osuna

Arrays of broadly-selective chemical sensors, also known as electronic noses, have been developed during the past two decades as a low-cost and high-throughput alternative to analytical instruments for the measurement of odorant chemicals. Signal processing in these gas-sensor arrays has been traditionally performed by means of statistical and neural pattern recognition techniques. The objective of this dissertation is to develop new computational models to process gas sensor array signals inspired by coding and learning mechanisms of the biological olfactory system. We have used a neurodynamic model of the olfactory system, the KIII, to develop and demonstrate four odor processing computational functions: robust recovery of overlapping patterns, contrast enhancement, background suppression, and novelty detection. First, a coding mechanism based on the synchrony of neural oscillations is used to extract information from the associative memory of the KIII model. This temporal code allows the KIII to recall overlapping patterns in a robust manner. Second, a new learning rule that combines Hebbian and anti-Hebbian terms is proposed. This learning rule is shown to achieve contrast

enhancement on gas-sensor array patterns. Third, a new local learning mechanism based on habituation is proposed to perform odor background suppression. Combining the Hebbian/anti-Hebbian rule and the local habituation mechanism, the KIII is able to suppress the response to continuously presented odors, facilitating the detection of the new ones. Finally, a new learning mechanism based on anti-Hebbian learning is proposed to perform novelty detection. This learning mechanism allows the KIII to detect the introduction of new odors even in the presence of strong backgrounds. The four computational models are characterized with synthetic data and validated on gas sensor array patterns obtained from an e-nose prototype developed for this purpose.

To Mar

## ACKNOWLEDGMENTS

There is one person above all others who deserves my deepest thanks for her continued support during the origin, development, and writing of this dissertation: my beloved wife Mar. Her infinite understanding and invaluable help has been a source of strength during this long journey. I could not have done it without her.

I would like to thank my advisor, Dr. Ricardo Gutierrez-Osuna, for the great opportunity he offered me joining when I first joined his PAMI Lab at Wright State University and later when I joined his PRISM Lab at Texas A&M University. I am also thankful to Ricardo for introducing me to this exciting field of research and for sharing his broad knowledge in this area with me. From him I have learned uncountable aspects of the fascinating world that is research.

I would like also to thank my committee members, Dr. Yoonsuck Choe, Dr. Bruce McCormick, Dr. Michael Pilant, and Dr. Santiago Marco, for their support and suggestions. Special thanks go to Dr. Santiago Marco, who was the originator of this doctoral experience and also for his wise advice in critical moments.

There are four people that have decisively contributed to this dissertation: Alex Perera, Joaquin Garcia, Barani Raman, and Takao Yamanaka. I am in debt to all of them for their support, understanding, and uncountable thought-provoking conversations.

I would also like to thank the members of the PAMI Lab at Wright State University: Nilesh Powar, Ping Sun, Praveen Kakumanu, and Nishant Balan, for their kind help during my first year in the US. I am also grateful to my friends: Cristina, Todd, Edith, Angel, Zulmaris, and many more, for sharing with me the College Station experience.

Additionally, I would like to thank NSF (CAREER Award 0229598), TAMU-Conacyt (Award 246186), and the Center for Integrated Microchemical Systems (CIMS) for the funding support.

Finally, I would like to thank my parents, Arsenio and Maria, and my sisters, Sabina and Isabel, for their love and confidence in me.

## TABLE OF CONTENTS

	Page
ABSTRACT .....	iii
ACKNOWLEDGMENTS .....	vi
TABLE OF CONTENTS .....	viii
LIST OF FIGURES .....	xii
LIST OF TABLES .....	xix
 CHAPTER	
I INTRODUCTION .....	1
I.1. Contributions of this work .....	3
I.2. Organization of the dissertation .....	4
II THE ELECTRONIC NOSE .....	5
II.1. The electronic nose technology .....	5
II.1.1. Gas sensor types .....	7
II.1.1.1. Metal Oxide Semiconductor (MOS) sensors .....	8
II.1.1.2. Conducting Polymer (CP) sensors .....	13
II.1.1.3. Metal Oxide Semiconductor Field Effect Transistor (MOSFET) sensors .....	15
II.1.1.4. Quartz Crystal Microbalance (QCM) sensors .....	16
II.1.1.5. Surface Acoustic Wave (SAW) sensors .....	17
II.1.2. Temperature modulation in MOS sensors .....	19
II.1.3. Signal processing for gas sensor arrays .....	22
II.1.3.1. Statistical and ANN methods .....	23
II.1.3.2. Neuromorphic processing for chemical sensor .....	25
II.2. The PRISM e-nose prototype .....	27
II.3. Collected datasets .....	34
II.3.1. Temperature-modulation dataset .....	35
II.3.2. Isothermal dataset .....	39
III CODING AND LEARNING OF OLFACTORY INFORMATION .....	46
III.1. Coding and learning in the olfactory system .....	46
III.1.1. A review of the olfactory pathway .....	47

CHAPTER	Page
III.1.2. Experimental evidence for coding schemes and learning mechanisms in the olfactory bulb.....	50
III.2. Coding and learning with dynamical systems: computing with attractors .....	51
III.2.1. Dynamical systems and attractors .....	53
III.2.2. Fixed-point attractor networks .....	54
III.2.3. Limit-cycle attractor networks .....	57
III.2.4. Chaotic attractor networks .....	62
III.2.5. Neurodynamic models of the olfactory system.....	64
IV THE KIII MODEL .....	70
IV.1. The advent of the KIII model.....	70
IV.2. The KIII as a hierarchical model: the K sets.....	72
IV.2.1. The K0 set .....	72
IV.2.2. The KI set.....	74
IV.2.3. The KII set .....	77
IV.2.4. The KIII model.....	79
IV.3. Implementation aspects of the KIII.....	85
IV.3.1. Our implementation of the KIII .....	86
IV.4. Applications of the KIII model .....	88
V TEMPORAL CODING.....	92
V.1. Temporal coding and coherent oscillations.....	93
V.2. Phase coding in the KIII model .....	94
V.3. Scaling invariance .....	97
V.3.1. Bit recovery .....	101
V.3.2. Pattern recovery: preliminary results .....	102
V.4. Symmetry of the associative memory matrix.....	104
V.5. Pattern recovery: final results.....	106
V.6. Phase code with continuous patterns.....	110
V.7. Conclusions .....	114
VI CONTRAST ENHANCEMENT .....	117
VI.1. Contrast enhancement in the olfactory bulb .....	117
VI.2. Contrast enhancement through Hebbian/anti-Hebbian learning.....	119
VI.2.1. Adapted Hebbian/anti-Hebbian rule .....	120
VI.3. Formal analysis of the Hebbian/anti-Hebbian rule .....	125
VI.3.1. Feed-forward linear model.....	126
VI.3.2. Necessary conditions for orthogonalization.....	127

CHAPTER	Page
VI.3.3. Cross-talk elimination .....	130
VI.3.4. Formal proof of orthogonalization .....	131
VI.4. Characterization with synthetic inputs .....	135
VI.4.1. Qualitative analysis of the learning model .....	135
VI.4.2. Comparison with other methods .....	139
VI.5. Validation with sensor-array patterns .....	142
VI.5.1. Performance of the amplitude code .....	144
VI.5.2. Performance of the phase code .....	147
VI.5.3. Effect of concentration on the performance of the model....	149
VI.6. Discussion .....	150
VII BACKGROUND SUPPRESSION .....	153
VII.1. Habituation in the KIII model.....	155
VII.2. Characterization with synthetic data.....	160
VII.2.1. Binary patterns.....	160
VII.2.2. Continuous patterns .....	163
VII.2.2.1. Habituation without contrast enhancement .....	165
VII.3. Validation with sensor array patterns .....	167
VII.3.1. Habituation without contrast enhancement .....	168
VII.4. Conclusions.....	171
VIII NOVELTY DETECTION.....	173
VIII.1. Novelty detection with neural networks.....	175
VIII.2. Novelty detection with anti-Hebbian learning .....	176
VIII.3. Novelty detection in the KIII through anti-Hebbian learning .....	181
VIII.4. Characterization with synthetic data .....	184
VIII.4.1. Static inputs .....	184
VIII.4.2. Dynamic inputs.....	186
VIII.4.3. Receptive operating characteristic analysis.....	187
VIII.5. Validation with gas sensor array data.....	192
VIII.5.1. Cancellation of fluctuations in two simultaneous stimuli ..	194
VIII.5.2. Detection of a novel stimulus in the presence of a fluctuating background.....	196
VIII.5.3. Suppression of strong backgrounds.....	201
VIII.5.4. Sequential novelty detection .....	203
VIII.6. Discussion .....	208
IX CONCLUSIONS.....	212
IX.1. Future work .....	215
IX.1.1. Experimental .....	216

	Page
REFERENCES .....	218
APPENDIX A .....	249
APPENDIX B .....	251
VITA .....	253

## LIST OF FIGURES

	Page
Fig. 1. Operating principle of stannic oxide semiconductor sensors .....	10
Fig. 2. Structure of a MOS sensor. ....	13
Fig. 3. Pyrrol monomer and polypyrrol molecule .....	14
Fig. 4. MOSFET sensor .....	16
Fig. 5. QCM sensor.....	17
Fig. 6. SAW sensor in delay line configuration .....	19
Fig. 7. Statistical and ANN methods for gas sensor array processing.....	24
Fig. 8. Building blocks of the PRISM e-nose.....	28
Fig. 9. Experimental setup: sensor chamber, diluters, pump, instrumentation electronics, manifold and valves, air filters, flow buffer, flow meter, and analyte samples .....	29
Fig. 10. Close-up view of the sensor chamber.....	30
Fig. 11. Pump driver circuit.....	31
Fig. 12. Valve driver circuit.....	31
Fig. 13. Heater driver circuit .....	32
Fig. 14. MOS resistance measurement circuit .....	33
Fig. 15. Temperature measurement circuit.....	34
Fig. 16. Response of four MOS sensors Response of four MOS sensors to three analytes: allyl alcohol, tert-butanol, benzene at five different concentrations.....	37

Fig. 17. Repeatability of the response of four MOS sensors to three analytes: allyl alcohol, tert-butanol, benzene .....	38
Fig. 18. Discrimination measure between the three odors as a function of the heater voltage .....	40
Fig. 19. Experiment with tert-butanol and humidity .....	41
Fig. 20. Experiment with benzene and allyl alcohol .....	42
Fig. 21. Experiment with allyl alcohol and low concentration of benzene .....	43
Fig. 22. Experiment with tert-butanol, allyl alcohol, and benzene .....	44
Fig. 23. Experiment with tert-butanol, allyl alcohol, and benzene at low concentration .....	45
Fig. 24. Structure of the olfactory system .....	48
Fig. 25. Different attractor types: Fixed point, limit cycle, and chaotic.....	54
Fig. 26. Lyapunov function of a dynamical system.....	55
Fig. 27. Excitatory and inhibitory connections in the olfactory bulb model of Li and Hopfield.....	66
Fig. 28. Structure of the olfactory system model of Li and Hertz (2000) .....	67
Fig. 29. Inhibitory and excitatory connections in the neocortex model of Liljestrom .	69
Fig. 30. Recordings of a rabbit's olfactory bulb with a 8x8 array of electrodes when amyl acetate (banana oil) and air are presented.....	72
Fig. 31. Impulse response of an anesthetized population of neurons .....	74

Fig. 32. (left) The K0 set. (center) The KI excitatory set. (right) The KI inhibitory set.....	75
Fig. 33. Experimental determination of the output of a population of neurons in terms of its internal state .....	76
Fig. 34. (left) The regular KII set. (right) The reduced KII set. ....	78
Fig. 35. KII model structure .....	80
Fig. 36. The KIII dynamical behavior. ....	84
Fig. 37. Comparison of 1/f spectra of the basal state. ....	88
Fig. 38. Extracting phase information from the KIII model.....	96
Fig. 39. Overlap between input patterns for a 16-channel KIII.....	97
Fig. 40. Scatter plot of amplitude vs. phase codes for different input-stimulus → desired-response cases.....	99
Fig. 41. Univariate density functions for the amplitude and phase codes. ....	101
Fig. 42. Likelihood ratio test for the classification of channel activity. ....	103
Fig. 43. Performance of a Hamming-distance classifier on the two codes. ....	104
Fig. 44. Reduction of a 4-channel model to 11 non-isomorphic classes. ....	106
Fig. 45. (a) Pattern and overlap bits for a given Hebbian graph.....	108
Fig. 46. Overall performance of phase and amplitude codes as a function of pattern overlap.....	109
Fig. 47. Phase difference and amplitude as a function of distance (number of edges) to the input node .....	110

Fig. 48. Retrieval of continuous patterns through the amplitude and phase of the oscillations in the KIII.....	112
Fig. 49. Two bell-shaped patterns are used to train the KIII .....	113
Fig. 50. Ability of the phase and amplitude codes to recall an overlapping pattern ..	114
Fig. 51. Contrast enhancement in the olfactory bulb.....	118
Fig. 52. Linear associative memory with a feed forward network .....	120
Fig. 53. The network correlates or decorrelates the input and the output depending on their causal relationship .....	121
Fig. 54. Mitral to mitral connections of the reduced KIII model are trained with the Hebbian/anti-Hebbian rule .....	125
Fig. 55. Unfolding in time of a recurrent neural network.....	127
Fig. 56. Orthogonalization through competition across channels and within features	132
Fig. 57. Overlapping synthetic patterns used to characterize the Hebbian/anti-Hebbian learning rule .....	136
Fig. 58. Connections matrix. ....	137
Fig. 59. Activity of four KIII channels for the three synthetic odors patterns .....	138
Fig. 60. Overlapping binary patterns used to test model performance.....	140
Fig. 61. Separability of the output patterns against the level of noise introduced in the input patterns .....	141

Fig. 62. Response of the four MOS sensors to five different concentrations of allyl alcohol, tert-butanol, and benzene, first to third columns respectively.....	143
Fig. 63. Contrast enhancement in the KIII with experimental data from gas sensors	145
Fig. 64. Activity across odors of channels 34, 75, 98, 111, 219 and 224.....	146
Fig. 65. Contrast enhancement through phase coding in the KIII with experimental data from gas sensors .....	148
Fig. 66. Pattern separability at the input and output of the KIII as a function of the concentration of the analytes .....	150
Fig. 67. Connections from mitral cells to any other cells in the KIII model are adapted through habituation .....	156
Fig. 68. Habituation and dishabituation processes. ....	157
Fig. 69. (a) Habituation in the KIII is effected through mitral connections .....	159
Fig. 70. Binary patterns used to characterize the habituation mechanism.....	160
Fig. 71. Habituation scenarios .....	162
Fig. 72. Overlapping bell-shaped patterns used to characterize the habituation mechanism.....	164
Fig. 73. Evolution of the KIII activity in a habituation experiment with synthetic patterns .....	165
Fig. 74. Habituation experiment without contrast enhancement .....	166

Fig. 75. Gas sensor response to tert-butanol, a binary mixture of tert-butanol and allyl alcohol, and a ternary mixture of tert-butanol, allyl alcohol, and benzene.....	168
Fig. 76. Habituation scenario with experimental data from a gas sensor .....	169
Fig. 77. Habituation to gas-sensor-array responses without contrast enhancement ...	170
Fig. 78. Novelty detection with a feed forward single-layer network .....	177
Fig. 79. Novelty detection with a single-layer recurrent network as used by Kohonen and Oja (1976) .....	179
Fig. 80. Periglomerular to periglomerular lateral connections are trained with the proposed anti-Hebbian rule .....	182
Fig. 81. Two layers of PG cells .....	183
Fig. 82. Characterization with synthetic data .....	185
Fig. 83. Projection performed by the novelty detector .....	186
Fig. 84. Novelty detection with oscillatory patterns.....	187
Fig. 85. Simulated scenario to perform ROC analysis .....	191
Fig. 86. ROC curves for three different values of the maximum amplitude of the target odor .....	192
Fig. 87. Novelty detection with DC offset and without DC offset.....	193
Fig. 88. Cancellation of fluctuations in two simultaneous stimuli .....	195
Fig. 89. Detection of benzene in the presence of a fluctuating background of tert-butanol .....	197

	Page
Fig. 90. Effect of the anti-Hebbian learning rate on the detection of a new odor .....	198
Fig. 91. Detection of benzene with discontinuous training .....	199
Fig. 92. Detection of benzene on a background of tert-butanol using only the response of sensors 1 and 2 in Fig. 89(b) .....	200
Fig. 93. Suppression of strong background odor with continuous anti-Hebbian training .....	202
Fig. 94. Suppression of a strong background when anti-Hebbian learning is stopped after the system habituates .....	203
Fig. 95. Novelty detection with two background odors .....	205
Fig. 96. Output of the KIII model to the experiment in Figure 95 .....	206
Fig. 97. Exploring the detection limits of the novelty detector .....	207
Fig. 98. Variations on humidity and allyl alcohol concentration .....	209
Fig. 99. Response of the MOS sensors to increasing concentrations of allyl alcohol under fluctuations in humidity .....	210
Fig. 100. Spike-time dependent learning rule .....	250
Fig. 101. Illustration of the between class-scatter $S_B$ , and within class-scatter $S_w^1, S_w^2$ for a two-class problem .....	252

## LIST OF TABLES

	Page
Table 1. Survey on e-nose research (1982-2005).....	6
Table 2. Dilution factors.....	36
Table 3. Parameter values for the KIII model.....	87
Table 4. Euclidean distance and corresponding overlap between patterns A and B....	113

# CHAPTER I

## INTRODUCTION

Arrays of broadly-selective chemical sensors, also known as electronic noses, have been developed during the past two decades as a low-cost and high-throughout alternative to analytical instruments for the measurement of odorant chemicals. Signal processing in these sensors arrays has been performed by means of statistical and neural pattern recognition techniques. The objective of this dissertation is to develop new computational models for gas sensor arrays inspired by information processing in the biological olfactory pathway.

The olfactory system and gas sensor arrays rely on an analogous approach for the representation of odorant information: distributed activation across a population of cross-selective sensory units (Pearce, 1997a; Pearce, 1997b). Each odorant elicits a particular pattern of activity across olfactory receptor neurons (Malnic et al., 1999) (the biological counterparts of odor sensors) and, likewise, a particular response pattern across gas sensors in an array (Persaud and Dodd, 1982). This analogy suggests that olfactory information processing mechanisms in the olfactory system may also be applicable to the processing of gas sensor array signals.

Particularly, we propose to explore two relevant aspects of olfactory information processing, namely neural coding (Laurent, 1997) and learning (Brennan and Keverne, 1997). Given that both concepts (coding and learning) are broadly used in a number of disciplines, a concrete definition of these terms in the context of this dissertation is first proposed. By *neural coding* we shall refer to how information is transmitted from neuron to neuron. A number of coding mechanisms have been proposed in the literature, including frequency rate, inter-spike latency and firing synchrony (Cariani, 1995). **(i)** We propose to explore and compare two such coding schemes, one based on temporal information, namely synchrony of neural activity (i.e., phase coding), and a second based on stationary information, namely temporal averaging of neural activity (i.e., firing-rate coding). By *learning* we shall refer to the modification of a neural circuit to optimize the function performed by the system with respect to the stimuli. We propose to use two biologically-inspired learning mechanisms, Hebbian and habituation learning, to realize three known processing functions of the olfactory system: **(ii)** Odor contrast enhancement, **(iii)** Background suppression, and **(iv)** Novelty detection. Items **(i)** through **(iv)** above form the backbone of the research developed in this dissertation.

We propose to investigate these processing principles using the KIII, a neurodynamic model of the olfactory system that has been developed by Freeman and colleagues over the past thirty years (Yao and Freeman, 1990). The KIII captures the mesoscopic oscillatory behavior of the olfactory system (Freeman, 1975), which emerges as a result of the coupling between excitatory and inhibitory neuron populations. We argue that the

KIII operates at an appropriate level of abstraction (i.e., neural ensembles) for the study of biologically-inspired pattern recognition, yet the model displays a richer dynamic behavior, in the form of oscillatory patterns, than fixed-point attractor networks (e.g., Hopfield models). In recent years, encoding schemes using bifurcational limit-cycle patterns (Freeman, et al., 2000), such as those produced by the KIII, have been shown to have resistance to noise and higher storage capacity (Kozma and Freeman, 2000; Kozma and Freeman, 2001; Kuzmina et al., 2001).

### **I.1. Contributions of this work**

Despite the parallelisms between the olfactory system and gas sensor arrays, as well as the successful application of neuromorphic solutions with other sensory modalities (Mahowald and Mead, 1991), biologically-inspired solutions have been mostly disregarded in the gas-sensor-array community (Pearce et al., 2003). The research conducted in this dissertation aims at exploring this largely uncharted territory: neuromorphic processing mechanisms for gas sensor arrays. The main contributions of the research conducted in this dissertation can be summarized as follows:

- (1) We propose a new coding mechanism for the KIII model based on the synchrony of oscillations in the network.
- (2) We propose a new learning mechanism with Hebbian and anti-Hebbian terms that improves contrast between gas sensor array patterns
- (3) We develop a local habituation mechanism and combined it with the contrast enhancement rule to perform background suppression on gas sensor array patterns.

- (4) We propose an anti-Hebbian rule that allows the KIII model to perform novelty detection on experimental data from gas sensor arrays.

## **I.2. Organization of the dissertation**

Chapter II and Chapter III present a review of the two key areas upon which this dissertation builds: electronic nose technology and coding and learning of olfactory information, respectively. Chapter II also includes description of the e-nose prototype built to address the experimental requirements of this dissertation. Chapter IV is devoted to a thorough description of the KIII model. In Chapter V we address the issue of temporal coding in the KIII model, and study how the information extracted from an oscillatory network can be enhanced by considering the temporal dimension. In Chapter VI, we propose a combination of Hebbian and anti-Hebbian learning to increase the contrast between sensor response patterns across odors. Habituation is used in Chapter VII to perform background suppression following the previous contrast-enhancement stage. In Chapter VIII anti-Hebbian learning is used to adapt the system to previous stimuli and environmental changes, keeping it ready to detect new stimuli. Finally, Chapter IX draws conclusions from this dissertation and suggests directions for future work. Supplementary information describing the relationship between spike-dependent synaptic plasticity and the Hebbian rule proposed in Chapter VI is included in Appendix A; the use of the Fisher discriminant ratio as a distance measure is covered in Appendix B.

## **CHAPTER II**

### **THE ELECTRONIC NOSE**

This chapter presents a review of the electronic nose technology, including different gas sensing technologies as well as statistical and neuromorphic approaches to signal processing for gas sensor arrays. The prototype system built for the purpose of data collection is also described in this chapter.

#### **II.1. The electronic nose technology**

An electronic nose (e-nose) consists of an array of cross-selective gas sensors coupled with a pattern recognition engine capable of detecting, identifying and quantifying volatile compounds. Since the e-nose paradigm was first conceived by Persaud and Dodd (1982), a number of gas sensor technologies and pattern recognition techniques have been used to tackle a large number of gas detection applications. Table 1 presents a sample of the last twenty years of research on electronic noses. Applications using MOS sensors clearly outnumber those using any other gas sensor type, mainly due to their broad commercial availability and higher sensitivity to a number of industrial volatiles (an overview of the different gas sensor technologies is provided in section II.1.1). Pattern recognition for e-noses has in turn been dominated by statistical methods and artificial neural networks, whereas neuromorphic processing, the subject of this

dissertation, has been largely disregarded. A few notable exceptions of biological inspired processing for e-noses are reviewed in section II.1.3.2.

Table 1 Survey on e-nose research (1982-2005). Sensor types: quartz crystal microbalance (QCM), surface acoustic waves (SAW), metal oxide semiconductor field effect transistor (MOSFET), metal oxide semiconductor (MOS). Pattern recognition techniques: multilayer perceptron (MLP), principal components analysis (PCA), linear discriminant analysis (LDA), fuzzy learning vector quantization (FLVQ), optimal control theory (OCT), cluster analysis (CA), perceptron (P), adaptive least squares (ALS), probability neural networks (PNN), correlation (CO), discrete function analysis (DFA), multivariate analysis of variance (ANOVA), partial least squares (PLS), self-organizing maps (SOM), least squares (LS), k nearest neighbors (KNN), fuzzy C means (FUZZ), radial basis functions (RBF), and multi-exponential analysis (MA).

Chemo-sensor type	Number of sensors	Applications	Pattern recognition	Reference
QCM	8	Perfume, fruity flavors	MLP, PCA	Nakamoto et. al (1993)
QCM	8	Essential oils	PCA	Ide et al. (1993)
QCM	6	Alcoholic drinks	MLP, LDA	Ema et al. (1993)
QCM	8	Whisky aroma	MLP	Nakamoto et al. (1991)
QCM	8	Whisky aroma	MLP	Nakamoto et al. (1990)
QCM	8	Fragrances	PCA	Yokohama and Ebisawa (1993)
QCM	3	Harmful gases	PCA	Mosley, (1988)
QCM	6	Perfumes	FLVQ	Okahata and Shimizu (1997)
QCM	8	Bitter substances	none	Okahata and En-na (1989)
QCM	15	Citrus flavor	OCT	Wyszynski et al. (2005)
SAW	4	Organic gases	none	Chang et al. (1991)
SAW	12	Organic gases	PCA, CA, P,	Ballentine et al. (1986)
SAW	10	Hazardous gases	CA	Rose-Pehrsson, et al. (1988)
SAW	12	Organic gases	CA	Rose-Pehrsson and Grate (1993)
SAW	8	Wines	LDA, PCA	Santos et al. (2005)

Table 1 Continued

Chemo-sensor type	Number of sensors	Applications	Pattern recognition	Reference
FET, MOS	15	Meats	MLP	Winqvist et al. (1993)
FET	324	Ammonia, hydrogen, and ethanol	none	Lundström et al. (1991)
MOS	3	Alcohols and tobacco	CO	Shurmer et al. (1989)
MOS	12	Coffees	DFA, ANOVA	Gardner and Shurmer (1992)
MOS	12	Alcohols and beverages	PCA, CA	Gardner (1991)
MOS	12	Alcohols	MLP	Gardner and Hines (1990)
MOS	12	Alcohols and beers	MLP	Gardner et al. (1992)
MOS	3	Organic gases	PCA, CA, PLS	Wamsley et al. (1991)
MOS	12	Wines	MLP, SOM	Corcoran and Lowery (1995)
MOS	6	Organic gases	LS	Hoffheins and Lauf (1998)
MOS	8	Methanol and acetone	MLP	Wang et al. (1993)
MOS	8	Benzene, toluene, and acetone, trichloroethylene	MLP	Wang et al. (1993)
MOS	6	Organic gases	LS	Ikegami and Kaneyasu (1985)
MOS	8	Alcohols and ketons	CA	Abe et al (1987)
MOS	7	Alcohols and ketons	k-NN, CA	Abe et al. (1988)
MOS	6	coffee	PCA	Aishima (1991a)
MOS	6	Alcoholic drinks	LDA, CA	Aishima (1991b)
MOS	3	Organic gases	MLP	Nakamoto et al. (1992)
MOS	6	Simulated	SOM	Davide et al. (1994)
MOS	4	Teas	PCA, FUZ, SOM, RBF, PNN, MA	Dutta et al. (2003)
MOS	4	Organic gases	PCA	Gutierrez-Osuna et al. (2003)
MOS	14	Wines	PCA	Rodriguez-Mendez et al (2004)

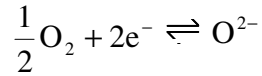
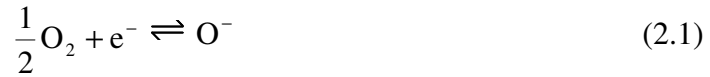
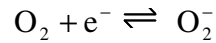
### II.1.1. Gas sensor types

Several types of broadly selective gas sensors are commonly employed in e-noses: chemoresistors, potentiometric sensors, and gravimetric sensors (Pearce et al., 2003). Chemoresistors are the most widely used gas sensor technology. These devices are

based on changes in the conductivity of an active material by chemical reaction with or absorption of gaseous molecules. Chemoresistive sensing materials include metal oxide semiconductors (MOS) and organic conducting polymers (CP). Potentiometric sensors exploit changes in the gate voltage of a MOS field effect transistor (MOSFET) when a volatile chemical is present. The last type of device discussed here are gravimetric gas sensors, which measure the mass of volatile chemicals adsorbed by certain active materials. This transduction principle includes quartz crystal microbalance (QCM) and surface acoustic waves (SAW) sensors. Optical sensors are an alternative but not commonly used type of gas sensors; for this reason they are not included in this review.

#### **II.1.1.1. Metal Oxide Semiconductor (MOS) sensors**

MOS sensors detect chemical volatiles through a change of their conductivity. Different materials have been used to build this type of sensors, including  $\text{SnO}_2$ ,  $\text{ZnO}$ ,  $\text{Fe}_2\text{O}_3$ , and  $\text{WO}_3$ . However, only sensors based on stannic oxide ( $\text{SnO}_2$ ) have been widely manufactured and utilized (Ikohura and Watson, 2000). Fig. 1(a) shows a micrograph of the stannic oxide material ( $\text{SnO}_2$ ) used in commercial MOS sensors. The transduction principle of these sensors is based on the adsorption and desorption of ambient oxygen molecules by the stannic oxide. At temperatures of 100-520°C (Yamazoe, 1979), these semiconductor materials adsorb ambient oxygen as negatively-charged ion species  $\text{O}^-$ ,  $\text{O}_2^-$ ,  $\text{O}^{2-}$  (Fig. 1(b)) (Mizokawa, 1997). The adsorbed oxygen ions bind electrons of the semiconductor conduction band according to the following equilibrium reactions (Ikohura and Watson, 2000):



These reactions occur at different temperatures creating a different distribution of oxygen ions at the surface of the stannic oxide for different temperatures. As reviewed in (Yamazoe , 1979),  $\text{O}_2^-$  is formed at about 100°C, while  $\text{O}^-$  and  $\text{O}^{2-}$  appear at higher temperatures. In a different study (Iwamoto, 1989), it was reported that  $\text{O}_2^-$  exist on the surface of the stannic oxide only in a temperature range below 150°C, whereas  $\text{O}^-$  can be found at temperatures up to 400°C. This study also suggested that between 400°C and 500°C the only oxygen ion present is  $\text{O}^{2-}$ . This distribution of oxygen ions on the surface of the sensor makes it possible for the semiconductor to interact with reducing chemical gases in contact with the sensor. The temperature dependence of the oxygen ion species is used to customize sensors for different applications (e.g.,  $\text{CO}_2$  vs.  $\text{NO}$ ) by operating them at the temperature of maximum sensitivity to the target gas, and is also the basis of the temperature modulation procedures we will employ in this dissertation.

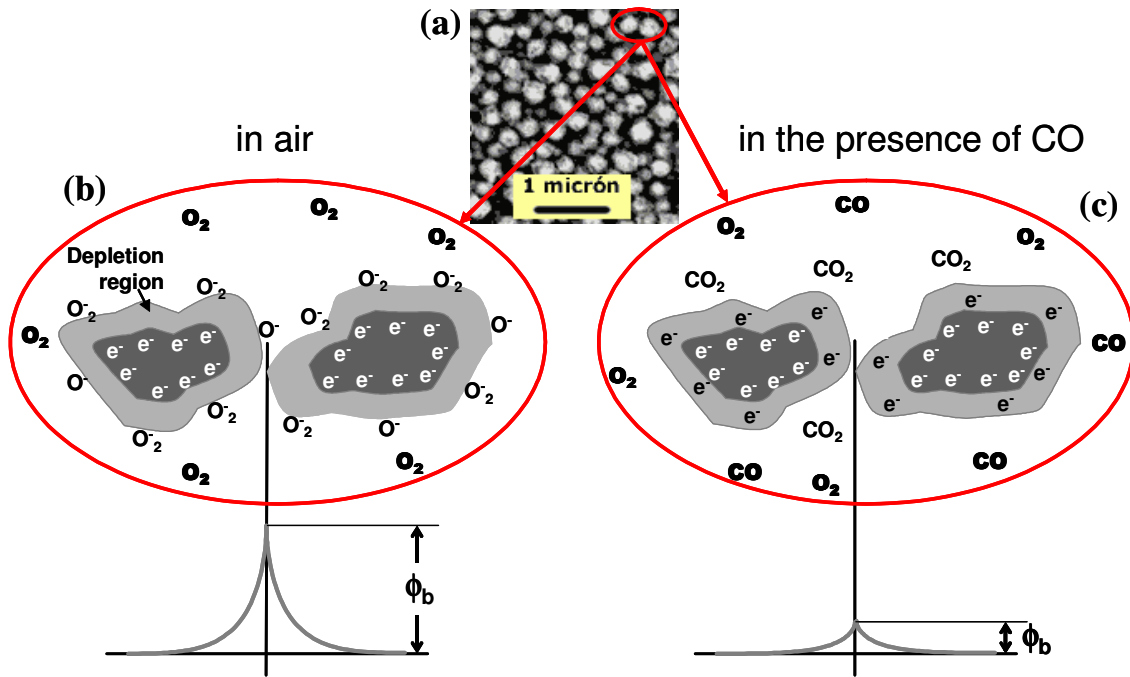
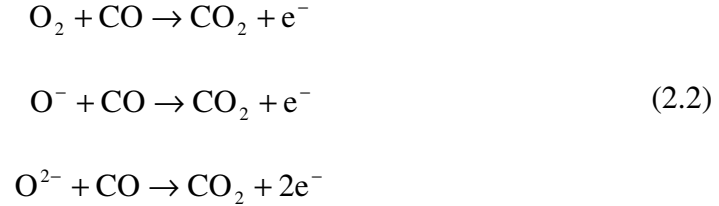


Fig. 1 Operating principle of stannic oxide semiconductor sensors. (a) Micrograph of the stannic oxide material (SnO<sub>2</sub>). (b) Stannic oxide in the presence of air. Oxygen ions are adsorbed at the surface, trapping electrons from the semiconductor conduction band. This increases the potential barrier  $\phi_b$ , which represents a decrease in the conductivity of the semiconductor. (c) Stannic oxide in the presence of CO. Carbon monoxide molecules react with adsorbed oxygen ions, releasing trapped electrons back into the conduction band. This causes the potential barrier  $\phi_b$  to decrease, which in turn increases the conductivity of the semiconductor (adapted from Figaro, 1996).

When presented to the sensor (Fig. 1(b)), a reducing volatile chemical such as CO or a combustible gas will react with the chemisorbed oxygen molecules, altering their

concentration at the surface of the semiconductor. In the case of CO, the reaction with adsorbed oxygen species follows Ikohura and Watson, 2000:



These reactions will then release the electrons trapped by the oxygen molecules back into the conduction band of the semiconductor, causing an increase in the conductivity of the sensor. This conductivity change is a common response of the semiconductor to any reducing gas. The opposite response can also be obtained from the stannic oxide semiconductor when interacting with oxidizing gases. In this case, the conductance increases since the oxidizing gas will trap electrons from the conductance band of the semiconductor.

These interactions can be explained by Potential barrier theory (Morrison, 1977), which links the trapping of electrons on the surface with the change in conductivity of the semiconductor. The trapping of electrons builds up a potential barrier between the grains of stannic oxide (Fig. 1(a)) that decreases the conductivity of the semiconductor. The potential barrier is lowered when a reducing gas reacts with the surface oxygen species releasing the trapped electrons (Fig. 1(b)). As a consequence, the conductivity

of the stannic oxide increases. The height of the potential barrier and the conductance of the semiconductor are related by the following expression:

$$G = G_0 \exp\left(-\frac{\phi_b}{kT}\right) \quad (2.3)$$

where  $G_0 = gq\mu_s N_d$ ,  $g$  is a constant determined by the semiconductor geometry,  $q$  is the electronic charge,  $\mu_s$  is the mobility of the electrons,  $N_d$  is the density of donors in the semiconductor,  $\phi_b$  is the potential barrier shown in Fig. 1(a) and (b),  $k$  is Boltzman's constant, and  $T$  is the temperature.

Fig. 2(a) shows the different components of a MOS sensor: a sensing layer, sensing electrodes (to measure changes in the conductivity of the sensing layer), and a resistive element. The resistive element is needed to bring the oxide to an optimal temperature (typically between 300 and 500 °C) since oxygen molecules are not chemisorbed at room temperature. Traditionally, MOS sensors have been operated at a fixed temperature. In recent years, however, it has been shown that by modulating the temperature of the sensor it is possible to obtain more information about the chemical stimulus (Gutierrez-Osuna, et al., 2003). This technique, known as temperature modulation (Lee and Reedy, 1999), is used in most of the experiments conducted in this dissertation, and will be reviewed in section II.1.2.

MOS have several advantages as compared with other sensor types: namely high sensitivity (sub-ppm for a number of volatile species), temperature modulation, and economic manufacturing cost. On the other hand, these materials have poor selectivity and high power consumption.

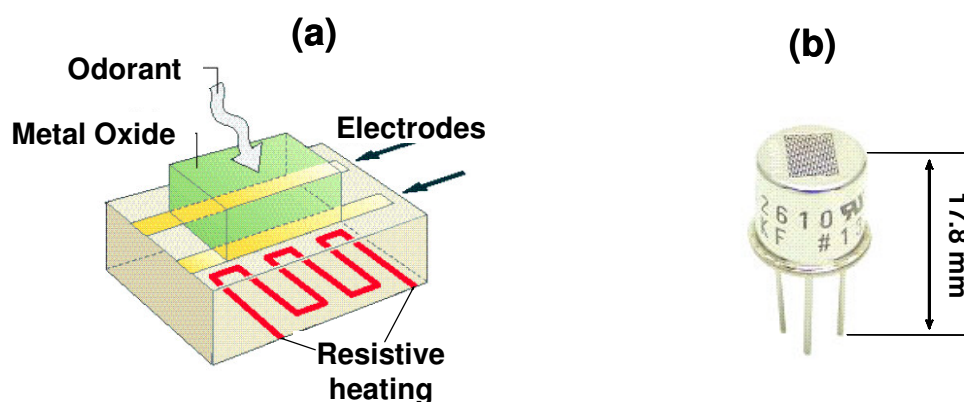


Fig. 2 Structure of a MOS sensor. (a) A MOS sensor comprises a metal oxide material, sensing electrodes, and a resistive heater (adapted from Nagle, Schiffman, and Gutierrez-Osuna, 1998). (b) Typical TO-5 packaging for a commercial MOS sensor TGS2610 (adapted from Figaro, 1996).

#### II.1.1.2. Conducting polymer (CP) sensors

CP sensors are also based on the chemoresistive principle: interaction with organic vapors changes the conductivity of the sensing layer. The most commonly utilized sensing materials in these devices are polypyrrole (Fig. 3), polyaniline, polythiophene, and polyacetylene, which are based on pyrrole, aniline or thiophene monomers, respectively (Pearce et al., 2003). Fig. 3 shows a polypyrrol polymer formed by six

pyrrole monomers. The polymer structure is formed by a chain of organic molecules which generate a large molecular orbital along the chain, allowing conductivity through the polymer. Chemical gases produce reversible changes in the conductivity of the polymers when they are absorbed and desorbed. The exact mechanism through which this conductivity change occurs is not clear at present (Pearce et al., 2003).

CPs have high sensitivity (below 20 ppm for a number of volatiles), and their selectivity can be altered by substitution of the side groups in the backbone. This makes it possible to design a large number of different CP sensors. An added advantage of CP sensors is that they are operated at room temperature, which reduces power consumption when compared with MOS sensors. The main drawback of CP sensors is high sensitivity to humidity and ambient temperature changes.

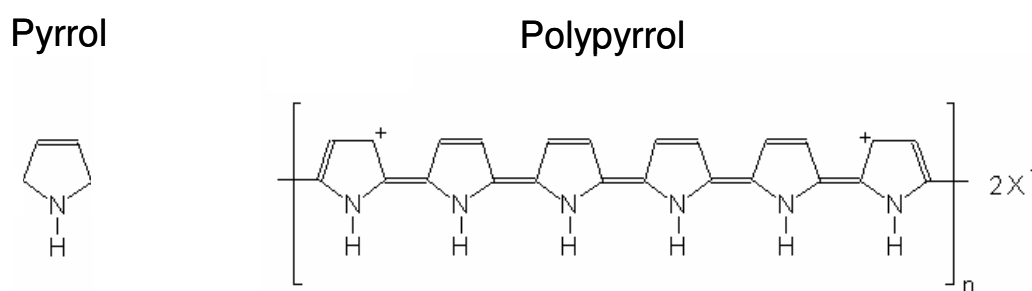


Fig. 3 Pyrrole monomer and polypyrrole molecule (adapted from Mark, Alloc, and Lampe, 1990).

#### **II.1.1.3. Metal Oxide Semiconductor Field Effect Transistor (MOSFET) sensors**

MOSFET gas sensors are regular MOSFET transistors in which the gate is made of a catalytic metal, such as palladium, platinum, or iridium (Gardner and Barlett, 1999; Pearce et al., 2003). These catalytic metals can produce a reaction when in contact with volatile organic compounds. The products of this reaction diffuse through the gate of the MOSFET (Fig. 4), creating a dipole layer at the metal-insulator (metal-oxide) interface. This dipole layer, change the I-V characteristic of the transistor. This metal-oxide-semiconductor structure has been also used as a gas sensitive capacitance. In this case, the dipole layer changes the capacitance-voltage characteristic of the device (Gardner and Barlett, 1999).

The main advantage of MOSFET sensors is that they can be fabricated using integrated circuit technology, which also increases their repeatability. However, because of the lack of variety in sensitive materials, MOSFET have not been used as widely as MOS or CP devices.

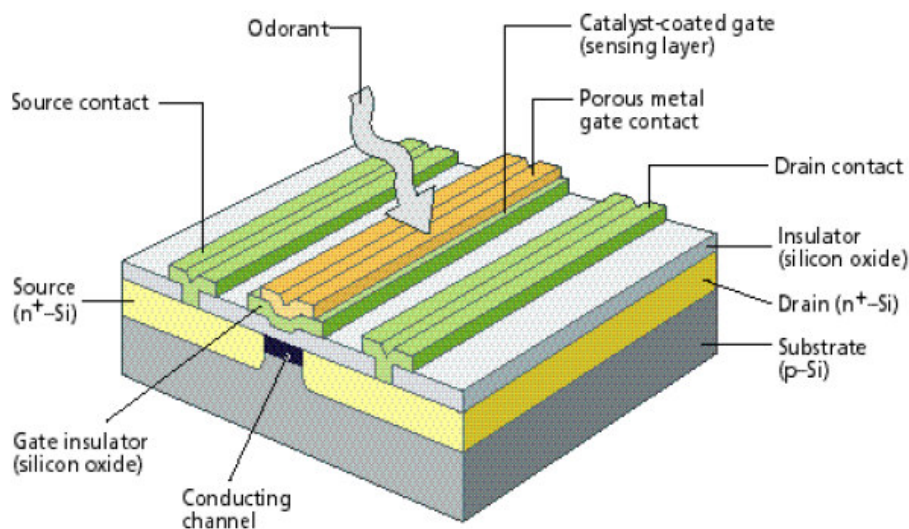


Fig. 4 MOSFET sensor. The gate of the sensors is made of a catalytic metal, such as palladium, platinum, or iridium, which makes the sensor sensitive to volatile organic compounds (adapted from Nagle, Schiffman, and Gutierrez-Osuna, 1998).

#### II.1.1.4. Quartz Crystal Microbalance (QCM) sensors

Depicted in Fig. 5, a QCM device consists of a (typically) AT-cut of a single crystal quartz, a metal electrode on each surface of the crystal, and a sensing material deposited atop the crystal (Gardner and Barlett, 1999; Pearce et al., 2003). The device operates as a resonator: application of an AC voltage between the electrodes causes the quartz crystal to oscillate at a characteristic frequency due to the piezoelectric effect. Since the oscillation frequency of the QCM varies with the mass of the sensor, absorption of odorants in the coating material can be detected as shift in resonant frequency. Several types of coating materials can be used to build QCM devices with different response

profiles to odorants. The most commonly used materials are stationary phases from GC columns, which can have different polarities, and lipid materials. The main advantage of these sensors is their high selectivity due to the different coatings that can be deposited on the sensor. Drawbacks are low sensitivity, high cost, reproducibility, drift, and a relatively large size of the sensor.

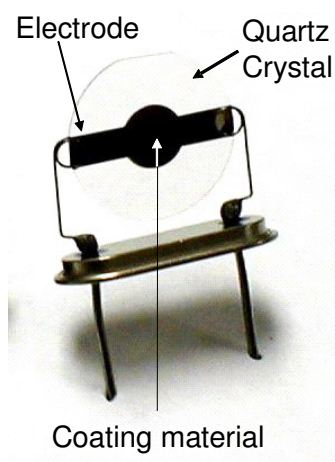


Fig. 5 QCM sensor. A QCM sensor comprises a cut of a single crystal quartz with one metal electrode on each surface. An active coating material is deposited on top of the electrodes (Adapted from: <http://www.4timing.com/crypicture/FTQCMA-HC51U.jpg>).

#### **II.1.1.5. Surface Acoustic Wave (SAW) sensors**

SAW sensors are also based on piezoelectric materials, but they rely on a different transduction principle than QCM sensors. SAW sensors comprise a thick plate of piezoelectric material (e.g., ZnO and lithium niobate) coated with a sorbent membrane (polymer), and interdigitated electrodes to excite the oscillation of the surface (Fig. 6)

(Gardner and Barlett, 1999; Pearce et al., 2003). This type of sensors can be operated in two different configurations: delay line or resonator. In the delay line configuration, two interdigitated electrodes are situated at both extremes of the piezoelectric plate (Fig. 6). One of the set of electrodes is excited with an AC signal which, by virtue of the piezoelectric effect, generates a mechanical oscillation on the surface of the plate. These oscillations are transmitted as a wave crossing the active membrane, and reach the other side of the plate, where they are converted back into an electrical signal at the output electrode. The amount of gas adsorbed is measured as the delay of the acoustic wave in reaching the second group of electrodes, since the wave velocity is affected by the adsorbed gas. In the resonator configuration, there is only one group of interdigitated electrodes, which are used as emitters and receivers. The electrodes are situated at the middle of the piezoelectric plate and two grooves are formed at both extremes of the plate to reflect the acoustic waves. The operation principle of the resonator is the same as the delay line configuration. SAW sensors can be built using photolithographic methods, and there are many polymer coatings available. The main disadvantage of SAW sensors is the complexity of the instrumentation required to interface the devices.

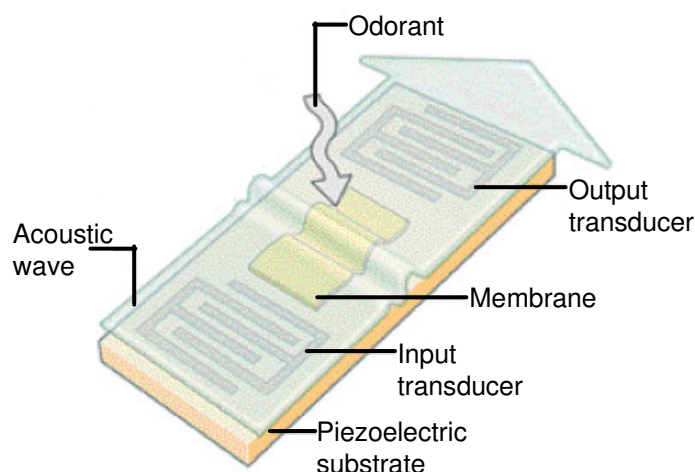


Fig. 6 SAW sensor in delay line configuration. An acoustic wave is generated by one of the group of electrodes and received by the opposite interdigitated electrodes. The traveling time of the acoustic wave is used to estimate the amount of gas adsorbed by the active material (adapted from Nagle et al., 1998).

### II.1.2. Temperature modulation in MOS sensors

As already described in section II.1.1.1, the selectivity of a MOS sensor is a function of its operating temperature. This temperature-selectivity dependence can be exploited to improve the information content of the sensor by modulating the operating temperature of the device during exposure to analytes and processing the resulting dynamic response (Lee and Reedy, 1999). Temperature modulation approaches for MOS sensors can be broadly classified into two categories: temperature cycling and thermal transients. In temperature cycling, the sensor is excited with a periodic heater voltage, typically a sinusoidal waveform or a ramp. To help resolve the various peaks in sensitivity that

may occur during the cycle, a slow varying profile (sinusoidal or ramp) is often desirable (Gutierrez-Osuna et al., 2003). If the heater waveform is slow enough to allow the sensor to approach the set-point temperature, the behavior of the sensor at each temperature may then be treated as a “pseudo-sensor” by virtue of the relationship between operating temperature and sensor selectivity. In thermal transients, on the other hand, the sensor is driven by a step or pulse waveform in the heater voltage, and the discriminatory information is contained in the chemical transient induced by the fast change in temperature.

To the best of our knowledge, the work of Sears, Colbow, and Cansadori, 1989a, and Sears, Colbow, and Cansadori, 1989b constitutes one of the first studies on temperature cycling for metal-oxide sensors. The authors used a Figaro sensor with a sinusoidal heater voltage, and analyzed selectivity and sensitivity as a function of the frequency and the heater voltage for different analyte concentrations. For more than a decade, Nakata and co-workers (Nakata et al., 1991; Nakata, Nakamura, and Yoshikawa, 1992; Nakata, et al., 1998) have also used a sinusoidal heater voltage for temperature modulation purposes. The authors transformed the sensor response into the frequency domain by means of the fast Fourier transform (FFT), and used the coefficients of higher harmonics to discriminate various analytes. Nakata et al. (1996) and Nakata and Yoshikawa (1996) also applied these procedures to qualitatively characterize the mixtures of two gases. However, no quantitative classification was performed. Heilig et al. (1997) used multi-layer perceptrons (MLPs) to process FFT features from the sensor response to a

sinusoidal temperature modulation. The authors utilized two separate MLPs to perform a quantitative and qualitative analysis of the gases. The MLPs were able to detect the presence of an analyte in a mixture and predict the concentration of a single gas and gas mixtures. Llobet et al. (2001) applied the discrete wavelet transform to extract features from the sensor response, and showed that they are more informative than those provided by the FFT. The authors used two different neural networks, fuzzy ARTMAP and MLPs, coupled with leave-one-out and bootstrap for validation purposes. Perez-Lisboa et al. (1999) used the DC and AC root-mean-squared (RMS) values from the sensor response to a periodic excitation signal. Wlodek et al. (1991) used a ramp as a heater excitation signal. The response of the sensor was modeled with a family of Gaussian curves, after which the parameters of the curves were used as features. Using micro-hotplate sensors, Kunt and co-workers (Kunt, 1997; Kunt et al., 1998) developed a numerical optimization procedure capable of deriving a temperature profile that maximized the discrimination between two analytes of interest.

In the realm of temperature modulation with transients, Hiranaka et al. (1992) analyzed the cooling temperature transients when the heater supply was switched from a high voltage to a low voltage.

The response of the sensor for different odors presented peaks at different positions in the transient. Similar results were also achieved by Amamoto et al. (1993). Kato et al. (1997) used a pulse signal to drive the heater voltage of a stannic oxide gas sensor. A phenomenological equation with four parameters was used to model the sensor response to each analyte, after which the model parameters were used as features. Yea et al. (1997) used a train of pulses to discriminate and quantify flammable gases. The authors processed the sensor response with the FFT, and the AC components were passed to an MLP to determine which odor was present. Once the odor was recognized, the output of the MLP and the DC component of the FFT were passed to a neuro-fuzzy algorithm to estimate the concentration.

### **II.1.3. Signal processing for gas sensor arrays**

The multivariate response of the gas sensor array can be used as a fingerprint to identify odors. This response has been traditionally processed with statistical methods (Duda et al., 2001) and artificial neural networks (ANN) (Haykin, 1999) (Table 1). Recent work has started to consider alternative processing strategies for gas sensor arrays based on biologically-inspired models (Pearce, 1997a; Pearce, 1997b). In this section, we review both approaches to gas sensor array signal processing.

### **II.1.3.1. Statistical and ANN methods**

Following the classical pattern-recognition architecture, the processing of gas sensor array signals can be divided into a number of steps (Gutierrez-Osuna, 2002): (1) preprocessing, where the sensor signal is prepared for further processing (e.g., drift compensation, concentration normalization); (2) dimensionality reduction, where the dimensionality of the input signal is reduced to avoid problems associated with high-dimensionality data; (3) prediction, where the interesting properties of the sample are estimated (e.g, class membership, related odor samples) ; and (4) validation, where model and parameter settings are selected in order to optimize a criterion function (e.g., classification rate, mean-squared error).

Fig. 7 shows a summary of statistical and ANN methods that have been used to process gas sensor array signals. These methods are broadly classified into three categories: dimensionality reduction, classifiers, and clustering methods. Readers are referred to (DeCoste et al. 2001; Gutierrez-Osuna, 2002; Pearce et al., 2003) for a thorough review of these methods.

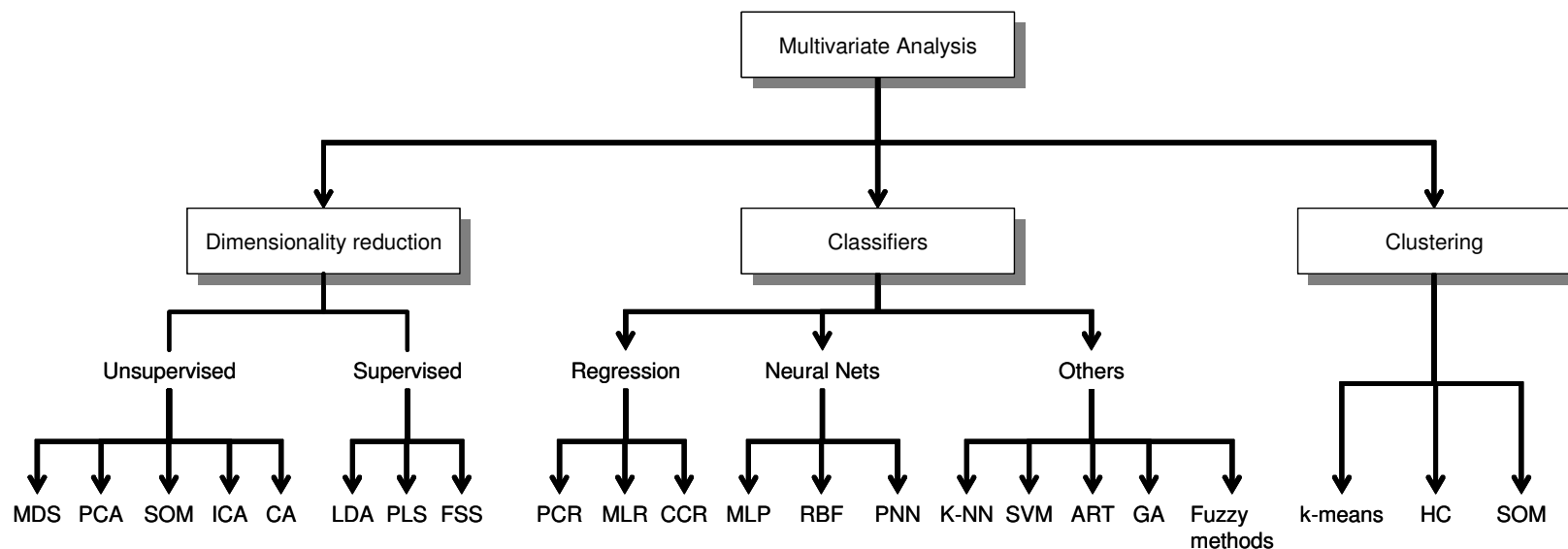


Fig. 7 Statistical and ANN methods for gas sensor array processing (DeCoste et al. 2001; Gutierrez-Osuna, 2002; Pearce et al., 2003). MDS- Multi-Dimensional Scaling, PCA- Principal Component Analysis, SOM- Self-Organized Maps, ICA- Independent Component Analysis, CA- Cluster Analysis, LDA- Fisher's Linear Discriminant Analysis, PLS- Partial Least Squares, FSS- Feature Selection Search, PCR- Principal Component Regression, MLR- Multi Linear Regression, CCR- Canonical Correlation Regression, MLP- Multi-Layer Perceptron, RBF- Radial Basis Functions, PNN- Probabilistic Neural Network, k-NN- k-Nearest Neighbors, SVM-Support Vector Machines, ART- Adaptive Resonance Theory, GA- Genetic Algorithms, and HC- Hierarchical Clustering.

### **II.1.3.2. Neuromorphic processing for chemical sensor**

Neuromorphic approaches for gas sensor arrays have been traditionally disregarded by the e-nose community. However, recent neurophysiological findings (Buck and Axel, 1991; Vassar et al., 1994) in the olfactory system along with a growing body of knowledge from computational neuroscience (Davis and Eichenbaum, 1991), have made neuromorphic signal processing techniques a recent focus of attention.

Ratton et al. (1997) employed the olfactory model of Ambros-Ingerson et al. (1990), which simulates the closed-loop interactions between the olfactory bulb and higher cortical areas. The model performs a hierarchical processing of an input stimulus into increasingly finer descriptions by repetitive projection of bulbar activity to (and feedback from) the olfactory cortex. Ratton et al. (1997) used the model to classify data from a micro-hotplate MOS excited with a saw-tooth temperature profile. Sensor data was converted into a binary representation by means of thermometer and Gray coding, which was then used to simulate the spatial activity at the olfactory bulb. Their results showed that classical approaches (Gram-Schmidt orthogonalization, fast Fourier transform and Haar wavelets) yield better classification performance. This is, however, a reasonable result given that the thermometer and Gray codes are unable to faithfully simulate the spatial activity at the olfactory bulb, where the most critical representation of odor stimuli is formed.

White et al. (1998) and White and Kauer (1999), employed a spiking neuron model of the peripheral olfactory system (White et al., 1992) to process signals from a fiber-optic sensor array. In their model, the response of each sensor was converted into a pattern of spikes across a population of ORNs, which then projected to a unique mitral cell (MC). Different odors produced unique spatio-temporal activation patterns across MCs, which were then discriminated with a delay line neural network (DLNN). Their OB-DLNN model was able to produce a decoupled odor code: odor quality being encoded by the spatial activity across units, and odor intensity by the response latency of the units. Pearce et al. (2001) investigated the issue of concentration hyperacuity by means of massive convergence of ORNs onto GL. Modeling spike trains of individual ORNs as Poisson processes, the authors showed that an enhancement in sensitivity of  $\sqrt{n}$  can be achieved at the GL, where  $n$  is the number of convergent ORNs. Experimental results on an array of optical micro-beads were presented to validate the theoretical predictions.

Raman et al. (2004) processed data from MOS sensors with a model of the early stages of the olfactory pathway. A self-organizing map was used to group the response of the sensors at different temperatures in a manner akin to the chemotopic projection of ORNs onto the glomerular layer. Center-ON surround-OFF connectivity was used to model the olfactory bulb. In (Raman et al., 2004), the authors used a first-order neuron model with adaptation, whereas in (Raman and Gutierrez-Osuna, 2004) integrate-and-fire neurons were used instead. Their model was able to code the quality and intensity of odors,

yielding glomerular images similar to those observed in the olfactory bulb through optical imaging. .

## **II.2. The PRISM e-nose prototype**

We have built an electronic nose prototype to address the experimental requirements of this dissertation. The instrument is composed of three basic parts (Fig. 8, Fig. 9, Fig. 10):

1. Sensor array. The array consists of four MOS gas sensors (TGS2602, TGS2610, TGS2611, and TGS2620), in addition to an integrated temperature-humidity sensor (HIH-3602-C) to measure environmental variables in the sensor chamber.
2. Delivery system. A dynamic headspace delivery system was built to transport odorants to the sensor chamber. The delivery system comprises of seven components:
  - a. three gas diluters to control the concentration of up to three analytes;
  - b. an air filter with drierite® to remove humidity from the air used to dilute the analytes;
  - c. a manifold with three valves to control which odorants are delivered to the sensors;
  - d. flow buffers to remove small oscillations on the gas flow;
  - e. a sensor chamber housing the sensors;
  - f. a flow meter to control and measure the gas flow; and

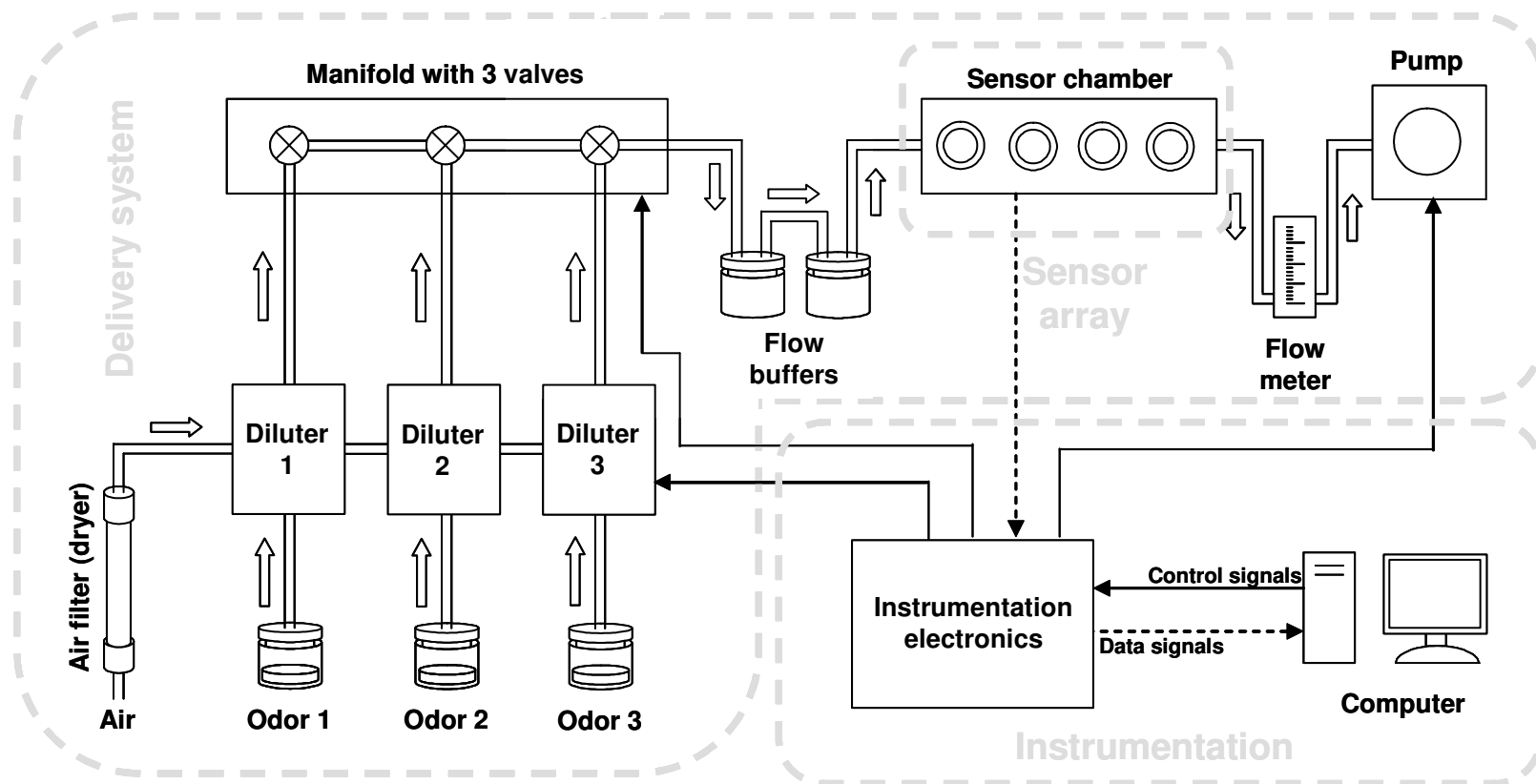


Fig. 8 Building blocks of the PRISM e-nose. The prototype system is composed of three basic blocks: (1) sensor array, including four MOS sensors, one temperature and one humidity sensor; (2) delivery system, composed of three diluters, air filter, manifold with three valves, flow buffers, sensor chamber, flow meter, and a miniature pump, (3) instrumentation, comprised of a computer with two data-acquisition cards and several interface circuits.

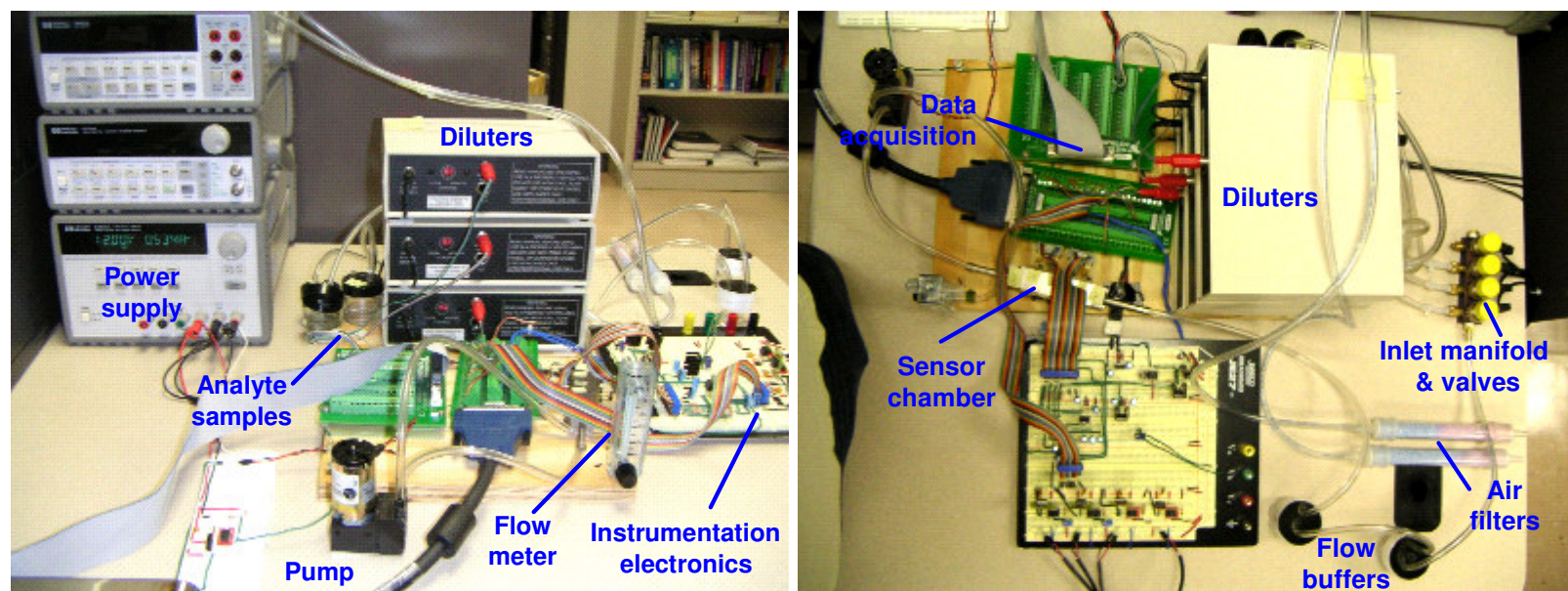


Fig. 9 Experimental setup: sensor chamber, diluters, pump, instrumentation electronics, manifold and valves, air filters, flow buffer, flow meter, and analyte samples.

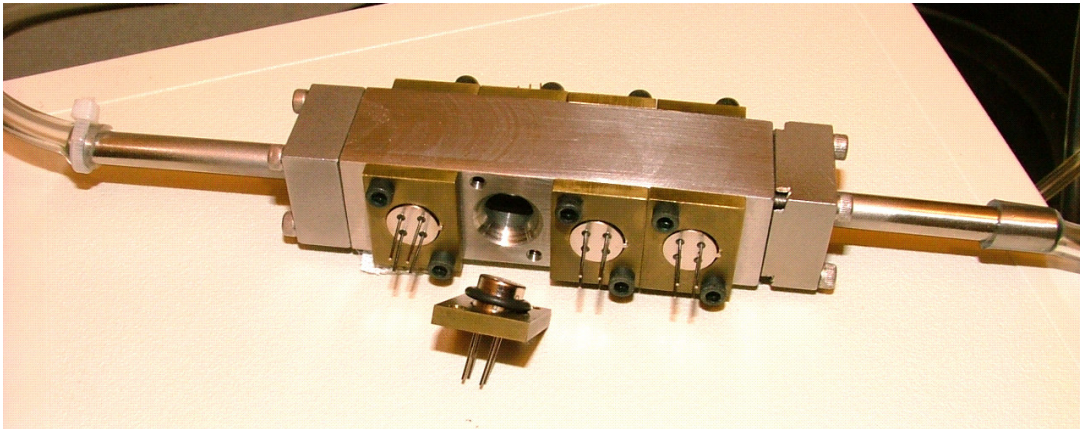


Fig. 10 Close-up view of the sensor chamber. The four MOS sensors are shown in front side of the chamber. The humidity/temperature sensor is placed on opposite side of the chamber, which contains sockets for an additional four sensors.

- g. a hydraulic miniature pump downstream from the sensor chamber to create a negative pressure that draws the odorants through the system.

3. Instrumentation: A computer with two data-acquisition cards (PCI-6024E, PCI-6713) and several interface circuits:

- a. Pump driver circuit (Fig.11): This circuit produces an output of 0V and 12V when the digital output (*DO*) of the data-acquisition card (DAQ) is enabled or disabled. This output is used to turn on and off the miniature pump.

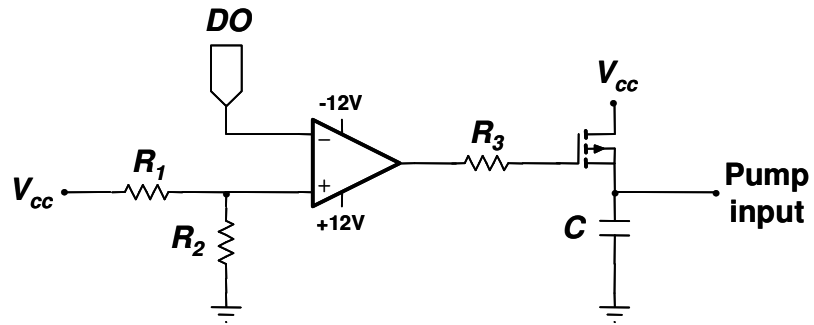


Fig. 11 Pump driver circuit.  $V_{CC} = 12\text{ V}$ ,  $R_1 = 300\text{ k}\Omega$ ,  $R_2 = 100\text{ k}\Omega$ ,  $R_3 = 10\text{ k}\Omega$ , and  $C = 100\text{ pF}$ .  $DO$  is a digital output of the DAQ. The operational amplifier used is a 741; the MOSFET is an IRF9520.

b. Valve driver circuit (Fig. 12): The same circuit as for the pump driver is used to control the state of the valves. Three replicas of the circuit were built to control each one of the valves.

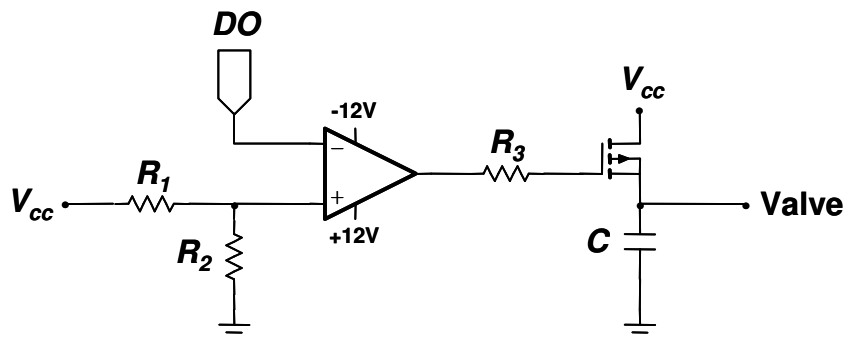


Fig. 12 Valve driver circuit.  $V_{CC} = 12\text{ V}$ ,  $R_1 = 300\text{ k}\Omega$ ,  $R_2 = 100\text{ k}\Omega$ ,  $R_3 = 10\text{ k}\Omega$ , and  $C = 100\text{ pF}$ .  $DO$  is a digital output of the DAQ. The operational amplifier used is a 741; the MOSFET is an IRF9520.

c. Heater driver circuit (Fig. 13): This circuit supplies enough current to drive the heater of the MOS sensors. It works as a voltage follower: the voltage introduced through the analog output of the DAQ to the circuit is the same applied to the heater.

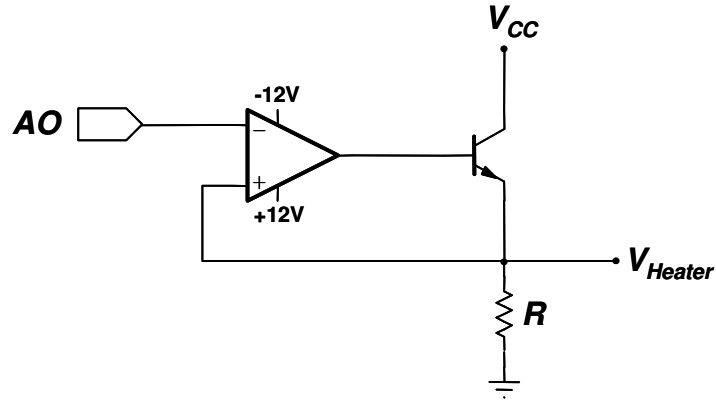


Fig. 13 Heater driver circuit.  $V_{CC} = 9V$ ,  $R = 10k\Omega$ , and the operational amplifier used was a 741. The BJT was a TIP29C.

d. MOS resistance measurement circuit (Fig. 14): A voltage divider is used to measure the resistance/conductance change in the MOS sensors. In this circuit, the MOS sensor resistance ( $R_S$ ) and the output voltage ( $V_{out}$ ) follow:

$$R_S = \frac{R_L \cdot V_{out}}{V_{CC} - V_{out}} \quad (2.4)$$

This expression allows us to compute  $R_S$  through  $V_{out}$ , which is captured by an analog input (AI) of the DAQ. One replica of the

circuit was built to measure the resistance change of each of the four sensors.

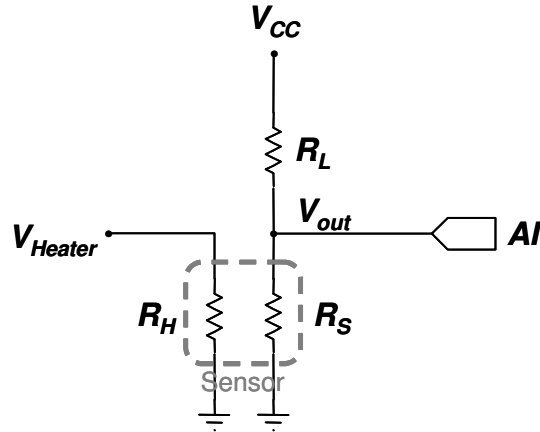


Fig. 14 MOS resistance measurement circuit.  $V_{CC} = 10\text{V}$  and  $R_L = 1\text{ k}\Omega$ ,  $R_H$  is the resistance of the MOS sensor heater,  $R_S$  is the resistance of the MOS sensor,  $V_{Heater}$  is the voltage introduced to the heater through the previous circuit,  $V_{out}$  is the output of the circuit, and  $AI$  is the analog input of the DAQ. It is worth to note that the same load resistance ( $R_L$ ) was used for the four sensors.

e. Temperature measurement circuit (Fig. 15): The temperature sensor is a thermistor, which changes its resistance with temperature. We use a voltage divider to capture the resistance changes of the thermistor.

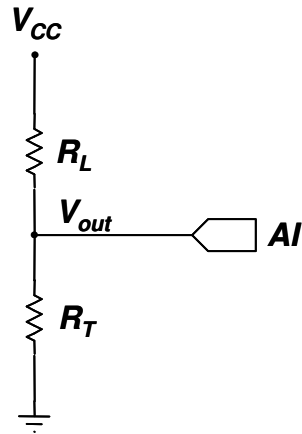


Fig. 15 Temperature measurement circuit.  $V_{CC} = 5V$ ,  $R_L = 1k\Omega$ ,  $V_{out}$  is the output of the circuit, and  $AI$  is an analog input of the DAQ.

Note: The three diluters and the humidity sensor do not need any interface circuitry. The diluters are driven directly with three analog outputs of the DAQ and the humidity sensor output is captured with one of the analog inputs.

### II.3. Collected datasets

Two datasets were collected with the PRISM e-nose prototype: (1) a temperature modulation dataset, which was used to validate the contrast enhancement (Chapter VI) and background suppression (Chapter VII) mechanisms; and (2) an isothermal dataset, which was designed to validate the novelty detection mechanism (Chapter VIII).

### II.3.1. Temperature-modulation dataset

This dataset contains the response of four MOS sensors (TGS2602, TGS2610, TGS2611, and TGS2620) to five different concentrations of allyl alcohol, tert-butanol, benzene, as well as their binary and ternary mixtures. Pure analytes were introduced in a 30 ml vial to obtain the base concentration of each sample. This base concentration was subsequently diluted in air to obtain the different concentrations. Table 2 shows the dilution factors used to generate the seven odors (3 single analytes, 3 binary mixtures and 1 ternary mixture) at five different concentrations each. Dilution factors in Table 2 denote the percentage at which the analytes are diluted before mixing with other analytes. It is worth notice that the dilution factors used for tert-butanol are double than those used for allyl alcohol and benzene. This is done to balance the sensor response level to the three analytes.

Repeats for each sample were collected on seven consecutive days to determine the repeatability of the sensors patterns. On each day 35 samples were prepared, 7 odors at 5 concentrations, for a total of 245 samples in 7 days. Additionally, 7 air samples were taken every day. To increase the information content of the response, the MOS sensors were modulated in temperature (Gutierrez-Osuna et al., 2003) with a ramp profile on the heater voltage from 2V to 4.5V over a period of 200 seconds. Fig. 16 shows the response of the four sensors to the three analytes for the five different concentrations. The error bars of this sensor response are shown in Fig. 17.

Table 2 Dilution factors. Samples of seven odors (3 single, 3 binary, and 1 ternary) at five different concentrations each were used. Each sample is considered to be formed by certain contribution of allyl alcohol (A), tert-butanol (B), and benzene (C). Dilution factors denote the percentage at which the analytes were diluted before mixing with other analytes.

	Conc. 1			Conc. 2			Conc. 3			Conc. 4			Conc. 5		
	A	B	C	A	B	C	A	B	C	A	B	C	A	B	C
Allyl alcohol <b>A</b>	10	-	-	20	-	-	30	-	-	40	-	-	50	-	-
tert-Butanol <b>B</b>	-	20	-	-	40	-	-	60	-	-	80	-	100		
Benzene <b>C</b>	-	-	10	-	-	20	-	-	30	-	-	40	-	-	50
Allyl alcohol tert-Butanol	10	20	-	20	40	-	30	60	-	40	80	-	50	100	-
Allyl Alcohol Benzene	10	-	10	20	-	20	30	-	30	40	-	40	50	-	50
tert-Butanol Benzene	-	20	10	-	40	20	-	60	30	-	80	40	-	100	50
Allyl alcohol tert-Butanol Benzene	10	20	10	20	40	20	30	60	30	40	80	40	50	100	50

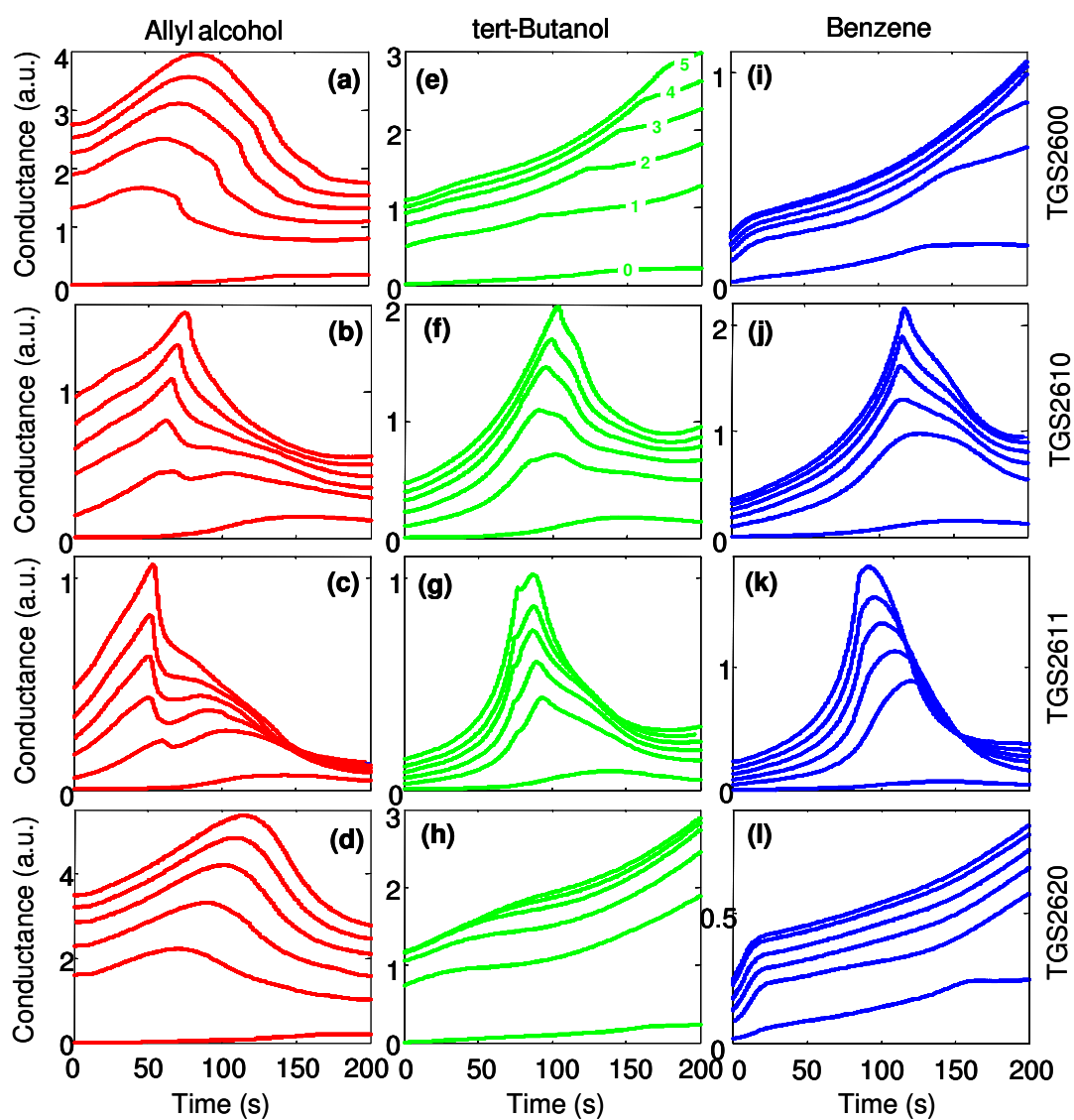


Fig. 16 Response of four MOS sensors (TGS2602, TGS2610, TGS2611, and TGS2620) to three analytes: allyl alcohol, tert-butanol, benzene at five different concentrations.

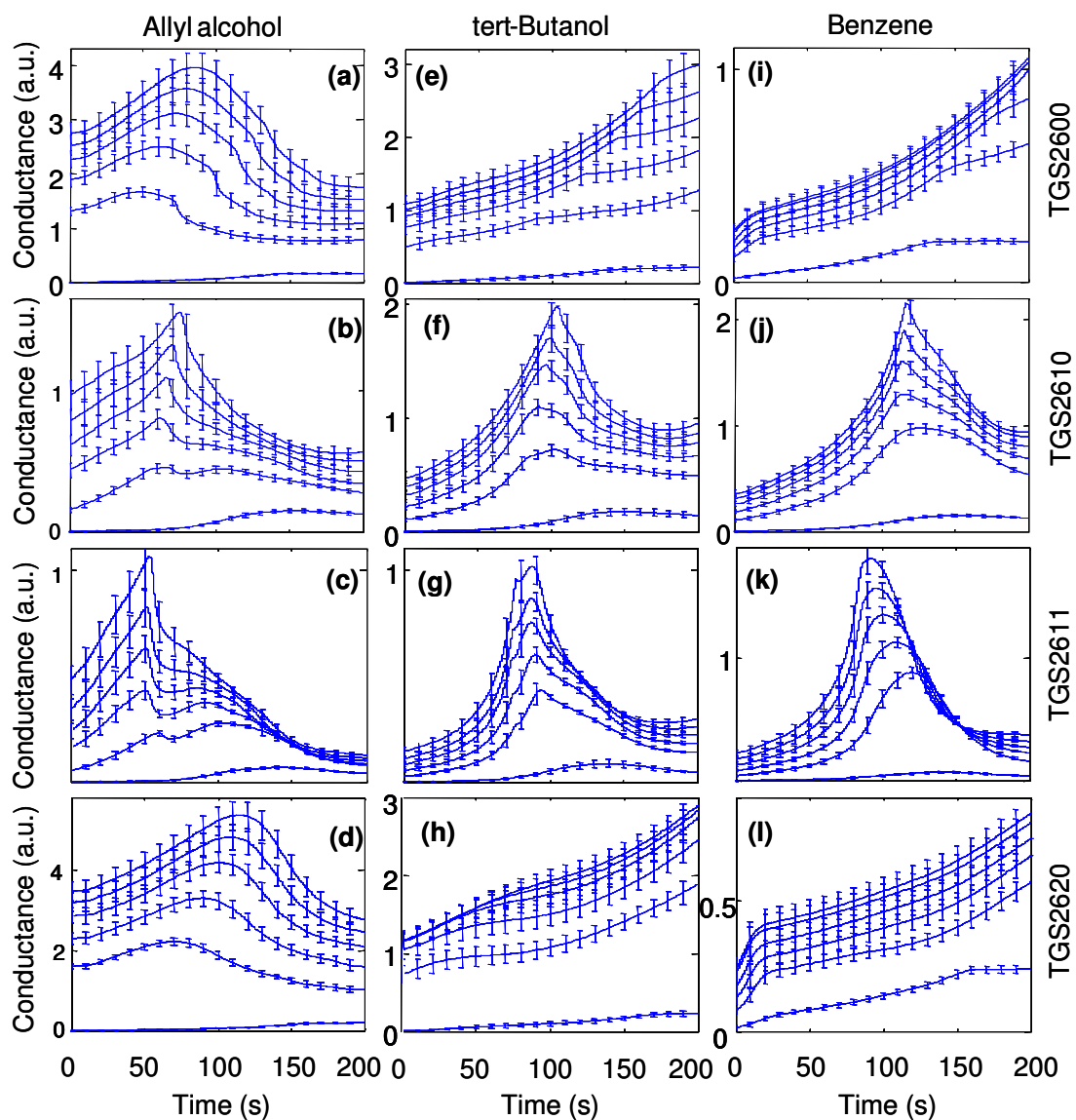


Fig. 17 Repeatability of the response of four MOS sensors to three analytes: allyl alcohol, tert-butanol, benzene. The error bars represent one standard deviation of the distribution obtained with repetitions from seven different days.

### II.3.2. Isothermal dataset

This database consists of the response of four MOS sensors (TGS2600, TGS2610, TGS2611, and TGS2620) to the introduction of allyl alcohol, tert-butanol, and benzene with isothermal operation of the heater voltage. The heater voltage value was selected to maximize the separability of the sensor-array response to the three analytes. For each possible heater voltage, we used the discrimination measure:

$$D(h) = \sum_{C=1}^5 \sum_{S=1}^4 (d_{12,CS}(h) + d_{13,CS}(h) + d_{23,CS}(h)) \quad (2.5)$$

where  $h$  is the heater voltage, and  $d_{ij}$  is the distance between the output of sensor  $S$  to analytes  $i$  and  $j$  at concentration  $C$ . Fig. 18 shows the discrimination measure  $D$  as a function of the heater voltage. Maximum discrimination is obtained at  $h=3.25V$ ; this heater voltage was therefore used in all subsequent experiments.

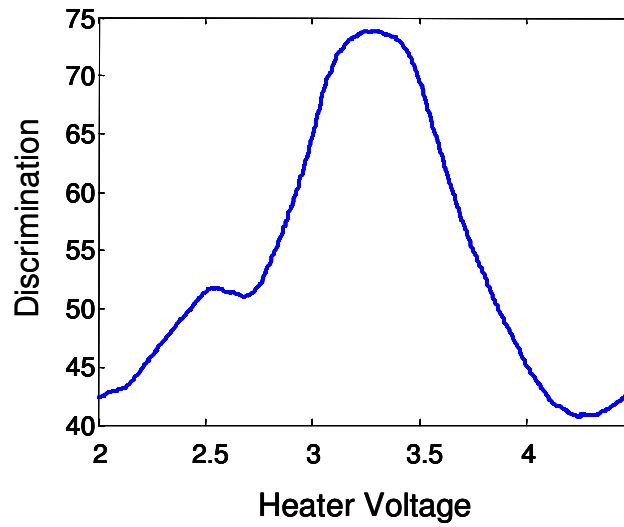


Fig. 18 Discrimination measure between the three odors as a function of the heater voltage. Maximum discrimination is obtained for  $h = 3.25$ .

Five different experiments were performed, depending on the number of odors introduced as well as the concentration profile of the odors and humidity. We designed one experiment with one odor and humidity, two experiments involving two odors, and two experiments with three odors. In the first experiment, tert-butanol was presented to the sensors with the concentration profile shown in Fig. 19(a). Humidity was also made to fluctuate by using water vapor as an additional odorant (Fig. 19(b)). Fig. 19(d) shows the response of the four sensors.

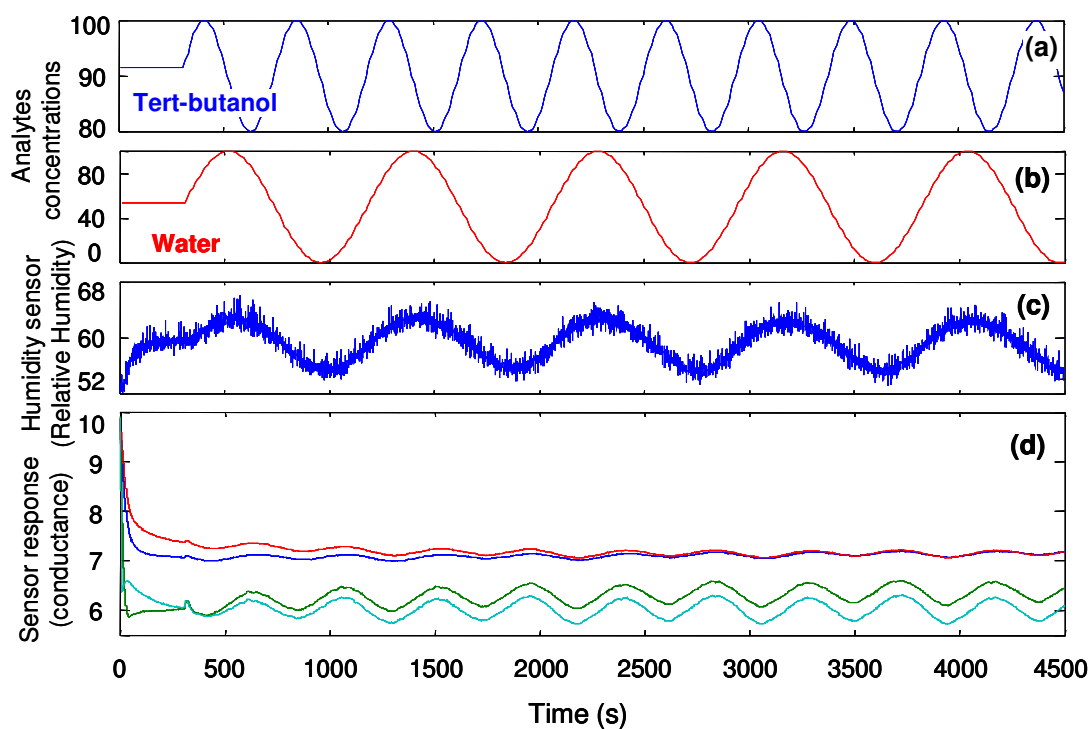


Fig. 19 Experiment with tert-butanol and humidity. (a) Concentration profile of tert-butanol. (b) Concentration profile of water vapor. (c) Response of the humidity sensor. (d) Response of the four MOS sensors.

The second experiment involved two odors: benzene and allyl alcohol. Benzene was introduced first; allyl alcohol was not introduced until  $t = 5300$  s, and at a lower concentration than benzene. The concentration profile for both odors is shown in Fig. 20(a). The sensor array response in this experiment is shown in Fig. 20(b).

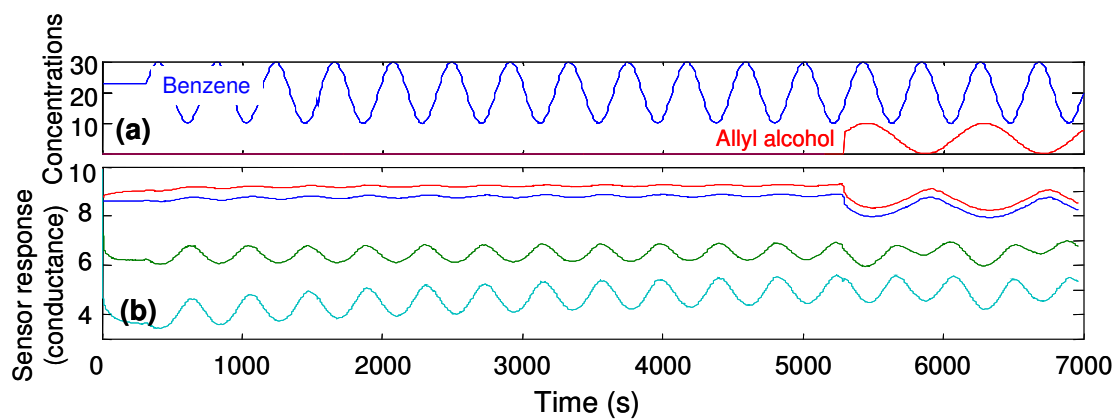


Fig. 20 Experiment with benzene and allyl alcohol. (a) Concentration profile of both benzene and allyl alcohol. (b) Response of the four MOS sensors.

The third experiment was very similar to experiment 2. Benzene and allyl alcohol were also used; however, the order of introduction of the analytes was inverted with respect to experiment 2. Furthermore, the concentrations were made more dissimilar than experiment 2 in order to determine the sensitivity of the system. Fig. 21(a) shows the concentration profile of both analytes. Fig. 21(b) shows the sensor response.

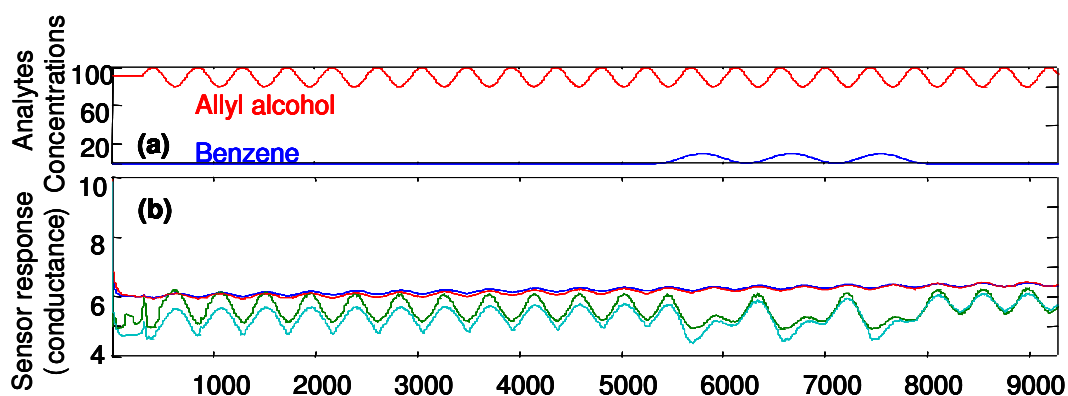


Fig. 21 Experiment with allyl alcohol and low concentration of benzene. (a) Concentration profile of both benzene and allyl alcohol. (b) Response of the four MOS sensors.

In experiment 4, the four MOS sensors were presented with three odors: tert-butanol, allyl alcohol, and benzene. Tert-butanol was introduced at  $t = 300$  s, followed by allyl alcohol at  $t = 5300$  s with lower concentration, and benzene at  $t = 10300$  s with the lowest concentration. The concentration profiles of tert-butanol, allyl alcohol, and benzene are shown in Fig. 22(a), (b), and (c) respectively. Fig. 22(d) shows the sensor response.

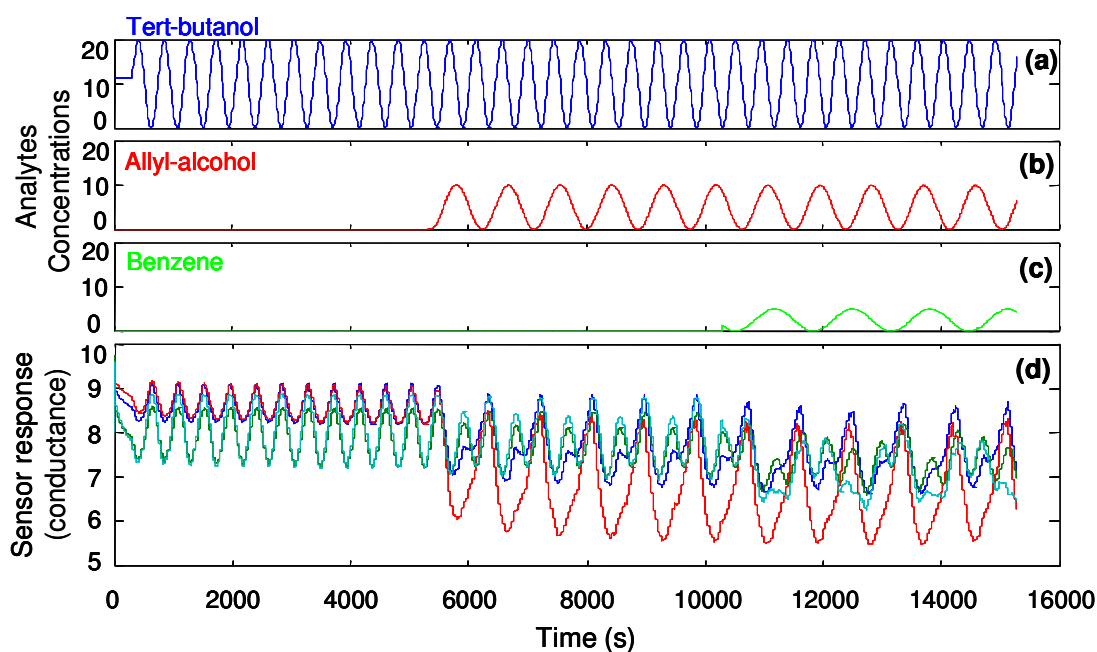


Fig. 22 Experiment with tert-butanol, allyl alcohol, and benzene. (a) Concentration profile of tert-butanol. (b) Concentration profile of allyl alcohol. (c) Concentration profile of benzene. (d) Response of four MOS sensors.

In the last experiment, the same three odors were used, but we further increased the difference between their concentrations in order to identify the detection limits of the system. Fig. 23(a), (b), and (c) show the concentration profile of tert-butanol, allyl alcohol, and benzene respectively. The response of the four MOS sensors is shown in Fig. 23(d).

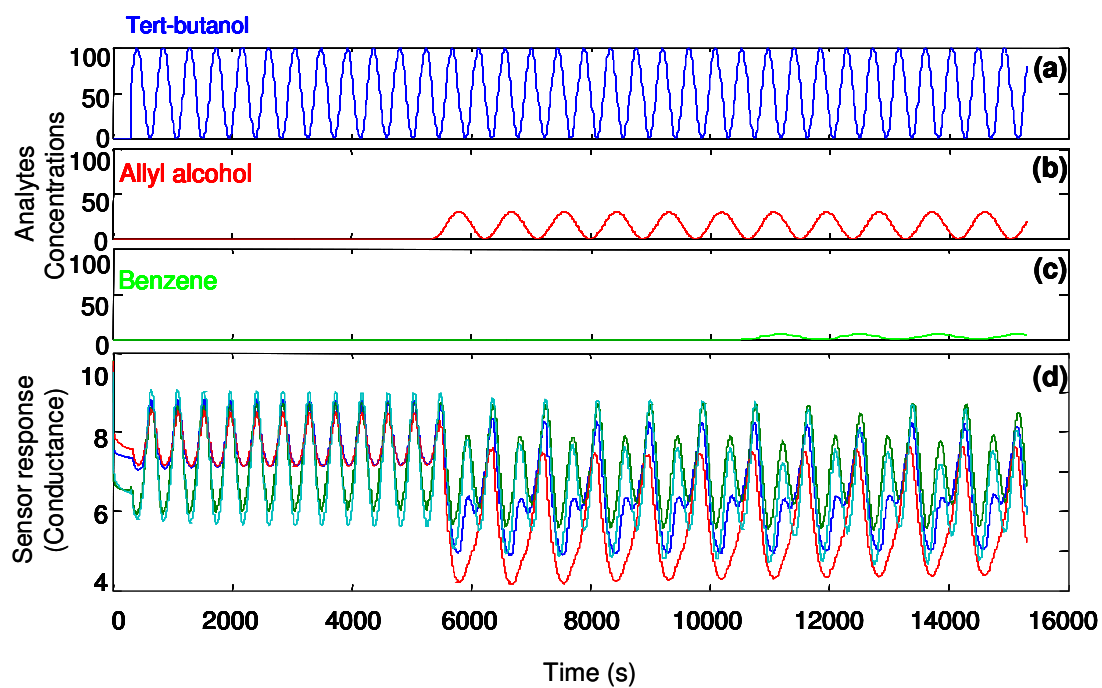


Fig. 23 Experiment with tert-butanol, allyl alcohol, and benzene at low concentration. (a) Concentration profile of tert-butanol. (b) Concentration profile of allyl alcohol. (c) Concentration profile of benzene. (d) Response of four MOS sensors.

## **CHAPTER III**

### **CODING AND LEARNING OF OLFACTORY INFORMATION**

The objective of this chapter is to provide an introduction to the role of dynamics in coding and learning of odor signals. We first examine the olfactory pathway to identify the specific signal processing functions that are later modeled in the dissertation, and identify the coding schemes and learning procedures underlying these functions. We describe how dynamical systems theory provides the necessary mathematical tools to model these mechanisms and analyze their computational functions: coding and learning have a natural interpretation in dynamical systems through the concept of attractor. This review will provide the necessary background to understand the dynamics of odor encoding and learning explained in subsequent chapters.

#### **III.1. Coding and learning in the olfactory system**

The olfactory system has been optimized over evolutionary time to perform an exquisite function: analyze odorant molecules by their molecular features, and synthesize holistic representations of them when presented in complex mixtures. It has been estimated that the olfactory system is able to detect approximately 10,000 odors (Axel, 1995) over a large range of concentrations. However, unlike the sense of hearing or vision, this modality has been elusive to psychophysical analysis because no simple set of physical properties, such as light wavelengths for sight or sound frequency for hearing, have been

found. Rather, olfaction appears to be intrinsically multidimensional. Along with the multidimensional nature of olfaction, the striking similarity of different olfactory systems across phyla (Hildebrand and Shepherd, 1997) suggests that its architecture has been optimized to reflect basic properties of olfactory stimuli.

### **III.1.1. A review of the olfactory pathway**

The olfactory pathway can be divided into three basic building blocks (Fig. 24): olfactory epithelium, olfactory bulb, and piriform (or olfactory) cortex. In the olfactory epithelium, the molecular properties of the odorants are transduced into electrical signals through a collection of olfactory receptor neurons (ORN). Mammals have tens of millions of ORN (Hildebrand and Shepherd, 1997; Doty, 1991) which belong to as many as 1,000 different types of receptors (Ma and Shepherd, 2000). The prevailing hypothesis about olfactory primary reception is that ORNs do not respond to specific molecules, but rather to specific molecular features of an odorant molecule, commonly referred to as 'odotopes' (Shepherd, 1987; Shepherd, 1994), such as carbon-chain length, the presence of benzene rings, or different functional groups (e.g., ester, aldehydes). Considering that most odorants in the environment consist of mixtures of volatile molecules (e.g., roasted coffee has been estimated to contain the order of 600 volatile components), and that each molecule can contain several odotopes, an odorant is then detected as a large combination of specific odotopes.

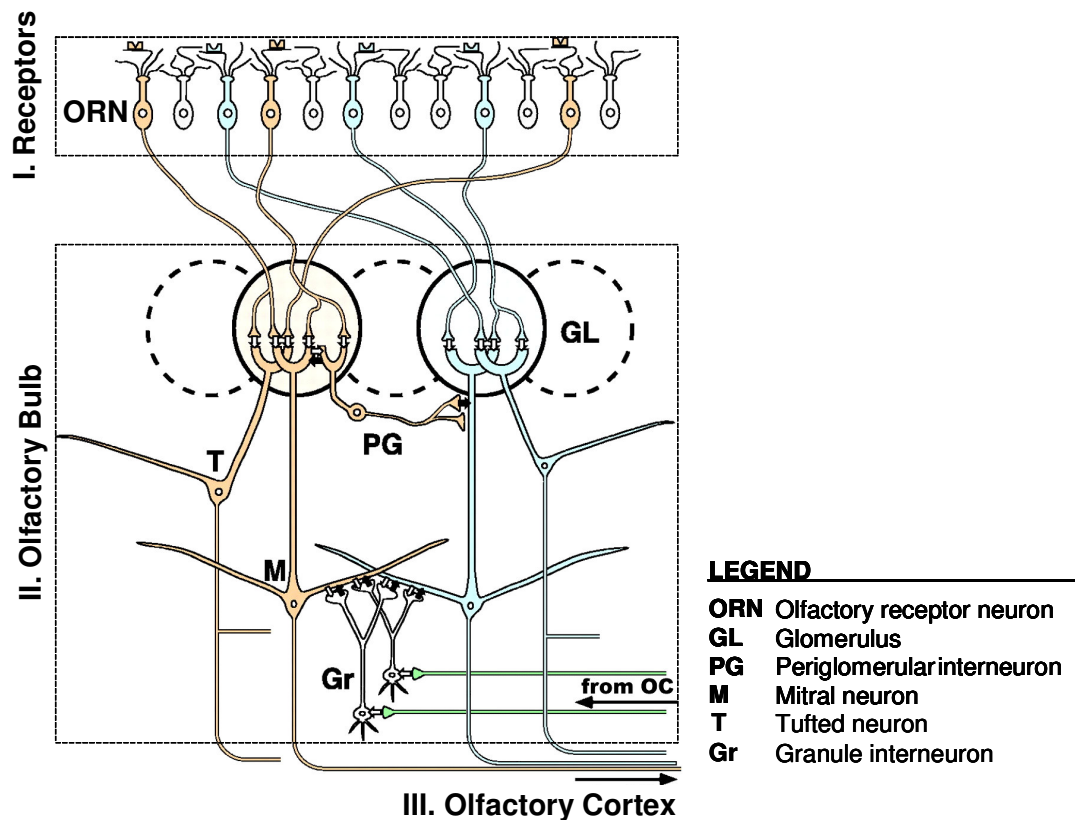


Fig. 24 Structure of the olfactory system. The olfactory pathway is composed of three basic stages: epithelium, bulb and cortex. (I) The olfactory epithelium is where the molecular information of the odor is detected and transformed into electrical signals by ORNs. ORNs project their axons in an orderly fashion onto spherical regions of neuropil known as glomeruli GL. (II) The olfactory bulb processes information at the glomerular level through a series of excitatory-inhibitory circuits (M, T, PG, and GR cells) to enhance the contrast between odors. (III) The olfactory cortex is where the holistic representation of an odor is formed, and where odors are identified (adapted from Mori, Nagao, and Yoshihara, 1999).

ORN axons synapse the first relay of the olfactory system inside the brain: the olfactory bulb. ORNs project in a very orderly fashion into spherical regions of neuropil known

as glomeruli. Each glomerulus receives axons from one type of ORN, and each ORN type projects into one or a few glomeruli (Vassar, 1994; Ressler et al., 1994). Therefore, at the glomerular level, olfactory information can be thought of as being represented by an image of the molecular features of the stimulus. Two types of neurons can be found in the olfactory bulb: projection neurons (mitral and tufted cells), and local interneurons (periglomerular and granule cells) (Shepherd and Greer, 2004). Projection neurons receive inputs from their main dendrite, which is located at the glomeruli, and send their axons to the olfactory cortex. Thus, projection neurons serve as the output channels of the olfactory bulb. The second type of cells, local interneurons, provides lateral connectivity between projection neurons at two different levels in the olfactory bulb. First, periglomerular interneurons synapse projection neurons dendrites at the glomerular level. There is some controversy as to whether periglomerular cells are excitatory or inhibitory (Shepherd and Greer, 2004). However, it is commonly accepted that their role is a form of volume control (Freeman, 1999). Second, granule interneurons synapse secondary dendrites of projection neurons at the level of their cell body. Granule cells play an essential role in the olfactory bulb, namely the enhancement of odor representation (Yokoi, et al., 1995), which facilitates the odor identification performed at the following stage in the signal pathway, the olfactory cortex.

The olfactory cortex is where the holistic representation of an odor is formed and where odors are identified (Haberly, 2004). Recurrent connections are pervasive in cortex (Mountcastle, 1998), and the olfactory system is no exception. There exist feedback

connections from cortex to granule cells, which are believed to modulate their inhibitory effect in the olfactory bulb.

Among these three building blocks (i.e., epithelium, bulb and cortex), the olfactory bulb is the most clearly involved in the processing of odor information (Shepherd and Greer, 2004). For this reason, our research is focused on the study of coding and learning mechanisms at this stage.

### **III.1.2. Experimental evidence for coding schemes and learning mechanisms in the olfactory bulb**

The encoding of olfactory information in the first stages of the olfactory pathway, before it is processed by the olfactory bulb, has been elucidated by the findings of Buck and Axel (1991), 2004 Nobel laureates in Physiology/Medicine. Their findings have also helped discover a highly ordered projection of ORNs onto the olfactory bulb (Vassar, 1994; Ressler et al., 1994) and better understand the information content of these signals. Despite these advances, the coding of olfactory information in the olfactory bulb has not been entirely elucidated. Recent experimental results indicate that time is an important coding dimension, information about odor identity being stored/recalled as a spatio-temporal pattern across mitral cells (Spors, 2002). Specifically, Laurent and colleagues have proposed an odor coding mechanism based on synchronization of neural population activity (MacLeod and Laurent, 1996; Laurent and Davidovich, 1994). These findings form the basis of the neural coding studies that are described in Chapter V of this dissertation.

Learning mechanisms are used to achieve different processing functions in the olfactory bulb, including odor contrast enhancement through associative learning (Hebbian) or odor segmentation through habituation. Experimental support for learning in the olfactory bulb is provided by Fletcher and Wilson (2000), who have shown that the molecular receptive range of mitral cells becomes more highly tuned following sustained exposure to an odorant, thus reducing the overlap among the representation of different odorants. These findings form the basis of the Hebbian/anti-Hebbian learning model that will be proposed in Chapter VI as a mechanism to improve the initial contrast among odor patterns.

Habituation has been also observed in the olfactory bulb (Wilson, 2000), and proposed as a mechanism to reduce the response to an odor previously presented. These findings form the basis for the odor segmentation studies that are proposed in Chapter VII as a mechanism to suppress background odors.

### **III.2. Coding and learning with dynamical systems: computing with attractors**

The origin of dynamical systems theory goes back to the work of Isaac Newton (1999) on the description of the dynamical laws of motion. With these laws, Newton created a framework to describe the dynamical evolution of any object subjected to a force. This framework was redefined a hundred years later by Lagrange with the analytical mechanics theory. This theory introduced the concept of “phase space” as the space of those variables that are needed to univocally describe the state of a physical system. In

phase space, the evolution of any dynamical system is defined by its equations of motion, usually defined as a set of differential equations.

In the 1970's, dynamical system theory started to be applied to the study of biological neural systems (Arbib, et al., 1997). These models consist of a number of interconnected non-linear processing units, representative of neurons or neuron ensembles, where the dynamic evolution of each unit is modeled with a differential equation. Connections between units result in a coupling of their differential equations. Consequently, the time course of the complete system is defined by a set of coupled non-linear differential equations. The non-linearity and coupling of the neurons make these dynamical systems unusually complex and very difficult to study analytically. However, since neural systems are dissipative (Arbib, et al., 1997), their dynamics typically settles on subsets of phase space known as attractors (Eckmann and Ruelle, 1985). The number and type of attractors displayed by the dynamical system can be used to understand its properties and behaviors. This paradigm, which has been known as “computing with attractors” (Hirsch and Baird, 1995; Hertz, 1995), elegantly captures the concept of coding and learning in neural systems. Coding is implemented by the different types of attractors and the itinerancy of the system between them (Arbib, et al., 1997), whereas learning shapes the attractor landscape, creating and altering the attractors of the system (Hirsch and Baird, 1995).

### III.2.1. Dynamical systems and attractors

A dynamical system consists of a set of possible states along with a rule that determines the present state in terms of past states (Alligood, et al., 1997). This rule takes the form of  $s: T \times Q \rightarrow Q$  (autonomous system), where  $T$  is the time dimension, and  $Q$  is the phase space, which defines the set of all possible states in the system. The phase space is also known as the state space. In the continuous case, this rule usually takes the form of an Ordinary Differential Equation (ODE). Provided that the state of a dynamical system can be completely described at any time by a point in phase space, the ODE will generate trajectories in this space that represent the temporal evolution of the system. An attractor can be defined as a subset  $A$  of the state space that “attracts” the trajectory of nearby states. More formally,  $A$  is an attractor if (Arbib, et al., 1997):

1.  $s(t, x) \in A$  for  $x$  in  $A$  and all  $t \geq 0$ .
2. No proper subset of  $A$  has the previous property.
3. Stability property:  $A$  is said to be stable if for every  $x \in A$  there exists  $\varepsilon > 0$  such that each state  $y$  whose distance to  $x$  satisfying  $d(y, x) < \varepsilon$  has the property that  $d(g(t, y), A) \rightarrow 0$  as  $t \rightarrow \infty$  (i.e., every point “close enough” to  $A$  tends to move towards  $A$ ).

An important magnitude of an attractor  $A$  is its basin of attraction, which is defined as the set of all states  $y$  such that  $d(g(t, y), A) \rightarrow 0$  as  $t \rightarrow \infty$ .

Attractors can be classified in three broad types: fixed points, limit cycles, and strange attractors (Fig. 25). The simplest form of attractor is a *fixed point*, a situation in which trajectories will converge to a stable equilibrium point of the system. The second type of attractor, known as a *limit cycle*, is defined by a closed periodic trajectory. Finally, the most complex type of attractor is the *strange attractor*, which is a set that has zero measure in the embedding phase space and has a fractal dimension. Trajectories within a strange attractor appear to wander around randomly, yet they are deterministic in nature.

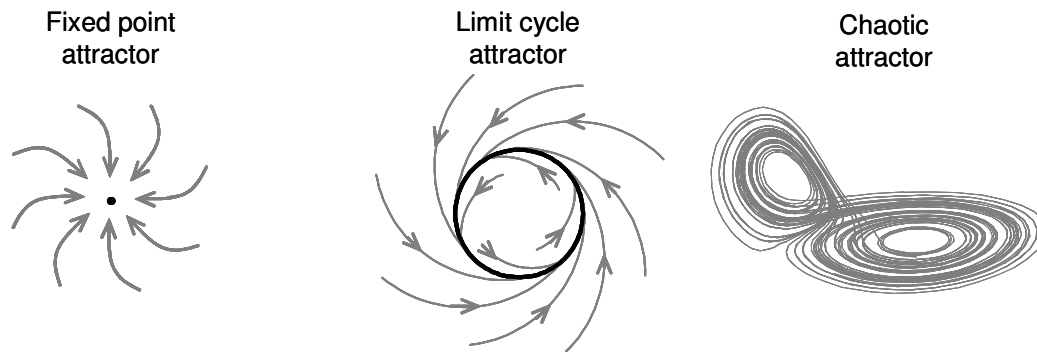


Fig. 25 Different attractor types: Fixed point, limit cycle, and chaotic.

### III.2.2. Fixed-point attractor networks

Cohen and Grossberg (1983) have shown that non-linear recurrent networks (networks with feedback connections) always converge to fixed point attractors if the connections between the neurons are symmetric. The analysis of this type of networks is facilitated by the existence of a Lyapunov function: a function of the state variables of the system

that monotonically decreases with the temporal evolution of the system (except for the fixed points, where it remains constant). Therefore, the evolution of these systems can be thought of as sliding downhill the surface of the Lyapunov function, following the direction of maximum slope (gradient) until the system reaches a fixed point, as illustrated in Fig. 26 (Haykin, 1999).

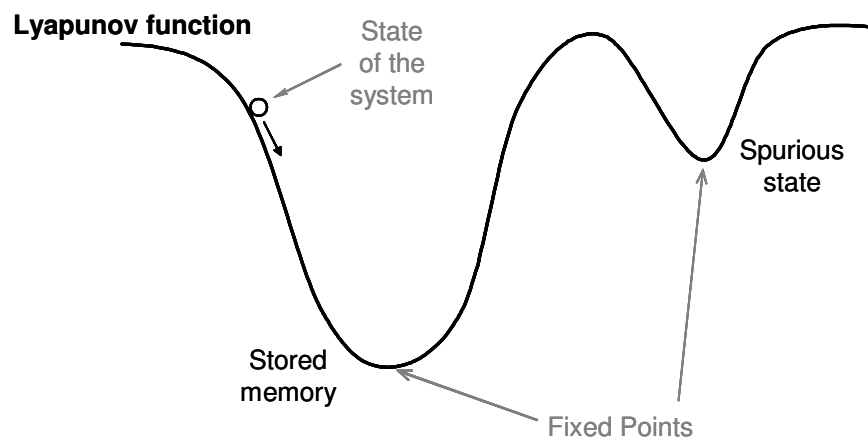


Fig. 26 Lyapunov function of a dynamical system. The state of the system is represented as a ball sliding downhill. The minimums of the Lyapunov function are fixed points of the system. The absolute minimum represents a stored memory, whereas the local minimum is a spurious state.

Many fixed point networks have been proposed, including those studied by Grossberg (1988), and the more recently proposed for the orientation tuning in primary visual cortex (Ben-Yishai et al., 1995), eye position (Seung , 1993), and spatial location in the hippocampus (Samsonovich and McNaughton, 1997). However, the more famous fixed

point network proposed is the celebrated Hopfield (1982), Hopfield (1984) net. Hopfield took motivation from the spin glass to propose a binary network that is able to work as a content addressable memory (CAM). Binary patterns are stored in the connection weights of the net through a learning rule based on the outer product of the stored patterns. Each one of the stored pattern generates a fixed point (memory state) in state space. The Hopfield net operates as follows: an input is presented to the system at iteration zero and is then removed to let the system evolve without any external interference (i.e., the input is only used to initialize the state of the neurons). After the input (initial conditions) is presented to the system, the system will converge to the nearest fixed point, which represents a memory state. This allows the system to perform pattern completion: stored patterns can be recalled from noisy or incomplete versions. The size of the basin of attraction of the fixed points gives an idea of the robustness of the net to recover the stored patterns. The size of these basins is reduced with the number of stored patterns, since each stored pattern requires a separate basin of attraction to be allocated in the same state space. An additional factor that reduces the capacity of the network, and probably represents the major drawback of the model, is the existence of spurious memories (Fig. 26); the outer-product learning rule not only creates one fixed point attractor per pattern, but also additional fixed points (spurious memories) in which the system can become trapped.

Even though imposing symmetry on the neural connections give rise to interesting computational functions, this constraint seems far from what occurs in its biological

counterpart. Connections in the brain are almost never symmetrical, which lead to more complex dynamics on the system than just fixed point attractors. Furthermore, a fixed point attractor does not seem compatible with the continuous activity that is observed in all types of biological neural systems (Arbib et al., 1997). Therefore a different type of attractor is necessary to describe the temporal evolution of neural systems.

### **III.2.3. Limit-cycle attractor networks**

Oscillatory behavior is pervasive in the central nervous system; it has been consistently found in many neural systems and at different hierarchical levels: single neurons, groups of neurons, and populations of neurons (Arbib et al., 1997). This oscillatory behavior clearly suggests the presence of limit cycle attractors in neural systems. When compared with fixed points, limit cycles present several advantages in terms of computing and coding, the most important one being the use of time as additional degree of freedom.

The seminal work of Kuramoto (1984), who studied the synchronization of groups of coupled intrinsic oscillators, set the foundations for subsequent studies on oscillatory networks. Kuramoto took inspiration from the previous studies of Wiener (1958), Wiener (1961) and Winfree (1967) in collective synchronization, and laid them on a firmer mathematical foundation. Kuramoto's model is based on Winfree's intuition that there exists a weakly-coupled regime for any group of nearly identically coupled oscillators in which their state can be totally defined by their phases. In this way, Kuramoto defined the following group of  $N$  coupled limit-cycle oscillators:

$$\dot{\theta}_i = \omega_i + \frac{K}{N} \sum_{j=1}^N \sin(\theta_j - \theta_i), \quad i = 1, \dots, N \quad (3.1)$$

where  $\theta_i$  is the phase,  $\omega_i$  is the natural frequency of oscillator  $i$ ,  $\omega_i$  has a distribution with negligible spread since the oscillators are nearly identical, and  $K$  is the coupling strength. This model was used by Kuramoto to study the onset of synchronization with increasing coupling strength  $K$ . He showed that from a totally desynchronized system, the network goes through a phase of partial synchronization, where some oscillators are synchronized and some are not, and reaches a state where all oscillators are in synchrony. Since this early work, synchronization has been shown to be one of the central mechanisms in oscillatory networks, one that has a fundamental role in the various computational functions that are achieved with these networks. A large number of neural networks based on limit cycle attractors have been proposed in the literature. These neural networks have been shown to perform a variety of computational functions, including associative memory, pattern segmentation, binding, and object selection, as reviewed below.

In a similar manner to fixed-point Hopfield network, oscillatory neural networks with limit-cycle attractors can also act as associative memories. Aonishi and Kurata (1999) showed that by making the connections on Kuramoto's model adaptable and ignoring the natural frequency term in Eq. 3.1, the oscillatory network can work as an associative memory. The memory patterns, stored through Hebbian learning, are defined through

neuron synchronization: neurons that oscillate in synchrony belong to the same pattern. The capacity of this associative memory was shown to be  $\alpha_c = 0.042$ , where  $\alpha_c$  is the ratio between the maximum number of patterns stored and the number of neurons of the network. Yamana et al. (1999) studied the same model, but as opposed to Kuramoto considered a set of oscillators with non-negligible spread on the oscillators frequency distribution (first term on the right of Eq. 3.1). Using the same Hebbian learning mechanism and synchronization retrieval scheme as Aonishi and Kurata (1999), their results showed that the capacity of the network can be improved by using distributed neural frequencies. The error-free capacity of the oscillatory networks mentioned thus far is smaller than that of the fixed-point Hopfield network. To improve the capacity the associative memories derived from Kuramoto's model, Nishikawa, Lai and Hoppensteadt (2004) introduce a second-order term in the coupling function of Eq. 3.1. The dynamic equations of the system become:

$$\dot{\theta}_i = \omega_i + \sum_{j=1}^N C_{ij} \sin(\theta_j - \theta_i) + \frac{\epsilon}{N} \sum_{j=1}^N \sin 2(\theta_j - \theta_i) \quad i = 1, \dots, N \quad (3.2)$$

With this new equation for the oscillators, the capacity of the system is comparable to that of the Hopfield network. One advantage of networks based on Kuramoto's model is that synchronization has a natural hardware implementation with phase-locked loops (Hoppensteadt and Izhikevich, 2000).

Aoyagi (1995) proposed a network of oscillators, defined by complex first order differential equations, that is able to store and retrieve patterns from the relative phase of the oscillators. The network follows the weakly-coupled regime as the Kuramoto's model, and the patterns are stored through a generalized Hebbian rule. As in the Hopfield network, an external input is applied as the initial condition of the network in order to retrieve a stored pattern. The author also proved the convergence of the system towards the stored limit cycle states by finding a Lyapunov function for the model.

Wang, et al. (1990) showed how a limit-cycle based associative memory can perform computational functions besides of pattern storage and retrieval. Their model is able to perform temporal segmentation, separating the basic components of a mixture pattern. The basic building block in the model is an excitatory and an inhibitory neuron, mutually connected and with self-connection. The temporal evolution of the neurons follows a first-order differential equation, defined on the state of the neuron rather than on the phase of that state as had been done in previously explained models. Therefore, the oscillations of the system do not arise from the individual neurons, as is the case in all previous models, but from the positive-negative interactions of the basic building block. The basic units are fully connected laterally through the excitatory neurons, and these lateral connections are trained through Hebbian learning to form an associative memory. The authors stored eight binary patterns using a model with 50 basic units. The system is able to recover the stored patterns from incomplete or corrupted versions of it, as in a regular associative memory. In addition, when the network is presented with three

patterns simultaneously, the system oscillates so that each individual pattern can be recovered sequentially. Thus, the system is able to segment the excitation pattern into its three stored components. Lourenço, et al. (2000) extended the model of Wang et al. in two ways. First, they proposed a feature binding scheme based on the synchrony of the oscillators. Second, they introduced an on-line rule for synaptic changes that allows the model to learn patterns continuously, as they are presented at the inputs.

Limit-cycle networks have also been used to perform object selection based on oscillatory correlations. Wang (1999) presented a model that is capable of selecting the largest among a set of objects in a binary image. The model consists of a 2-D layer of basic oscillatory blocks, each of which is connected to its 4 neighbors, and two inhibitory neurons that are connected to all the oscillators in the 2-D layer. Each basic oscillatory block is composed of coupled excitatory and inhibitory neurons. When an image containing different objects is presented to the model, the oscillators that belong to the same object phase lock because of their local positive connectivity, whereas oscillators that belong to different objects will have different phase since they are only connected through the global inhibitory neurons. This process will start a competition among the different objects, and the object with larger number of elements wins.

Note: Spiking neuron models are not considered in this review since they are rarely studied as limit cycle systems, even though they are oscillatory networks.

### **III.2.4. Chaotic attractor networks**

Chaotic behavior has been found in the central nervous system both at the level of single neurons, and at the level of populations of neurons (Arbib, et al. 1997). This third type of attractor is different to the two previous ones in that chaotic attractors can be high dimensional whereas fixed-point and limit-cycle attractors are low dimensional. This unique feature has been hypothesized to play an important role in the ability of a neural system to visit all possible lower dimensional attractors (limit cycles) (Tsuda, 1992). Furthermore, chaotic behavior inherently possesses an infinite amount of cyclic regimes that can be exploited for the purpose of coding information. Though the role of this non-periodic behavior in the brain is still not well understood at large (Tsuda, 1992), some functional roles of chaos have been proposed and successfully tested in dynamical neural network models. These computational functions include associative memory, avoidance of spurious memories, memory search, and signal to noise ratio improvements, as reviewed below.

Associative memories can also be built using chaotic neural networks. Kojima and Ito (1998) derived a basic neural model with three neurons, which is equivalent to the Lorenz equations, and also displays chaotic dynamics. This basic model is used as a building block to construct a larger network. By linking a group of these building blocks through Hebbian connections, the system is able to act as an associative memory. When a stored pattern is introduced at the input, the system wanders through several stored patterns until it settles on the correct one. Depending on the strength of the input, the

number of stored patterns that are visited vary. If the input is strong enough, the system settles directly into the stored pattern. As the strength of the input decreases, the system visits new patterns at increasingly larger Hamming distances from the desired pattern. This temporal evolution of the system reflects a hierarchical structure of the memorized patterns. When a non-stored pattern is introduced at the input, the system evolves chaotically through all the stored patterns. This chaotic trajectory is interpreted by the authors as a “memory searching” state. Molter, et al. (2005) studied how Hebbian learning can lead a network of continuous Hopfield neurons to chaotic behavior when the learning is applied in sequences. The network was also shown to work as a chaotic associative memory. Quoy (1995) proposed an associative memory with chaotic behavior, also trained with a Hebb-like rule. They observed that this kind of learning rule reduces the attractor dimension during learning. This increases the separation between the resulting attractors and also increases the capacity of the system. Tsuda (1992) observed that the chaotic behavior of an associate memory prevents the system from falling into spurious memories, thus increasing the number of successful retrievals.

The chaotic wandering among different patterns displayed by Kojima’s network is an example a common behavior observed in chaotic neural networks known as chaotic itinerancy (Rowe, 2002; Freeman, 1995). The concept of chaotic itinerancy was first introduced by Tsuda (1996), and later by Kaneko and Tsuda (2001), but has been reported by a number of researchers (Kay et al., 1996). During chaotic itinerancy, the dynamical system wanders in a high dimensional orbit while repeatedly entering and

leaving domains of low-dimensional behavior (limit cycle attractors). In the context of this dissertation, chaotic itinerancy will be used to denote the basal state of a model of the olfactory system. Without external stimuli the model will show a chaotic wandering. This state allows the system to be ready to jump to limit-cycle attractor as soon a new odor is introduced.

Chaotic behavior is also characterized by an extremely high sensitivity to the initial state: two trajectories of the same system that start close diverge rapidly as time goes on. This behavior seems to hold promise in signal detection, since differences between signals introduced to a chaotic neural network can be greatly amplified. However, this approach is not directly useful for classification purposes since the chaotic neural network will amplify irrelevant differences in the input patterns as well (i.e. amplification of noise). This issue has been addressed by (Kozma and Freeman, 2001) through chaotic resonance with the KIII model. Similarly to stochastic resonance, chaotic resonance uses noise to improve the classification performance of the system. The added noise allows the network to remain in a stable global attractor that improves the classification performance of the system.

### **III.2.5. Neurodynamic models of the olfactory system**

The olfactory system has been extensively modeled because of its simple organization when compared to other sensory systems, and easy accessibility for experimentation. The olfactory system has also been used as a “test model” to understand fundamental

mechanisms in the central nervous system at large. Thus, these models capture many of the computational functions of the olfactory system.

Li and Hopfield (1989) proposed a model of the olfactory bulb that reproduces electroencephalogram (EEG) recordings in the olfactory bulb. The proposed neural system models mitral and granule cells, which are distributed as a two ring-shaped sets of neurons, one for excitatory mitral cells and the second one for inhibitory granule cells. Mitral cells are only connected to the closest granule cells and, conversely, granule cells only synapse the closest mitral cells (Fig. 27). Inputs are presented to the model through the mitral layer. Each neuron is modeled with a first-order differential equation. The limit-cycle behavior of the model is generated by excitatory-inhibitory connections between mitral and granule cells. Simulations show that the system acts as a patterns classifier, since some input patterns drive the bulb to high activity and others patterns do not. However, the reason for this behavior it is not clear since there is no relation between the patterns and the connections of the network. In other words, the patterns have not been directly stored in the system.

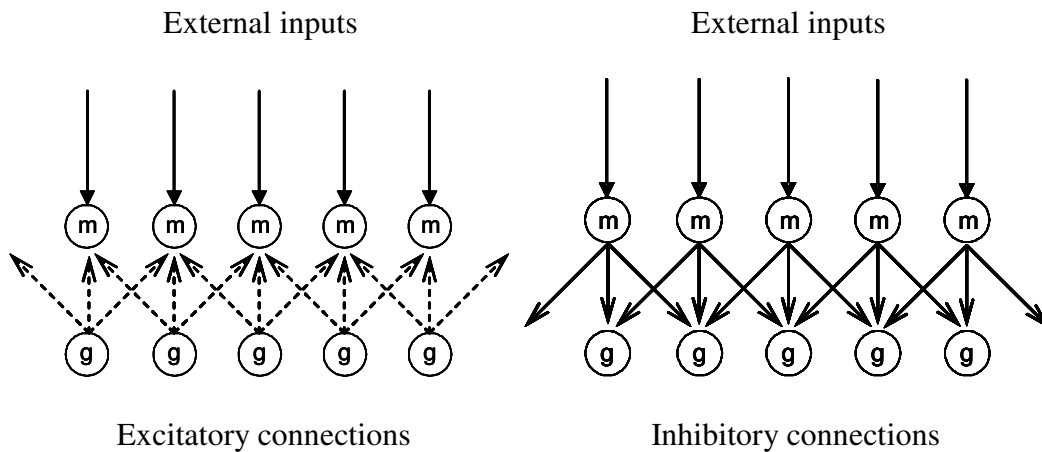


Fig. 27 Excitatory and inhibitory connections in the olfactory bulb model of Li and Hopfield, (1989) (adapted from Li and Hopfield, 1989).

Aradi et al. (1995) modified the model of Li and Hopfield by introducing mitral to mitral connections, which were learned through Hebbian learning. The authors studied the behavior of the model for different values of the mitral lateral connection, and showed that the system can display fixed point, limit cycle, and chaotic behavior depending on the strength of the lateral connections.

Li and Hertz (2000) expanded the original model of Li and Hopfield (1989) by adding an olfactory cortex layer to the original model. The olfactory cortex was modeled as one layer of excitatory pyramidal cells and two layers of inhibitory interneurons (Fig. 28). The layer of pyramidal cells was fully interconnected, and pyramidal to pyramidal connections were trained through Hebbian learning. The model also contained a feedback loop that connected the pyramidal cells in the olfactory cortex with granule

cells in the olfactory bulb. Since the feedback loop excited inhibitory neurons, the effect of the feedback was shown to lead to a reduction in the activity of the olfactory bulb. When a mixture of odors is presented to the system, the strongest component of the mixture is first recognized by the olfactory cortex as an increase in the activity of the pyramidal cells. Subsequently, and as a result of the feedback loop, the recognized pattern is inhibited at the bulb, allowing other components of the input mixture to dominate the activity in the bulb, effectively segmenting the input.

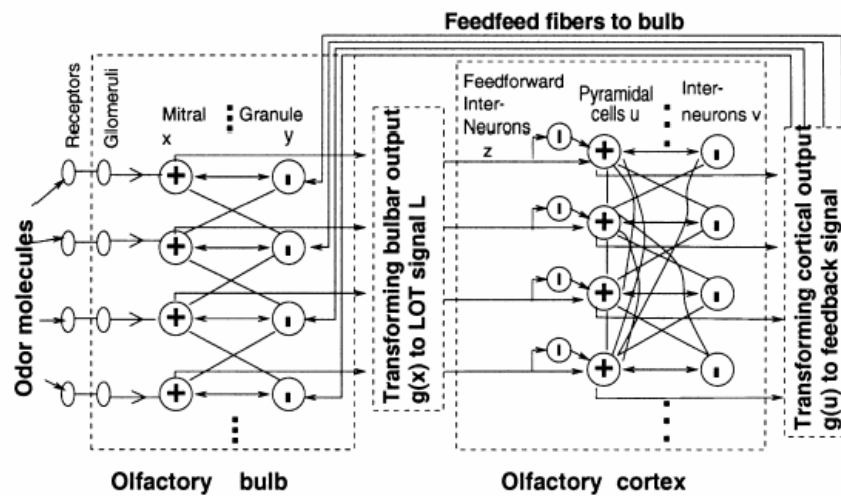


Fig. 28 Structure of the olfactory system model of Li and Hertz (2000) (adapted from Li and Hertz, 2000).

Ambros-Ingerson et al. (1990) developed a model of the olfactory system that performs hierarchical clustering of patterns. The bulb contains both mitral and granule cells; the former receive an external input and project onto the cortex, whereas the latter receive

feedback projections from cortex. The synaptic strength of the feedback projection is set during a development period in which hundreds of patterns are presented to the system and the strength of feedback synapses is allowed to vary according to a Hebb-like rule. The model is able to learn a multilevel hierarchical memory that uncovers statistical relationships inherent in collections of learned patterns.

Liljestrom (1995) proposed a model of neuron populations in the olfactory cortex that also displays chaotic dynamics. The model consists of three layers of neurons: two layers of inhibitory neurons and one layer of excitatory neurons. The neurons are connected as represented in Fig. 29. The top and bottom layers of inhibitory neurons are different in that only the top layer receives external input, and also because their temporal evolution is characterized by different time constants. Excitatory-to-excitatory connections are trained with Hebbian learning, thus allowing the model to store and retrieve patterns. The system presents limit-cycle attractors with oscillation in two separate frequency bands, and also chaotic attractors. To model the effect of neuromodulators, the author increased the slope of the sigmoidal function of the neurons and also reduced the weights of excitatory and inhibitory network to simulate depression of the excitatory and inhibitory transmission. Through computer simulations, the author showed that neuromodulatory control improves the associative memory performance by reducing recall time and improving robustness. He also showed that limit-cycle attractors are more robust and require less recall time as associative memory than fixed-point attractors.

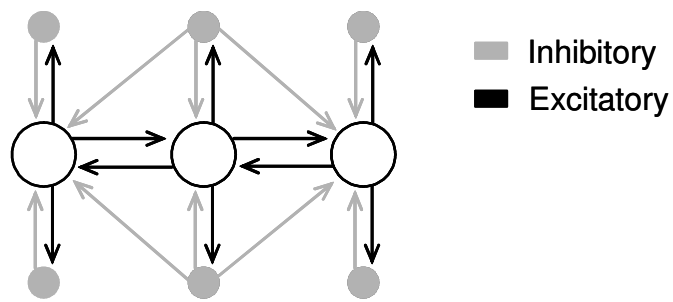


Fig. 29 Inhibitory and excitatory connections in the neocortex model of Liljestrom, (1995) (adapted from Liljestrom, 1995).

The next chapter describes the KIII model, which is arguably the more complete neurodynamic model of the olfactory system. The KIII captures chaotic and limit cycle behaviors observed in the olfactory system, and uses the itinerancy of the system through these attractors to process olfactory information.

## **CHAPTER IV**

### **THE KIII MODEL**

The objective of this chapter is to provide a detailed introduction to the KIII model. We will describe the hierarchical structure of the KIII, implementation issues, and also provide a review of the work performed on the KIII model during the last three decades.

#### **IV.1. The advent of the KIII model**

The KIII is a neurodynamic model of the olfactory system developed by Freeman and colleagues over the last thirty years (Freeman, 1978; Yao and Freeman, 1990). The model was designed to reproduce electroencephalographic (EEG) recordings in the olfactory system of rabbits. Two factors were crucial for the development of the KIII model (Freeman, 1975): (1) advances in multi-electrode measurement systems, and (2) the emergence of a new computational paradigm based on dynamic attractors. When the KIII was first proposed (Freeman, 1975), the possibility of taking simultaneous recordings from multiple electrodes had recently become available. The development of simultaneous recordings was made possible by advances in two areas: integrated circuit technology, which allowed the construction of a large number of reliable amplifiers, and digital computers, which allowed the acquisition and storage of simultaneous multi-electrode measurements. This new technology made it possible to obtain patterns of

response in the olfactory system instead of single readings, as it had been done previously. A wealth of experimental data became available as a result of this emerging technique, which allowed Freeman and colleagues to develop and test the KIII model.

Freeman recorded EEGs on the olfactory system of rabbits (Fig. 30); these recordings revealed two main types of behavior at the level of neural populations. First, nearly periodic oscillations (limit-cycle attractor) were observed when an odorant stimulus was presented. Second, aperiodic oscillations (strange attractors) emerged in the absence of an odorant stimulus (Freeman, 1992; Freeman, 1991). Based on these observations, Freeman hypothesized that computations in the olfactory system were performed by the itinerancy of the system through different attractor states. More interestingly, he also hypothesized that the chaotic behavior observed in the olfactory system plays an important role in the system's ability to process odor information (Freeman, 1988; Freeman, 1992). At the time those observations were made (throughout the 1970s), multiple examples of chaotic behavior were also found in experiments on fluids, chemical reactions, electronic circuits, mechanical oscillations, and semiconductors (Strogatz, 1994). It was known that the chaotic behavior arose from the non-linear dynamics of these systems. Furthermore, mathematical models of these systems based on non-linear differential equations were also found to accurately predict chaotic behavior. In light of these findings, Freeman proposed to model the attractor itinerant behavior of the olfactory system, including chaotic dynamics, using a system of non-linear differential equations that later became known as the K-set model. As stated by

Freeman (1975): “the aim of building a model is to construct nonlinear Ordinary Differential Equations (ODE) under the known constraints of the anatomy and physiology, and to find aperiodic solutions that simulate the statistics, spectra, and visually displayed patterns of the EEG.”

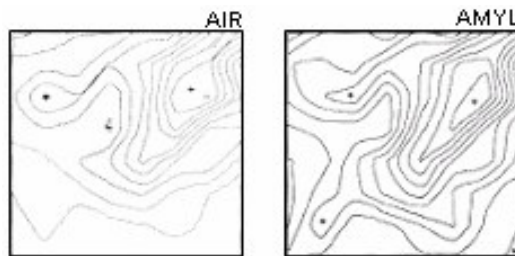


Fig. 30 Recordings of a rabbit's olfactory bulb with a 8x8 array of electrodes when amyl acetate (banana oil) and air are presented (Freeman , 1975).

## IV.2. The KIII as a hierarchical model: the K sets

The KIII follows a hierarchical architecture with four different levels (Yao and Freeman, 1990; Freeman, 1978): K0, KI, KII, and KIII. The basic building block is the K0, which represents a neuron population. Higher hierarchical levels (KI, KII, and KIII) are formed by interconnection of K0 sets. These are described next.

### IV.2.1. The K0 set

The lowest building block in the K-set hierarchy is the K0 set, which models a set of neurons ( $10^3$ - $10^8$ ) with a common source of input, a common sign of output (*e* for excitatory or *i* for inhibitory), and no interaction between neurons within the set. To

study the behavior of neural populations, experiments were conducted where an impulse current was introduced to one such population and its extracellular response was recorded (Freeman, 1975) (Fig. 31). This extracellular response or mean field potential (MFP) was used as a measure of the neural population activity. To avoid any interaction between neurons, the synaptic activity of the neural population was suppressed by anesthetizing the animal. From the impulse response, the neuron ensemble was determined to be of second order. The neural population was then modeled with a 2<sup>nd</sup> order ODE (Eq. 4.1), and the parameters of the system were found by fitting the experimental impulse response curve to Eq. 4.1 (Fig. 31).

$$\frac{d^2 X(t)}{dt^2} + (a + b) \frac{dX(t)}{dt} + ab \cdot X(t) = I(t) \quad (4.1)$$

where  $X(t)$  is the population activity (MFP),  $a = 220 \text{ sec}^{-1}$ ,  $b = 720 \text{ sec}^{-1}$ , and  $I(t)$  is the external input applied to the neuron population.

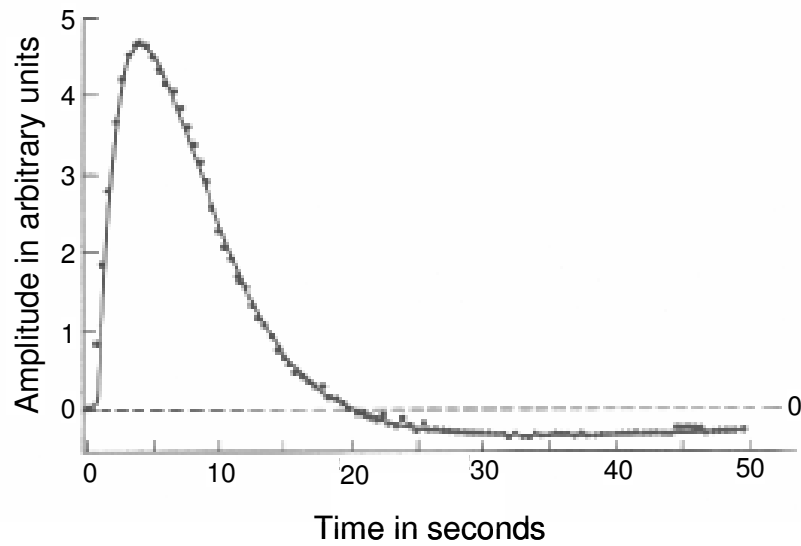


Fig. 31 Impulse response of an anesthetized population of neurons (adapted from Freeman, 1975).

#### IV.2.2. The KI set

The second hierarchical level is the KI set, which consists of a group of neuron populations with a common source of input, a common output sign, and dense interactions between them. There are two types of KI sets: KI with excitatory interactions or  $KI_e$ , and KI with inhibitory interactions or  $KI_i$ , as illustrated in Fig. 32. To model the interaction between neural populations it is necessary to first determine the relationship between the internal state variable of the neural population and its output. Due to the large number of neurons in a single neural population ( $10^3$  to  $10^8$ ), its output can be considered to be a pulse density and therefore continuous. Furthermore, assuming that the pulse trains of individual neurons are uncorrelated (Freeman, 1975) and nearly random, the functional relationship between the neuron population output and

its MFP (activity of the neuron population) can be considered to be time-invariant. The expression for this function can be derived as a generalization of the Hodgkin-Huxley model (Freeman, 1975), and is shown in Eq. 4.2. Experimental data are obtained by exciting the neural population with different levels of extracellular electrical activity with one electrode and recording its output value with a different electrode (Fig. 33). The model in Eq. 4.2 is then fitted to the data in order to estimate  $Q_m$ , a parameter that captures the state of arousal of the animal.

$$Q(v) = Q_m \left[ 1 - \exp\left(\frac{-(e^v - 1)}{Q_m}\right) \right] \quad v > -u_0$$

$$Q(v) = -1 \quad \text{otherwise}$$
(4.2)

where  $u_0 = -\ln\left[1 - Q_m \cdot \ln\left(1 + \frac{1}{Q_m}\right)\right]$ ,  $v$  is the MFP or activity of the neuron population,

and  $Q_m$  is the abovementioned parameter.

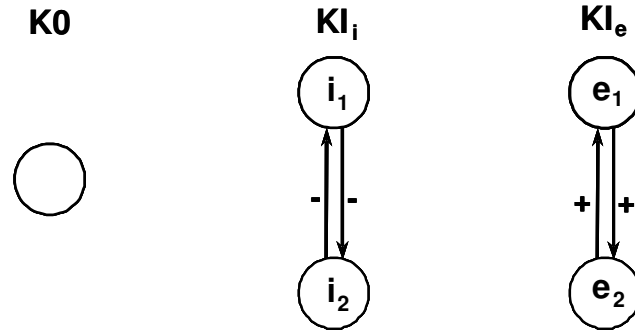


Fig. 32 (left) The K0 set. (center) The KI excitatory set. (right) The KI inhibitory set.

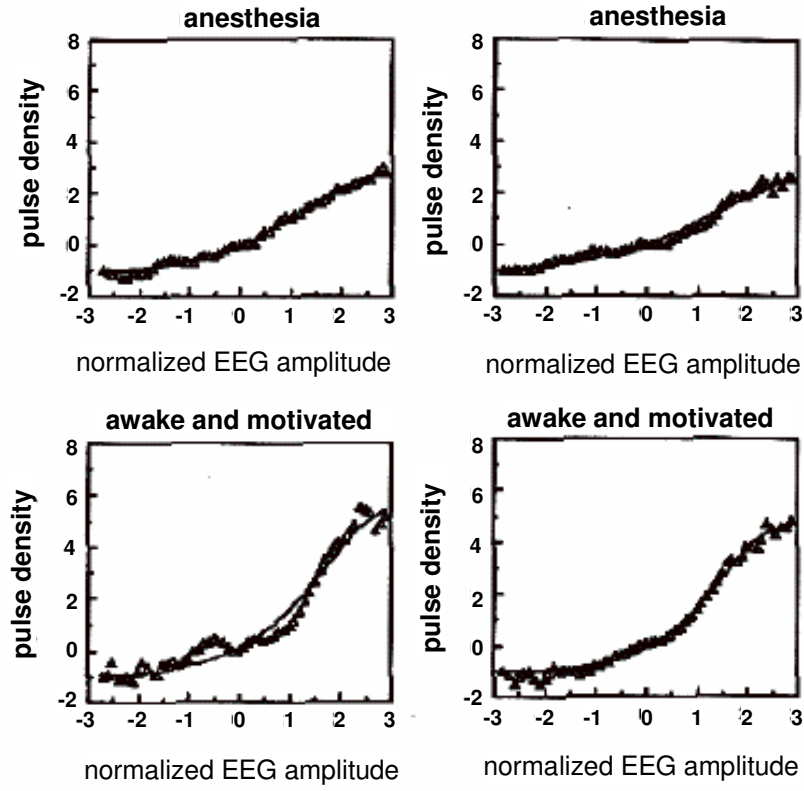


Fig. 33 Experimental determination of the output of a population of neurons in terms of its internal state (adapted from Freeman, 1975).

Merging Eqs. 4.1 and 4.2, the dynamics of the KI sets is expressed by a set of two coupled non-linear ordinary differential equations:

KI<sub>i</sub>:

$$\frac{d^2 X_{i1}}{dt^2} + A \frac{dX_{i1}}{dt} + B \cdot X_{i1} = -K_{ii} \cdot Q(X_{i2}) + I \quad (4.3)$$

$$\frac{d^2 X_{i2}}{dt^2} + A \frac{dX_{i2}}{dt} + B \cdot X_{i2} = -K_{ii} \cdot Q(X_{i1})$$

KI<sub>e</sub>:

$$\begin{aligned} \frac{d^2 X_{e1}}{dt^2} + A \frac{dX_{e1}}{dt} + B \cdot X_{e1} &= K_{ee} \cdot Q(X_{e2}) + I \\ \frac{d^2 X_{e2}}{dt^2} + A \frac{dX_{e2}}{dt} + B \cdot X_{e2} &= K_{ee} \cdot Q(X_{e1}) \end{aligned} \quad (4.4)$$

where  $X_{i1}$ ,  $X_{i2}$ ,  $X_{e1}$ , and  $X_{e2}$ , are the population activity (MFP) of neural populations  $i_1$ ,  $i_2$ ,  $e_1$ , and  $e_2$ , respectively (Fig. 32),  $A = a + b$ ,  $B = ab$ , and  $K_{ee}$  and  $K_{ii}$  are the connection strengths between K0 sets (See the table on page page 82)

#### IV.2.3. The KII set

The next hierarchical level is the KII set, which consists of two pairs of densely interconnected KI<sub>e</sub> and KI<sub>i</sub> sets. A compact version of the KII set, (commonly referred to as a reduced KII set), which consists of only one pair of connected KI<sub>e</sub> and KI<sub>i</sub> sets, has also been used for computational savings (Chang et al. 1998b). The regular and reduced KII sets are shown in Fig. 34. As a result of the positive and negative interconnections, the KII set acts as a coupled oscillator. It is the oscillatory behavior of the KII sets what gives the olfactory system model its oscillatory properties.

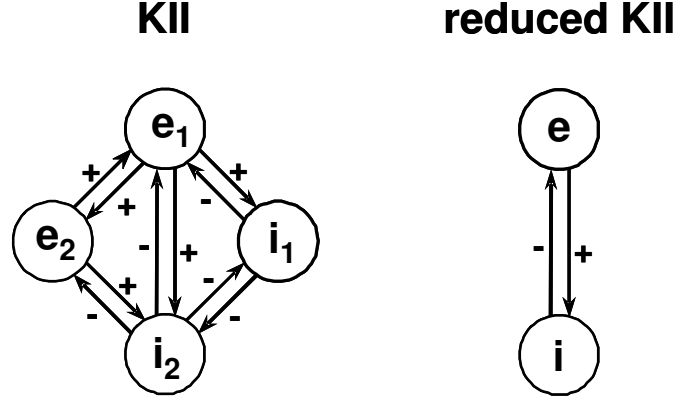


Fig. 34 (left) The regular KII set. (right) The reduced KII set.

The dynamics of the regular KII set are specified by the following system of ODEs.

KII:

$$\frac{d^2 X_{e1}}{dt^2} + A \frac{dX_{e1}}{dt} + B \cdot X_{e1} = K_{ee} \cdot Q(X_{e2}) - K_{ei} \cdot Q(X_{i1}) - K_{ei} \cdot Q(X_{i2}) + I \quad (4.5)$$

$$\frac{d^2 X_{e2}}{dt^2} + A \frac{dX_{e2}}{dt} + B \cdot X_{e2} = K_{ee} \cdot Q(X_{e1}) - K_{ei} \cdot Q(X_{i2})$$

$$\frac{d^2 X_{i1}}{dt^2} + A \frac{dX_{i1}}{dt} + B \cdot X_{i1} = K_{ie} \cdot Q(X_{e1}) - K_{ii} \cdot Q(X_{i2})$$

$$\frac{d^2 X_{i2}}{dt^2} + A \frac{dX_{i2}}{dt} + B \cdot X_{i2} = K_{ie} \cdot Q(X_{e1}) + K_{ie} \cdot Q(X_{e2}) - K_{ii} \cdot Q(X_{i2})$$

whereas the dynamics of the reduced KII set are modeled by the simpler system:

$$\frac{d^2 X_e}{dt^2} + A \frac{dX_e}{dt} + B \cdot X_e = -K_{ei} \cdot Q(X_i) + I \quad (4.6)$$

$$\frac{d^2 X_i}{dt^2} + A \frac{dX_i}{dt} + B \cdot X_i = -K_{ie} \cdot Q(X_i)$$

where  $X_{e1}$ ,  $X_{e2}$ ,  $X_{i1}$ ,  $X_{i2}$ ,  $X_e$ , and  $X_i$ , are the population activity (MFP) of  $i_1$ ,  $i_2$ ,  $e_1$ ,  $e_2$ ,  $e$ , and  $i$  respectively (Fig. 33),  $A = a + b$ ,  $B = ab$ , and  $K_{ee}$ ,  $K_{ei}$ ,  $K_{ie}$ , and  $K_{ii}$  are the connection strengths between KO sets (Table 3)

#### IV.2.4. The KIII model

The KIII is the highest level of the K-set hierarchy, and is specifically aimed at modeling the broad anatomical units of the olfactory system and their interconnections. (Yao and Freeman, 1990; Freeman, 1978). Shown in Fig. 35, the KIII is composed of four stages: (1) receptor layer, representing the inputs to the system; (2) olfactory bulb (OB), composed of a layer of fully-connected periglomerular cells modeled with a K0 set, and mitral/granule cells represented as a fully-connected KII network; (3) anterior olfactory nucleus (AON), modeled as a single KII set; and (4) prepyriform cortex (PC), composed by one KII and one K0 set. Two feedforward and four feedback sets of connections link these four stages. The OB has a feedforward connection with the AON and the PC. Feedback connections link the PC with the AON and OB, and also link the AON with the OB at two different levels ( $G_1$  and  $P$ ). Feedback connections are implemented considering cable delays. Additionally, random noise is introduced at two different stages in the KIII model: at the receptor layer and in the AON. The presence of noise stabilizes the attractors of the KIII model (Freeman et al., 1997; Chang et al 1998c; Kozma, 2003), and is biologically justified by its widespread presence in neural systems.

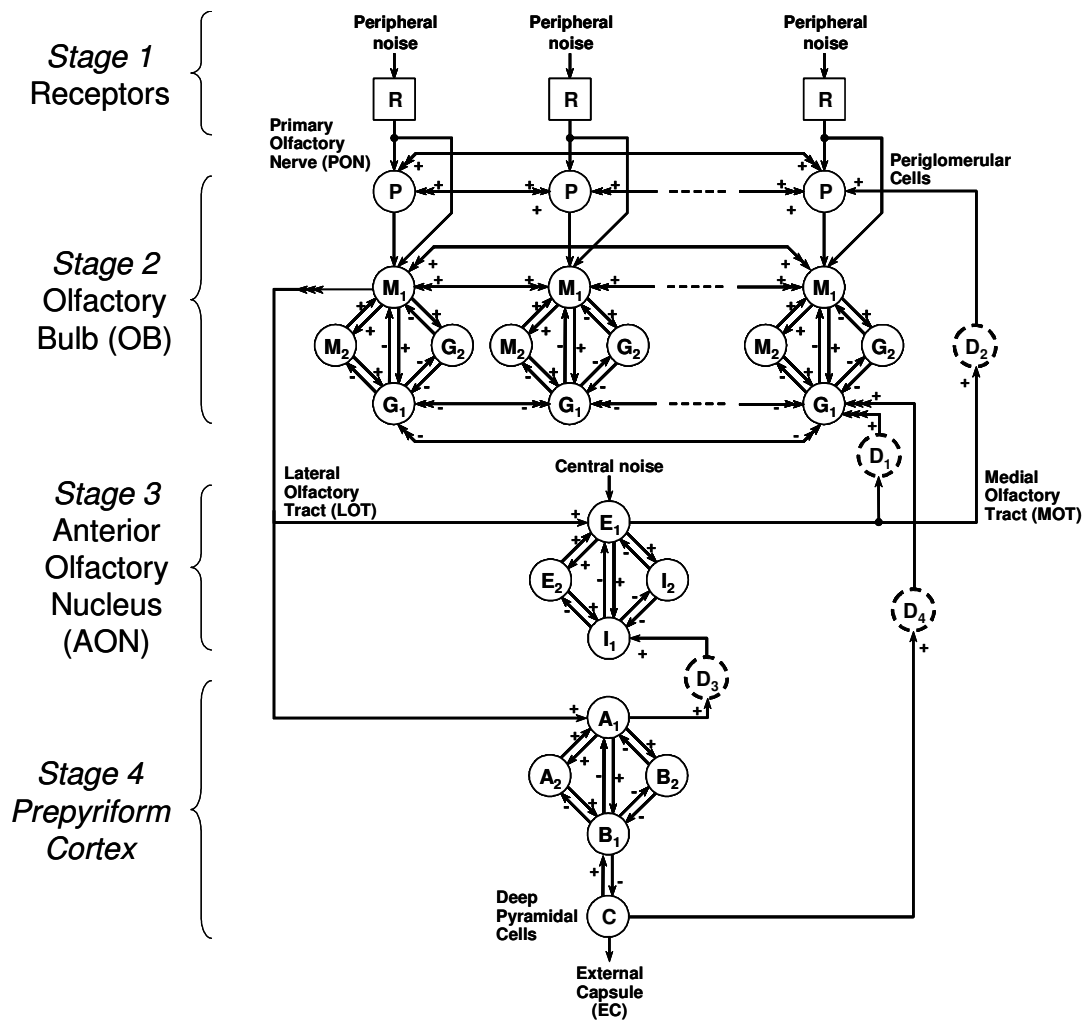


Fig. 35 KII model structure. The KIII model is built after the basic architecture of the olfactory system: (1) receptors; (2) olfactory bulb; (3), anterior olfactory nucleus; and (4) prepyriform cortex. The basic building blocks in the KIII are modeled after their counterparts in the olfactory system: R, olfactory receptor neurons; P, periglomerular cells; M, mitral cells; G, granule cells; E and I cells from the anterior olfactory nucleus; A and B cells from piriform cortex; C represents deep pyramidal cells (adapted from Chang, et al. 1998).

Following these topological connections, and the differential equations governing the time evolution of the K sets, the time course of the KIII model is described by the following set of massively-coupled non-linear delay differential equations:

Olfactory bulb (OB):

(4.7)

$$\begin{aligned}
& \frac{d^2 X_P[i]}{dt^2} + A \frac{dX_P[i]}{dt} + B \cdot X_P[i] = \frac{1}{N} \cdot \sum_{\substack{j=1 \\ j \neq i}}^N K_{pp} \cdot Q(X_P[j]) + K_{pr} \cdot I \\
& + \frac{K_2}{T_{s2} - T_{e2}} \sum_{k=t-T_{s2}}^{t-T_{e2}} Q(X_{E1}(k)), \\
& \frac{d^2 X_{M1}[i]}{dt^2} + A \frac{dX_{M1}[i]}{dt} + B \cdot X_{M1}[i] = K_{mm} \cdot Q(X_{M2}[i]) - \\
& K_{mg} \cdot (Q(X_{G1}[i]) + Q(X_{G2}[i])) + K_{mp} \cdot Q(X_P[i]) \\
& + \frac{1}{N} \cdot \sum_{\substack{j=1 \\ j \neq i}}^N K_{mm}[i, j] \cdot Q(X_{M1}[j]) + K_{mr} \cdot I, \\
& \frac{d^2 X_{M2}[i]}{dt^2} + A \frac{dX_{M2}[i]}{dt} + B \cdot X_{M2}[i] = K_{mm} \cdot Q(X_{M1}[i]) - K_{mg} \cdot Q(X_{G1}[i]), \\
& \frac{d^2 X_{G1}[i]}{dt^2} + A \frac{dX_{G1}[i]}{dt} + B \cdot X_{G1}[i] = -K_{gg} \cdot Q(X_{G2}[i]) \\
& + K_{gm} \cdot (Q(X_{M1}[i]) - Q(X_{M2}[i])) - \frac{1}{N} \cdot \sum_{\substack{j=1 \\ j \neq i}}^N K_{ggl} \cdot Q(X_{G1}[j]) \\
& + \frac{K_1}{T_{s1} - T_{e1}} \sum_{k=t-T_{s1}}^{t-T_{e1}} Q(X_{E1}(k)) + \frac{K_4}{T_{e4} - T_{s4}} \cdot \sum_{k=t-T_{s4}}^{t-T_{e4}} Q(X_C(k)), \\
& \frac{d^2 X_{G2}[i]}{dt^2} + A \frac{dX_{G2}[i]}{dt} + B \cdot X_{G2}[i] = K_{gm} \cdot Q(X_{M1}[i]) - K_{gg} \cdot Q(X_{G1}[i]),
\end{aligned}$$

Anterior olfactory nucleus (AON):

$$\begin{aligned} \frac{d^2 X_{E1}}{dt^2} + A \frac{dX_{E1}}{dt} + B \cdot X_{E1} &= K_{ee} \cdot Q(X_{E2}) - K_{ei} \cdot (Q(X_{I1}) + Q(X_{I2})) \\ &+ \frac{1}{N} \cdot \sum_{j=1}^N K_{em} \cdot Q(X_{M1}[j]), \end{aligned}$$

$$\frac{d^2 X_{E2}}{dt^2} + A \frac{dX_{E2}}{dt} + B \cdot X_{E2} = K_{ee} \cdot Q(X_{E1}) - K_{ei} \cdot Q(X_{I1}),$$

$$\begin{aligned} \frac{d^2 X_{I1}}{dt^2} + A \frac{dX_{I1}}{dt} + B \cdot X_{I1} &= -K_{ii} \cdot Q(X_{I2}) + K_{ie} \cdot (Q(X_{E1}) + Q(X_{E2})) \\ &+ \frac{K_3}{T_{s3} - T_{e3}} \cdot \sum_{k=t-T_{s3}}^{t-T_{e3}} Q(X_{A1}(k)), \end{aligned}$$

$$\frac{d^2 X_{I2}}{dt^2} + A \frac{dX_{I2}}{dt} + B \cdot X_{I2} = K_{ie} \cdot Q(X_{E1}) - K_{ii} \cdot Q(X_{I1})$$

Prepyriform cortex (PC):

$$\begin{aligned} \frac{d^2 X_{A1}}{dt^2} + A \frac{dX_{A1}}{dt} + B \cdot X_{A1} &= K_{aa} \cdot Q(X_{A2}) - K_{ab} \cdot (Q(X_{B1}) + Q(X_{B2})) \\ &+ \frac{1}{N} \cdot \sum_{j=1}^N K_{am} \cdot Q(X_{M1}[j]), \end{aligned}$$

$$\frac{d^2 X_{A2}}{dt^2} + A \frac{dX_{A2}}{dt} + B \cdot X_{A2} = K_{aa} \cdot Q(X_{A1}) - K_{ab} \cdot Q(X_{B1}),$$

$$\frac{d^2 X_{B1}}{dt^2} + A \frac{dX_{B1}}{dt} + B \cdot X_{B1} = -K_{bb} \cdot Q(X_{B2}) + K_{ba} \cdot (Q(X_{A1}) + Q(X_{A2})) + K_{bc} \cdot Q(X_C),$$

$$\frac{d^2 X_{B2}}{dt^2} + A \frac{dX_{B2}}{dt} + B \cdot X_{B2} = K_{ba} \cdot Q(X_{A1}) - K_{bb} \cdot Q(X_{B1})$$

$$\frac{d^2 X_C}{dt^2} + A \frac{dX_C}{dt} + B \cdot X_C = -K_{cb} \cdot Q(X_{B2})$$

where  $i = 1, 2, \dots N$ ;  $N$  is the number of channels of the model;  $A = a+b$ ;  $B = ab$ ;  $K_1, K_2, K_3$ , and  $K_4$  are feedback gains;  $T_{Sj}$  and  $T_{Ej}$  ( $j=1,2,3,4$ ) are the starting and ending delay times. Finally,  $t- T_{Sj}$  through  $t-T_{Ej}$  defines the time window over which delay connection  $j$  integrates; the value of this integral is the output of the delay connection at time  $t$ .

Odor stimuli are presented to the KIII as activation patterns across the input layer of receptors. Each receptor is connected to a periglomerular cell and to a KII set (two mitral and two glomerular ensembles), forming a channel. Each of these channels can then be associated with one dimension of the input stimulus and also to the corresponding output pattern. The KIII is able to store previously seen patterns by means of Hebbian lateral connections at the M1 mitral layer (Freeman et al., 1998). This form of learning allows the KIII to recover not only the originally stored pattern when presented at the input, but also incomplete or distorted versions of it. Therefore, the KIII acts as an associative memory. The global behavior of the KIII is scale invariant (i.e., independent of the number of input channels) (Yao and Freeman, 1990), an essential property to allow the model to process inputs of any dimensionality.

In the absence of an external stimulus, the KIII channels follow an aperiodic oscillatory or chaotic behavior, which is known as a basal state (Fig. 36 (b)). When an input is

presented, the system moves into a limit-cycle attractor in state space (Fig. 36 (c)), which can also be observed as pseudo-periodic oscillations in the output channels. Once the input is removed, the KIII returns to an aperiodic basal state (Fig. 36 (d)). The amplitude of the oscillations at each channel depends on the activation level of its receptor input, but is also influenced by activity in other receptors as a result of the Hebbian lateral connections. The output pattern of the KIII is commonly assumed to be encoded in the amplitude or root mean square (RMS) of the oscillations of each channel (Yao and Freeman, 1990).

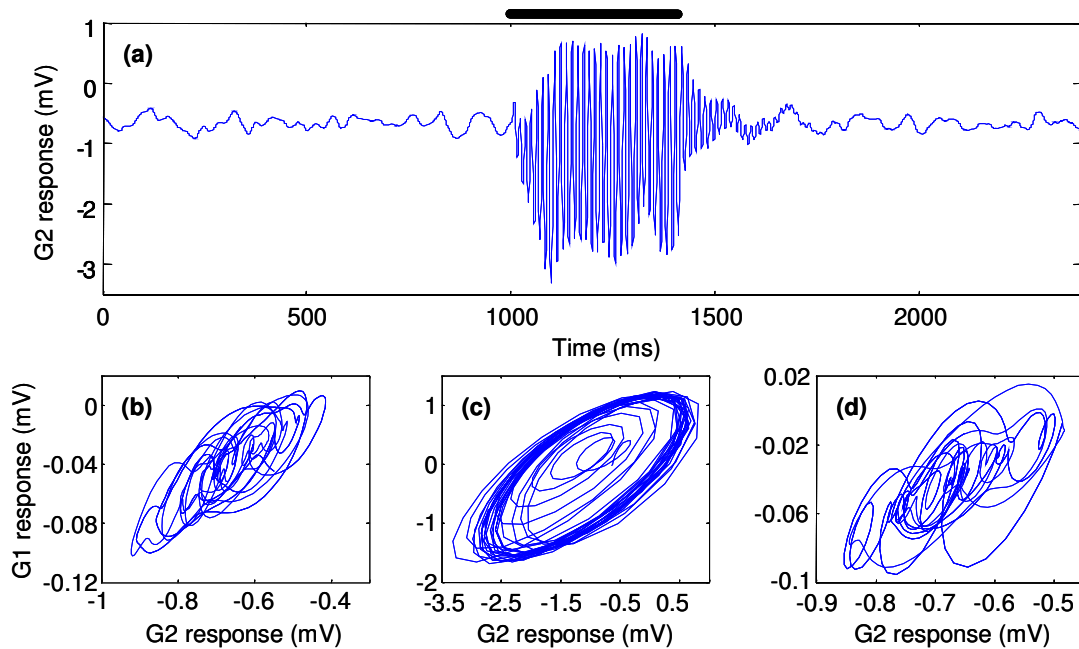


Fig. 36 The KIII dynamical behavior. (a) Temporal evolution of a  $G_2$  cell. Without external input, the model shows aperiodic oscillations (b). When an input is introduced from 1,000 to 1,400 ms (top thick black line), the system jumps into a limit cycle (c). Once the input is removed, the system returns to the basal state (d).

### **IV.3. Implementation aspects of the KIII**

The first numerical implementation of the KIII model (Freeman, 1978) solved the set of non-linear coupled delay differential equations (DDE) using the Euler method. However, the numerical solutions of the model lacked robustness, and oftentimes changed with the implementation of the numerical algorithm and the precision of the machine.

Chang et al., (1998c) proposed an alternative solution to work around the DDE integration problem. The authors replaced the DDE with equivalent ordinary differential equations using a kernel. Using the Laplace transform, the authors were able to show that both representations of a delay line are equivalent. Being able to convert the DDE system into an ODE system, the authors were able to solve the system in a much more reliable manner with conventional numerical methods such as Runge-Kutta (Hoffman, 1992).

Even though more reliable solutions were obtained with an ODE implementation of the KIII, the stability of the attractors was still very sensitive to the choice of parameters. To solve this problem, Freeman and colleagues proposed the introduction of additive noise into the system as a mechanism to stabilize the attractors (Freeman et al., 1997; Kozma, 2003). As shown in Fig. 35, noise was injected at two different levels in the model: at the peripheral level (R populations) and at the central level (E1 population). It was shown that the presence of noise allowed the system to stay in the attractors for an indefinite amount of time. The ability of noise to stabilize the KIII was later

hypothesized by the authors to be a possible role for the pervasive presence of noise in neural systems (Chang et al., 1998c; Kozma and Freeman, 2001).

The abovementioned work on practical implementation issues has tremendously facilitated our ability to reproduce previous results in the literature.

#### **IV.3.1. Our implementation of the KIII**

Following the abovementioned improvements, our implementation of the KIII model consists of an ODE system with additive noise. The model has been implemented in MATLAB using fourth-order Runge-Kutta ODE integration and a fixed time step of 1.0 ms. Initial conditions for all variables and their derivatives are set to zero. Parameter values and notation have been borrowed from (Chang et al., 1998b), and are summarized in Table 3. This unique set of parameters will be used throughout the dissertation, with the following exceptions:

- In Chapter VI,  $W_{MM}$  will be trained with Hebbian/anti-Hebbian learning.
- In Chapter VII,  $W_{MM}$  and  $W_{GM}$  will be adapted through habituation.
- In Chapter VIII,  $W_{PPL}$  will be trained with anti-Hebbian learning.

Table 3 Parameter values for the KIII model (from Chang et al., 1998b).

a	0.22	$q^C$	5.000
b	0.72	$w_{M1P}$	0.050
$q^P$	1.824	$w_{M1M1L}^{low}$	0.599
$w_{PPL}$	0.900	$w_{M1M1L}^{high}$	2.100
$k_{PR}$	0.500	$w_{E1M1}$	1.311
$q^{OB}$	5.000	$w_{A1M1}$	1.710
$w_{MM}$	1.500	$w_{G1G1L}$	-0.580
$w_{MG}$	-2.063	$w_{CB1}$	-1.543
$w_{GM}$	2.323	$w_{B1C}$	0.698
$w_{GG}$	-2.445	$w_{G1D1}$	2.349
$k_{M1R}$	1.000	$w_{PD2}$	1.087
$q^{AON}$	5.000	$w_{I1D3}$	2.553
$w_{EE}$	1.202	$w_{G1D4}$	2.305
$w_{EI}$	-1.426	$T_1^s$	20.000
$w_{IE}$	1.372	$T_1^e$	11.000
$w_{II}$	-1.571	$T_2^s$	22.000
$q^{PC}$	5.000	$T_2^e$	15.000
$w_{AA}$	0.823	$T_3^s$	21.000
$w_{AB}$	-1.938	$T_3^e$	12.000
$w_{BA}$	1.947	$T_4^s$	30.000
$w_{BB}$	-2.354	$T_4^e$	24.000

Three conditions are commonly checked when validating a given implementation of the KIII model, (Chang et al., 1998a):

- (1) the frequency distribution of the basal state follows a  $1/f$  distribution,
- (2) when an odor is introduced, the system moves from the aperiodic basal state to a limit cycle and remains there as long as the input is maintained, and
- (3) when the input is removed, the system returns to the original aperiodic basal state.

These necessary conditions have also been used to verify the correctness of our KIII implementation. Fig. 37(a) shows the power spectra of a 2,000 ms simulation of the basal state with our model. For comparison purposes, Fig. 37(b) shows the power spectra of the basal state in (Chang et al., 1998c). It can be observed that our

implementation of the KIII model follow a  $1/f$  power spectra very similar to that obtained by Chang et al. (1998c). Thus, our model satisfies condition (1). Conditions (2) and (3) are also satisfied, as illustrated in Fig. 36 (c) and (d). These three conditions will later be used in Chapter V, Chapter VI and Chapter VII to determine the range of values that the learnable/habituable parameters ( $W_{MM}$ ,  $W_{GM}$ , and  $W_{PPL}$ ) must have in order for the KIII to operate in a well-behaved region.

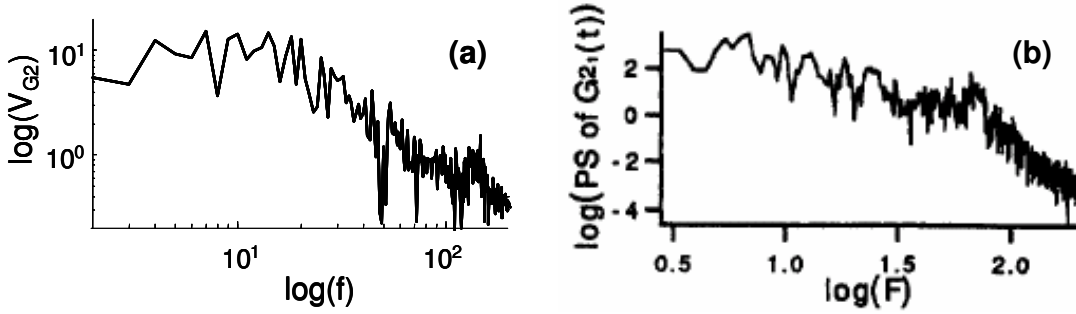


Fig. 37 Comparison of  $1/f$  spectra of the basal state. (a) Power spectra for a 2000ms simulation of basal state of  $G_2$  cells in our implementation of the KIII. (b) Power spectra of basal state in  $G_2$  cell from Chang et al. (1998c) (adapted from Chang et al. 1998c).

#### IV.4. Applications of the KIII model

In recent years, a handful of research groups have explored the use of K-set models for real-world problems. The earliest application was proposed by Yao et al. (1991), who used the KIII model to process binary images from two types of manufacturing parts (screws and bolts); the objective was to classify them as faulty or acceptable. The classification performance of the KIII model was compared with that of a KII network, a

Hopfield network, a three layer multi-layer perceptron, and a Bayesian network. Their results showed that computations in the KIII (based on limit cycles with a chaotic basal state) outperformed the limit-cycle-based computations of the KII network (which does not exhibit a chaotic basal state), the fixed-point-attractor computations of the Hopfield network, as well as the multilayer perceptron and the Bayesian classifier. The authors argued that the classification task was facilitated by the chaotic dynamics of the KIII, which helped suppress noise and irrelevant information.

Kozma and Freeman (2003) and Kozma and Ankaraju (2003) have used K sets to perform spatial navigation with autonomous agents. K-sets were used to model activity in the hippocampus and cortex, which are the brain regions responsible for spatial navigation. Their navigation model was able to perform goal finding, detouring, shortcutting, maze-learning and goal-finding with cluttered environments. Kozma et al. (1997) and Li and Kozma (2003) have also employed the KIII for time series predictions.

Hardware implementations of the KIII were developed by Freeman and colleagues in order to speed up computations. Eisenberg et al. (1989) and Yao and Freeman (1989), performed an analog-circuit implementation of a fully connected network with eight reduced KII units. The dynamical behavior of each K0 set was modeled in three stages: a summation stage, a two pole network, and a non-linearity stage. Each one of the stages was modeled with a different configuration of operational amplifiers. The reduced KII sets were connected with fixed weights (i.e., without any learning capabilities). This analog implementation of a KII network was able to reproduce the oscillatory behavior

of the olfactory system. It was also able to reduce noise, allowing a stored pattern to emerge from incomplete and noisy input.

Principe and colleagues have also developed several hardware implementations of Freeman's model. Ozturk et al. (2003) proposed a discrete-network implementation of the KII and KIII models to facilitate implementation with a digital multi-purpose processor such as a microcontroller or a DSP. The impulse response of a K0 set was sampled and decomposed over the gamma basis, which is set of complete real basis functions. The expression of the gamma basis in discrete time makes possible the digital implementation of the K0 dynamics. Afterwards, the digital KIII was implemented in a DSP and compared with the solutions obtained by software version of the KIII. The results showed similar solutions for both systems, but the DSP implementation performed significantly faster. Xu and Principe (2004) performed an analytical characterization of the KIII model. The authors were able to identify the different regions in parameter space within which a reduced KII set can operate.

Of particular interest for the research in this dissertation is the work of Clussnitzer et al. (2001) and Otto et al. (2000), who applied the KIII to process data from Fourier Transform Infrared (FT-IR) spectrometers and chemical sensors using habituation and Hebbian learning.

The FT-IR spectrum of each analyte was decimated, Hadamard-transformed, and normalized before being passed as an input vector to the KIII model. The authors showed that the principal components of the mitral cell state-space attractors can be used to discriminate different analytes. To the best of our knowledge, the work of Otto is the first and only attempt to use the KIII to process data from chemical sensors/instruments.

These previous efforts have shown that models based on K-set theory are able to solve practical application problems. Even so, the KIII model fails to capture some of the fundamental functions of the olfactory system, particularly those that affect the pattern-recognition capabilities of the model. This should come as no surprise since the KIII was not designed as a pattern classifier, but as a model of EEG activity in the rabbit's olfactory system. In this dissertation, we propose to improve the processing capabilities of the KIII model through alternative coding and learning mechanisms. In Chapter V, we use phase coding to enhance the performance of the KIII's associative memory. In Chapter VI, we propose a new Hebbian/anti-Hebbian rule that allows the KIII to increase the contrast between stored patterns. In Chapter VII, habituation is used in the KIII to allow the model to do background suppression. Finally, in Chapter VIII, the KIII model is trained with anti-Hebbian learning to perform novelty detection.

## **CHAPTER V**

### **TEMPORAL CODING**

The objective of this chapter is to study how the associative memory performance of the KIII model can be enhanced by considering temporal information. Our experience with the KIII model shows that the information provided by the amplitude of the channels tends to degrade when the input patterns have a significant degree of overlap, as is oftentimes the case in electronic-nose data due to the cross-selectivity of the chemical sensors. These observations prompt us to question whether or not additional and more robust information can be extracted from the output of the model (i.e., a “read-out”). In particular, we have consistently observed that the KIII has a tendency to display similar phases in channels that encode for the same odor. This observation, along with experimental evidence for a neural code based on coherent oscillations in neural populations, motivates the study presented in this chapter. Such neural coding schemes, based on firing synchrony, are the most compelling hypothesis for a temporal code spatially distributed across large neural populations. These types of codes have been found experimentally in different neocortical areas (Recce, 2001), and also play an important role in the integration of visual information (Singer and Gray, 1995) and coding of odors (Laurent and Davidowitz, 1994; MacLeod and Laurent, 1996).

### **V.1. Temporal coding and coherent oscillations**

Work by Adrian more than 75 years ago showed that the firing rate of stretch receptor neurons is related to the force being applied to the muscles (Adrian, 1926; Adrian, 1928). This seminal contribution led to the widespread belief that firing rate was the code used by neural systems to transmit information. As a consequence, early neural network models interpreted the output of artificial neurons as an abstraction of the neural firing rate in their biological counterparts. In recent years, this view has been challenged with ample experimental evidence showing the need to take into consideration the temporal dimension in neural information processing.

Undisputable evidence for a temporal code is best illustrated by the work of Thorpe, Delorme, and Van Ruelen (2001) and Van Ruelen and Thorpe (2000), who have shown that humans and monkeys are able to respond to a visual categorization problem in a very short period of time. In their experiments, an image is briefly flashed and the subject has to decide if it belongs to a target category or not. Considering (i) the pathway of the visual signal as it propagates through the brain, (ii) the minimum time required for a neuron to generate an action potential and (iii) the response time of the subjects in these experiments, it is possible to determine that there is time for only one spike to be generated at every relay station in the visual pathway. This result clashes with a frequency-rate coding hypothesis, and clearly points to the existence of a temporal dimension.

A number of possible temporal coding mechanisms have been proposed, including interspike interval codes, time of arrival (latency) codes and synchrony codes (Cariani, 1995). Among these, the synchronous oscillation of ensembles presents the most empirical evidence. Synchronization has been proposed as a potential mechanism to correlate information from different senses or different parts of the brain (Recce, 2001). It has also been found to play a role in visual feature integration (Singer and Gray, 1995). Of particular interest to our work, Laurent and Davidowitz (1994) and MacLeod and Laurent (1996) have found that synchronous oscillations of neuron populations in insects are used as an odor encoding mechanism. Their work has shown that different odors evoke coherent oscillations in different but usually overlapping ensembles of neurons in the olfactory system.

## **V.2. Phase coding in the KIII model**

Information at the output of the KIII is commonly assumed to be encoded by the amplitude or RMS of the oscillations of each channel (Yao and Freeman, 1990). However, considering that the KIII is a model of neuron populations, it is appealing to consider the phase of the oscillations across channels as an analogous of the coherent oscillation coding scheme in biological neural systems.

Hence, the goal of this chapter is to investigate the extent to which this phase information can be used as a coding mechanism, and compare its pattern-recovery performance against the conventional amplitude code.

In order to efficiently compute phase information, we consider the state-space trajectory of pairs of KIII channels (G1 populations) as a two-dimensional distribution. As shown in Fig. 38, differences in phase ( $\theta$ ) can be mapped into the correlation coefficient ( $\rho$ ) of the 2D distribution, and vice versa. Two sinusoidal waveforms with the same phase will lead to a correlation coefficient  $\rho=1$  (Fig. 38(a)), whereas a phase difference of  $\theta=180^\circ$  results in a correlation coefficient of  $\rho=-1$ . Intermediate phase differences result in correlation coefficients between those two extremes (-1, 1).

The waveforms and trajectories in Fig. 38 were obtained by first training a 32-channel KIII on two binary patterns (shown in Fig. 38(e)), and then introducing a distorted version of the first pattern. It can be seen that the shape and orientation of the attractors can be associated to different types of errors in the input stimulus. It is also important to note that the correlation coefficient not only captures information about the orientation of the principal eigenvector but also about the area enclosed by the trajectory (i.e. the shape of the attractor.)

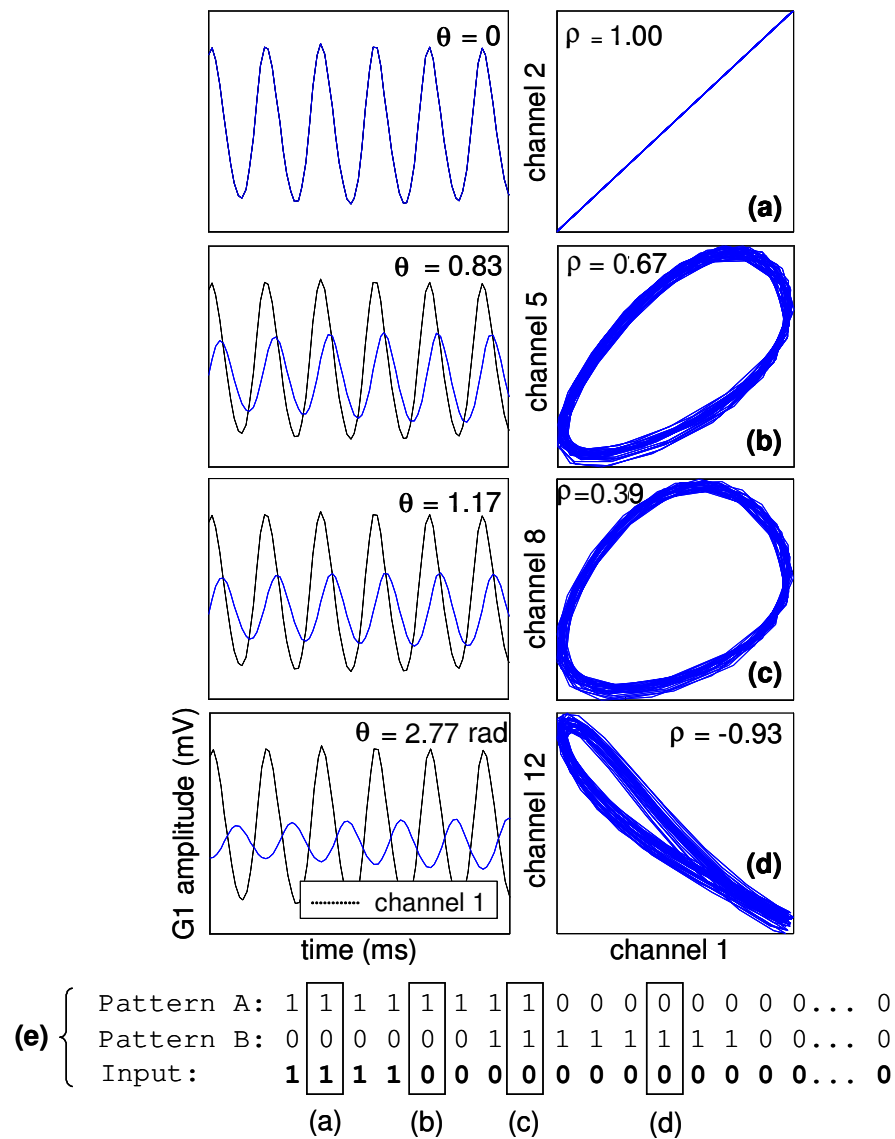


Fig. 38 Extracting phase information from the KIII model. Phase is computed as the correlation coefficient of each channel with respect to a reference channel (channel 1). In this toy problem (refer to inset (e)), pattern A is recalled with an incomplete input. (a) Output of a channel that belongs to pattern A and is also excited at the input. (b) Output of the channel that belongs to pattern A and is not excited at the input. (c) Output of a channel that belongs to pattern A and pattern B and is not excited at the input. (d) Output of a channel that does not belong to pattern A and is not excited at the input.

### V.3. Scaling invariance

Yao and Freeman (1991) showed that some properties of the KIII model are invariant with respect to the number of channels: the amplitude and general shape of the oscillations at each channel are independent of the number of inputs in the model. To determine if their results also apply to phase information, we first present a thorough study on three KIII models with 16, 32 and 64 channels. The study simulates a two-odor classification problem with varying levels of complexity in terms of:

- (i) the degree of overlap between the two stored patterns, and
- (ii) the number of missing or corrupted channels at the input.

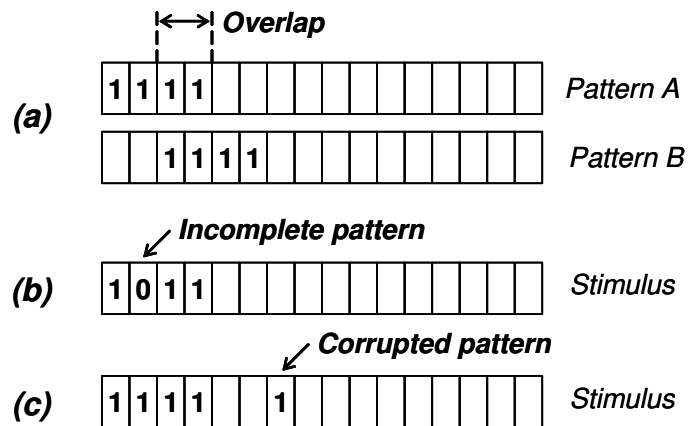


Fig. 39 Overlap between input patterns for a 16-channel KIII. (a) Simulating an incomplete (b) and a corrupted (c) input pattern.

Fig. 39 illustrates the two input patterns for the 16-channel case. Each pattern consists of four active channels, each represented by a bit set to 1, and twelve inactive channels, represented by a blank bit. Due to the symmetry of the problem, in what follows the KIII model is always excited with a stimulus from pattern A. To incorporate different degrees of overlap, three patterns sets are considered having 0, 1 and 2 bits of overlap. Each one of these three sets leads to a unique Hebbian associative matrix and, therefore, a separate KIII model. Fig. 39(a) illustrates the situation where the patterns have an overlap of 2 bits. To simulate incomplete patterns (e.g. caused by sensor degradation), 0, 1 or 2 of the active bits in the stimulus may be set to zero. Fig. 39(b) illustrates the case where the stimulus for pattern A is incomplete by one bit. Finally, to simulate corrupted patterns (e.g. to due to background odors), 0, 1 and 2 bits not belonging to either pattern may be set to one. Fig. 39(c) shows a stimulus for pattern A with one corrupted bit. All these different combinations lead to  $3 \cdot 3 \cdot 3 = 27$  possible scenarios for a 16-channel KIII model. Data for the 32- and 64-channel models is obtained by scaling the stored patterns and input stimuli by a factor of 2 and 4, respectively.

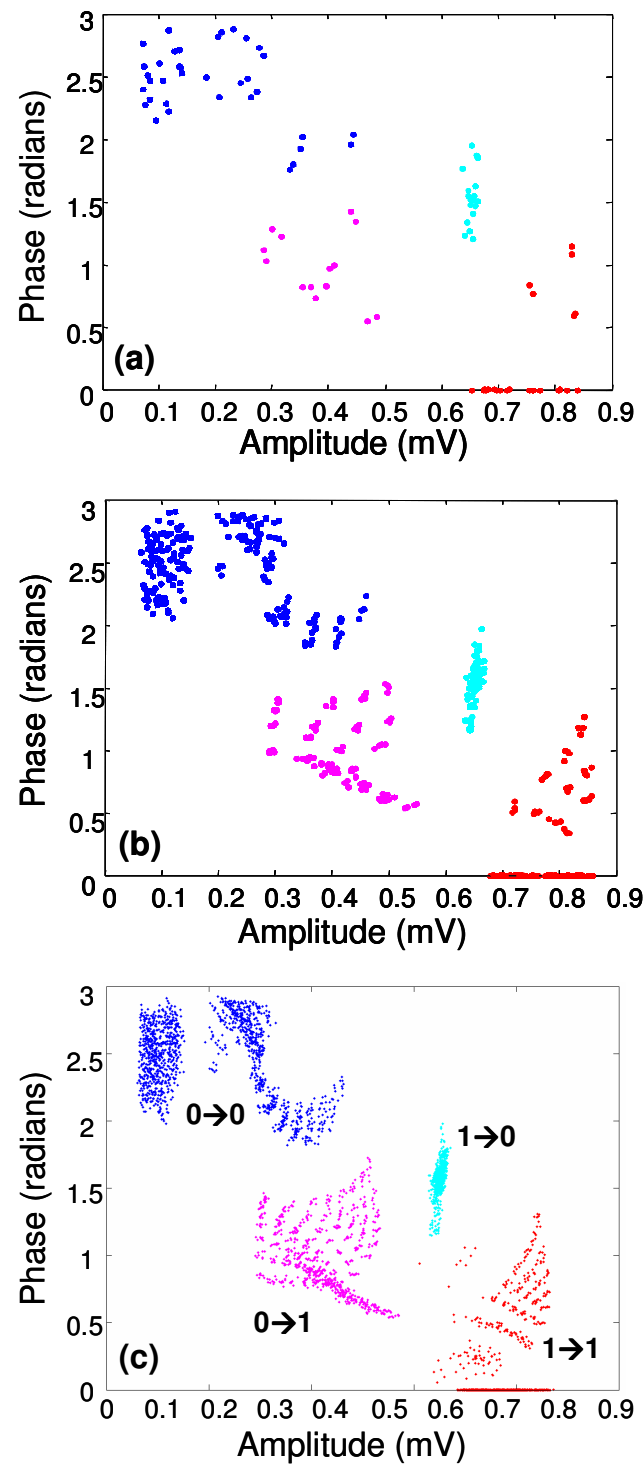


Fig. 40 Scatter plot of amplitude vs. phase codes for different input-stimulus→desired-response cases.

Simulation results are presented in Fig. 40 in the form of bivariate scatter plots. Each point in the scatter plots represents the output of one KIII channel for one stimulus. The abscissa is the RMS amplitude of the channel, whereas the ordinate is the phase relative to channel 0, which is consistently activated and used as a reference. Four different cases of input-stimulus  $\rightarrow$  desired-response are considered in the study, which correspond to two correct and two erroneous input stimuli:

- $1 \rightarrow 1$  (no error): stimulus in a channel that encodes for pattern A
- $0 \rightarrow 0$  (no error): no stimulus in a channel that does not encode for pattern A
- $0 \rightarrow 1$  (incomplete pattern): missing stimulus in channel that encodes for pattern A
- $1 \rightarrow 0$  (corrupted pattern): noisy stimulus in a channel that does not encode for pattern A

The results in Fig. 40 show that, although a higher number of channels yields a more detailed structure of the amplitude/phase clusters, these scatter plots have a similar structure regardless of the number of channels. This result leads to the conclusion that the KIII model is not only scale invariant with respect to amplitudes, a result previously established in (Yao and Freeman, 1990), but also with respect to phase information.

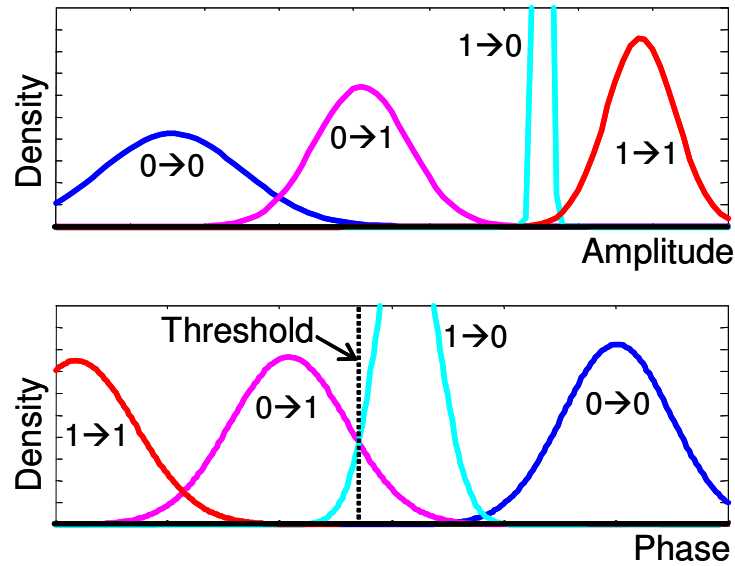


Fig. 41 Univariate density functions for the amplitude and phase codes.

### V.3.1. Bit recovery

An important conclusion can also be extracted from these scatter plots. Fig. 41 shows the univariate distribution of the amplitude and phase codes in the 64-channel model for the each of the four input-stimulus→desired-response cases. A Gaussian distribution has been assumed for visualization purposes. It can be observed that the amplitude code is able to recover either incomplete or corrupted bits, but not both, since the  $0 \rightarrow 1$  and  $1 \rightarrow 0$  densities lie on opposite sides of their desired response. This result indicates that the amplitude of a particular channel tends to be driven primarily by the input stimulus rather than by the lateral connections in the Hebbian matrix. In the case of a phase code, a simple threshold can be obtained to correct the majority of the incomplete or corrupted

bits, indicating a higher sensitivity to lateral connections. Bit recovery is, therefore, more reliable using phase information.

### **V.3.2. Pattern recovery: preliminary results**

The results in the previous sections demonstrate the significant advantage of a phase code in the recovery of individual errors at the channel level (bit-wise). How do these results translate into classification performance at the pattern level? To explore this issue, we employed a Hamming-distance classifier (Lippmann, 1987) at the output of the KIII. Oscillatory activity (phase or amplitude) at each KIII output channel was first discretized using a Likelihood Ratio Test: samples from the  $0 \rightarrow 0$  (true negatives, T-) and  $1 \rightarrow 0$  (false negatives, F-) conditions were assigned to one Gaussian density, samples from the  $1 \rightarrow 1$  (true positives, T+) and  $0 \rightarrow 1$  (false positives, F+) condition were assigned to a second Gaussian density, and a decision threshold was computed to minimize the probability of error of the two densities (van Trees, 1968). The process is illustrated in figure Fig. 42. Inputs and prototype patterns were generated using a 16-channel KIII model with 8 active channels (as opposed to the 4 active channels in Fig. 39) to explore higher levels of overlap between patterns. The number of incomplete or corrupted bits was allowed to range between 0 and 2.

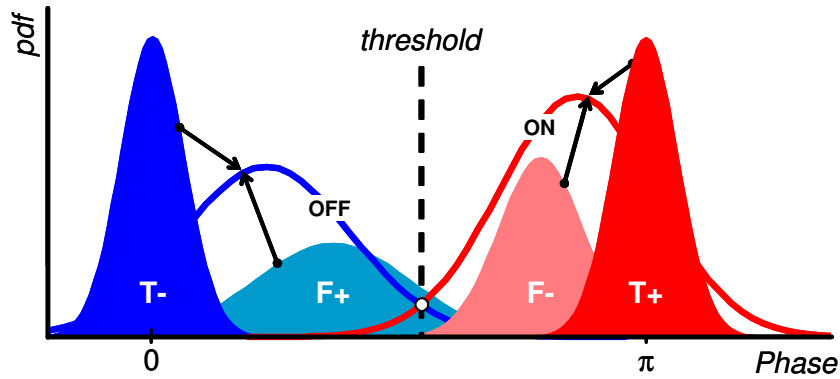


Fig. 42 Likelihood ratio test for the classification of channel activity. True negatives (T-) and false positives (F+) are assigned to a Gaussian distribution (OFF). False negatives (F-) and true positives (T+) are assigned to a second Gaussian distribution (ON) (Gutierrez-Osuna and Gutierrez-Galvez, 2003).

The average classification rate as a function of the overlap between prototypes is shown in Fig. 43, where ties (e.g., the input pattern is equidistant from the two prototypes) are counted as miss-classifications. With zero overlap between the two prototypes (1111111100000000 and 0000000011111111), both codes provide 100% classification rate since the Hamming-distance classifier is robust against errors in a few bits. As the overlap between the prototypes grows, discrimination between them becomes more difficult. As a result, bit-wise corrections become increasingly relevant, allowing the phase code to clearly outperform amplitude information<sup>1</sup>.

---

<sup>1</sup> Not shown in the figure, for overlaps of 7 bits (1111111100000000 and 0111111110000000) and 8 bits (the two prototypes are identical), the performance of both codes drops to 0%.

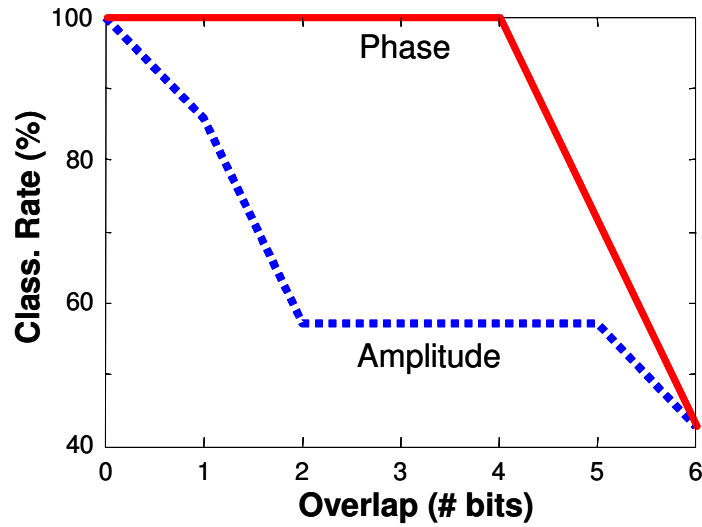


Fig. 43 Performance of a Hamming-distance classifier on the two codes.

#### V.4. Symmetry of the associative memory matrix

Once the scale invariance of the KIII model with respect to phase information has been validated, the study can now be focused on a lower dimensional model where an exhaustive evaluation of every possible combination of input stimulus and pattern sets is computationally feasible. Although 2- and 4-channel models could be used to this effect, the results in Fig. 40 show that more channels lead to higher resolution. For this reason, an 8-channel model is chosen for the final study.

In order to avoid exploring redundant combinations, symmetries in the KIII associative-memory matrix will also be exploited. Following Yao and Freeman (1990), mitral-mitral lateral connections can be computed as:

$$W_{MI} = \sum_{\forall i} f(p_i p_i^T) \quad (5.1)$$

where  $p_i$  is the correct input pattern for the  $i$ -th odor class, and  $f(\cdot)$  is a threshold function so that the elements in  $W_{MI}$  are binary, either HIGH or LOW<sup>2</sup>; diagonal elements in the matrix are set to zero. Thus, a HIGH element in the Hebbian matrix represents two KIII channels that are simultaneously active for *at least* one odor pattern. Since different pattern sets can lead to the same Hebbian matrix, an exhaustive evaluation of every possible pattern set can be reduced to the study of all possible matrix configurations.

A representation of the Hebbian matrix as an undirected graph will be used to illustrate the existing symmetries. For simplicity, assume a 4-channel model with only one connection between channels. Since the channels are symmetric, the behavior of the system will be the same regardless of where this connection is located, as illustrated in Fig. 44. Generalizing this idea, graphs with the same number of connections and the same topology (i.e. isomorphic graphs) have to be considered just once. As a result, a 4-channel model with  $2^6 = 64$  possible configurations is reduced to the 11 non-isomorphic graphs in Fig. 44. Similarly, a 8-channel model can be reduced from  $2^{28} = 2,7 \cdot 10^8$  to 1,192 cases, for a significant savings in CPU time.

---

<sup>2</sup> LOW and HIGH values are denoted by  $W_{MIMIL}^{low}$  and  $W_{MIMIL}^{high}$ , respectively Yao and Freeman (1990).

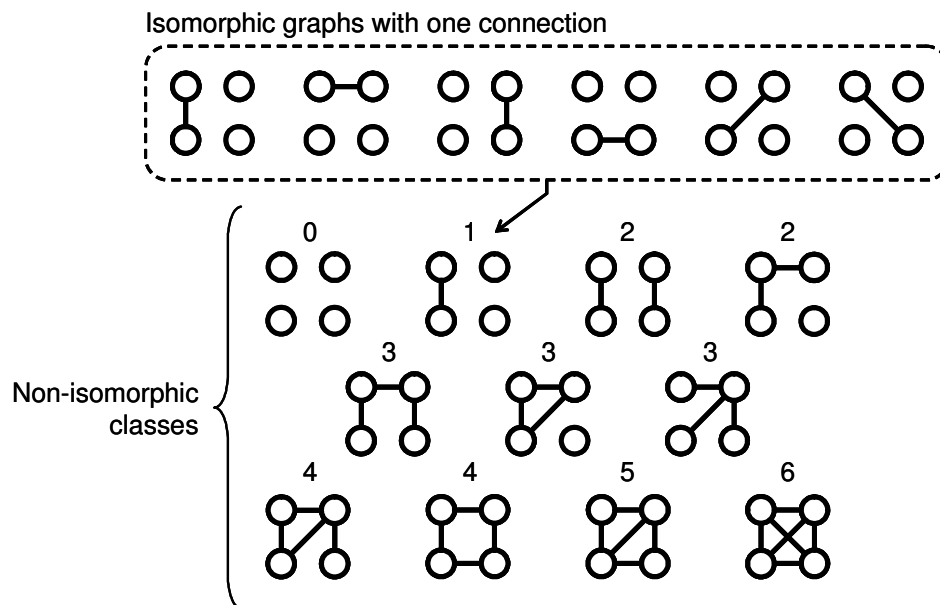


Fig. 44 Reduction of a 4-channel model to 11 non-isomorphic classes. The index above each graph denotes the number of active Hebbian connections.

### V.5. Pattern recovery: final results

The final comparison of the two coding schemes will be performed on an 8-channel KIII model, for a total of 1,192 non-isomorphic cases. As opposed to the preliminary study in section V.3.1, where performance was studied as a function of degrees of overlap in the pattern set and distortions in the input stimulus, the pattern recovery capabilities in this final study can only be evaluated in terms of the properties of each graph since the relationship between pattern sets and graphs is many-to-one. Two observations will greatly simplify this analysis. First, any two neighboring nodes (those that are connected directly by an edge) represent channels that are simultaneously active for at least one stored pattern. Conversely, any two nodes that are more than one edge away represent

channels where two or more patterns overlap. Therefore, it is possible to analyze the pattern-recovery performance of the phase and amplitude codes by comparing the activation between nodes connected by a single edge (which represents a true pattern) against the activation between nodes connected by a multi-edge path (which represents an undesirable overlap).

This idea is illustrated in Fig. 45(a). For a given graph, a single input stimulus is applied to the channel with the highest number of lateral connections ( $d_0$  in the figure), and the activity on the remaining channels is analyzed. Nodes within one edge from  $d_0$  (denoted by  $d_1$ ) are part of a pattern. Nodes two edges away (denoted by  $d_2$ ) are the effect of an overlap between two or more patterns. The remaining nodes ( $d_3$  through  $d_\infty$ ) can be neglected since they involve higher-order overlaps between patterns. Fig. 45(b) illustrates the situation where the response of  $d_0$  and  $d_1$  nodes is linearly separable from the rest, indicating that a simple threshold function could be used to recover an incomplete pattern from an input stimulus having a single active channel. Fig. 45(c) illustrates the opposite situation, where the response of  $d_0$  and  $d_1$  nodes is not linearly separable from the rest and, as a result, the incomplete pattern cannot be recovered.

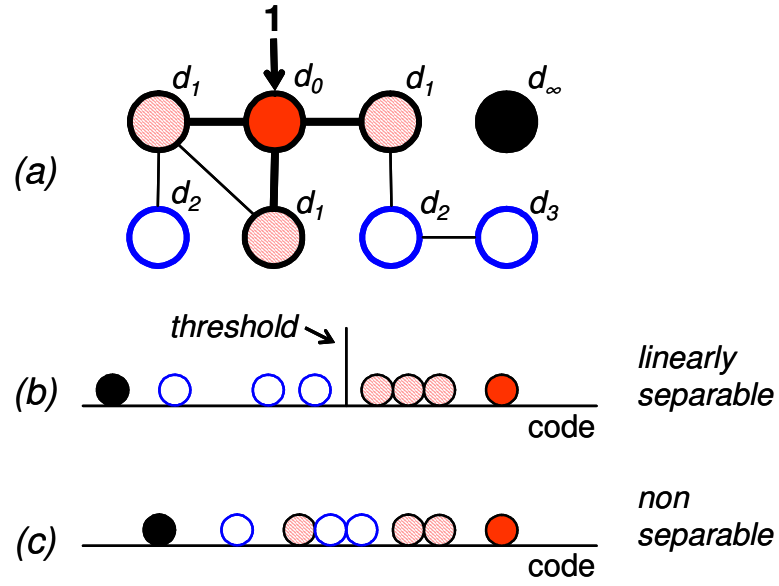


Fig. 45 (a) Pattern and overlap bits for a given Hebbian graph. (b, c) Pattern recovery as a linear separability problem.

The procedure outlined in Fig. 45 is repeated individually for each of the 1,192 non-isomorphic cases in the 8-channel KIII in order to measure the pattern recovery capabilities of the amplitude and phase codes. The results are presented in Fig. 46 as a function of the number of  $d_2$  connections in each graph, which can be related to the overlap (e.g. the complexity) of the corresponding pattern sets. Each point in the plot represents the percentage of graphs where the linear separability in Fig. 45(b) is achieved, relative to the total number of graphs. This result shows that the performance of the amplitude code decreases dramatically as the degree of overlap increases, whereas the phase code degrades in a more graceful manner and always provides higher classification rates.

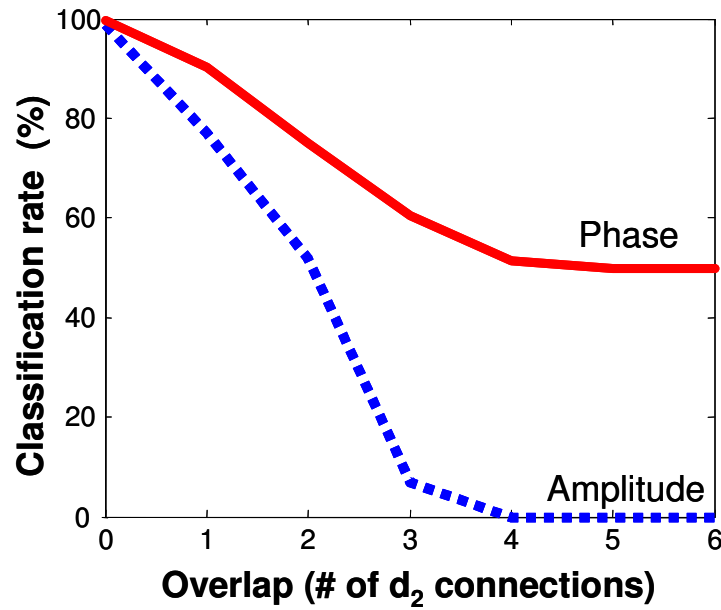


Fig. 46 Overall performance of the phase and amplitude codes as a function of pattern overlap.

The average phase difference between the input node ( $d_0$ ) and all remaining nodes is shown in Fig. 47(a). The phase of  $d_1$  nodes is closer to the input node than to the remaining nodes. For comparison, the corresponding average amplitudes are shown in Fig. 47(b). In this case the situation is reversed, with the amplitude of  $d_1$  nodes being farther from the input node than to the other nodes. These results provide additional evidence for the superiority of the phase code.

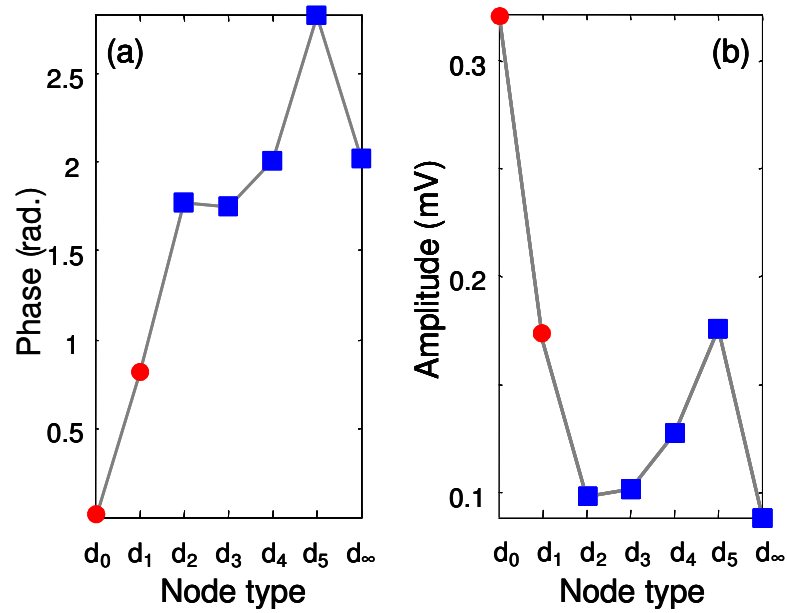


Fig. 47 Phase difference and amplitude as a function of distance (number of edges) to the input node.  $d_0$  and  $d_1$  correspond to nodes that belong to the same pattern.

## V.6. Phase code with continuous patterns

Previous sections in this chapter explored the performance of the phase code when the KIII operates with binary inputs. In this section, we extend our study of the phase code to continuous inputs. It is worth to note that, with the exception of (Kozma and Freeman, 2001) all previous studies on the KIII model have used binary input patterns.

In order to process continuous inputs, the Hebbian rule in Eq. 5.1 must be modified. With binary patterns, mitral-to-mitral connections were forced to have one of two possible values: HIGH if the channels connected were active for the same patterns and LOW otherwise (refer to section V.4). In the case of continuous patterns, however,

these connections must be allowed to have a continuous range of values. This is achieved by removing the threshold function  $f(\cdot)$  in Eq. 5.1:

$$W_{M1} = \sum_{\forall i} p_i p_i^T + B \quad (5.2)$$

where  $W_{M1}$  is the lateral connectivity between mitral cells, and  $B$  is an offset term that defines the minimum strength of any connection. We found that this offset term is critical to the computation of the phase code: without such offset, aperiodic oscillations in the basal state make it difficult to obtain a stable estimate of the phase of each channel (if such “phase” can at all be defined for an aperiodic signal). The offset term  $B$  allows all channels to jump to a limit cycle whenever an input is introduced, thus facilitating computation of the phase.

To study the performance of the phase and amplitude codes with continuous patterns, we trained a 64-channel KIII model with the three overlapping bell-shaped patterns shown in Fig. 48(a). Fig. 48(b) and (c) shows the amplitude and phase of the KIII, respectively, when the target pattern (pattern B) was introduced. The amplitude read-out retrieves not only the target pattern (pattern B) but also interfering contributions from the other stored patterns (A and C). This is because the overlapping patterns are excited to some extent by the input applied to the common channels (pattern completion). In contrast, the phase read-out retrieves the target pattern with minimum interference from the other stored

patterns, as shown in Fig. 48(c). This behavior is consistent with that we have reported earlier in this chapter for binary patterns.

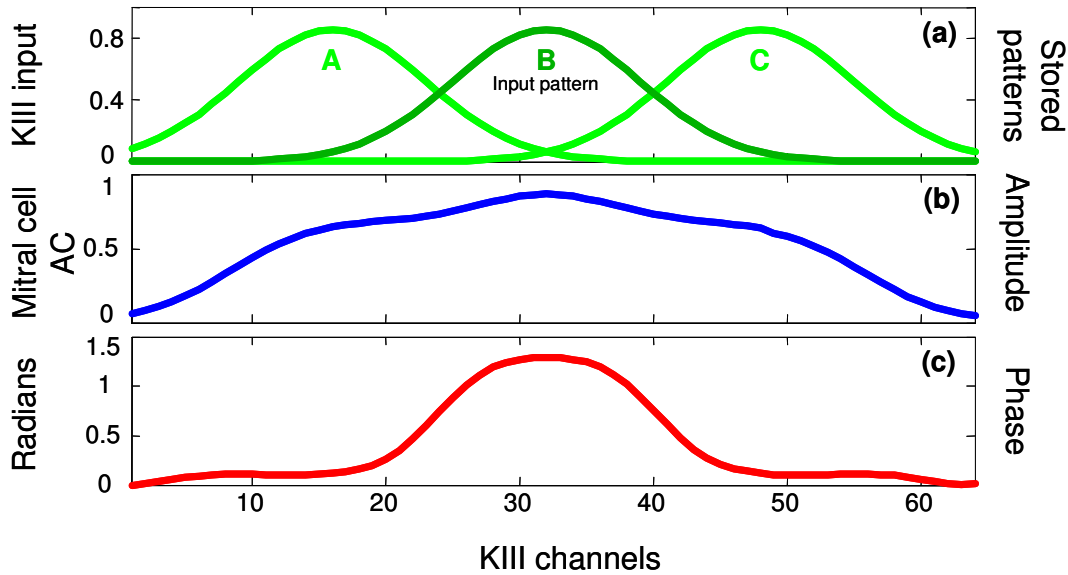


Fig. 48 Retrieval of continuous patterns through the amplitude and phase of the oscillations in the KIII. (a) Three overlapping bell-shaped patterns are stored in the KIII. (b) When the central pattern is presented as an input, the AC amplitude of the oscillation in the KIII channels shows a high degree of cross-talk with previously stored patterns. (c) When the same central pattern is introduced, the relative phase of the oscillations in the KIII channels shows minimum interference with other patterns.

Next, we further characterize the performance of the amplitude and phase code as a function of the degree of overlap between stored patterns. For this purpose, we trained the KIII with the two bell-shaped patterns shown in Fig. 49. Increasingly higher levels of overlap between the two patterns were achieved by shifting pattern A to the right

(Table 4). The Euclidian distance between the recalled pattern (the output of the KIII) and the target pattern (pattern B) was used to evaluate the performance of amplitude and phase codes<sup>3</sup>. Results are shown in Fig. 50. It can be observed that both phase and amplitude are able to achieve near-perfect retrieval of the target pattern when the overlap is low. As the overlap increases, the performance of the amplitude code degrade faster compared to that of the phase code. It is also worth noting that the phase code always performs better than the amplitude code. Therefore, we can conclude that the phase code is more reliable than the amplitude code, also for continuous patterns.

Table 4 Euclidean distance and corresponding overlap between patterns A and B.

Euclidean distance	4.96	4.96	4.96	4.93	4.87	4.76	4.56	4.25	3.78	3.14
Overlap (%)	1.23	2.67	3.82	7.39	10.01	17.44	22.42	35.27	43.16	61.68

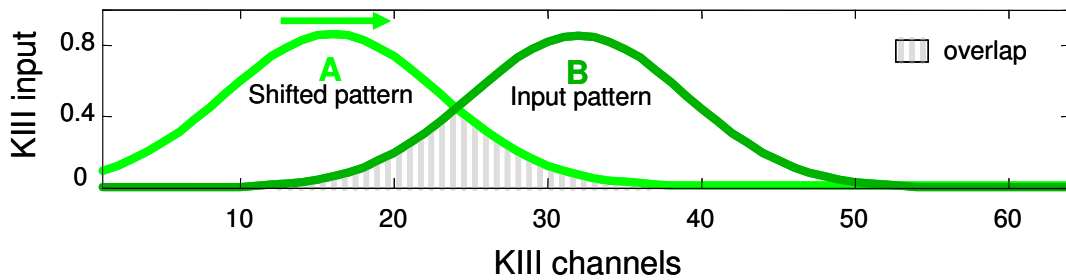


Fig. 49 Two bell-shaped patterns are used to train the KIII. Different degrees of overlap are achieved by shifting pattern A to the right.

<sup>3</sup> For each output pattern (phase and amplitude) and the stored pattern, the activity of each channel was divided by the maximum activity across all channels. This form of normalization is necessary since the three representations (phase, amplitude, and stored patterns) have different scales.

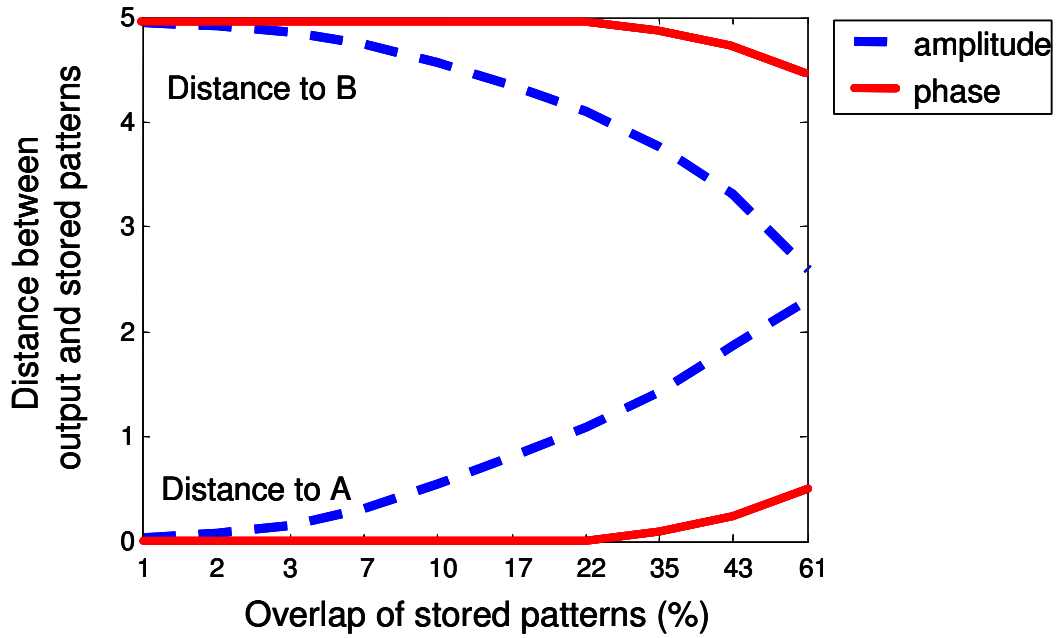


Fig. 50 Ability of the phase and amplitude codes to recall an overlapping pattern. The KIII is trained with patterns A and B from Fig. 49; pattern B is used as input. The figure shows the distance between the recalled pattern and the stored patterns A and B. As the overlap between the stored patterns (A and B) increases, the performance of the amplitude code degrades faster compared to that of the phase code.

## V.7. Conclusions

This chapter has proposed an analogy between coherent oscillations in neural populations and phase locking in the KIII model. We have shown that phase differences between channels can be efficiently measured by treating the state-space trajectory as a two-dimensional distribution and computing its correlation coefficient. Scale invariance of the KIII with respect to phase information has been empirically validated on three

models with binary patterns and 16, 32 and 64 channels. The performance of the phase code has been demonstrated in terms of (1) bit-wise error recovery from a decision-theoretic viewpoint, and (2) pattern-level completion with a Hamming-distance classifier. An exhaustive comparison of the pattern-recovery capabilities of the phase and amplitude codes has been presented on an 8-channel model *with binary patterns*. In order to avoid a combinatorial explosion, redundant pattern and stimulus combinations have been eliminated by means of graph isomorphism. Experimental results show that information embedded in the phase of the KIII channels clearly outperforms the amplitude code.

The performance of the phase code has also been evaluated *with continuous patterns*. The ability of both codes to recover an input pattern has been established as a function of the overlap between stored patterns. Our results show that phase code is more robust than amplitude code as the overlap of the stored patterns increases. The output patterns obtained with the amplitude code tend to have more interference from overlapping stored patterns than those obtained with the phase code. Thus, our initial results on binary patterns (reported in section V.5 and in Gutierrez-Osuna and Gutierrez-Galvez, 2003) also extend to the continuous case: the phase code provides a better recovery of the target pattern than the amplitude code.

It appears that an amplitude code would be easier to decode as it does not require the precision involved in decoding the information from phase. It has been reported in the

literature that the olfactory system uses both amplitude and phase information (Stopfer, 1997).

Additional information other than correlation coefficients, which are equivalent to phase differences in sinusoidal oscillations, could also be extracted from the KIII dynamic attractors in two- or higher-dimensional state spaces. This area constitutes promising directions for future work.

## CHAPTER VI

### CONTRAST ENHANCEMENT

The objective of this chapter is to develop a new learning rule to enhance the separability of gas-sensor-array patterns. Inspired by the ability of the olfactory bulb contrast enhancement through excitatory and inhibitory circuits, we propose a learning rule that employs a Hebbian term to build associations within odors and an anti-Hebbian term to reduce correlated activity across odors. First, a formal study of the learning procedure is performed on a feed-forward linear model. Then, the KIII model is trained with the new learning rule, and validated on both synthetic data and experimental sensor-array patterns.

#### **VI.1. Contrast enhancement in the olfactory bulb**

The olfactory bulb enhances the contrast across odors, facilitating their recognition in higher stages of the olfactory pathway. Following Yokoi et al. (1995) and Mori, et al. (1999), contrast enhancement in the olfactory bulb results from inhibition of mitral cells by nearby granule interneurons (Fig. 51). This inhibition has the effect of reducing the molecular tuning range (i.e., increasing the specificity) of a mitral cell relative to that of the olfactory receptor neurons that converge onto it. This effect is corroborated by experimental results, which are also illustrated in Fig. 51. The right hand side of the figure shows the response of three glomerular units (A, B, C) and one mitral cell output

(D) upon exposure of the ORN to n-aliphatic aldehydes with different carbon chain lengths. It can be observed that the output of mitral cell D is reduced with respect to its input (glomerulus B) for those n-aliphatic aldehydes for which nearby mitral cells have a high response. This effect is due to the inhibitory lateral connections of surrounding mitral cells.

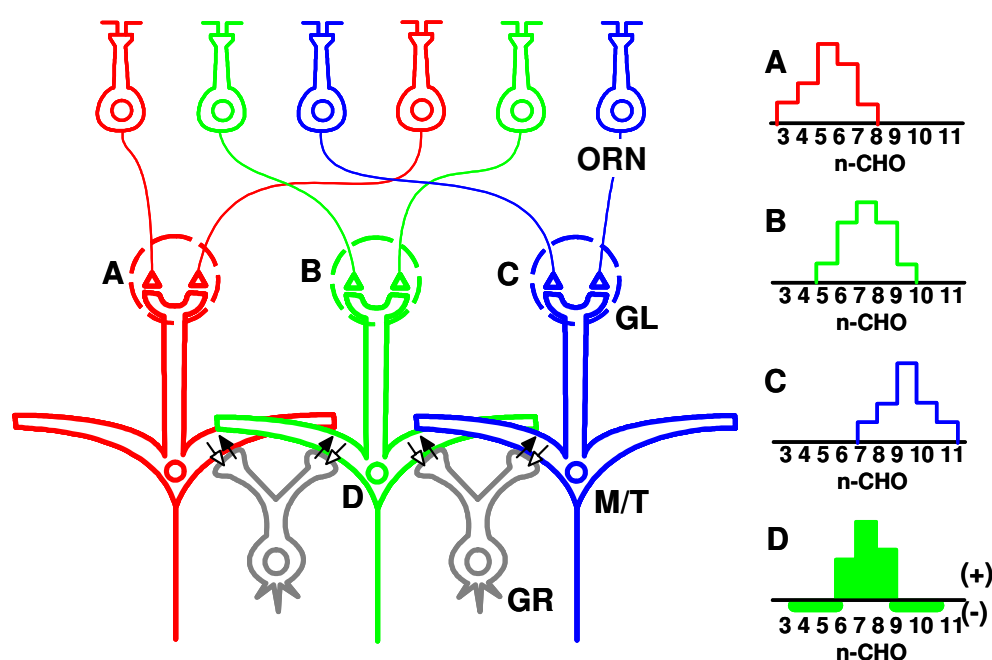


Fig. 51 Contrast enhancement in the olfactory bulb. (a) Architecture of the early stages of the olfactory pathway: Olfactory Receptor Neurons (ORN), Glomeruli (GL), Mitral/Tufted cells (M/T), Granule cells (GR). (b) Response of three glomerular units (A, B, C) and one mitral cell output (D) upon exposure of the ORN to n-aliphatic aldehydes with different carbon chain lengths. It can be observed that the output of mitral cell D is sharpened with respect of the input (B) as a result of the lateral interaction with neighboring M/T cells (adapted from Yokoi, Mori, and Nakanishi, 1995).

## VI.2. Contrast enhancement through Hebbian/anti-Hebbian learning

The effect of lateral inhibition through granule cells can be thought of as an orthogonalization of patterns. This computational function can be achieved by means of anti-Hebbian learning, a mechanisms known to decorrelate inputs (Principe et al., 1999). The anti-Hebbian learning rule is the opposite of the Hebbian rule, and states that the strength of the connection between two neurons should decrease when both activate simultaneously:

$$\Delta w_{kl} = -x_k x_l \quad (6.1)$$

where  $x_k$  and  $x_l$  are the  $k$ -th and  $l$ -th inputs to the system.

Application of the anti-Hebbian rule to the KIII model is not trivial because of the oscillatory nature of the KII sets: the interaction between laterally-connected oscillators is a vector operation. Depending on the relative phase of the two oscillators, it is possible for an inhibitory connection to have an excitatory effect. This problem has been previously reported with oscillatory neural networks by Hirsch and Baird (1995). To address this problem, we propose a new learning rule that avoids negative connections by combining Hebbian and anti-Hebbian terms. The role of the Hebbian term is two-fold. First, it preserves the associative-memory function of the KIII, allowing the model to learn odor-specific attractors. Second, it provides positive mitral-to-mitral

connections, which are subsequently reduced by an anti-Hebbian term without the risk of becoming negative. The use of both Hebbian and anti-Hebbian terms on the same connections has been linked to the mechanism of spike-dependent synaptic plasticity (Bi and Poo, 2001). This analogy is described in Appendix A.

### VI.2.1. Adapted Hebbian/anti-Hebbian rule

To derive a new learning rule inspired by the synaptic time dependent plasticity (STDP) mechanism (Appendix A), let us consider the linear-associative memory (LAM) in Fig. 52.

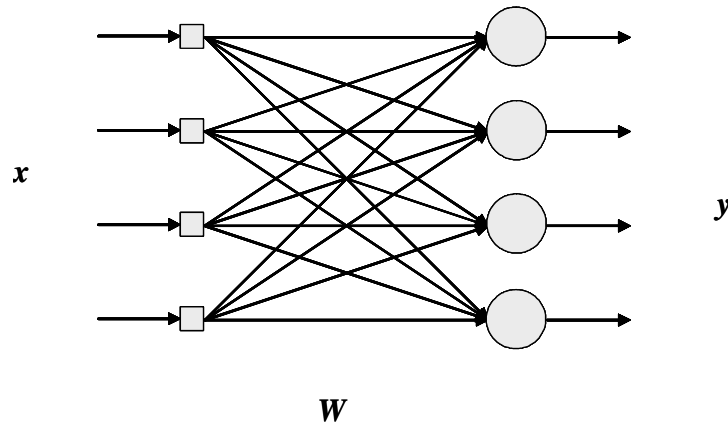


Fig. 52 Linear associative memory with a feed forward network.

The input-output relationship of a LAM is:

$$y(n) = w^T(n) \cdot x(n) \quad (6.2)$$

where  $x(n)$ ,  $y(n)$  and  $w(n)$  are the values of input, output, and weight matrix at the  $n^{\text{th}}$  iteration, respectively.

Following STDP, the weight update will have two terms:

$$w(n+1) = w(n) + \Delta w_{corr}(n) + \Delta w_{decorr}(n) \quad (6.3)$$

where  $\Delta w_{corr}$  and  $\Delta w_{decorr}$  are the correlation and decorrelation terms respectively. To understand how these two terms could emerge during learning, we assume that (1) inputs are presented to the LAM in a random fashion as a result of the system interacting with its environment and (2) the system's response is latched at the output until the system processes the next input. This sequence is illustrated in Fig. 53.

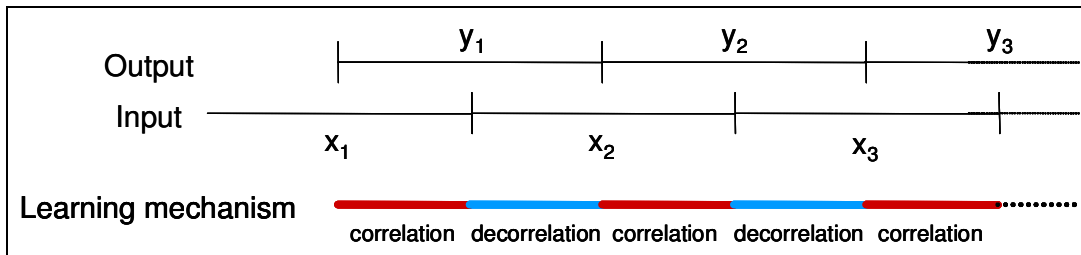


Fig. 53 The network correlates or decorrelates the input and the output depending on their causal relationship.

Causally related inputs-outputs  $(x(i), y(i))$  lead to correlation, whereas non-causally related inputs-outputs  $(x(i+1), y(i))$  lead to decorrelation. Therefore, the two terms take the following form:

$$\Delta w_{corr}(n) = \lambda \cdot x(n) \cdot y^T(n) \quad (6.4)$$

$$\Delta w_{decorr}(n) = -\rho \cdot x(n+1) \cdot y^T(n) \quad (6.5)$$

where  $\lambda$  and  $\rho$  capture the strength of the correlation and decorrelation mechanism respectively. Given that our model does not capture specific timing, we estimate  $\lambda$  and  $\rho$  to be proportional to the area enclosed by the positive and negative curves in Fig. 100 respectively. Since these areas are comparable, we set  $\lambda$  and  $\rho$  to an equal value ( $\lambda = \rho = 1$ ).

Considering Eq. 6.2, the correlation term can be rewritten as:

$$\Delta w_{corr} = x(n) \cdot (w^T(n) \cdot x(n))^T = x(n) \cdot x^T(n) \cdot w(n) \quad (6.6)$$

note that the first two terms  $x(n) \cdot x^T(n)$  are the outer product of the input with itself.

Similarly, the decorrelation term reads:

$$\Delta w_{decorr} = -x(n+1) \cdot \left( w^T(n) \cdot x(n) \right)^T = -x(n+1) \cdot x^T(n) \cdot w(n) \quad (6.7)$$

where  $x(n+1) \cdot x^T(n)$  is the outer product of input vectors  $x(n)$  and  $x(n+1)$ , which are presented at different times  $n$  and  $n+1$ , respectively.

To determine the final weight matrix  $w$  obtained by training the LAM with these two terms, let us consider that  $N$  *non-negative* patterns  $\{p^1, p^2, p^3, \dots, p^N\}$  are randomly presented to the system. Following Eq. 6.6 and assuming that the initial value of the weight matrix  $w(0)$  is zero, the correlation term will be a superposition of the outer product of all the inputs:

$$w_{corr} = \sum_{i=1}^N p^i \cdot (p^i)^T \quad (6.8)$$

Similarly, following Eq. 6.7, the decorrelation term will be a superposition of the outer product of each pattern with the rest. This term reads:

$$w_{decorr} = - \sum_{i=1}^N \sum_{\substack{j=1 \\ j \neq i}}^N p^i \cdot (p^j)^T \quad (6.9)$$

Combining the two terms, we obtain the proposed Hebbian/anti-Hebbian rule:

$$w = \underbrace{\sum_{i=1}^N p^i \cdot (p^i)^T}_{\text{correlation term}} - \underbrace{\sum_{i=1}^N \sum_{\substack{j=1 \\ j \neq i}}^N p^i \cdot (p^j)^T}_{\text{uncorrelation term}} \quad (6.10)$$

The Hebbian learning rule is ultimately applied to the mitral-to-mitral connections of a reduced KIII model, shown in Fig. 54. The first term in Eq. 6.10 is the Hebbian rule, which strengthens the connection between neurons that are active *within* a pattern. The second term is the anti-Hebbian component, which reduces the connection weights between neurons that are active for multiple patterns, on the average reducing the overlap *across* patterns. Negative mitral-to-mitral connections are avoided by forcing to zero all elements in Eq. 6.10 that become negative.

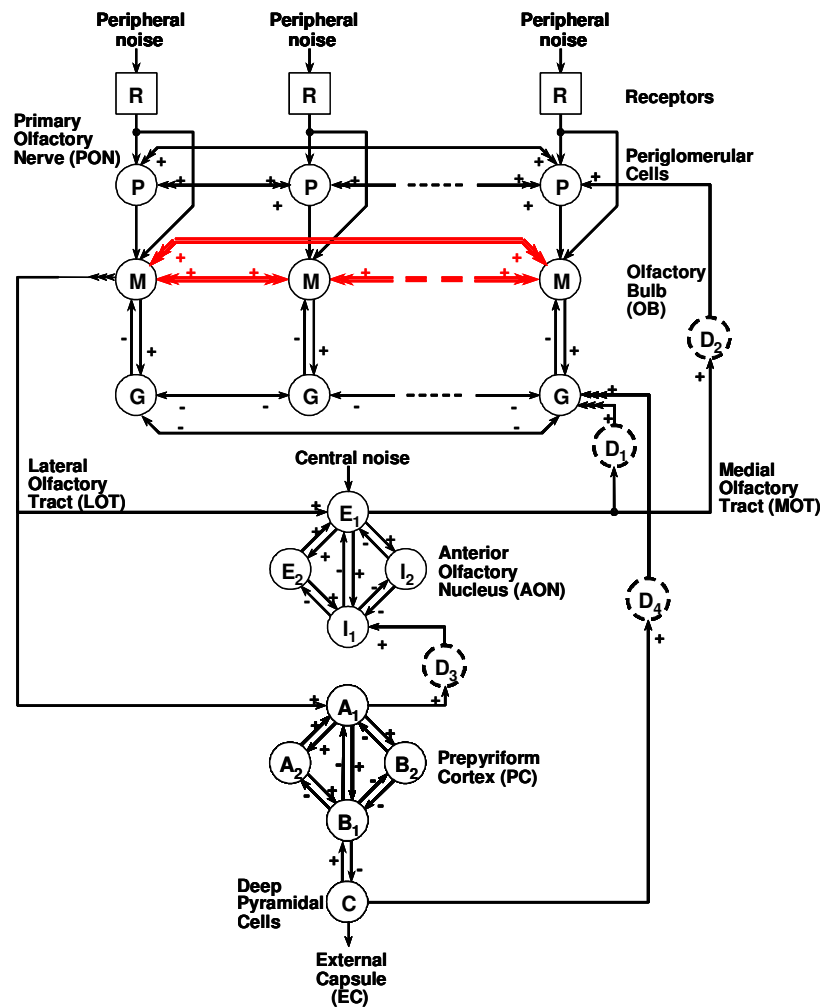


Fig. 54 Mitral to mitral connections of the reduced KIII model are trained with the Hebbian/anti-Hebbian rule (adapted from Kozma and Freeman, 2001).

### VI.3. Formal analysis of the Hebbian/anti-Hebbian rule

To isolate computational function from non-linear dynamics intricacies of the KIII model, a formal analysis of the proposed learning rule is performed on a simplified feed-forward network with linear neurons. The objective of this analysis is to prove that the

Hebbian/anti-Hebbian rule orthogonalizes stored patterns. First, we explain how the study of the learning rule in a feed-forward network with linear neurons can be used to infer the effect of the learning rule in the KIII model. Next, we determine necessary conditions for the learning rule to orthogonalize the stored patterns. In doing so, we will also show that the Hebbian/anti-Hebbian learning rule completely removes cross-talk<sup>4</sup>. Finally, we prove that, under the above mentioned conditions, the Hebbian/anti-Hebbian learning rule orthogonalizes the stored patterns. Therefore, the conditions are not only necessary but also sufficient to orthogonalize the patterns.

### VI.3.1. Feed-forward linear model

The simplified feed-forward linear network used for this analysis is equivalent to the unfolding in time of a recurrent structure with linear neurons (Haykin, 1999; pp. 732-789). Fig. 55(b) shows the unfolding of the fully-laterally-connected network in Fig. 55(a). At any specific time  $t$ , the activity on the network  $x_i(t)$  is computed as:

$$x_i(t) = w \cdot x_i(t-1) + b_i \quad (6.11)$$

The evolution of this system will differ from that of the KIII because of the non-linear behavior of K0 sets. However, the effect of one single linear step will be similar in both systems, and much information about the effect of the learning rule on the recurrent network can still be gained by studying this simplified model.

---

<sup>4</sup> Cross-talk is defined as the interference that a stored pattern has in the recall of any other pattern.

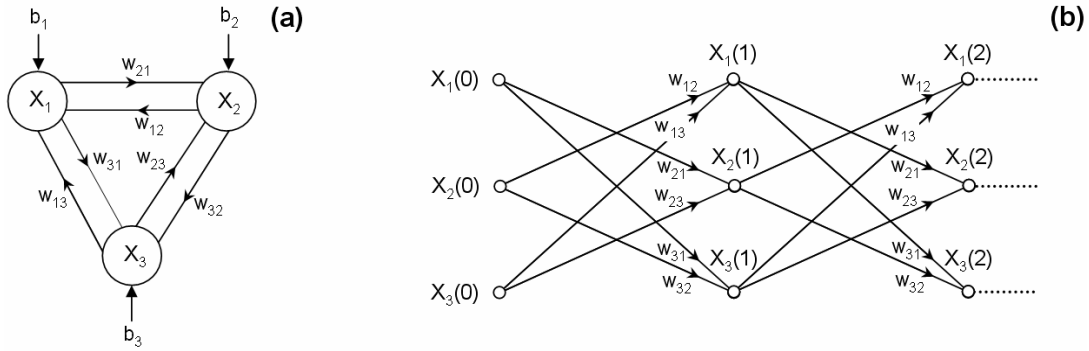


Fig. 55 Unfolding in time of a recurrent neural network. (a) Fully-connected recurrent neural network, where  $X_i$  is the state of neuron  $i$ ,  $b_i$  is the input to neuron  $i$ , and  $w_{ij}$  is the connection weight between neurons  $i$  and  $j$ . (b) Unfolding in time of the recurrent network.  $X_i(t)$  denotes the state of neuron  $i$  at time  $t$ , and  $w_{ij}$  is the connection weight between neurons  $i$  and  $j$ .

In this study, the bias term will be assumed to be zero; this will allow us to isolate the effect of learning on the output of the system. Specifically, we consider a network with  $M$  fully-connected neurons, analogous to the interconnectivity between mitral cells (Fig. 35, Chapter IV) that plays a major role in the processing of information in the KIII model (adapted from Haykin, 1999).

### VI.3.2. Necessary conditions for orthogonalization

We first determine necessary conditions for the Hebbian/anti-Hebbian learning rule to orthogonalize the stored patterns. We assume that  $N$  *non-negative* patterns

$p^i = [x_1^i \ x_2^i \dots x_M^i]^T$ ;  $1 \leq i \leq N$ ;  $x_j^i \geq 0$  have been stored according to Eq. 6.10. To ensure that

the model outputs are non-negative as well, a Heaviside function  $\Theta$  is used to threshold the output units. This step function does not affect the following derivations, and it will be only considered to prove that the learning rule leads to the orthogonalization of the input patterns. When presented with one of the previously stored patterns  $p^k$ , the output of a single linear step becomes:

$$w \cdot p^k = \sum_{i=1}^N p^i \cdot (p^i)^T \cdot p^k - \sum_{i=1}^N \sum_{\substack{j=1 \\ j \neq i}}^N p^i \cdot (p^j)^T \cdot p^k \quad (6.12)$$

Since the projection matrix  $w$  consists of the outer product of training patterns  $\{p^i\}$ , this linear transformation projects the M-dimensional input space onto the N-dimensional space spanned by the training patterns  $\{p^i\}$ . Therefore, the output of the system can be expressed as a linear combination of the stored patterns  $\{p^i\}$ . Separating the terms containing the input pattern  $p^k$  from the rest:

$$w \cdot p^k = p^k \cdot (p^k)^T \cdot p^k + \sum_{\substack{i=1 \\ i \neq k}}^N p^i \cdot (p^i)^T \cdot p^k - \sum_{\substack{j=1 \\ j \neq k}}^N p^k \cdot (p^j)^T \cdot p^k - \sum_{\substack{i=1 \\ i \neq k}}^N \sum_{\substack{j=1 \\ j \neq i}}^N p^i \cdot (p^j)^T \cdot p^k \quad (6.13)$$

and regrouping, we can find the coefficients for each training pattern:

$$w \cdot p^k = \underbrace{\left[ (p^k)^T \cdot p^k - \sum_{\substack{j=1 \\ j \neq k}}^N (p^j)^T \cdot p^k \right]}_A \cdot p^k + \sum_{\substack{i=1 \\ i \neq k}}^N \underbrace{\left[ \overbrace{(p^i)^T \cdot p^k}^{\text{cross-talk}} - \sum_{\substack{j=1 \\ j \neq i}}^N (p^j)^T \cdot p^k \right]}_B \cdot p^i \quad (6.14)$$

From this expression, we can derive two conditions that guarantee orthogonalization:

$$(p^k)^T \cdot p^k > \sum_{\substack{j=1 \\ j \neq k}}^N (p^j)^T \cdot p^k \quad (6.15)$$

$$(p^i)^T \cdot p^k - \sum_{\substack{j=1 \\ j \neq i}}^N (p^j)^T \cdot p^k < 0 \quad 1 \leq i \leq N \quad (6.16)$$

The first constraint 6.15 requires that term  $A$  in Eq. 6.14 be positive, ensuring that the input pattern has a positive contribution to the output. This constraint is met when the norm of the target pattern ( $\|p^k\|$ ) is larger than the sum of the projections of all other training patterns onto it. The second constraint 6.16 requires that term  $B$  in Eq. 6.14 be negative, so that the overlap with other patterns is subtracted from the output.

It is worth notice that the two conditions are not independent; the second constraint 6.16 is a subset of the first 6.15. If constraint 6.15 is met, it then follows that:

$$(p^k)^T \cdot p^k > (p^i)^T \cdot p^k \quad (6.17)$$

since the right-hand side of 6.17 is simply one of the terms in the right-hand side of 6.15, and patterns are assumed to be non-negative. With this result in mind, and rearranging the left-hand side of constraint 6.16:

$$(p^i)^T \cdot p^k - \sum_{\substack{j=1 \\ j \neq i}}^N (p^j)^T \cdot p^k = \underbrace{(p^i)^T \cdot p^k - (p^k)^T \cdot p^k}_{\hat{0}} - \sum_{\substack{j=1 \\ j \neq i \\ j \neq k}}^N \underbrace{(p^j)^T \cdot p^k}_{\vee 0} < 0 \quad (6.18)$$

which shows that constraint 6.16 is always met when constraint 6.15 is met. *Therefore, constraint 6.15 is the only condition that is required in order for the Hebbian/anti-Hebbian rule to orthogonalize the stored patterns.*

### VI.3.3. Cross-talk elimination

A direct consequence of condition 6.15 is the elimination of cross-talk at the output of the linear network. The cross-talk term is illustrated in Eq. 6.14. This term causes interferences from other stored patterns in the recall of any pattern. To illustrate this, we consider the response of the model when only the Hebbian term in Eq. 6.10 is included:

$$w \cdot p^k \Big|_{\text{hebbian}} = [(p^k)^T \cdot p^k] \cdot p^k + \overbrace{\sum_{\substack{i=1 \\ i \neq k}}^N [(p^i)^T \cdot p^k] \cdot p^i}^{\text{cross-talk}} \quad (6.19)$$

In this case, the ideal response of the model is the original pattern  $p^k$ , which corresponds to the first term in Eq. 6.19. However, as a result of overlap with other patterns in the associative matrix  $(p^i, i \neq k)$ , a cross-talk term appears at the output of the system, as reflected in the second term of Eq. 6.19. The introduction of the anti-Hebbian term reduces the cross-talk as shown in 6.14. *In fact, imposing condition 6.15 the cross-talk is totally removed since  $(p^i)^T \cdot p^k - (p^k)^T \cdot p^k < 0$  (Eq. 6.18).*

#### VI.3.4. Formal proof of orthogonalization

We now prove that Eq. 6.15 is not only a necessary but also a sufficient condition to achieve orthogonalization of the training patterns. To do so, we prove that, when condition 6.15 is met, only one pattern per feature will have a positive value at the output of the network; the remaining patterns will have a negative value, which will be brought to zero by the Heaviside function. This process is illustrated in Fig. 56

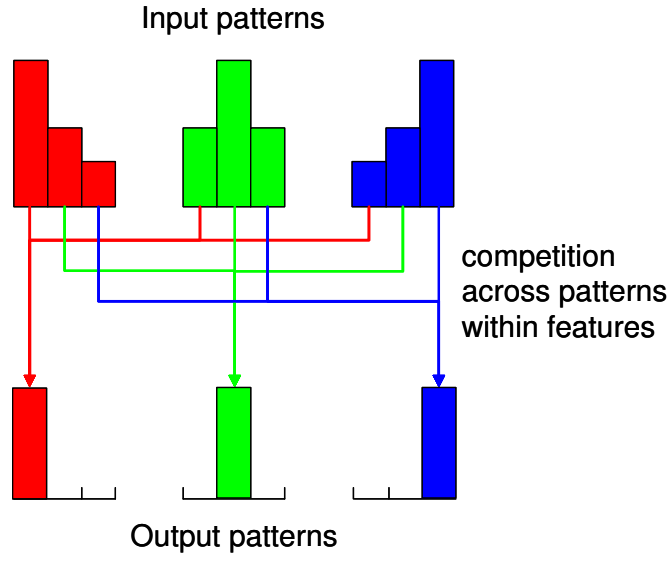


Fig. 56 Orthogonalization through competition across channels and within features. The KIII is trained with the three input patterns, and subsequently presented with the three of them. A feature is active at the output of any of the patterns if that feature is highest across patterns at the corresponding input pattern.

Considering the output of the linear network feature-wise, we can rewrite Eq. 6.12 as:

$$p_{out i}^k = \left[ (p^k)^T \cdot p^k - \sum_{\substack{j=1 \\ j \neq k}}^N (p^j)^T \cdot p^k \right] \cdot p_i^k + \sum_{\substack{r=1 \\ r \neq k}}^N \left[ (p^r)^T \cdot p^k - \sum_{\substack{j=1 \\ j \neq r}}^N (p^j)^T \cdot p^k \right] \cdot p_i^r \quad (6.20)$$

where  $p_i^k$  denotes the  $i^{th}$  feature (or component) of pattern  $p^k = [p_1^k, p_2^k, p_3^k, \dots, p_M^k]^T$ , and the subindex  $out i$  is used to differentiate the  $i^{th}$  component of the output pattern from

that of the stored patterns. Now consider that, among all the training patterns, there is a pattern  $p^t$  whose  $i^{\text{th}}$  component is highest across training patterns:

$$p_i^t > p_i^k \quad ; \quad k = 1, \dots, N; k \neq t \quad (6.21)$$

We want to show that the  $i^{\text{th}}$  component of the output pattern will be negative when any stored pattern  $p^k$  except for  $p^t$  ( $k \neq t$ ) is used as input. Introducing  $p^k$  at the input of the network, and redefining  $p^{jk} \equiv (p^j)^T \cdot p^k$ , Eq. 6.20 reads:

$$p_{out\ i}^k = \underbrace{\left[ p^{kk} - \sum_{\substack{j=1 \\ j \neq k}}^N p^{jk} \right]}_A \cdot p_i^k + \underbrace{\sum_{\substack{r=1 \\ r \neq k}}^N \left[ p^{rk} - \sum_{\substack{j=1 \\ j \neq r}}^N p^{jk} \right]}_B \cdot p_i^r \quad (6.22)$$

Unfolding of terms  $A$  and  $B$  in Eq. 6.22 leads to:

$$p_{out\ i}^k = \left[ p^{kk} - p^{tk} - \sum_{\substack{j=1 \\ j \neq k \\ j \neq t}}^N p^{jk} \right] \cdot p_i^k + \left[ p^{tk} - p^{kk} - \sum_{\substack{j=1 \\ j \neq k \\ j \neq r}}^N p^{jk} \right] \cdot p_i^t + \sum_{\substack{r=1 \\ r \neq k \\ r \neq t}}^N \left[ p^{rk} - p^{kk} - \sum_{\substack{j=1 \\ j \neq k \\ j \neq r}}^N p^{jk} \right] \cdot p_i^r \quad (6.23)$$

Regrouping Eq. 6.23 we obtain:

$$\begin{aligned}
 p_{out\ i}^k = & \underbrace{(p^{kk} - p^{tk}) \cdot (p_i^k - p_i^t)}_{III} - \underbrace{p_i^k \cdot \sum_{\substack{j=1 \\ j \neq k \\ j \neq t}}^N p^{jk}}_{IV} - \underbrace{p_i^t \cdot \sum_{\substack{j=1 \\ j \neq k \\ j \neq r}}^N p^{jk}}_{V} + \underbrace{\sum_{\substack{r=1 \\ r \neq k \\ r \neq t}}^N \left[ p^{rk} - p^{kk} - \sum_{\substack{j=1 \\ j \neq k \\ j \neq r}}^N p^{jk} \right]}_{VI} \cdot p_i^r
 \end{aligned}
 \tag{6.24}$$

Term *I* in Eq. 6.24 is positive because of condition 6.17, whereas term *II* is negative because of condition 6.22; as a result, term *III* is negative. Terms *IV* and *V* are negative since all training patterns are positive-defined and the dot products  $p^{ij}$  are also positive. Since  $p^{kk} > p^{rk}$  6.17, term *VI* is also negative. Since the four terms in Eq. 6.24 are negative, the left-hand side  $p_{new\ i}^k$  is also negative, and only pattern  $p^t$  will have a positive value for the *i*-th component. Therefore, each pattern will only have a non-zero value for those components for which it has the maximum value among all stored patterns, which proves that the learning rule performs pattern orthogonalization.

## **VI.4. Characterization with synthetic inputs**

The behavior of the KIII with the new learning rule will be characterized on two different synthetic datasets. The first dataset consists of three overlapping bell-shaped patterns (similar to those used in Chapter IV) with 64 dimensions, as shown in Fig. 57. This dataset will be used to qualitatively characterize the behavior of the new learning rule on continuous patterns. The second dataset consists of a training set of three overlapping binary patterns, and a test set with noisy versions of these patterns. This dataset will be used to compare our model against other pattern classifiers.

### **VI.4.1. Qualitative analysis of the learning model**

Input patterns for this dataset are shown in Fig. 57(a). To facilitate visual interpretation, the input channels are sorted such that activity for a particular odor pattern is localized in a specific region of the feature vector<sup>5</sup>.

---

<sup>5</sup> Note that a permutation of the input channels would lead to exactly the same configuration because of the symmetry of the KIII with respect to the channels.

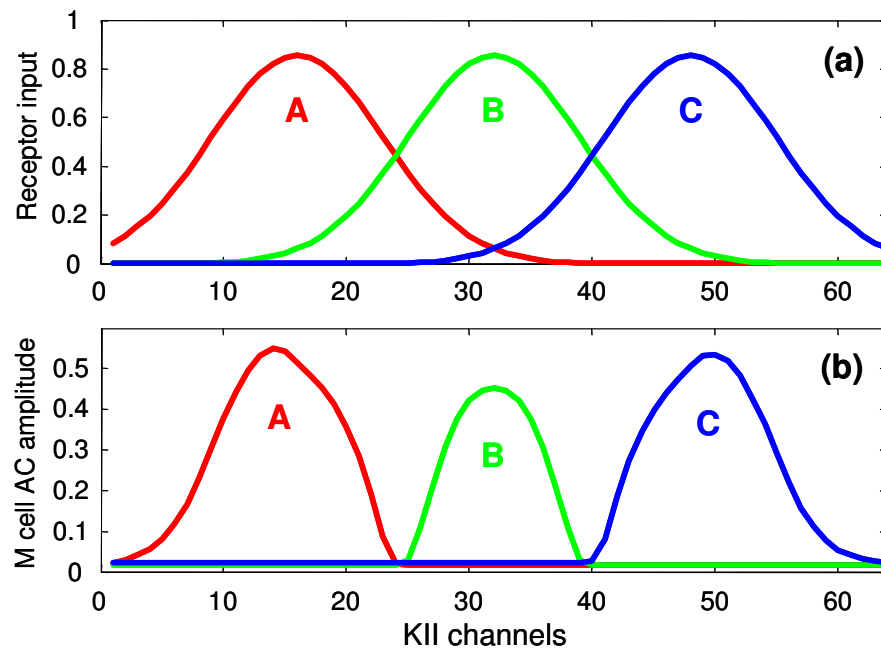


Fig. 57 (a) Overlapping synthetic patterns used to characterize the Hebbian/anti-Hebbian learning rule. (b) Output of the KIII model (i.e., AC amplitude of mitral cells) when each odor pattern is presented at the input. Note that the overlap between odor patterns at the outputs of the KIII model has been eliminated.

To better understand the role of the new Hebbian/anti-Hebbian rule, it is useful to isolate the connection matrices that result from each term in Eq. 6.10. Fig. 58(a) show the connection matrix for the Hebbian term, which is the sum of the outer product of each odor pattern with itself. As shown in the figure, the Hebbian term leads to associative connections, where input channels that are active for a given odor reinforce each other. Fig. 58(b) shows the connectivity matrix for the anti-Hebbian term, which is computed as the outer product of each odor pattern with the rest of the odor patterns. This matrix reinforces connections between channels that are active for more than one odor. By

subtracting the anti-Hebbian term from the Hebbian term, and forcing negative connections to zero, the resulting connectivity matrix is able to depress incoming/outgoing connections from/to overlapping channels. This has two important effects. First, it eliminates cross-talk between patterns, as shown analytically in the previous section. As a result, recalling one odor pattern will not elicit other stored odors. Second, the contrast between odors is significantly enhanced at the output of the KIII.

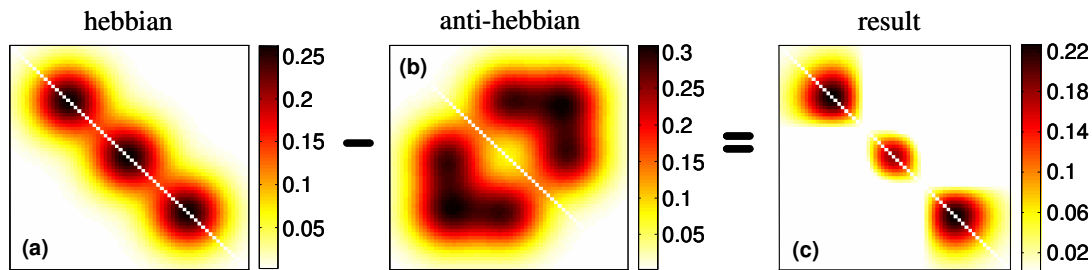


Fig. 58 Connections matrix. Lateral connections between mitral cells: (a) Hebbian term, (b) anti-Hebbian term, and (c) combined effect by subtracting anti-Hebbian from Hebbian terms.

A KIII model with 64 channels was trained on the three odor patterns shown in Fig. 57(a) using the Hebbian/anti-Hebbian learning rule. Each odor pattern was then presented to the model, and the AC amplitude of mitral activity was used as an output. Results are shown in Fig. 57(b). First, as predicted earlier, the recall of one odor pattern does not elicit activity in channels where other odor patterns are prevalent. Second, contrast among odor patterns is enhanced by reducing activity in channels of significant overlap.

Alternatively, one can analyze the response of individual KIII channels across odors to determine the effect of the lateral interaction on their individual receptive ranges. For this purpose, four channels with significant overlap across patterns (channels 23, 26, 38, and 41 in Fig. 57) were selected, and analyzed in terms of their inputs and KIII outputs for the three patterns. The results are shown in Fig. 59. The inputs to the KIII model respond significantly to two of the three odor patterns. In contrast, as a result of lateral interactions, each mitral cell in the KIII model becomes specifically tuned to one odor. This result is analogous to the sharpening of the molecular receptive field first described by Yokoi et al. (1995).

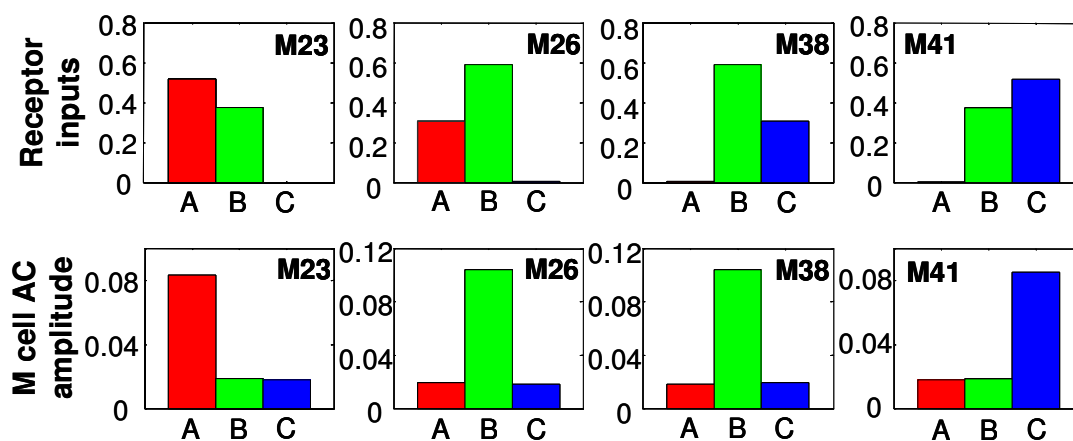


Fig. 59 Activity of four KIII channels (23, 26, 38 and 41) for the three synthetic odors patterns (A, B and C). Upper row: Input to the KIII. Lower row: AC amplitude of mitral cells.

#### **VI.4.2. Comparison with other methods**

In this section, the performance of the KIII model with the new Hebbian/anti-Hebbian rule is compared to that of three additional procedures: a Hopfield network (Hopfield, 1982), a KIII with only Hebbian learning, and a Linear Discriminant Analysis (LDA) (Duda, et al. 2001). The first two procedures are associative memories, and were chosen to determine the extent to which the proposed learning rule can improve the performance of a model trained with Hebbian learning. LDA was used to provide an upper bound on the optimum pattern separability; LDA is known to find the optimum projection for Gaussian likelihoods with equal covariances (Duda et al., 2001) by maximizing the Fisher Discriminant Function (Appendix B). In turn, the pattern separability of the raw inputs was used as a lower bound of performance for the models.

The three binary overlapping patterns shown in Fig. 60 were used as a training set. Test examples were generated by randomly mutating bits of these 16-dimensional patterns. Six levels of noise were considered by mutating between 1 and 6 bits, which corresponds to a 6-37% change in the original pattern. 1,000 examples were generated for each noise level.

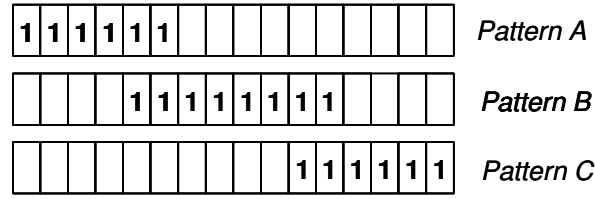


Fig. 60 Overlapping binary patterns used to test model performance.

Fig. 61 shows the pattern-separability obtained by the four procedures, and also that available at the input. The separability  $J$  (described in Appendix B) is plotted as a function of the amount of noise in the input patterns. The KIII-Hebbian/anti-Hebbian clearly outperforms the KIII-Hebbian and the Hopfield network, and performs close to the upper bound defined by LDA. This result can be understood in terms of the mechanisms that increase the pattern separability at each network. The Hopfield network and the KIII-Hebbian model are able to increase the separability of the input patterns through pattern completion. This mechanism is able to partially restore the stored patterns from the noisy version presented at the input, reducing the within-class scatter  $S_W$ . The KIII-Hebbian/anti-Hebbian takes advantage not only of the pattern-completion mechanism of Hebbian learning, but also performs a reduction of overlap/crosstalk by means of the anti-Hebbian term, which can be thought of as a mechanism to increase the between class-scatter  $S_B$  of the input patterns.

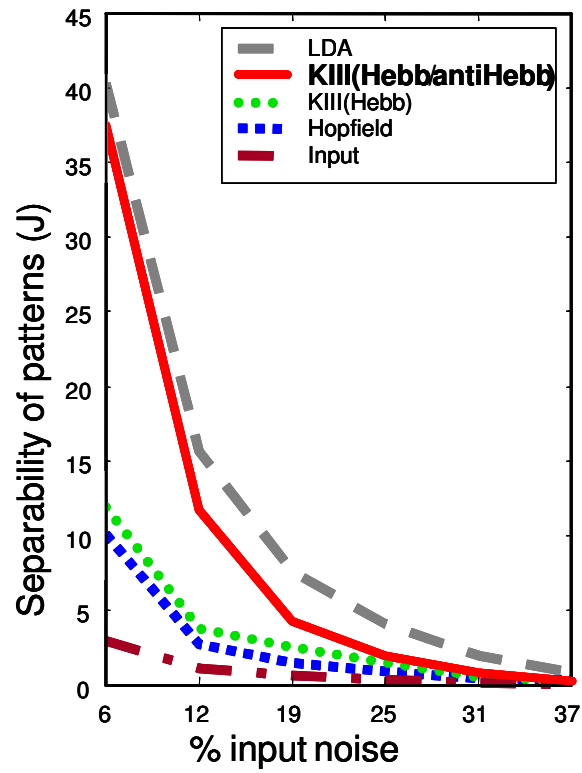


Fig. 61 Separability of the output patterns against the level of noise introduced in the input patterns. Separability of the output patterns of LDA, KIII-Hebbian/anti-Hebbian, KIII-Hebbian, Hopfield output, along with the separability of the raw input.

## **VI.5. Validation with sensor-array patterns**

The KIII-Hebbian/anti-Hebbian model was finally validated on experimental data with the temperature modulation database (section II.3.1, in Chapter II). The array consisted of four MOS sensors (TGS2600, TGS2610, TGS2611, and TGS2620) (Figaro, 1996). The delivery system, described in section II.2 of Chapter II, was used to expose the sensors to the dynamic headspace of three analytes: allyl alcohol (A), tert-butanol (B), and benzene (C) at five different concentrations. To increase the information content of the sensor response, the MOS sensors were modulated in temperature (Gutierrez-Osuna et al., 2003) with a ramp profile on the heater voltage from 2V to 4.5V over a period of 200 seconds. Fig. 62 shows the response of the four sensors to five different concentrations of each analyte. Using this excitation profile, we collected a database of sensor response patterns for the three analytes (A, B, C), five concentrations per analyte, and seven repetitions each, for a total of 35 samples. Each repetition was collected on a different day to determine the extent to which sensors patterns were repeatable.

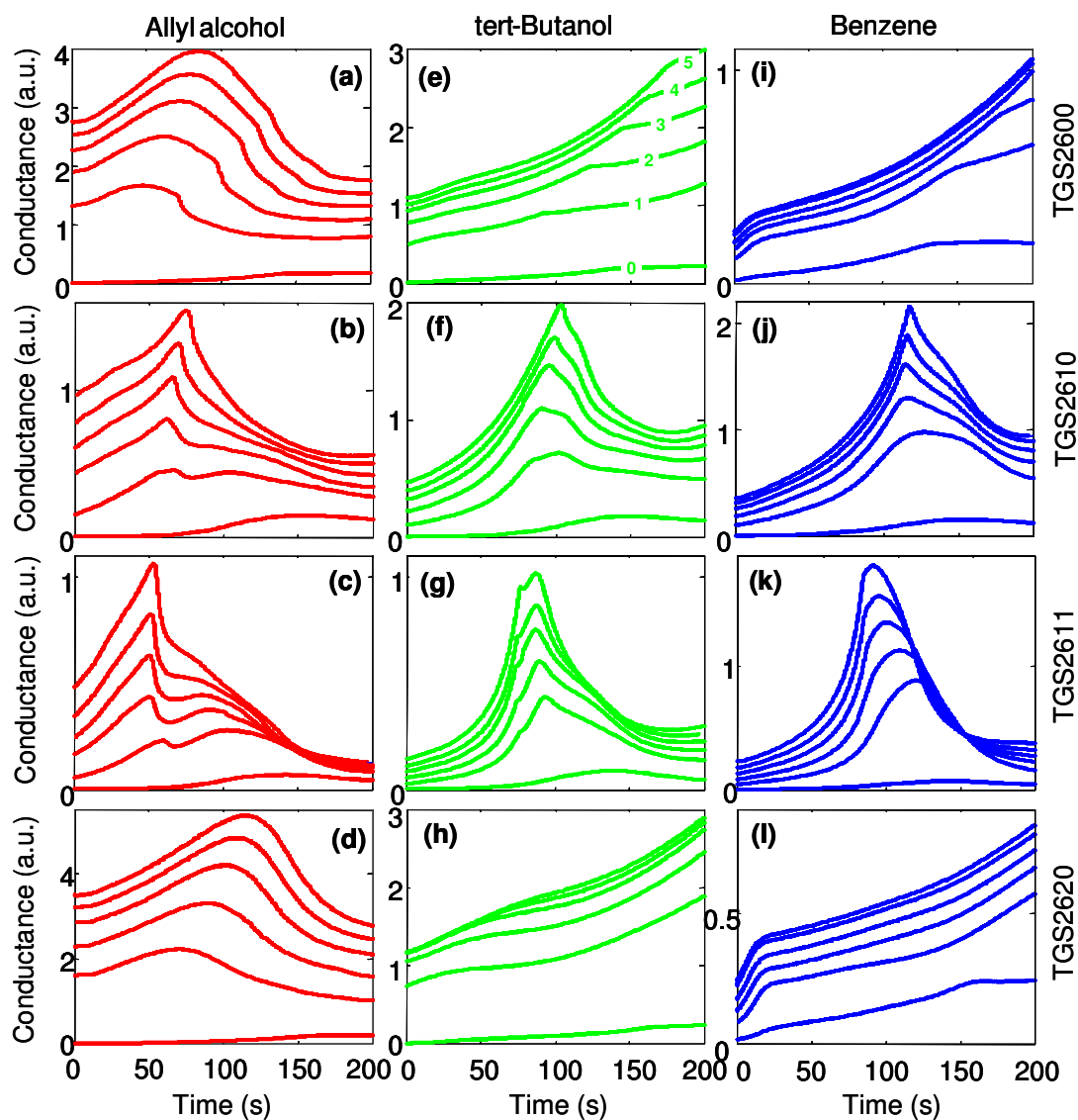


Fig. 62 Response of the four MOS sensors (TGS2600, TGS2610, TGS2611, TGS2620, first to fourth rows respectively) to five different concentrations of allyl alcohol , tert-butanol , and benzene, first to third columns respectively. The bottom curve in each plot is the sensor response to air. The heater voltage was modulated using a ramp profile (2V to 4.5V; 200 seconds).

The temperature-modulated response of the four MOS sensors at the highest concentration was concatenated to form a single pattern, and used to train the KIII. Each pattern was previously normalized individually to have a maximum value of one, and decimated to obtain 64 samples per sensor response. The resulting training patterns have 256 dimensions. This preprocessing, performed for every analyte at every concentration, is necessary to balance the inputs to the KIII and ensure that the model operates in a well-behaved dynamic region.

#### **VI.5.1. Performance of the amplitude code**

In this section, we employ the amplitude code to study the contrast enhancement achieved by the model. Fig. 63(a, c, e) shows the concatenated response from the four MOS sensors. Even though the sensors provide a unique response pattern to each analyte, there is also a significant degree of overlap that overshadows the most relevant discriminatory information. Fig. 63(b, d, e) shows the amplitude output of the KIII to the three analytes; the KIII is able to noticeably reduce the overlap across patterns and enhance the channels (i.e., operating temperatures) with highest selectivity. The response pattern for allyl alcohol is highly reduced on the right-hand side of the two peaks of sensors TGS2610 and TGS2611 since that region is highly overlapping with the response to tert-butanol and benzene. On the other hand, activity on the left-hand side of the peaks is preserved because this area contains discriminatory information of allyl alcohol. The response pattern for tert-butanol has a large overlap with the other two response patterns on both sides of the peaks; thus, the KIII narrowly sharpens the activity of the patterns around its peaks (Fig. 63). Finally, the sensor response pattern

for benzene is also sharpened around the two peaks of sensors TGS2610 and TGS2611, which is where discriminatory information for this analyte is highest.

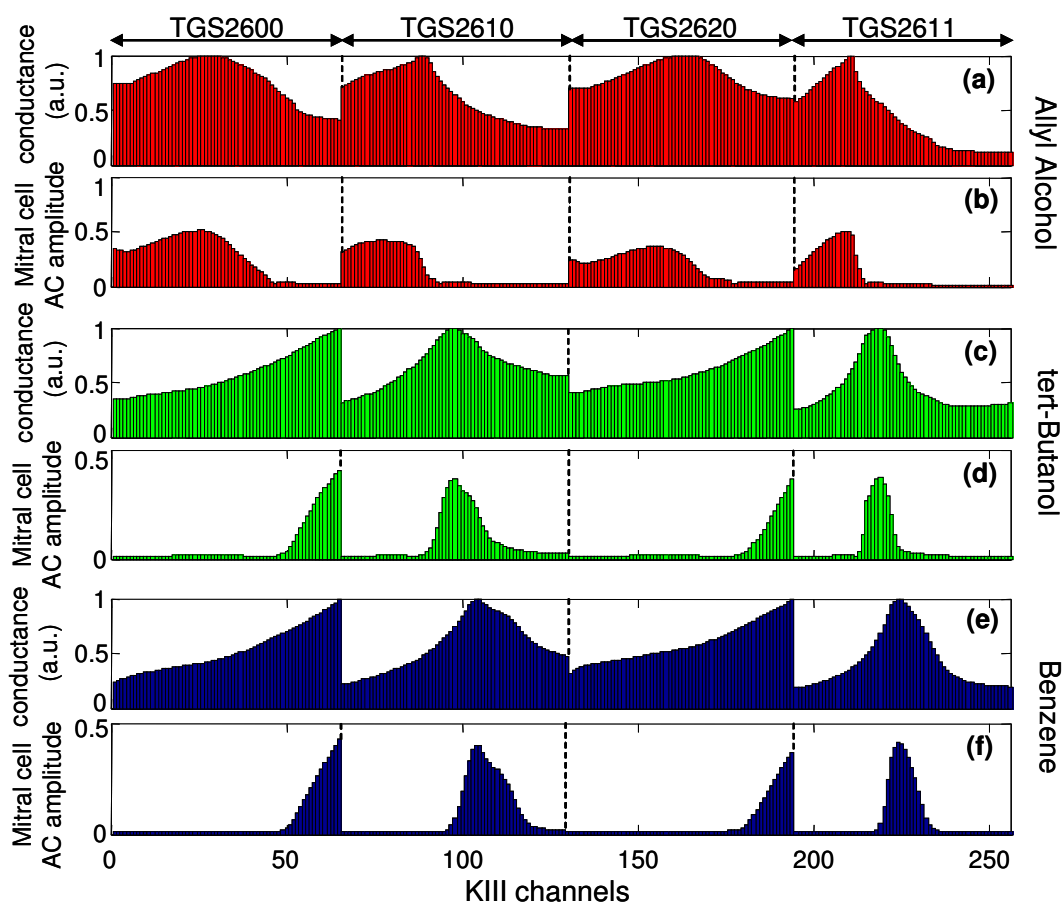


Fig. 63 Contrast enhancement in the KIII with experimental data from gas sensors. Plots (a, c, e) show the original sensor response to the three analytes, which serves as the input to the KIII. Plots (b, d, f) show the corresponding output of the KIII, measured as the AC amplitude of mitral cells.

The tuning range of six individual KIII channels (34, 75, 98, 111, 219 and 224) is shown in Fig. 64. These channels were chosen for temperatures that showed higher activity for each one of the three input odors. The top row shows the input to the KIII, whereas the bottom row shows the AC amplitude at the mitral outputs.

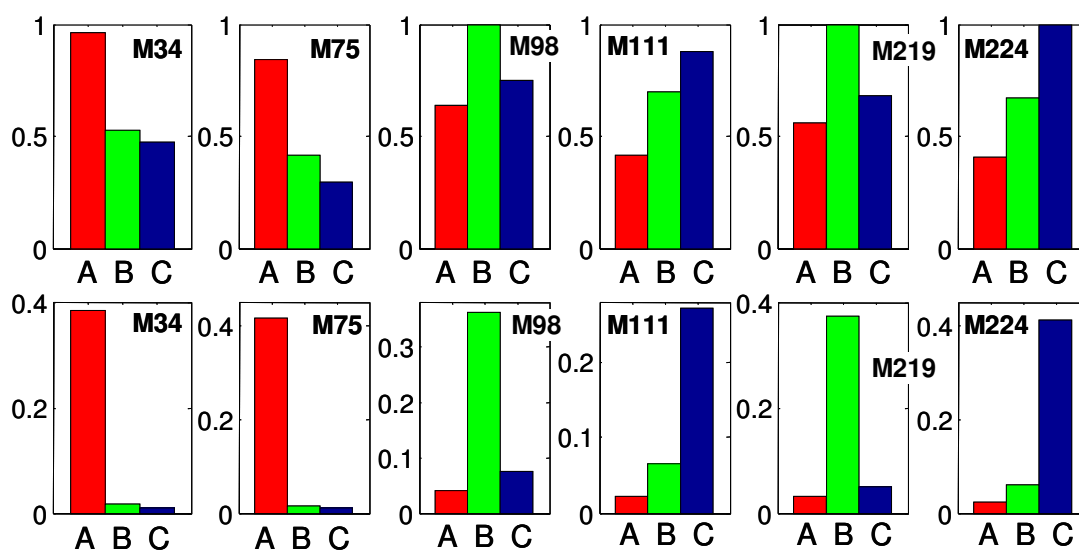


Fig. 64 Activity across odors of channels 34, 75, 98, 111, 219 and 224. Upper row: sensor response. Lower row: AC amplitude of mitral cells. A denotes allyl alcohol, B tert-butanol, and C benzene.

We can observe that the model is able to significantly sharpen the response of mitral nodes with respect to that in the sensor response, to where each mitral node becomes highly tuned to a particular odor. This sharpening is similar to winner-take-all competition, where only the response to the odor with highest response at the input is kept at the output.

### **VI.5.2. Performance of the phase code**

In this section, we study the performance of the phase code in recovering stored patterns resulting from the Hebbian/anti-Hebbian rule. Fig. 65(b, d, and e) shows the output patterns obtained using phase code. The response pattern for allyl alcohol is highly reduced on the right-hand side of the two peaks of sensors TGS2610 and TGS2611 since that region is highly overlapping with the response to tert-butanol and benzene. On the contrary, activity to the left of the peaks is preserved because this area contains discriminatory information of allyl alcohol. The response pattern for tert-butanol has a large overlap with the other two response patterns on both sides of the peaks. Thus, the KIII narrowly sharpens the activity of the patterns around its peaks (Fig. 65). Finally, the sensor response pattern for benzene is also sharpened around the two peaks of sensors TGS2610 and TGS2611, which is where discriminatory information for this analyte is highest.

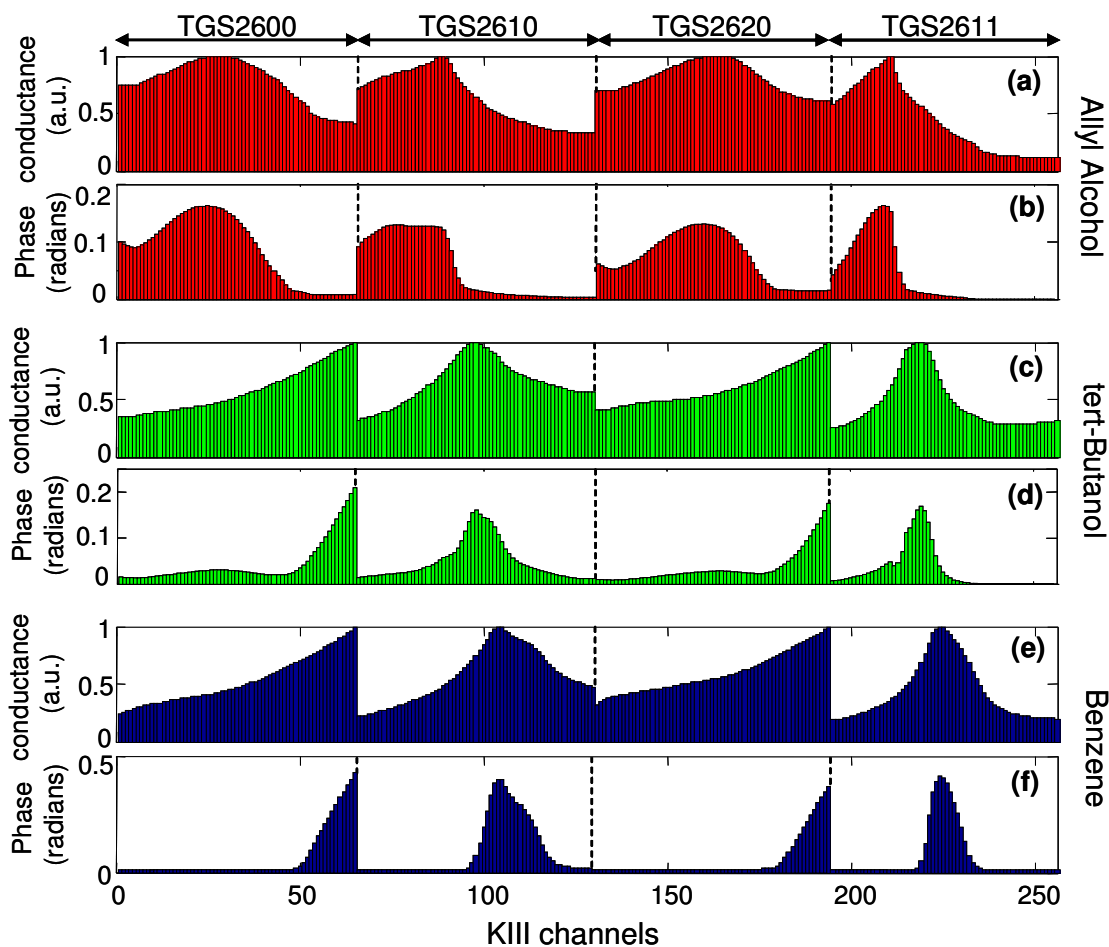


Fig. 65 Contrast enhancement through phase coding in the KIII with experimental data from gas sensors. Figures (a, c, and e) show the original sensor response to three analytes, which serves as the input to the KIII. Figures (b, d, and f) show the corresponding output of the KIII, measured as the relative phase of mitral cells.

From Fig. 63 and Fig. 65, we note that both phase and amplitude read-outs give similar performance on this dataset. This result, though, should come as no surprise. As mention in section V.6, the phase code is able to reduce the cross-talk between overlapping stored patterns. However, the anti-Hebbian component of the new learning

rule already performs contrast enhancement of the sensor patterns, thus reducing the overlap between stored patterns. As a result, the performance of amplitude and phase codes following contrast enhancement should be expected to be comparable.

### **VI.5.3. Effect of concentration on the performance of the model**

In this section, we study the ability of the KIII to increase the contrast of sensor-array patterns obtained with different concentrations of the analytes. As in section VI.4.2, model performance was measured using the Fisher discriminant ratio ( $J$ ) (Appendix B). The KIII model was trained with the sensor-array response at the highest concentration of each analyte, and subsequently tested with the entire database. Given that phase and amplitude codes perform similarly following Hebbian/anti-Hebbian learning (as shown in the previous section), only the amplitude code will be used in this section. Fig. 66 shows the pattern separability at the input and output of the KIII as a function of analyte concentration. Pattern separability increases with concentrations. This is due to two reasons. First, the analytes become more separable at increasing concentrations. This is clearly shown by the lower curve in Fig. 66, which represents separability in the raw sensor data. Second, the KIII is likely to display better performance at concentrations close to the one it was trained on (the highest concentration in our case). However, the model is also able to increase pattern separability at all lower concentrations as well, as can be observed in Fig. 66.

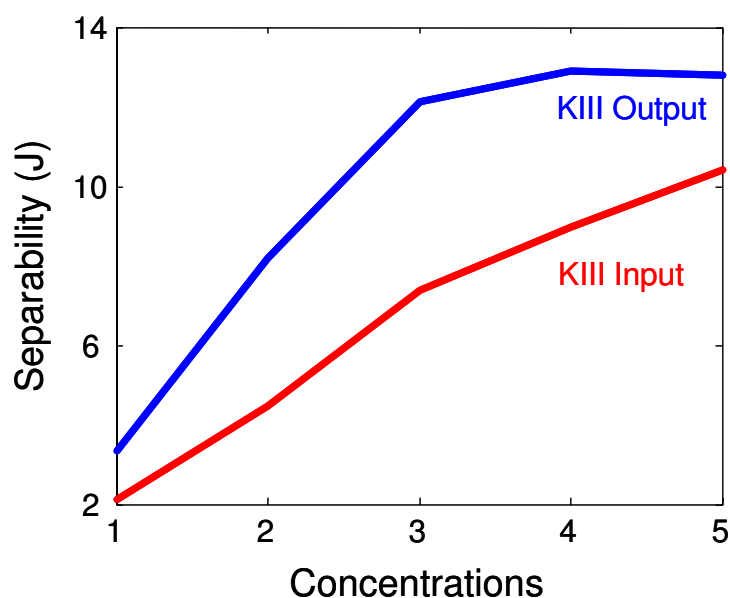


Fig. 66 Pattern separability at the input and output of the KIII as a function of the concentration of the analytes. The model was trained using only the sensor patterns at the highest concentration.

## VI.6. Discussion

There are two prevailing views on how odor contrast enhancement occurs at the olfactory bulb. The first, proposed by Yokoi et al. (1995) and Mori et al. (1999), states that lateral inhibitory connections sharpen the molecular receptive range (i.e. the tuning specificity) of projection neurons in the bulb, in a manner akin to edge detection through receptive fields in the retina. The second, more recent view of Laurent and colleagues (Laurent et al., 2001; Laurent, 2002) argues that contrast enhancement occurs as a global redistribution of activity across the entire olfactory bulb, as opposed to local improvements in the molecular receptive field of individual projection neurons or

winner-take-all selection of the most active units. According to this view, the representation in the olfactory bulb changes continuously throughout a stimulus in an odor-specific manner; this distributed temporal patterning progressively increases the contrast between bulb-wide odor representations. From this perspective, the model proposed in this paper is consistent with the view of Mori, since the main mechanism for contrast enhancement is a form of winner-take-all competition.

To achieve contrast enhancement, the proposed learning rule relies on (1) a Hebbian term to build associations within odors and (2) an anti-Hebbian term to reduce co-occurring activity across odors. Formal analysis on a linear neural network has shown that the anti-Hebbian term of the learning rule is able to completely eliminate cross-talk. We have also provided mathematical proof that the proposed learning rule also performs pattern orthogonalization.

The model has been characterized with a synthetic problem with binary patterns. The proposed learning rule has been shown to increase the separability (Fisher discriminant ratio) of the output patterns with respect to that available at the input. This is achieved by both a decrease of the within-class scatter and the increase of the between-class scatter of the output distribution. It is worth to notice that the simulated dataset in section VI.4.2 consisted of isotropic likelihoods and, therefore, all discriminatory information was contained in the mean of the distribution. This type of distribution was

used to ensure a fair comparison between the two KIII models and the Hopfield model, which are limited to first-order statistics, and LDA, which can also consider second-order statistics. Furthermore, having the same covariance matrix for all classes ensures that LDA finds the optimal solution. Thus, the close performance between the KIII-Hebbian/anti-Hebbian and LDA is a remarkable result.

The model has also been validated on the response of four MOS sensors to three analytes: allyl alcohol, tert-butanol, and benzene, at different concentrations. Our results have shown that the model is able to increase the separability of gas-sensor-array patterns, and also generalizes well across concentration levels.

The phase and amplitude codes have been shown to perform similarly. This is due to the reduction of cross-talk achieved by the Hebbian/anti-Hebbian rule. This result leads us to think that phase coding and the Hebbian/anti-Hebbian rule are two alternative solutions for the same problem: robust recovery of overlapping patterns. In Chapter V, the phase code was shown to recover stored patterns even with high degrees of overlap. In this chapter, the Hebbian/anti-Hebbian rule has been also shown to robustly recover overlapping patterns. However, the way in which both approaches operate is different. The phase code recovers the complete stored pattern, whereas the Hebbian/anti-Hebbian learning rule recovers an overlap-free version of the target pattern.

## **CHAPTER VII**

### **BACKGROUND SUPPRESSION**

Habituation is a process that allows a sensory system to reduce its sensitivity to previously detected stimuli, preventing sensory overflow in the central nervous system and improving the ability to detect new and, therefore, more informative stimuli (Wang, 1998). This computational function has great potential in sensor-based machine olfaction as a mechanism to reduce the effect of background odors and enhance selectivity towards the interesting components in a sample.

Wang et al. (1990) proposed a mechanism for the related problem of pattern segmentation. The authors employed a neural network of oscillatory units linked with Hebbian connections to perform temporal segmentation of the stored patterns. Alternating bursts of activity induced by self-inhibition are used to create a spatio-temporal pattern that sequentially extracts the components of a mixture.

Hendin et al. (1994) studied odor segmentation as a blind-source separation problem, where the different components in an odor mixture follow independent temporal fluctuations. Li and Hertz (2000) proposed a feedback mechanism for odor segmentation whereby the olfactory bulb activity is modulated with an efferent signal after an odor is recognized. Gutierrez-Osuna and Powar (2003) presented a statistical pattern recognition approach for odor segmentation with chemical sensor arrays where habituation is triggered by a central feedback signal, in a manner akin to (Li and Hertz, 2000).

The objective of this chapter is to investigate the habituation process using (1) a biologically plausible computational model and (2) an adaptation mechanism based on local activity. In order to facilitate the process of background suppression, the contrast-enhancement rule developed in the previous chapter will be used to reduce the overlap between odor patterns. The complete system is evaluated with synthetic data on a series of habituation scenarios to odor mixtures. Finally, the model is validated on gas-sensor array data.

### VII.1. Habituation in the KIII model

Following Kozma and Freeman (2001), the habituation process is assumed to induce depression of synapses from mitral nodes onto other neuron populations, as highlighted in Fig. 67. Following Wang (1998), changes in these synapses are assumed to be proportional to their instantaneous value and, thus, follow an exponential decay:

$$\Delta w = w(t + \Delta t) - w(t) = [B - w(t)][1 - \exp(-\Delta t / \tau)] \quad (7.1)$$

where  $w$  represents a synapse from the habituating mitral cell to other mitral or granule cells,  $\tau^6$  is a time constant governing the rate of habituation, and  $B$  is the final value that the connection will approach asymptotically. During the habituation process,  $B$  is the minimum strength of the connection (i.e., under complete habituation.) A suitable value of  $B=1.5$  was obtained through experimentation<sup>7</sup>. Under dishabituation,  $B$  is simply the original value of the connection which, along with all remaining KIII parameters, are borrowed from (Chang, Freeman, and Burke, 1998a).

---

<sup>6</sup> A value of  $\tau=500ms$  is used in this work to aid visualization. The implementation of Kozma and Freeman (2001) is equivalent to a slower time constant  $\tau=2s$ .

<sup>7</sup> For values of  $B \leq 1.5$ , we observed that the KIII response to a stimulus was similar to the basal state.

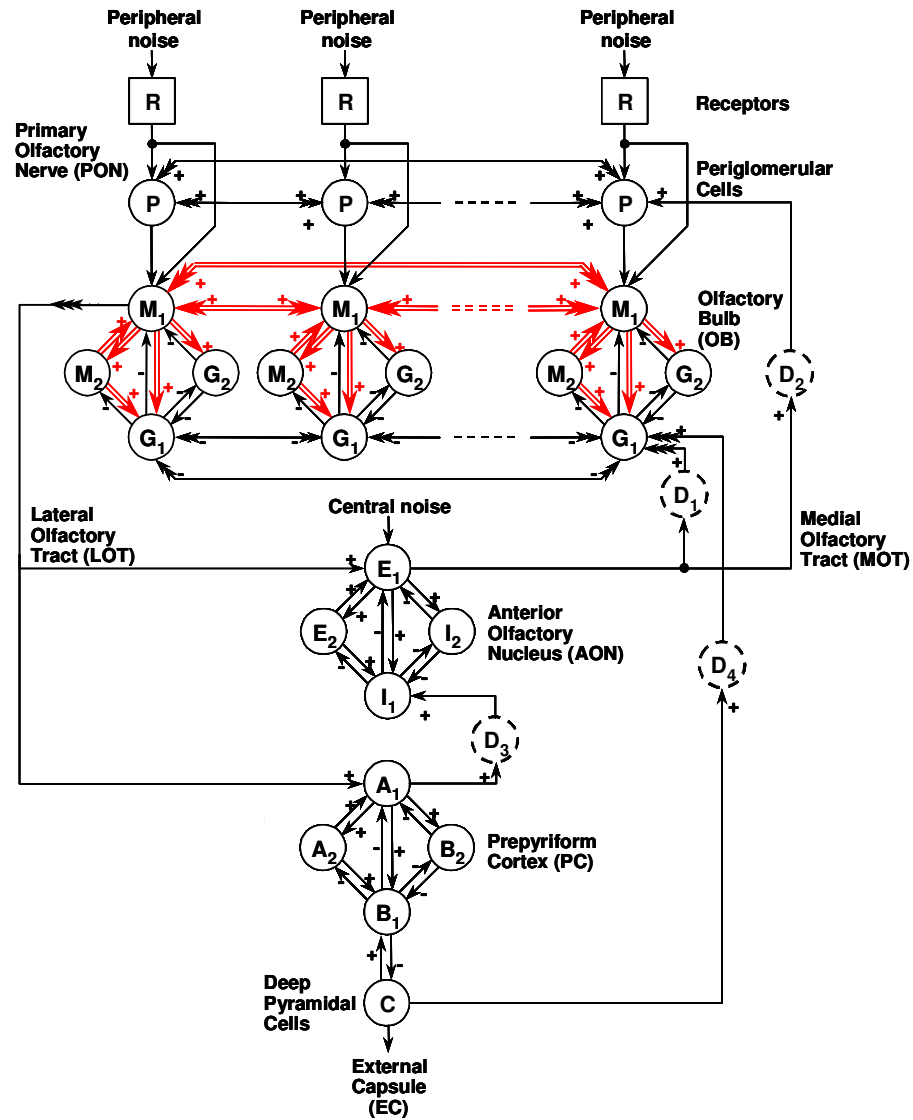


Fig. 67 Connections from mitral cells to any other cells in the KIII model are adapted through habituation (adapted from Chang, Freeman, and Burke, 1998).

Fig. 68 shows the evolution of parameter  $W_{gm}$ , which is the connection weight between mitral and granule cells under habituation and dishabituation.

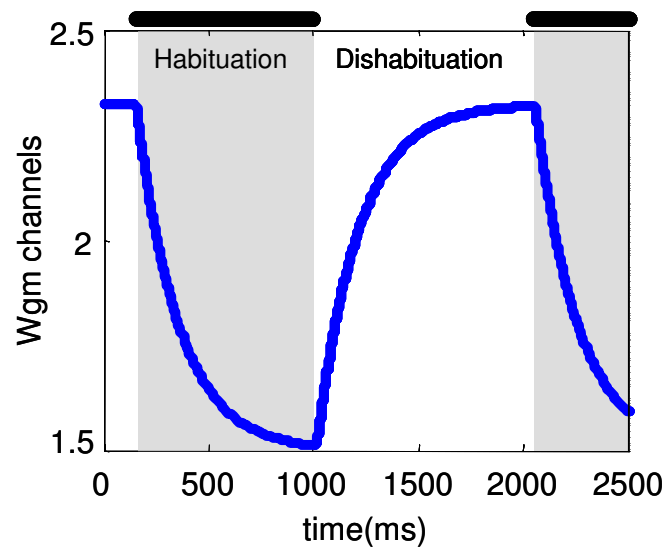


Fig. 68 Habituation and dishabituation processes. The weight of a mitral-to-granule connection is plotted against time. The habituation mechanism is triggered when an odor is introduced to the system (thick bar on top). Likewise, the dishabituation process is triggered by the removal of the odor.

In contrast with the mechanism of Kozma and Freeman (2001), in which a node undergoes habituation if it exceeds the average activity across the mitral layer, our habituation/dishabituation processes are initiated based solely on the local activity at each channel (for biological-plausibility purposes.)

Our triggers are illustrated in Fig. 69(b-d). Following (Chang et al. 1998a), the AC activity at each G2 node ( $G2_{AC}$ ) is computed with a 50ms-wide moving window.

The window is split into 10 non-overlapping segments, and the average of the standard deviation at each segment is used as a measure of AC amplitude (see Fig. 69(b)). From the derivative of  $G2_{AC}$  (see Fig. 69 (c)), suitable thresholds  $T_{hab}=0.6$  mV/ms and  $T_{dishab-AC}=0.4$  mV/ms are then used to detect the onset of habituation and dishabituation, respectively. The threshold  $T_{dishab-AC}$  works as long as the stimulus is removed before full habituation is reached. Otherwise, the AC amplitude cannot be discriminated from the basal state, as illustrated in Fig. 69(d). In this case, a sudden change in DC offset can be used to detect that the stimulus has been removed. The DC component of each G2 node ( $G2_{DC}$ ), shown in Fig. 69(e), is computed with a 200-ms causal moving average. A threshold  $T_{dishab-DC}=0.25$  mV/ms is then applied to the derivative of  $G2_{DC}$  (see Fig. 69(f)) to trigger dishabituation. To avoid false triggers, the threshold  $T_{dishab-DC}$  is applied only if the connection is near full habituation ( $w \leq 1.8$ ). The derivative of  $G2_{AC}$  ( $G2_{DC}$ ) is computed by subtracting from the signal its average activity on the previous 50ms (200ms).

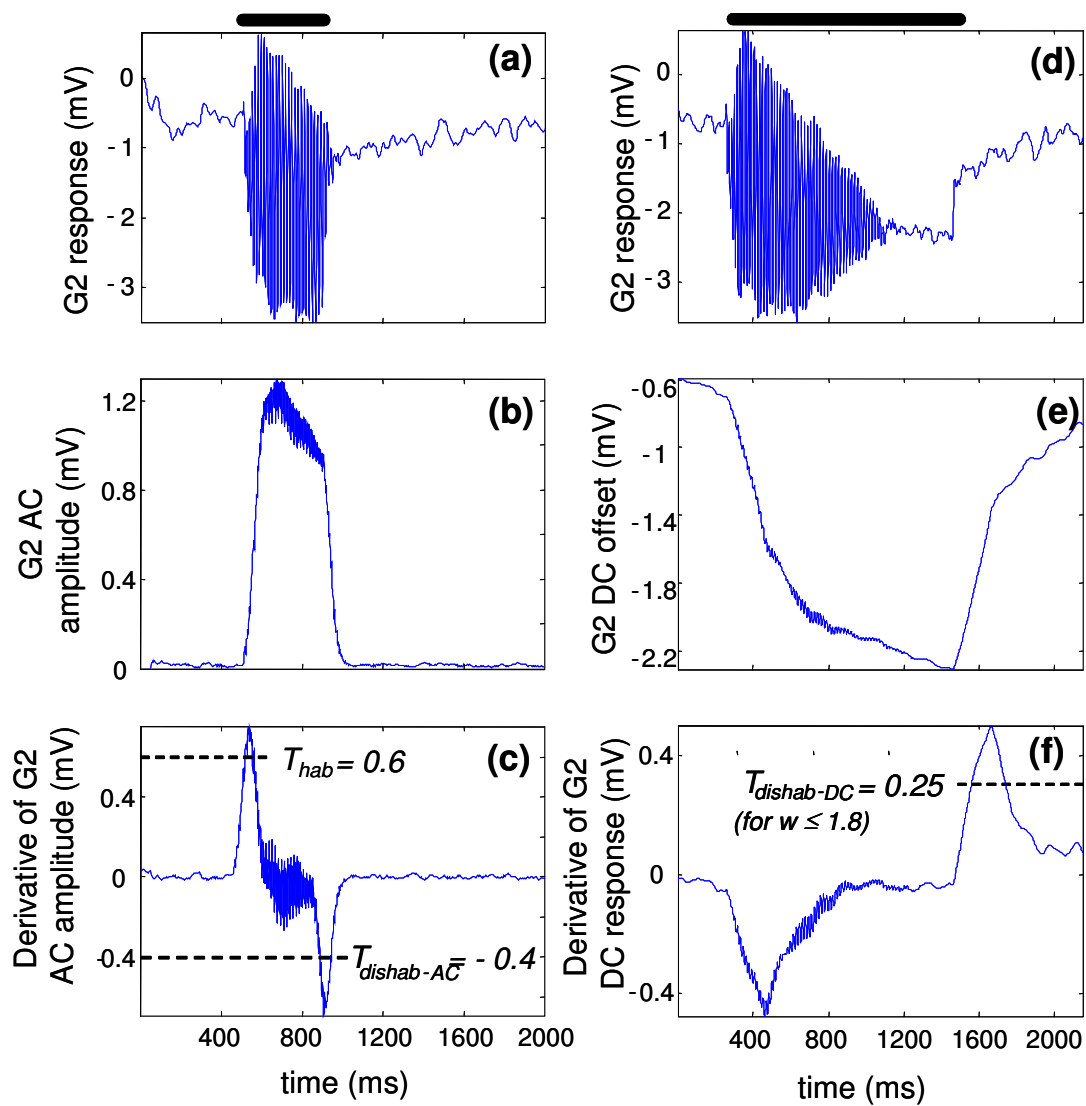


Fig. 69 (a) Habituation in the KIII is effected through mitral connections (Chang, Freeman, and Burke, 1998a). Triggering habituation and dishabituation from G2 activity: (a-c) stimulus is removed before and (d-f) after full habituation.

## VII.2. Characterization with synthetic data

The habituation mechanism is first characterized on a set of binary patterns in order to illustrate the processes of habituation, dishabituation, and pattern completion. Then, a dataset of bell-shaped overlapping patterns is used to demonstrate the ability of the habituation mechanism (combined with the Hebbian/anti-Hebbian learning rule of Chapter VI) to segment continuous patterns.

### VII.2.1. Binary patterns

The synthetic patterns of single odors and their binary mixtures used to study the effect of the habituation mechanism are shown in Fig. 70. Note that the mixtures patterns (AB, BC, and CA) are formed by addition of the single odors (A, B, and C). Fig. 71(a) shows the KIII response when exposed separately to samples of A, C and AC; the habituation process is disabled to emphasize the steady-state response.

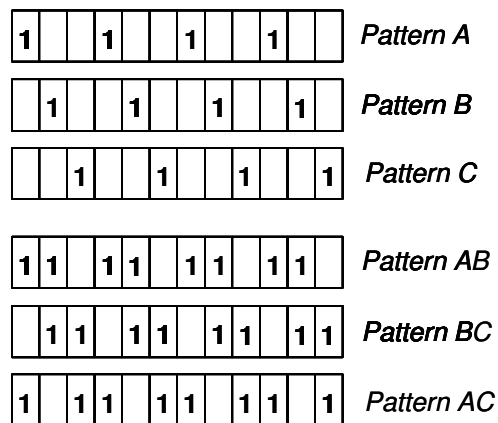


Fig. 70 Binary patterns used to characterize the habituation mechanism. Mixture patterns (AB, BC, and CA) are obtained by addition of the basic patterns (A, B, and C).

The performance of the KIII is analyzed on three separate scenarios. The *first experiment* is designed to illustrate a shift in the response to an odor mixture when the system has previously habituated to one of the components. The system is presented with odor A and allowed to habituate. At  $t = 800$  ms, binary mixture AC is presented. As shown in Fig. 71 (b), the response to AC is as if only C was present, suppressing the background odor. The *second experiment* shows the ability of the KIII to fully recover from habituation to an odor. The model is excited with odor mixture AC and allowed to habituate. The sample is then removed and the KIII is allowed to dishabituate. When the sample is reintroduced, the KIII does not show any memory effects, as shown in Fig. 71(c). The *final experiment* further illustrates the pattern-completion capabilities of the system. The KIII is presented with an incomplete version of pattern C, one where the 5<sup>th</sup> bit is missing. However, the system is able to induce an oscillation in the missing channel that is strong enough to trigger habituation. When subsequently exposed to a complete pattern of mixture BC, the KIII behaves as if it had been previously exposed to the complete pattern for odor B.

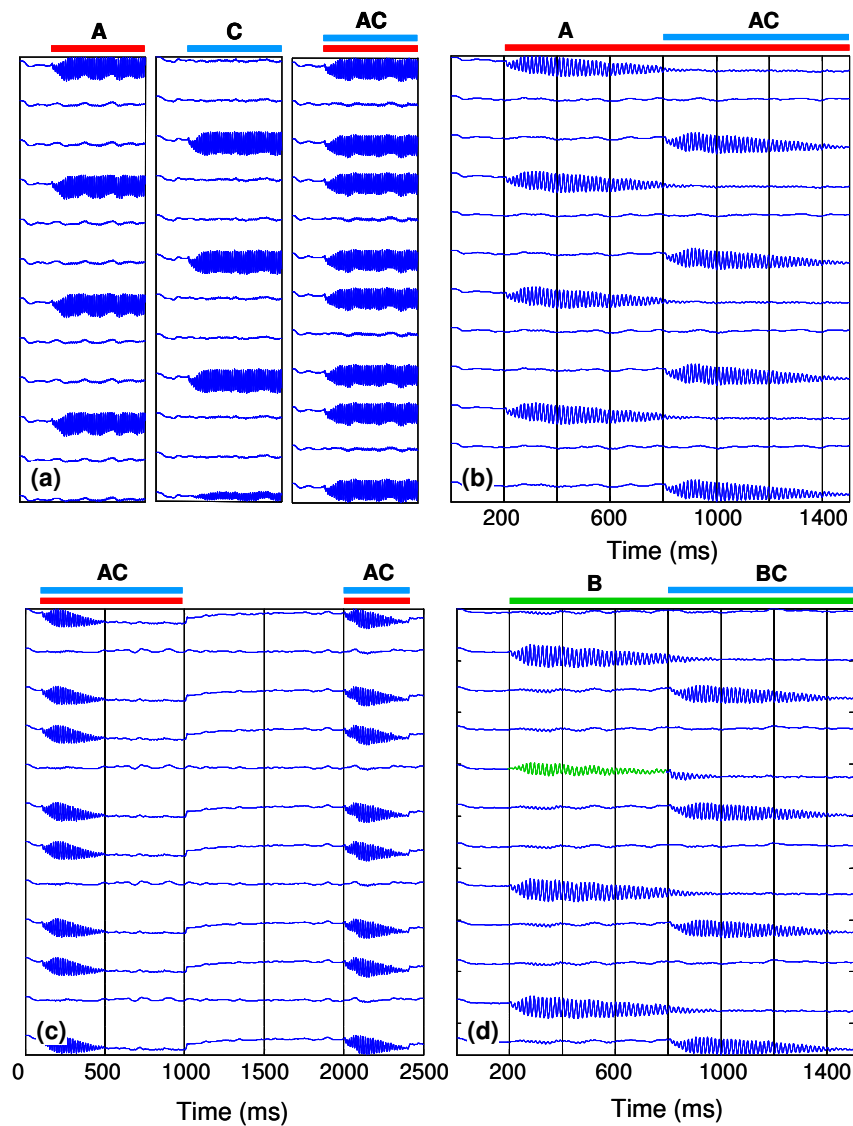


Fig. 71 Habituation scenarios. (a) Output patterns (G2 activity) of the KIII without habituation. (b) Mixture perception following habituation. The KIII habituates to odor A; when a mixture of A and C is presented at  $t=800$  ms, the system responds as if only odor C was presented (c) Reversibility of the habituation process. After habituation to mixture AC, the KIII undergoes dishabituation when the mixture is removed at  $t=1,000$  ms. This allows the KIII to respond to mixture AC again when is introduced at  $t=2,000$  ms. (d) Pattern recovery. An incomplete version of pattern B (with the fifth bit missing) is introduced at  $t=200$  ms.

### VII.2.2. Continuous patterns

In this section, the ability of the habituation mechanism to suppress continuous overlapping patterns is evaluated. The overlapping bell-shaped patterns shown in Fig. 72 will be used for these experiments. To facilitate habituation to overlapping odors, the Hebbian/anti-Hebbian rule is first used to orthogonalize the odor representations. Fig. 73 shows the response of the KIII model in a simple habituation scenario using the synthetic patterns in Fig. 72. The system is initially exposed to odor pattern A for 500 ms (100ms-600ms). As a result of the habituation term, the activity in the network decays towards zero in an exponential fashion. Following habituation to odor pattern A, the system is then presented with an additive mixture of odors A and B at time  $t=600$  ms. As shown in Fig. 73, after the introduction of the mixture of A and B, the KIII model is able to suppress the activity in those channels that code for odor A, to where the resulting output pattern is as if only odor B was present. This allows the system to tune its sensitivity to the new odor in the environment. At  $t=1,100$  ms an additive mixture of odors A, B, and C is introduced. Similarly to the result for the previous mixture, the KIII responds as if only odor C was present, further illustrating the background-suppression ability of habituation mechanism.

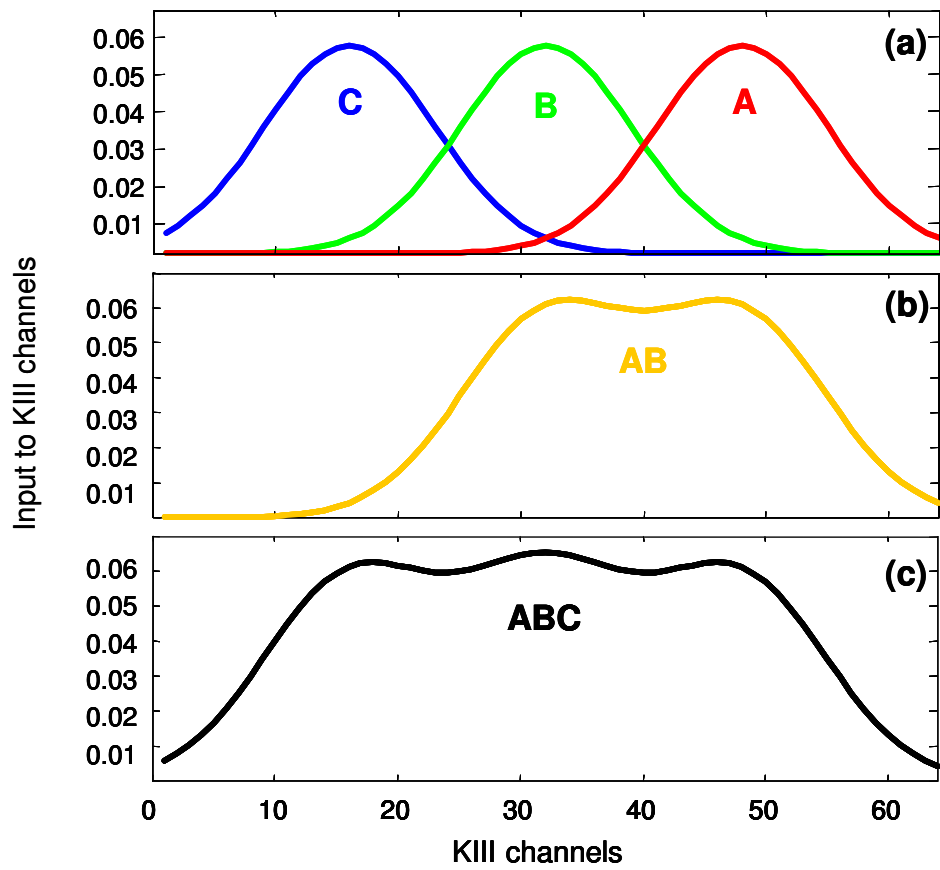


Fig. 72 Overlapping bell-shaped patterns used to characterize the habituation mechanism. (a) Single patterns. (b) Additive mixture of patterns A and B. (b) Additive mixture of patterns A, B, and C.

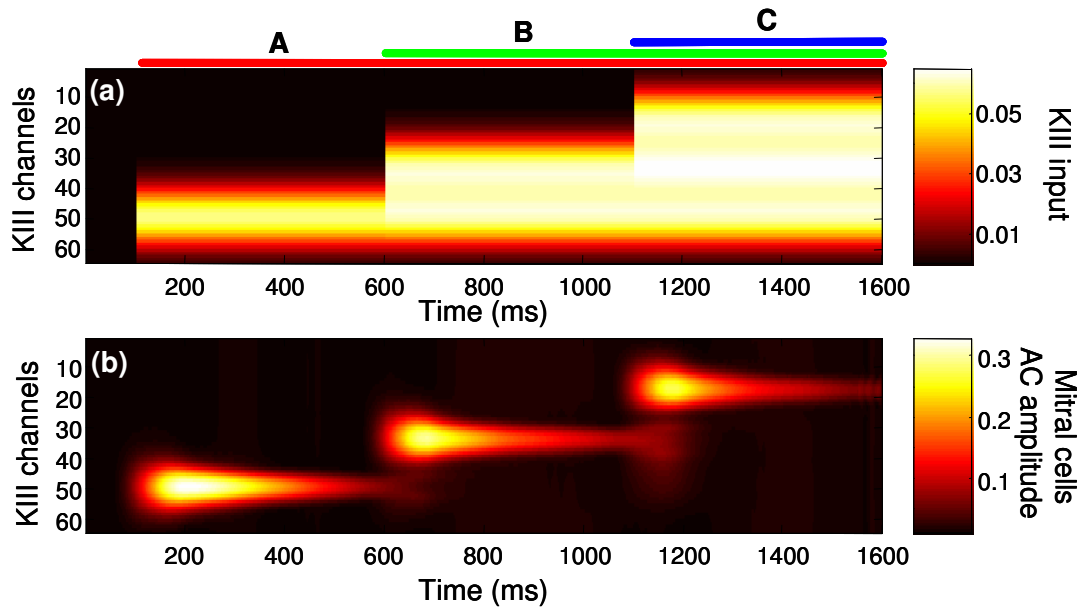


Fig. 73 Evolution of the KIII activity (AC amplitude of mitral cells) in a habituation experiment with synthetic patterns. (a) Input presented to the KIII. (b) Output of the KIII (amplitude of mitral cells). Odor A is presented at time  $t=100$  ms, and the system is allowed to habituate. At time  $t=600$  ms a mixture of odors A and B is introduced; the response of the system is as if only odor B was present. At time  $t=1,100$  ms a mixture of A, B, and C is introduced. The system responds as if only C was present.

#### VII.2.2.1. Habituation without contrast enhancement

To illustrate the need for contrast enhancement prior to habituation, we repeat the previous experiment, in this case training the KIII only with Hebbian learning. Fig. 74(b) shows the output of the KIII (amplitude of mitral cells) when the inputs in Fig. 74(a) are presented. The introduction of pattern A at  $t=100$  ms produces activation not only on the KIII channels where pattern A is active, but to some extent also on those

channels that encode for pattern B, and to a lesser extent on those channels for pattern C. This early activation of patterns B and C, due to cross-talk caused by the Hebbian learning rule, makes the KIII habituate to them. As a consequence, the KIII does not respond to the later introduction of odors B and C at  $t=600$  ms and  $t=1,100$  ms, respectively, as shown in Fig. 74(b). This result clearly illustrates the need to reduce cross-talk and increase contrast between patterns prior to the habituation mechanism.

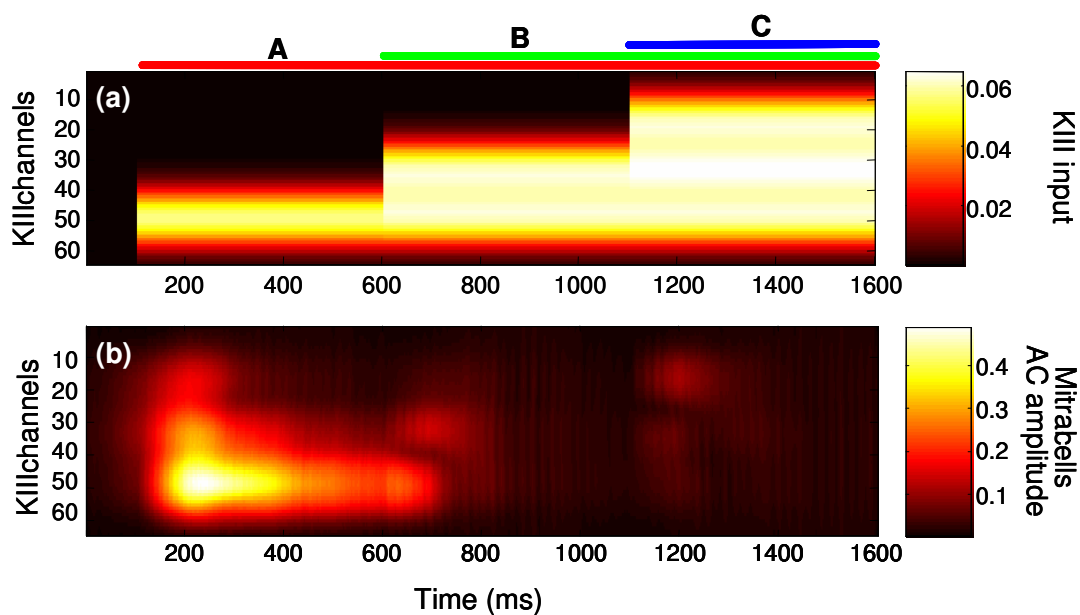


Fig. 74 Habituation experiment without contrast enhancement. (a) Input presented to the KIII. (b) Output of the KIII (amplitude of mitral cells). Odor A is presented at time  $t=100$  ms. As a result of cross-talk, the KIII recalls not only odor A, but to some extent also odors B and C. The early activation of odors B and C causes the KIII to habituate to them, which prevents them from being detected when they are introduced at  $t=600$  s and  $t=1,100$  s, respectively.

### VII.3. Validation with sensor array patterns

In this section, we finally validate the habituation mechanism on experimental data from a MOS sensor (TGS210) exposed to combinations of three analytes. Fig. 75 shows the sensor response to tert-butanol (A), allyl alcohol (B), benzene (C), the binary mixture of tert-butanol and allyl alcohol (AB), and the ternary mixture of tert-butanol, allyl alcohol, and benzene (ABC). The KIII model was trained on the sensor response to the three pure compounds, and then tested on the mixtures to simulate a background-suppression scenario. The system was first presented with odor A, which in this case served as a background odor, and allowed to habituate for 500 ms. At this time, the system was presented with the response pattern to a mixture AB. Fig. 76 shows the response of the KIII when trained using the new hebbian/anti-hebbian rule. Even though the two analytes are present at the input after  $t=600$  ms, the KIII shows sensitivity only to those temperatures (channels) that are specific to odor B. At time  $t=1,100$  ms a ternary mixture of A, B, and C is presented to the sensor. Fig. 76 shows that the KIII responds only to those temperatures specific for odor C. Note that the KIII response to mixture AB and ABC are not identical to the ideal response to odor B in Fig. 76 but a further contrast-enhanced version. The ability of the KIII model to respond only to one of the components in the mixture is consistent with a known olfactory perception phenomenon known as release from mixture suppression. According to this phenomenon, the odor quality of a binary mixture can be shifted to one of the components by adapting to the other one (Wijk, 1989).

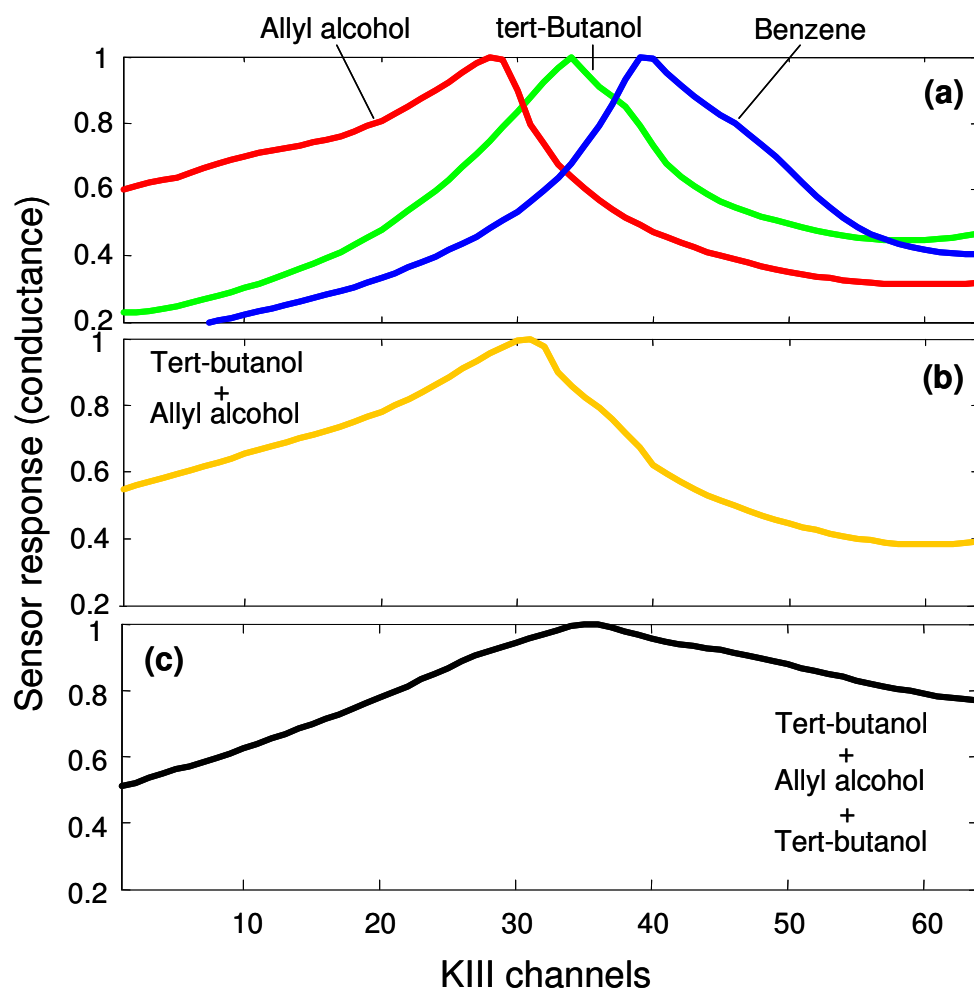


Fig. 75 Gas sensor response to (a) tert-butanol, (b) a binary mixture of tert-butanol and allyl alcohol, and (c) a ternary mixture of tert-butanol, allyl alcohol, and benzene.

### VII.3.1. Habituation without contrast enhancement

In analogy to section VII.2.2.1, we now illustrate the need to perform contrast enhancement in order for the habituation mechanism to work properly. The KIII is trained (Hebbian learning) with the sensor response to tert-butanol, allyl alcohol, and

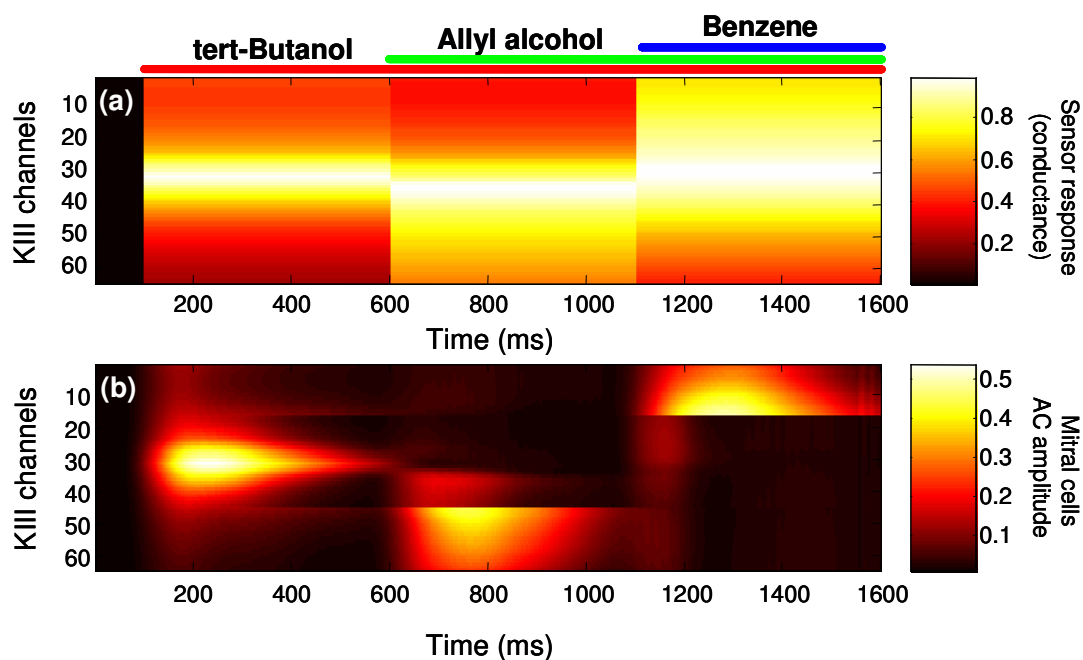


Fig. 76 Habituation scenario with experimental data from a gas sensor. (a) Sensor response used as input for the KIII. (b) AC amplitude of mitral cells in the KIII. Tert-butanol (A) is introduced at  $t=100$  ms. Following habituation of odor A, the KIII is presented with a mixture of odors A and B (allyl alcohol) at  $t=600$  ms. The system response to mixture A+B is a contrast-enhanced version of pattern B alone. At time  $t=1,100$  ms a ternary mixture A+B+C is introduced. It can be observed that the KIII is able to suppress background odors A and C, and respond as if only odor C was presented.

benzene, shown in Fig. 75(a). Fig. 77(b) shows the amplitude of the KIII mitral cells when the input sequence in Fig. 77(a) is introduced. Tert-butanol is presented at time  $t=100$  s. Due to cross-talk, the KIII response is a combination of the three stored patterns. As a consequence, the KIII habituates to the three odors and is unable to

respond later to the introduction of allyl alcohol and benzene at times  $t=600$  s and  $t=1,100$  s, respectively. This experiment clearly shows the need for the Hebbian/anti-Hebbian learning rule in order to segment highly-overlapping odors with the habituation mechanism.

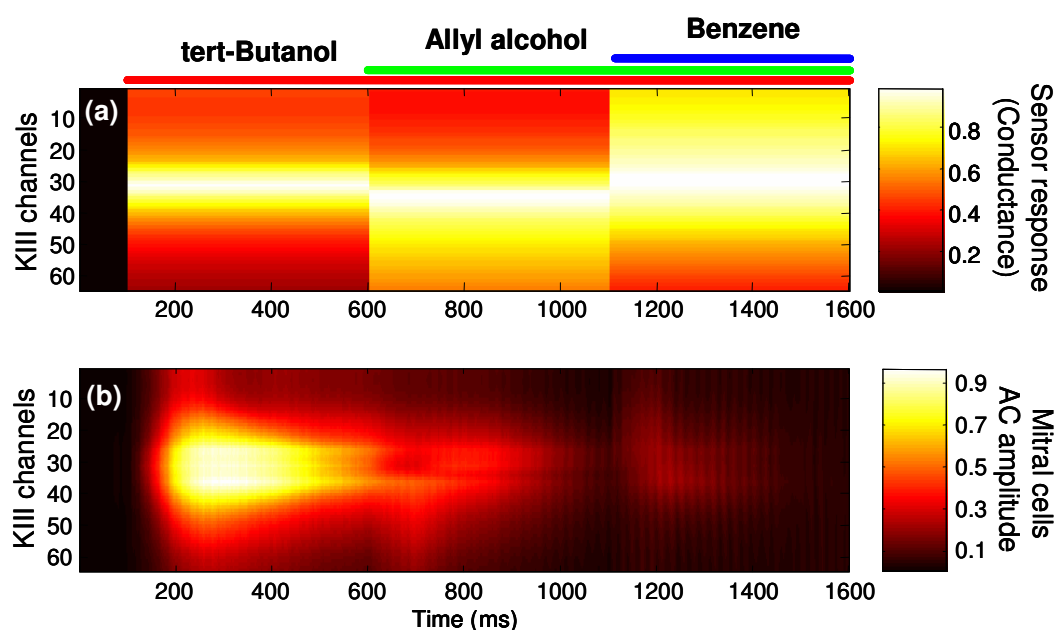


Fig. 77 Habituation to gas-sensor-array responses without contrast enhancement. (a) Sensor response sequence presented to the KIII. (b) Output of the KIII (amplitude of mitral cells). Tert-butanol is introduced at time  $t=100$  ms. As a result of cross-talk, the KIII recalls not only tert-butanol, but to some extent also allyl alcohol and benzene. The early activation of allyl alcohol and benzene causes the KIII to habituate to them, which prevents them from being detected when they are introduced at  $t=600$  s and  $t=1,100$  s, respectively.

#### **VII.4. Conclusions**

This chapter has shown that habituation and dishabituation of KIII channels can be triggered from changes in local AC and DC activity. When combined with Hebbian/anti-Hebbian learning, the system can simulate the effects of habituation in the processing of odor mixtures. The system has been validated on an array of temperature modulated metal-oxide sensors.

It is generally agreed that olfactory adaptation occurs at multiple levels in the olfactory system: olfactory receptors, olfactory bulb and olfactory cortex (Dalton, 2000). This adaptation is mediated by two mechanisms: feed forward and feedback adaptation. The former case is due to the input from a preceding area of the olfactory pathway. This adaptation occurs at the level of the olfactory receptors and the olfactory bulb. In the later case, the input causing the adaptation comes from an area downstream the olfactory pathway. This occurs at the olfactory bulb through the feedback projection from olfactory cortex. These two mechanisms complement each other: whereas feedforward adaptation is triggered and determined by the stimuli, feedback adaptation can be modulated by other areas of the brain depending on factors such as the state of arousal of the animal. Since the habituation scheme proposed in this dissertation models only feedforward adaptation at the olfactory bulb level, our model can only mimic adaptation effects that are directly produced by the stimulus.

The KIII has been shown to have limited performance when presented with overlapping patterns. This limitation is due to the lack of degrees of freedom when adapting connections: since *all* outgoing mitral connections are habituated when the mitral cell activity exceeds a threshold, the number of independent habituable connections is limited to the number of mitral cells. This places an upper bound on the number of independent odors that can be processed (i.e., habituated to) using this model. This issue is addressed in the next chapter by means of a novelty-detection scheme.

## **CHAPTER VIII**

### **NOVELTY DETECTION**

Detection of novel stimuli is a common function in sensory systems, including vision, audition, and olfaction. Novelty detection allows the system to focus on new inputs that are potentially more informative. Such computational function has a number of applications in chemical monitoring, including detection of gas leaks, chemical vessels breakages, filter breakdown, atmospheric contamination, and microbial contamination in central air conditioning systems (Russell et al., 2000; Perera, 2003). In order to perform novelty detection with MOS sensors, adequate processing is required to discriminate changes in sensor response due to humidity and temperature (i.e. background) from those that are produced by the introduction of a new stimulus.

In the preceding chapter, we developed a habituation mechanism that allowed the KIII to detect novel inputs. The proposed habituation mechanism affected all outgoing connections of each mitral cell. Therefore, the number of independently habituable connections was limited by the number of mitral cells ( $N$  degrees of freedom,  $N$  being the number of mitral cells). As a result, the KIII required that odor representations be orthogonal in order to adapt to as many as  $N-1$  odors. This limitation was overcome by combining the habituation mechanism with Hebbian/anti-Hebbian learning, which orthogonalizes the odor representations. Even though this allows the habituation

mechanism to deal with non-orthogonal odors, the degrees of freedom ( $N$ ) still limits the number of odors that the KIII can adapt to. Assuming that each odor has discriminatory information in a different channel, the system is able to adapt to at most  $N-1$  different odors. In general, however, odors have discriminatory information spread over across channels, making it more difficult to adapt to the maximum number of odors. Furthermore, the Hebbian/anti-Hebbian rule also has an upper bound on the number of heavy overlapping patterns that can orthogonalize; this limitation is due to condition (6.15).

With this in mind, the objective of this chapter is to develop a novelty-detection mechanism to allow the KIII model to perform novelty detection with non-orthogonal odor representations and allow adaptation to  $N$  odors. This new mechanism is based on anti-Hebbian learning. The advantage of this mechanism is that, since anti-Hebbian learning is based on the joint activity of pairs of neurons, each connection in the network is allowed to vary independently. As a result, the degrees of freedom of the network increase from  $N$  (the number of mitral cells) to  $N^2$  (the number of lateral connections between mitral cells).

We first present a literature survey of novelty-detection filters with neural networks. Next, we propose an anti-Hebbian rule for lateral connections between periglomerular cells that allows the KIII model to perform novelty detection. Finally, we characterize

the rule on synthetic data, and validate it on experimental data from a MOS gas sensor array.

### **VIII.1. Novelty detection with neural networks**

Several types of neural networks have been used to perform novelty detection, including Multi Layer Perceptrons (MLP), Self Organizing Maps (SOM), and Hopfield Networks (HN), as reviewed below.

Ryan et al. (1998) employed an MLP to identify intruders breaking into a computer system by analyzing the sets of commands typed by the users. The network consists of an input layer with 100 units, a hidden layer with 40 units, and an output layer with 10 units. The MLP is trained through backpropagation on sequences of commands usually typed by each authorized user. A separate output neuron is used to identify each one of the users. Novelty is detected when the activity of each output neuron drops below 0.5, indicating that the network is unable to assign the input sequence to one of the authorized users. LeCun et al. (1990) also used an MLP trained with backpropagation to recognize new handwritten characters. The authors rely on heuristics to define a rejection criterion. First, activity in the winning neuron has to be larger than certain threshold  $T_1$ . Second, activity in the second higher neuron has to be lower than certain threshold  $T_2$ . Finally, the absolute difference between the highest and the second highest neurons has to be larger than a threshold  $T_d$ .

Harris (1993) presented an approach using SOM for novelty detection in a health monitoring system. Comparing the distance between the input and the winning node, the authors were able to determine if the health of the patient could be considered as normal or not.

Bogacz et al. (1999; 2000) used a Hopfield network trained with Hebbian learning to detect novel inputs. The authors show that patterns not stored in memory lead to higher values of the energy function than stored patterns. Consequently a threshold on the value of the Hopfield energy function can be used to identify novel patterns. Crook and Hayes (2001) applied this novelty-detection concept to detect changes in the environment of a mobile robot. The performance of the Hopfield network is analyzed as a function of the number of stored patterns. Their results show that the value of the energy function is independent of the number of patterns stored in the network. However, the performance of the novelty detector still decreases with the number of stored patterns because the threshold becomes less effective.

## **VIII.2. Novelty detection with anti-Hebbian learning**

Novelty detection with anti-Hebbian learning has been studied using both feedforward and recurrent networks. Both approaches are reviewed in this section.

Principe et al. (1999) used a simple feed-forward network such as the one illustrated in Fig. 78 to achieve novelty detection. The network has the following transfer function:

$$y_j = w_{ij}x_i \quad (8.1)$$

where  $x_i$  is the input vector,  $y_j$  is the output vector, and  $w_{ij}$  is the connection strength between input nodes and neurons. Connections  $w_{ij}$  are randomly initialized and trained with anti-Hebbian learning as follows:

$$\Delta w_{ij} = -\alpha \cdot x_i y_j \quad (8.2)$$

The resulting connection matrix spans the subspace perpendicular to that of the input vectors. As a result, any of the learned input patterns or their linear combinations is mapped to the null vector, whereas novel inputs that do not lie in the subspace captured by the input vectors generate a non-zero response.

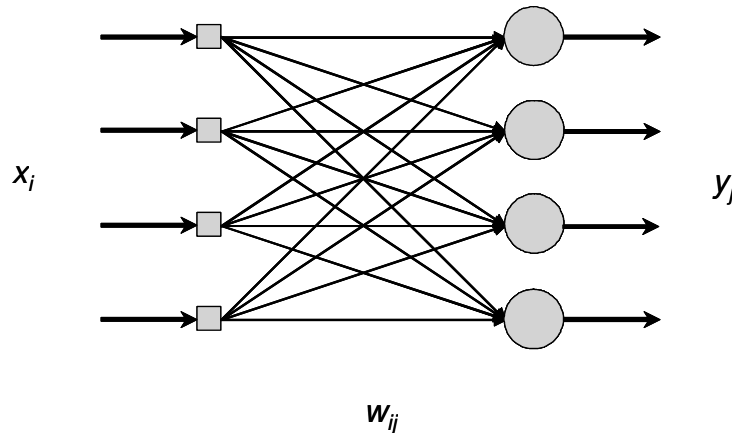


Fig. 78 Novelty detection with a feed forward single-layer network.  $x_i$ ,  $y_i$ , and  $w_{ii}$  represent the inputs, outputs, and the weight matrix, respectively. The weight matrix is trained with anti-Hebbian learning to achieve novelty detection.

More relevant for this work, since the KIII is a recurrent network, is the recurrent novelty detection network proposed by Kohonen and Oja (1976). Their model uses a single-layer fully-connected recurrent neural network (Fig. 79) with both positive and negative connections. These connections are trained with anti-Hebbian learning as follows:

$$\frac{dw_{ij}}{dt} = -\alpha \cdot y_i y_j \quad (8.3)$$

where  $y_i$  and  $y_j$  are the output of neurons  $i$  and  $j$  respectively,  $w_{ij}$  is the strength of the connections between neurons  $i$  and  $j$ , and  $\alpha$  is a learning rate. The dynamic response of the neural network when presented with input vector  $x_i$  is:

$$y_i(n) = \sum_{j=1}^N w_{ij} y_j(n-1) + x_i \quad (8.4)$$

from which the steady-state response of the network in vector form becomes:

$$(1 - w) \cdot y = x \quad (8.5)$$

Therefore, this network cannot produce a zero output for any input other than the null vector. This implies that the null space of the transformation generated by the recurrent network is the null vector. On the other hand, note that the null space of the feedforward network can contain vectors other than the null vector.

To overcome this problem, Kohonen and Oja (1976) introduced a continuous background activity to all neurons. The neuron activity is then represented in a scale in which the background activity is treated as zero. The network is able to learn the subspace spanned by the input vectors and respond only to vectors that have at least one component outside of this subspace.

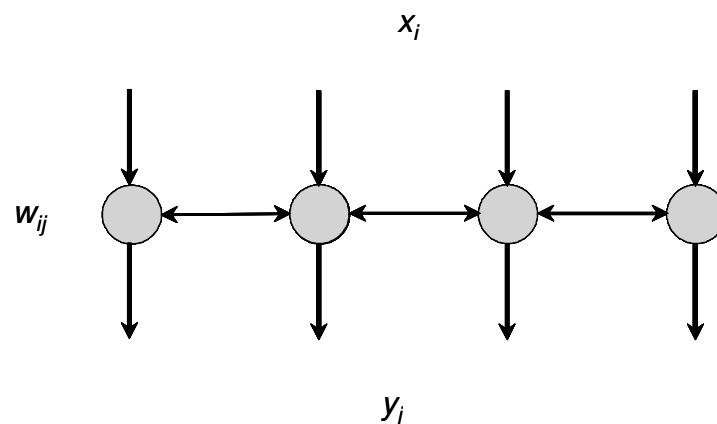


Fig. 79 Novelty detection with a single-layer recurrent network, as used by Kohonen and Oja (1976).

Following Kohonen and Oja (1976), the stability of the network in Fig. 79 can be determined by analyzing the temporal evolution of the network. First, let us consider the transfer function  $\Phi$  of the network:

$$y = \Phi x = (I - W)^{-1} x \quad (8.6)$$

From this expression and Eq. 8.4, we can compute the temporal evolution of the network:

$$\frac{d\Phi^{-1}}{dt} = -\Phi^{-1} \frac{d\Phi}{dt} \Phi^{-1} = -\frac{dW}{dt} \quad (8.7)$$

$$\frac{d\Phi}{dt} = -\alpha \cdot \Phi^2 x x^T \Phi^2 \quad (8.8)$$

Eq. 8.8 shows that the motion of the system can be described by a Bernoulli equation<sup>8</sup>, for which a solution is known to exist for  $\alpha \geq 0$  (Kohonen and Oja, 1976). Therefore, only negative values of  $dW/dt$  (Eq. 8.3) lead to stable solutions of the network. Positive values of  $dW/dt$  convert Eq. 8.3 into a Hebbian-like update rule, causing the weight values  $w_{ij}$  to increase without bound, which leads to unstable behavior.

---

<sup>8</sup> The general form of the Bernoulli equation is:  $\frac{dy}{dx} + p(x)y = q(x)y^n$

### VIII.3. Novelty detection in the KIII through anti-Hebbian learning

In this section, we study the application of anti-Hebbian learning to perform novelty detection with the KIII. As already mention in Chapter V, the oscillatory nature of KII sets prevents the use of anti-Hebbian learning for the lateral connections. For this, reason, we propose to apply anti-Hebbian learning at the level of periglomerular-to-periglomerular connections (shown in Fig. 80) since periglomerular cells follow a fixed-point behavior. It is worth noticing that adaptation of periglomerular to periglomerular connections is a novel contribution of our research; these connections have been considered fixed in all previous studies.

The anti-Hebbian learning rule used to train periglomerular lateral connections is:

$$\Delta w_{P,ij} = -\mu \cdot x_{P,i} x_{P,j} \quad (8.9)$$

where  $w_{P,ij}$  is the connection matrix between periglomerular cells, and  $x_{P,i}$  and  $x_{P,j}$  are the activity of periglomerular cells  $i$  and  $j$ , *respectively*.

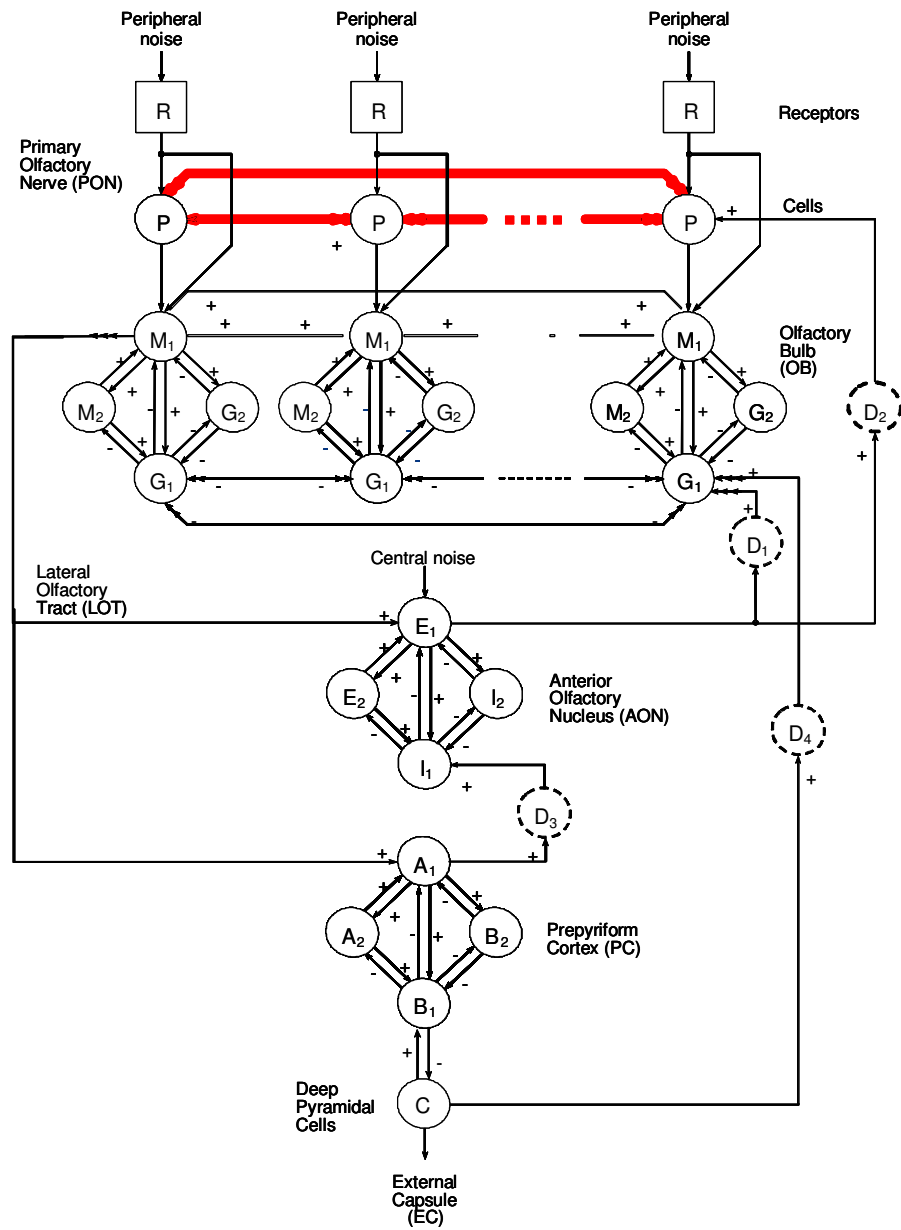


Fig. 80 Periglomerular to periglomerular lateral connections (thick lines) are trained with the proposed anti-Hebbian rule.

As discussed in section VIII.2, a recurrent neural network trained with anti-Hebbian learning cannot produce a null output with non-zero inputs. To overcome this limitation, we propose to adapt the KIII model to include an additional layer of periglomerular cells, as shown in Fig. 81. Each  $P_1$  cell connects to all  $P_2$  cells, which have fully lateral connectivity between  $P_2$  cells. All these connections between periglomerular cells ( $P_1$ - $P_2$  and  $P_2$ - $P_2$ ) are trained with anti-Hebbian learning following Eq. 8.9. In this case, the first layer of periglomerular cells provides feed forward inhibition that allows the model to produce a null output even for non-zero inputs.

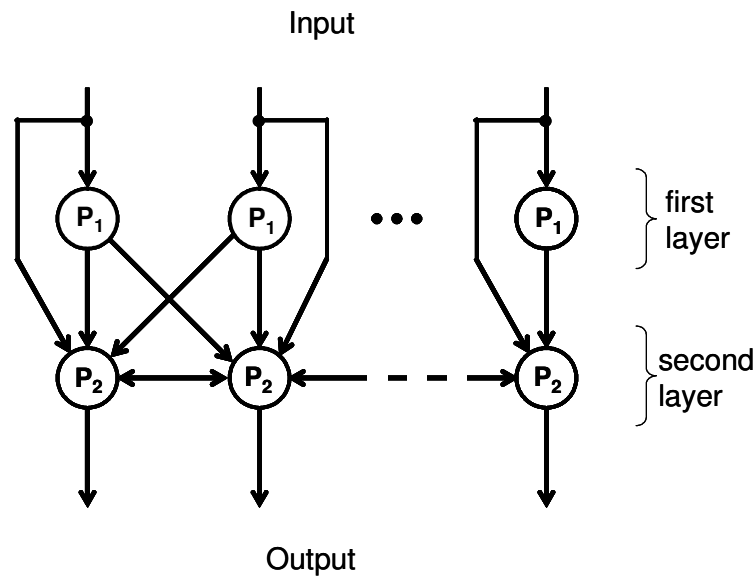


Fig. 81 Two layers of PG cells. The first layer of PG cells provides feed forward inhibition to the second layer of PG cells.

#### **VIII.4. Characterization with synthetic data**

In this section we characterize the ability of the proposed model to perform novelty detection on synthetic inputs, both static and dynamic.

##### **VIII.4.1. Static inputs**

First, the KIII model is trained on a synthetic problem consisting of two 3-dimensional input vectors:  $[1 \ 2 \ -3]$  and  $[4 \ 1 \ 2]$ . During the training phase, the two training vectors are presented alternatively, as illustrated in Fig. 82(a, b). Periglomerular cells respond to each presentation with an initial transient that eventually settles to zero as a result of anti-hebbian learning. During the subsequent testing phase, the KIII is presented with four input vectors: the two training vectors  $[1 \ 2 \ -3]$  and  $[4 \ 1 \ 2]$ , a linear combination of the two training vectors  $[5 \ 3 \ -1] = [1 \ 2 \ -3] + [4 \ 1 \ 2]$ , and a vector outside the linear subspace  $[2 \ 1 \ -3]$ . The response of periglomerular cells to the test vectors are shown in Fig. 82(d). As shown, the KIII displays a null steady-state for all vectors belonging to the linear subspace defined by the training patterns, yet generates a non-null response to the vector outside this subspace. This experiment illustrates the ability of the learning technique to desensitize the KIII to previous stimuli, allowing it to respond only to novel odors.

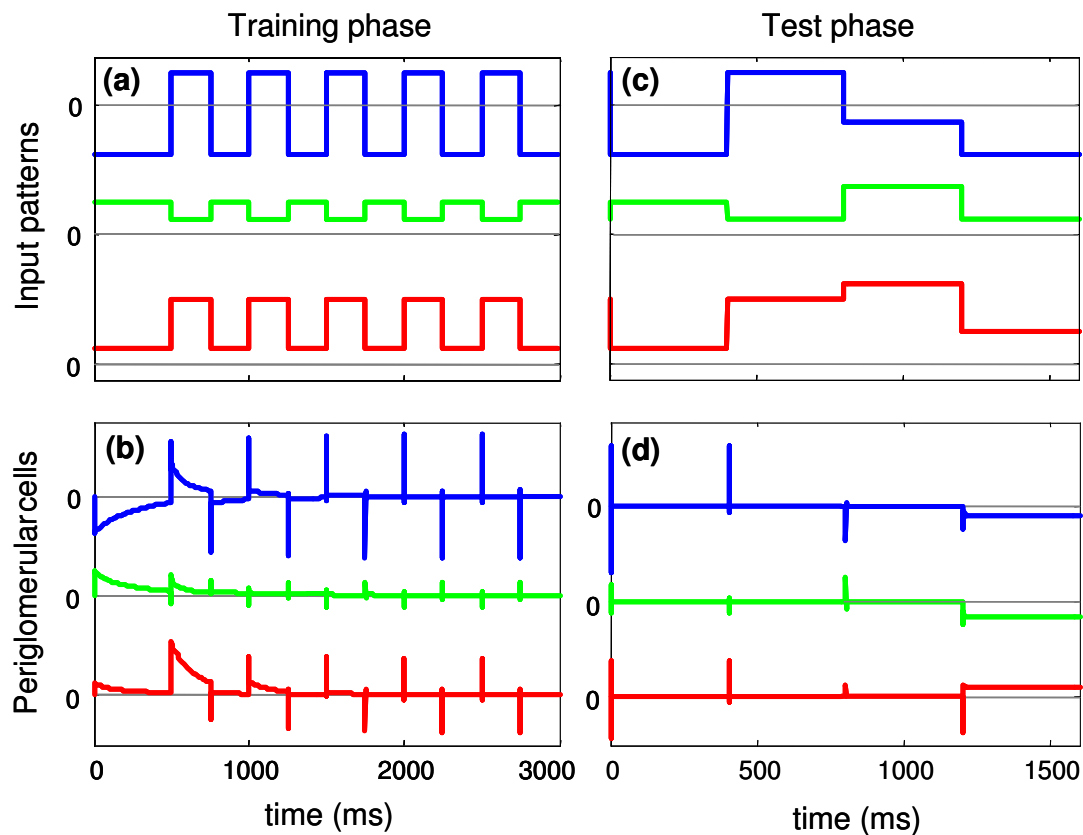


Fig. 82 Characterization with synthetic data. (a, b) Training of KIII with two inputs:  $[1 \ 2 \ -3]$  and  $[4 \ 1 \ 2]$ . (c, d) Testing the KIII with the two training vectors  $[1 \ 2 \ -3]$ ,  $[4 \ 1 \ 2]$ , a linear combination of them ( $[1 \ 2 \ -3] + [4 \ 1 \ 2]$ ), and a vector outside the linear subspace  $[2 \ 1 \ -3]$ .

A more detailed characterization of the KIII response as a function of the novelty of the pattern is shown in Fig. 83. The KIII is trained on vectors  $[1 \ 2 \ -3]$  and  $[4 \ 1 \ 2]$ , and subsequently tested with vector  $\mathbf{v}$ , which forms an angle  $\varphi$  with the plane  $S$  spanned by the training vectors. The angle  $\varphi$  is used as a measure of novelty. As shown in Fig. 83, periglomerular cells provide a higher response as the input vector moves away from the plane  $S$ .

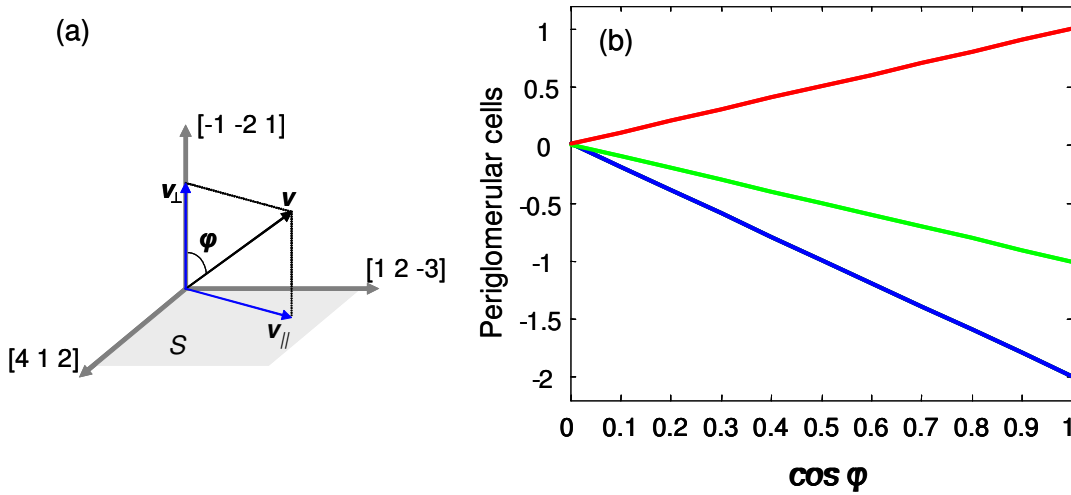


Fig. 83 Projection performed by the novelty detector. (a) Projection of an input vector  $v$  onto the space perpendicular to the subspace spanned by the training patterns  $[1 \ 2 \ -3]$  and  $[4 \ 1 \ 2]$ . (b) Output of periglomerular cells as a function of  $\cos(\varphi)$ , where  $\varphi$  is the angle between the input vector  $v$  and the vector perpendicular to the subspace spanned by the training inputs.

#### VIII.4.2. Dynamic inputs

The previous sections have validated the novelty-detection model on static inputs. Sensor responses are, however, typically dynamic. The objective of this section is to illustrate the ability of the KIII model to perform novelty detection on dynamic inputs.

For this purpose, a three channel KIII model was trained with the two oscillatory inputs shown in Fig. 84(a). First, the oscillatory input A is introduced at  $t=0$  ms and removed at  $t=2,500$  ms. The oscillatory pattern B is subsequently introduced at time  $t=2,500$  ms. Fig. 84(b) show the response of the three second-layer periglomerular cells to these two

patterns. The response to the oscillatory trajectory A is initially high, but slowly dies out as a result of adaptation. When oscillatory trajectory B is suddenly introduced, the activity of the KIII increases abruptly, but eventually dissolves as a result of the novelty-detection mechanism. These results parallel those obtained on static inputs, and show that the KIII trained with the proposed anti-Hebbian rule is able to reduce response to already presented inputs, but is also sensitive to novel inputs.

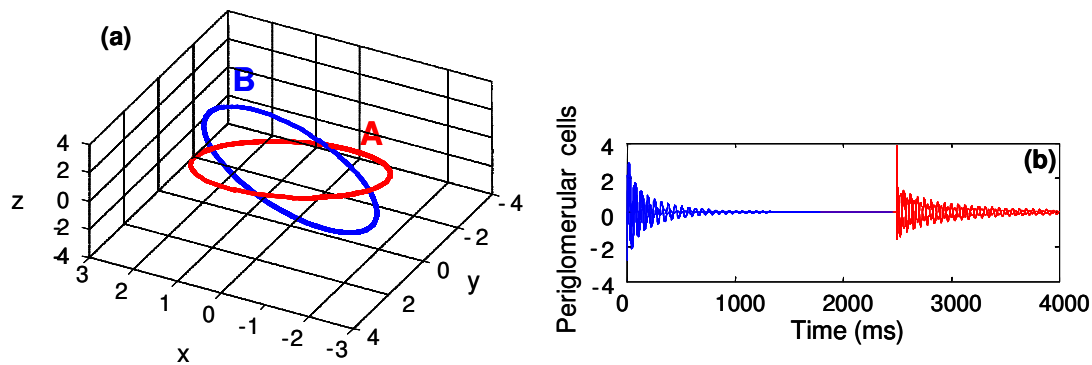


Fig. 84 Novelty detection with oscillatory patterns. (a) Trajectory of the two oscillatory patterns in the input space (three-dimensional). (b) Output of the KIII.

#### VIII.4.3. Receptive operating characteristic analysis

A more systematic characterization of our novelty detector is performed using the Receiver Operating Characteristic (ROC).

ROC analysis is an established method to evaluate the quality of a detector by considering the trade-off between the number of correct detections (true positives) and incorrect detections (false positives) (Egan, 1975; Perera et al. 2003).

This is accomplished by plotting the true-positive rate against the false-positive rate (ROC curve) as the sensitivity of the detector is changed (Zou et al., 1997; Provost and Fawcet, 1997). At position (0, 0) in the ROC curve, the detector has zero sensitivity and there are no detections, whereas at position (1, 1) the detector has very high sensitivity, and all true positives and all possible false positives are detected. The shape of the curve denotes the quality of the detector. The diagonal line between the (0,0) and (1,1) operating points represents an ineffective detector, since an increase in the true-positive rate incurs an equal increase in the false-positive rate. An ROC curve that lies above the diagonal line corresponds to a useful detector, since true positives outnumber false positives. The more the ROC curve approaches the upper left corner of the plot, the better the quality of the detector.

In the case of the proposed novelty-detector, the estimates of true-positives and false-positives are obtained by thresholding the activity of the periglomerular cells (i.e., activity above threshold corresponds to detection of a new odor). The value of the threshold determines the sensitivity of the novelty detector.

In order to obtain a ROC curve with good resolution, the detector needs to be tested for a large number of operating conditions, which would require an impractical amount of experimental data. For this reason, the ROC analysis is performed on synthetic data from an accurate model of the sensor response. Following Clifford and Tuma (1983), the sensor response to benzene ( $C_6H_6$ ) and tert-butanol ( $C_4H_{10}O$ ) is modeled as:

$$\frac{G}{G_0} = k_1 \cdot [C_6H_6]^{\beta_1} + k_2 \cdot [C_4H_{10}O]^{\beta_2} + k_3 \cdot [C_6H_6]^{\beta_3} \cdot [C_4H_{10}O]^{\beta_4} \quad (8.10)$$

where  $G$  is the conductance of the sensor,  $G_0$  the conductance of the sensor in air,  $[C_6H_6]$  and  $[C_4H_{10}O]$  are the concentrations of benzene and tert-butanol respectively, and  $k_1, k_2, k_3, \beta_1, \beta_2, \beta_3$ , and  $\beta_4$  are the parameters of the model. The sensor model was adjusted in a least-square fashion to fit the experimental response of four MOS sensors to a mixture of benzene and tert-butanol.

In the ROC experiments that follow, tert-butanol and benzene will be used as target and background odors, respectively. Tert-butanol is introduced and removed one hundred times during 23.6 hours of simulation (Fig. 85(a)). Each introduction of tert-butanol is modeled using the positive cycle of a sinusoidal waveform with a period of 400 seconds, as shown in Fig. 85(c).

The concentration amplitude of each of the 100 introductions of tert-butanol is chosen from a uniform random distribution.

The maximum value of this distribution is set to 0.1, 1, and 10 in three different experiments, and the minimum value is 0 for all the three experiments. Each one of these values will require to run the 23.6 hour simulated experiment for a total of  $23.6 \times 3 = 70.8$  hours.

For the duration of the simulated experiments, the concentration of benzene is made to fluctuate randomly between 10% and 30% (Fig. 85(a)) as follows. Random concentrations were generated every  $T = 50$  seconds from a uniform distribution in the range  $[10, 30]$ , and a cubic spline was used to interpolate the points between each random sample. Fig. 85(a,d) shows the resulting concentrations of benzene and tert-butanol, where the maximum concentration of tert-butanol was set to 10.

The simulated sensor response generated from this scenario is presented to the KIII, which has been trained with the simulated sensors response to oscillatory fluctuations of benzene. During the experiment, the training rate is set to a low value ( $\mu = 1 \cdot 10^{-5}$ ) to avoid fast adaptation to the target odor. The output of the KIII (training phase not shown) is shown in Fig. 85(b,e) where each vertical line indicates the introduction of benzene.

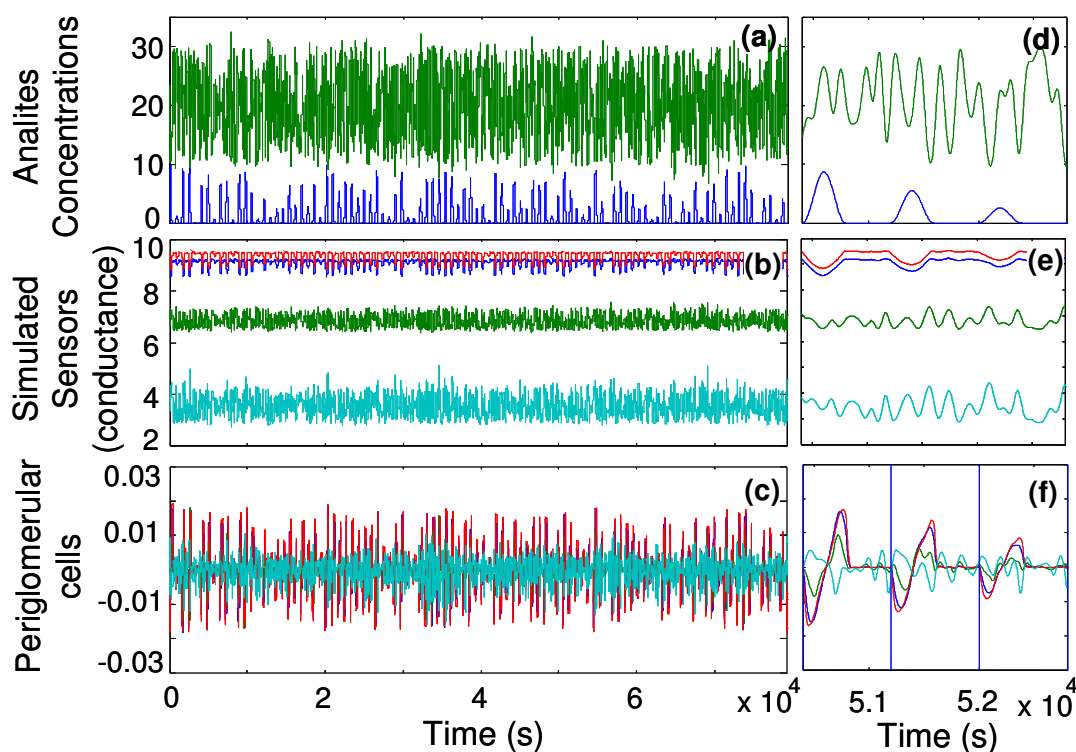


Fig. 85 Simulated scenario to perform ROC analysis. Tert-butanol (target odor) is introduced 100 times in a random background of benzene. (a,d) Concentration profile of tert-butanol and benzene. (b,e) Simulated response of the 4 MOS gas-sensors when simulated concentration profile (a,d) is used as input. (c,f) Periglomerular activity produced by the simulated sensor response to the concentration profile in (a,d); vertical lines in (f) denote each introduction of tert-butanol. Parts (c) and (d) are a close-up view for three of the one hundred introductions of tert-butanol.

Fig. 86 shows the ROC of the novelty-detector for three different values of the maximum amplitude ( $A$ ) of tert-butanol: 0.1, 1, and 10. The ROC curve for  $A=0.1$  is nearly a straight line, which indicates that the novelty detector fails to detect the target

odor. In this case, the true-positive rate is equal to the false-positive rate for any value of the threshold. When  $A=1$ , the ROC curve is above the diagonal line. This indicates that the true-positive rate is higher than the false-positive rate. The performance is improved even further when  $A$  is set to 10. This results show that the novelty detector is able to detect fluctuations in the concentration of the target odor that are up to one order of magnitude lower than fluctuations in the concentration of a background odor.

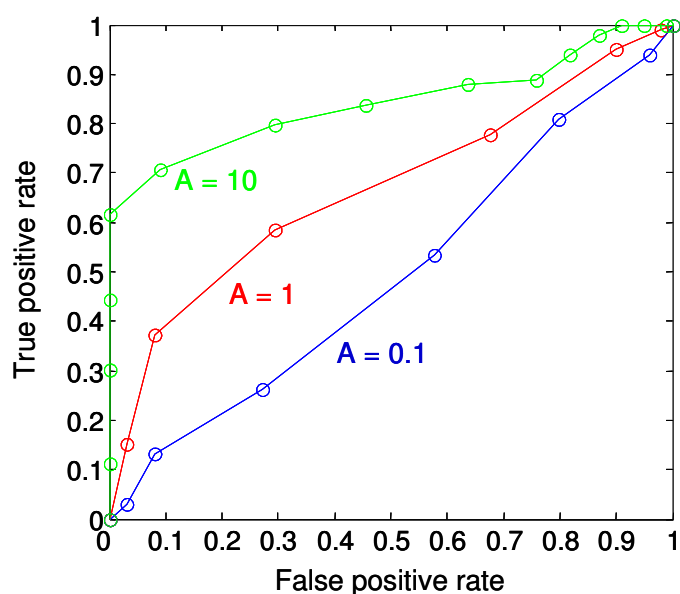


Fig. 86 ROC curves for three different values of the maximum amplitude of the target odor ( $A$ ).

### VIII.5. Validation with gas sensor array data

The novelty-detection model is finally validated with experimental data from MOS sensors. Specifically, we will illustrate the ability of the KIII model to cancel

fluctuations in humidity and up to two background odors. The isothermal database (section II.3.2; Chapter II) was used for this purpose.

A preprocessing stage that removes the DC offset of the sensor response is applied to simplify the training required by the system. To understand the need for this preprocessing stage, let us consider the following example shown in Fig. 87. The figure illustrates the response trajectory (thick line) of a system with three sensors as an operating parameter (temperature, humidity, or concentration) is varied. Illustrated in Fig. 87(a), in the case of sensor response with DC offset the KIII learns the subspace spanned by the vectors from the origin to the response trajectory instead of capturing the odor trajectory alone. This will prevent the detection of novel odors that may lie on this plane.

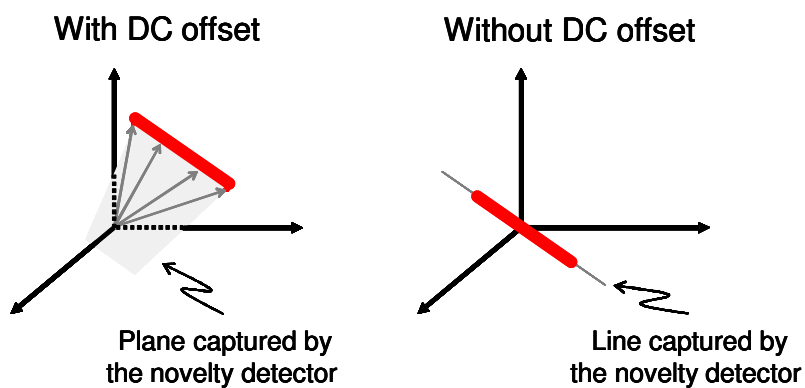


Fig. 87 Novelty detection (left) with DC offset and (right) without DC offset. The figure illustrates the trajectory of a system with three sensors. If the raw sensor response (i.e., with DC offset) is used, the KIII adapts to the plane spanned by the vectors from the origin to the odor trajectory. In the case of sensor response without DC offset, the KIII adapts exclusively to the direction of sensor responses to the odor.

To overcome this drawback, we perform DC offset removal, which translates the response trajectory to the origin, as shown in Fig. 87(b). In this case, the KIII captures exclusively the direction of the sensor responses to the odor.

#### **VIII.5.1. Cancellation of fluctuations in two simultaneous stimuli**

The objective of the first experiment is to demonstrate the ability of the novelty-detection model to compensate for fluctuations in background odors and humidity. For this purpose, the sensor array is exposed to a fluctuating concentration of tert-butanol (concentration range: 80-100% of the headspace concentration; oscillation period  $T = 440$  s) and humidity (52-65% relative humidity;  $T = 880$  s), as shown in Fig. 88(a) and (b), respectively. The response of the humidity sensor and the chemical sensor array is shown in Fig. 88(c) and (d), respectively. The output of the KIII, shown in Fig. 88(e) clearly illustrates that the novelty-detector is able to rapidly learn the subspace of variation due to fluctuations in tert-butanol and humidity, allowing the KIII model to cancel its response to those fluctuations.

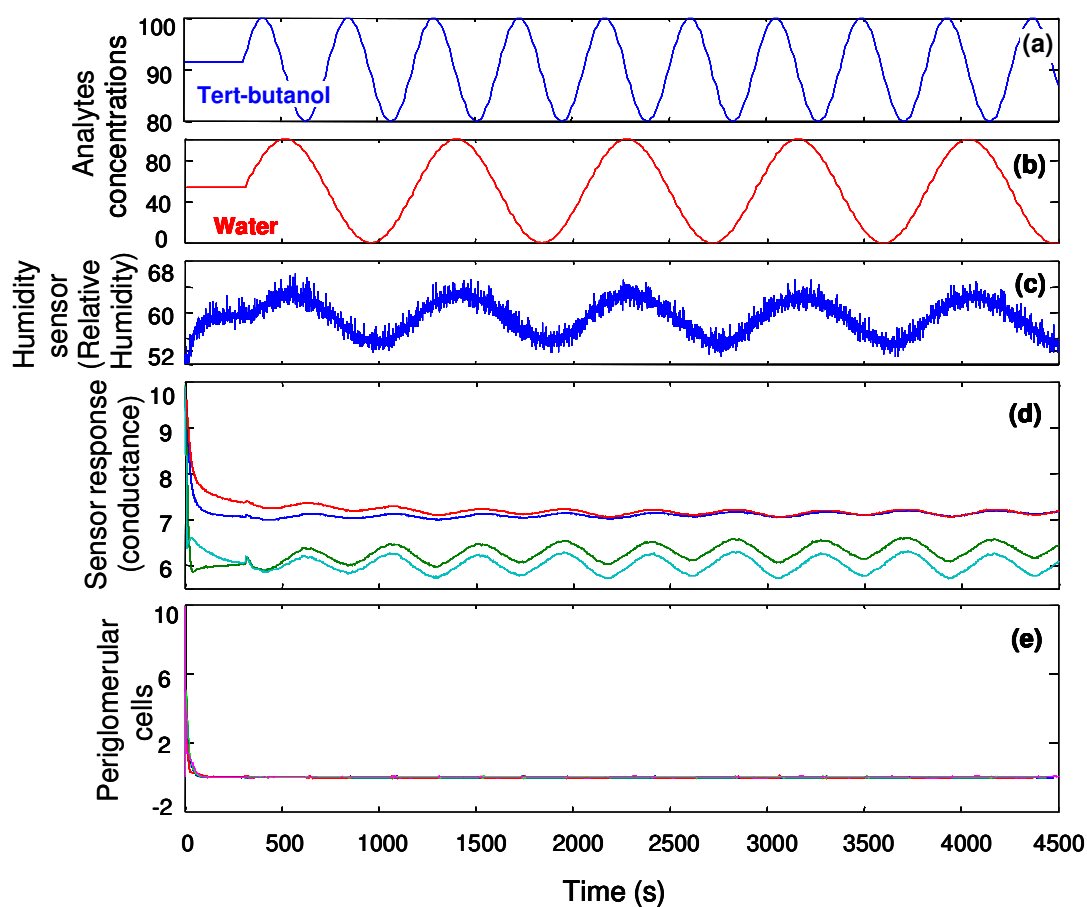


Fig. 88 Cancellation of fluctuations in two simultaneous stimuli (humidity and tert-butanol). (a) Concentration fluctuations of tert-butanol (b). Concentration fluctuations of water vapor used to vary the humidity at the sensor chamber. (c) Response of the humidity sensor. (d) Response of the gas sensor array; notice that the sensors respond mostly to fluctuations in tert-butanol. (e) Output of the periglomerular cells in the KIII model. As a result of anti-Hebbian learning, the model is able to cancel the effect of fluctuations in humidity and tert-butanol.

### VIII.5.2. Detection of a novel stimulus in the presence of a fluctuating background

The objective of this experiment is to determine the ability of the KIII to detect the introduction of a novel stimulus in the presence of a fluctuating background odor. For this purpose, the sensor array is exposed to a fluctuating concentration of benzene (concentration: 10-30%; period  $T=440$  s), as shown in Fig. 89(a). At time  $t=5,300$  s, tert-butanol is introduced (concentration: 0-10%; period  $T=880$  s) while maintaining the benzene fluctuations. Oscillations in concentration for the two analytes are chosen with different frequencies for visualization purposes. Fig. 89(b) shows the raw sensor response to these chemicals. Fig. 89(c) shows the sensor response after subtraction of the DC offset. This signal is the actual input to the KIII model. The output of the model is shown in Fig. 89(d). As a result of anti-Hebbian learning, the KIII adapts to fluctuations in tert-butanol, and significantly reduces its response to these fluctuations. When benzene is introduced at time  $t=5,300$  s, activity in the KIII significantly increases, indicating that the model has been able to detect the introduction of the novel stimulus.

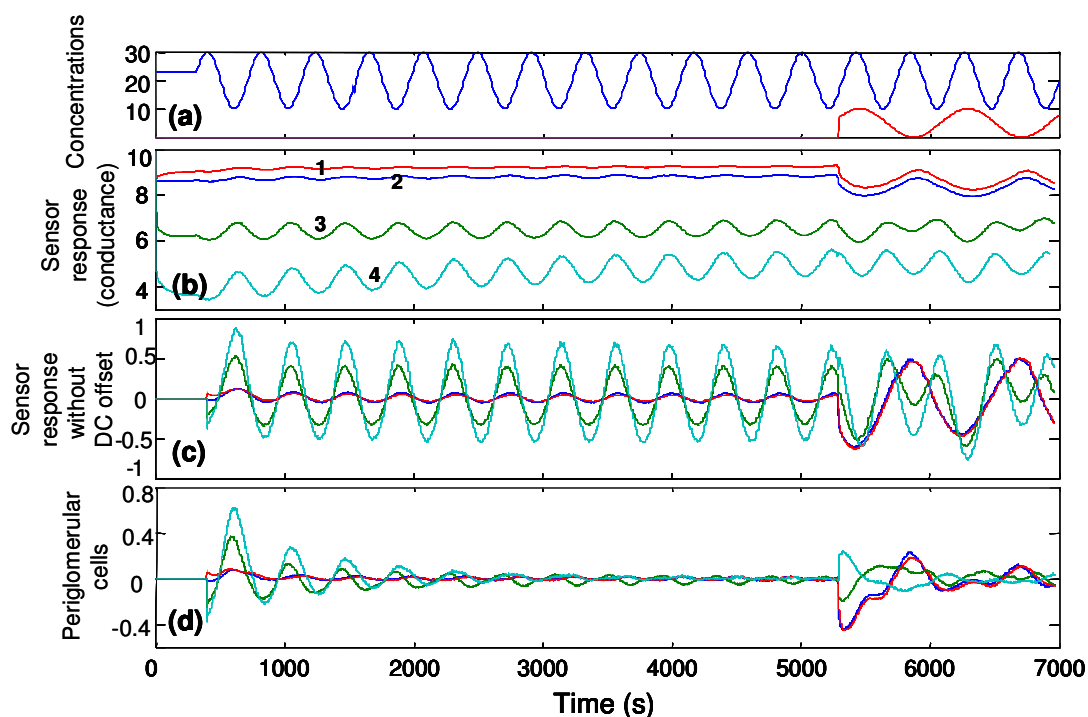


Fig. 89 Detection of benzene in the presence of a fluctuating background of tert-butanol. (a) Concentration of benzene (top trace) and tert-butanol (bottom). (b) Response of the four MOS sensors (labeled 1 through 4). (c) Response of the sensors after subtraction of their DC offset. (d) Periglomerular cell activity with anti-Hebbian learning. The increase of activity at time  $t=5,300$  ms indicates that the novel odor has been detected.

Fig. 90 shows the performance of the model as a function of the learning rate. Small learning rates lead to slower adaptation and larger responses when the new odors are presented. On the other hand, large learning rates allow for faster adaptation but result in a lower response to new odors. This leads to a shorter and weaker transient, but the model is still able to adapt to background odors and detect new ones. The role of the learning rate on the performance of the model is expected to be more important if the

period of the odor fluctuations and the time constants of the KO dynamics are comparable.

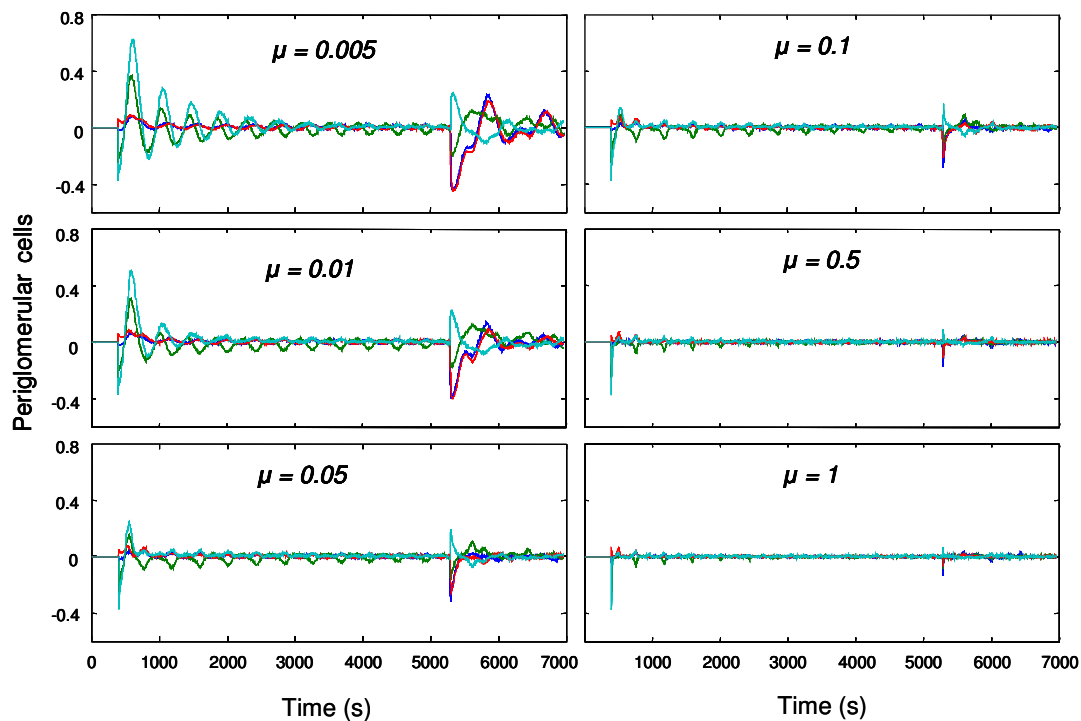


Fig. 90 Effect of the anti-Hebbian learning rate on the detection of a new odor.

The results in Fig. 89(d) were obtained by maintaining anti-Hebbian adaptation throughout the experiment. Better detection results can be achieved if adaptation is stopped once the system has learned to cancel fluctuations in the background analyte (benzene in that case).

Fig. 91 shows the output of the KIII model to the same stimulus in Fig. 89, but in this case anti-Hebbian learning is stopped at time  $t=4,000$  s. When the new odor (tert-butanol) is introduced at  $t = 5,300$  s, the KIII is able to recover its fluctuations, an indication that the new odor has been detected.

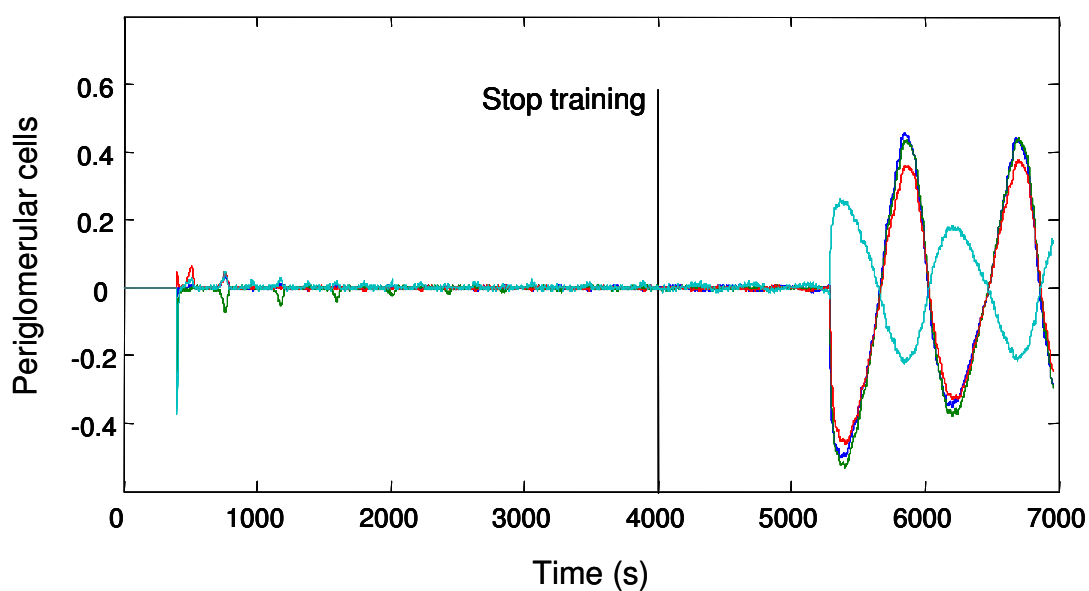


Fig. 91 Detection of benzene with discontinuous training. Anti-Hebbian adaptation is stopped at time  $t=4,000$  s. This allows the KIII model to better identify the presence of the novel analyte.

To further analyze the performance of the model, we also attempted to detect the introduction of the novel stimulus (tert-butanol) based on the response of sensors 3 and 4. As shown in Fig. 89(b), the introduction of benzene can be readily detected by a sudden change in the response of sensors 1 and 2, but the response of sensors 3 and 4 is rather subtle. The results of novelty detection when operating only on sensors 3 and 4 are shown in Fig. 92. Though the response in this case is less pronounced, the model is still able to identify the introduction of tert-butanol at time  $t = 5,300$  s. This additional result illustrates the sensitivity of our novelty detection mechanism, even when the introduction of a new stimulus produces only subtle responses in the sensors.

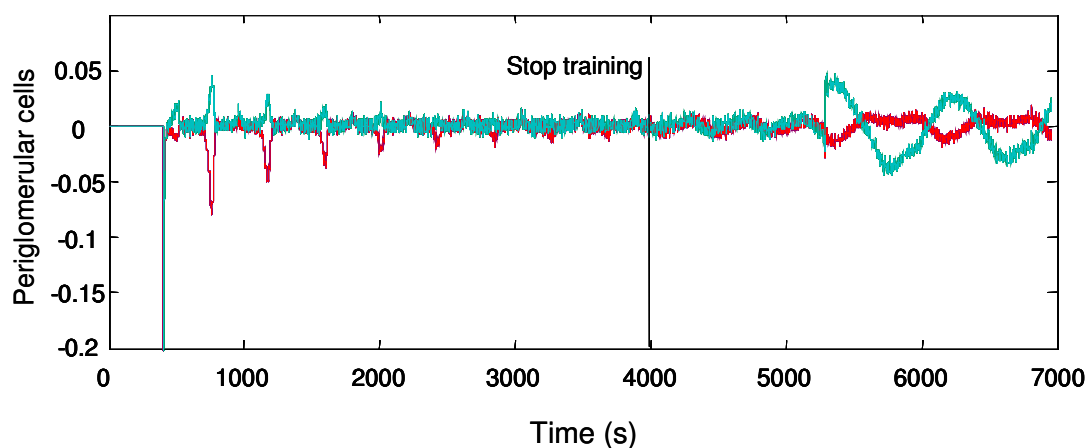


Fig. 92 Detection of benzene on a background of tert-butanol using only the response of sensors 1 and 2 in Fig. 89(b). The introduction of benzene at  $t = 4,000$  s is also clearly detected by the KIII.

### VIII.5.3. Suppression of strong backgrounds

In the previous section, we studied novelty detection when background and novel odors have comparable concentrations. In real-world scenarios, however, it is oftentimes critical to detect target odors that embedded in strong and fluctuating backgrounds. In this section we simulate a more realistic scenario in which a target odor at low concentrations (benzene: 0-10%; period  $T=880$  s), needs to be detected in the presence of a fluctuating background at high concentrations (concentration: 80-100%; period  $T=440$  s). Fig. 93 (a-e) shows the concentration profiles for the two analytes, sensor responses before and after DC offset removal, and the output of the KIII model with continuous anti-Hebbian learning. Similar to the results in the previous sections, the KIII model is able to identify the introduction of the novel odor, though the response is rather diminished. This response can be enhanced if anti-Hebbian adaptation is “turned off” once the fluctuations in the background odor have been learned. Results are shown in Fig. 94. In this case, the KIII is able to provide a significantly large response when the target odor is introduced; note that the model is also able to return to null activity once the target odor is removed at  $t = 8,000$  s. Finally, it is worth noting that the analytes used as background and target odors in this experiment are the opposite of those in the previous experiment (Fig. 89). This further illustrates the generality of our novelty-detection model.

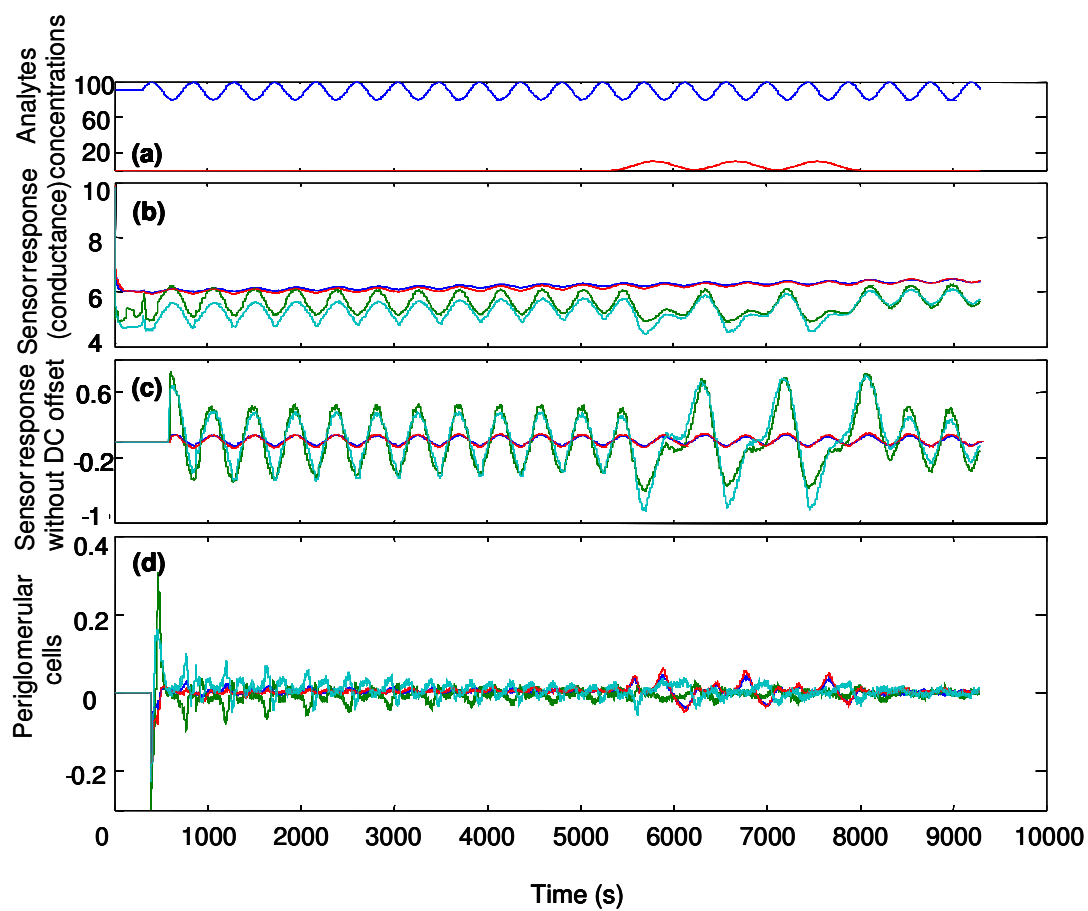


Fig. 93 Suppression of strong background odor with continuous anti-Hebbian training. (a) Concentration profile for the two analytes. (b) Raw sensor response. (c) Sensor response without DC offset. (d) Periglomerular cell activity.

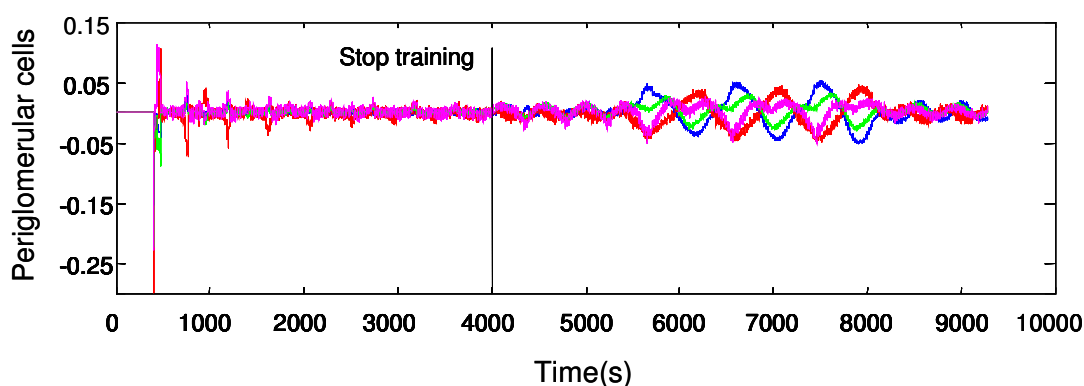


Fig. 94 Suppression of a strong background when anti-Hebbian learning is stopped after the system habituates (time  $t=4,000$  s). This allows the KIII model to better detect the introduction of a novel analyte at time  $t=5,300$  s. Note that KIII activity returns to background once the novel analyte is removed at time  $t=8,300$  s.

#### VIII.5.4. Sequential novelty detection

Real environments are usually formed by a melange of odorants with different concentrations. In this type of environment, a novelty detector should be able to adapt to odor mixtures in order to detect the presence of new odors. To test our novelty detection model in this type of scenario, the sensor array will be exposed to fluctuations in an increasing number of analytes: tert-butanol (concentration: 0-20%; period  $T=440$  s), followed by allyl alcohol (concentration: 0-10%; period  $T=880$  s), and finally benzene (concentration: 0-5%; period  $T=1,320$  s). Fig. 95(a-d) shows the concentration profile of each analyte, and the corresponding sensor response with and without DC offset.

Notice that the concentrations of the odors have different oscillation frequencies to facilitate visual interpretation of the KIII outputs, which are shown in Fig. 96. With continuous anti-Hebbian adaptation, the KIII model is able to adapt to fluctuations in tert-butanol and therefore detect the introduction of allyl alcohol at time  $t=5,300$  s. Subsequently, the model adapts to both tert-butanol and allyl alcohol, enabling the detection of benzene when it is introduced at time  $t=10,300$  s. As in the previous sections, stopping the anti-Hebbian adaptation prior to the introduction of an analyte enhances the response of the model to that analyte. Results are shown in Fig. 96(b, c) when adaptation is turned off before allyl alcohol and benzene are introduced, respectively. These results further illustrate the ability of the model to perform novelty detection in presence of one or more background odors.

Finally, we illustrate the limits of detection of the proposed model. For this purpose, the sensor array was exposed to weak fluctuations of a target odor (benzene: 0-5%; period  $T=1,320$  s) in the presence of two strong backgrounds (tert-butanol; 0-100%; period  $T=440$  s; and allyl alcohol; 0-30%; period  $T=880$  s). Fig. 97 shows concentration profiles (a,b,c), sensor response with (e) and without DC offset (d), and the output of the KIII model.

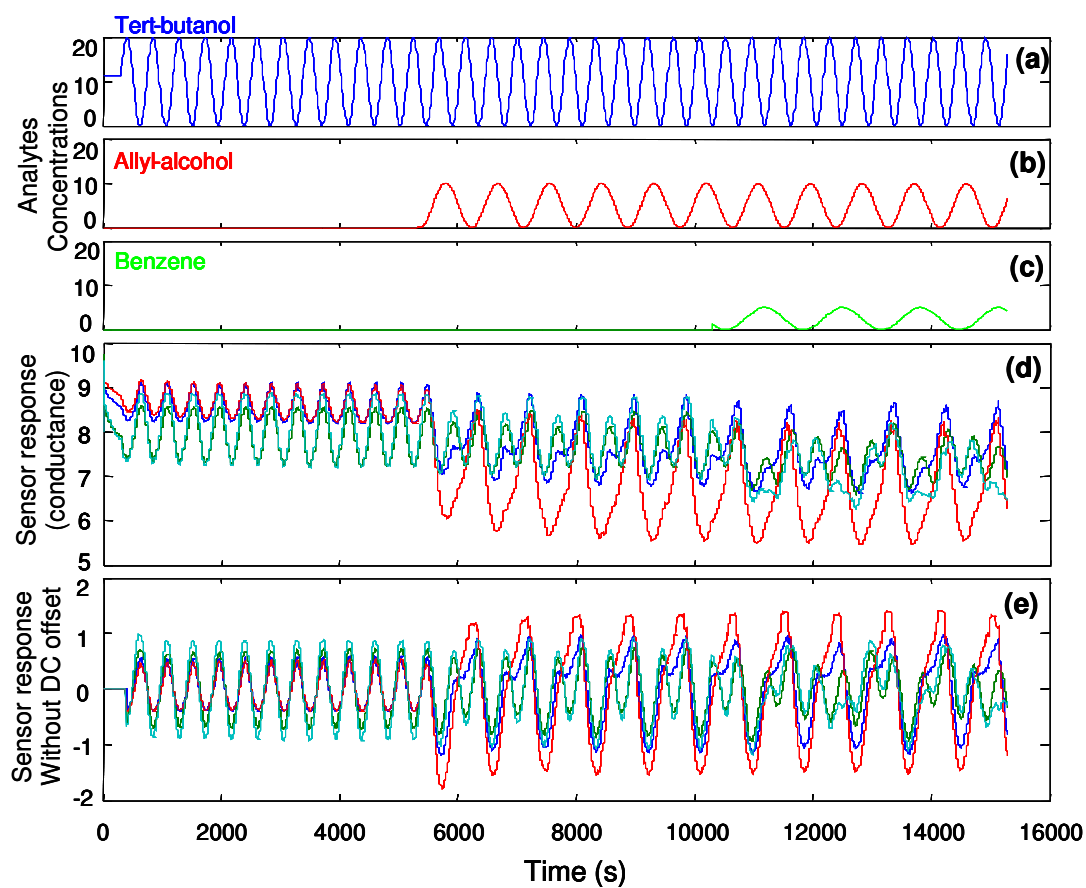


Fig. 95 Novelty detection with two background odors. (a,b,c) Concentration profile of the three analytes presented to the sensor array. Sensor response (d) with and (e) without DC offset.

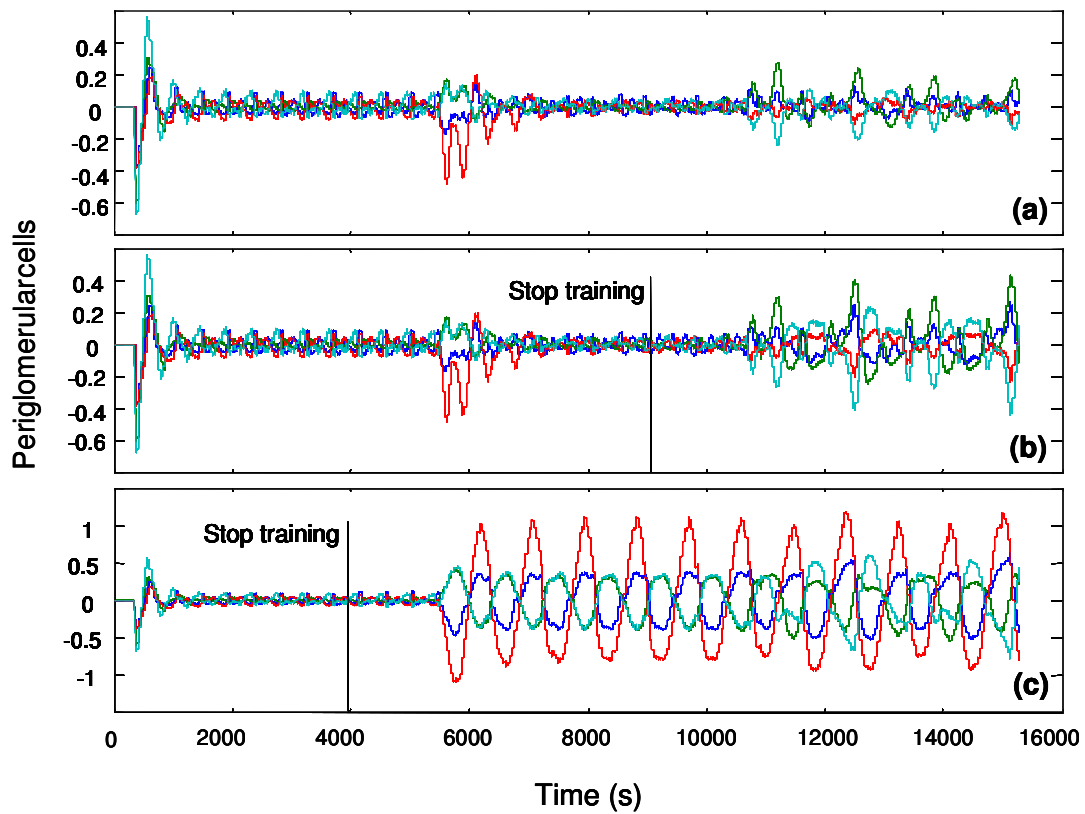


Fig. 96 Output of the KIII model to the experiment in Fig. 95. (a) Periglomerular cell activity with continuous anti-Hebbian training: the KIII is able to detect the introduction of allyl alcohol at  $t=5,300$  s and benzene at  $t=10,300$  s. (b) KIII response when anti-Hebbian adaptation is stopped just before benzene is introduced at time  $t=9,000$  s. (c) KIII response when anti-Hebbian adaptation is stopped just before allyl alcohol is introduced at time  $t=4,000$  s.

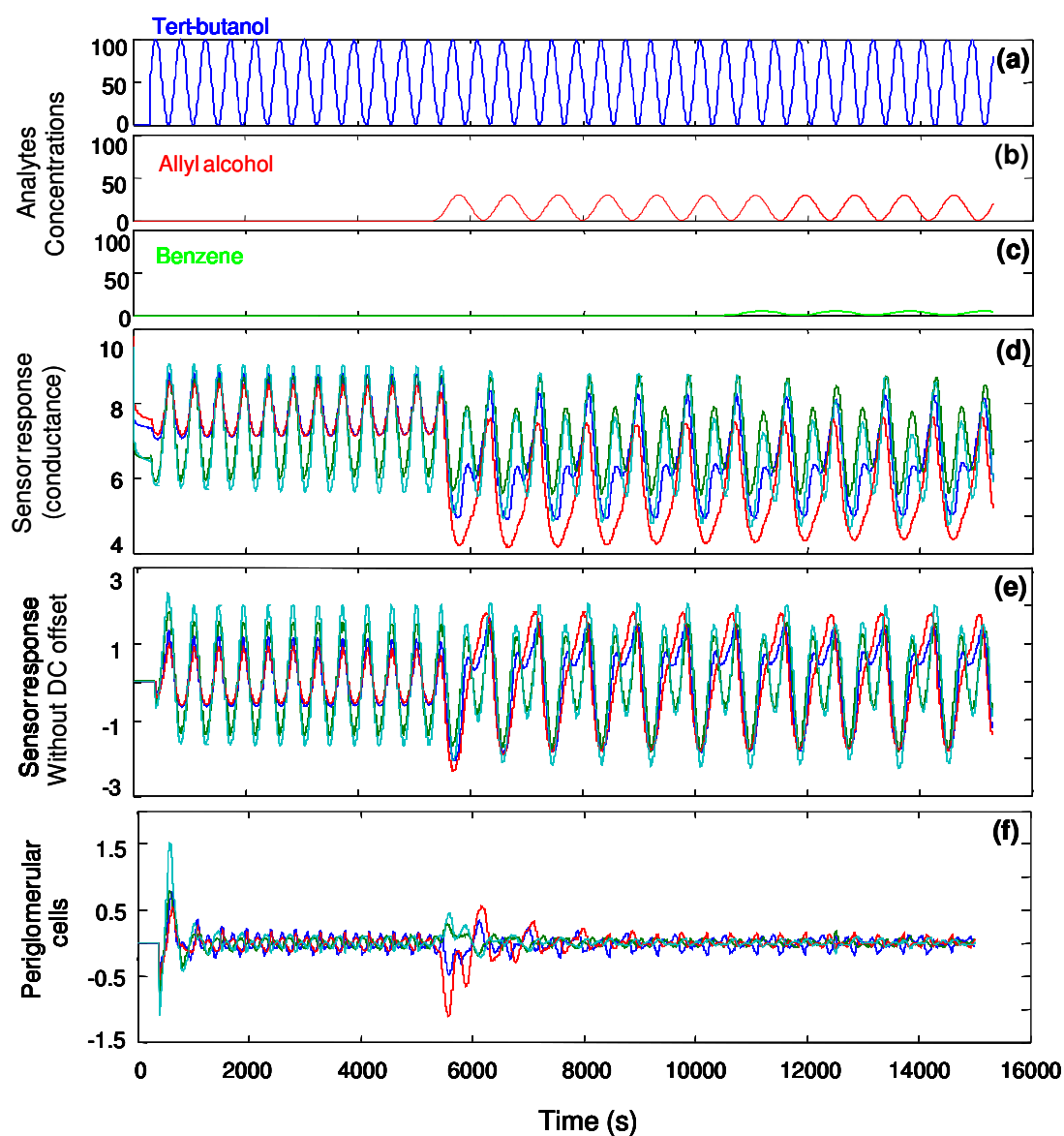


Fig. 97 Exploring the detection limits of the novelty detector. The sensors are exposed to a high concentrations of tert-butanol and allyl alcohol. The goal is to detect the introduction of benzene at very low concentrations. (a,b,c) Concentration profile of the analytes. Response of the four sensors (d) with DC offset and (e) without DC offset. (f) Output of the KIII; the model is unable to detect the introduction of benzene at low concentrations.

The model is able to detect the introduction of allyl alcohol against the strong tert-butanol background, but fails to detect the introduction of benzene in presence of two strong background odors. The concentration of benzene in this experiment is not enough to elicit a significant response in the novelty detector.

### **VIII.6. Discussion**

In this chapter we have presented a mechanism that allows the KIII model to perform novelty detection. The mechanism employs anti-Hebbian learning to adapt lateral connections at the level of periglomerular units. No biological plausibility claims can be made about the proposed model; to the best of our knowledge, anti-Hebbian learning on periglomerular cells has not been reported (or suggested) in the literature.

The novelty-detection model has been characterized on synthetic data, both static and dynamic, and validated on a number of scenarios with experimental data from a MOS sensor array. Our results show that the KIII is able to cancel the sensor response due to fluctuations on humidity, one and two analytes, allowing it to detect the introduction of new odors.

As discussed earlier in this chapter, anti-Hebbian learning allows the KIII model to capture the subspace in which background inputs are embedded, and consequently respond only to inputs outside this subspace (i.e., novel inputs). Thus, this approach can be expected to be successful with gas-sensor-array responses whenever novel odors

introduce different directions of variance in the sensor response from those due to backgrounds. Such is the case for the experimental data employed in this chapter; the input sequence of Fig. 98 generates the sensor output shown in Fig. 99. Note how allyl alcohol and water produce different directions of variance in the sensor response. It is this sensor behavior what allows the novelty-detection model to perform well.

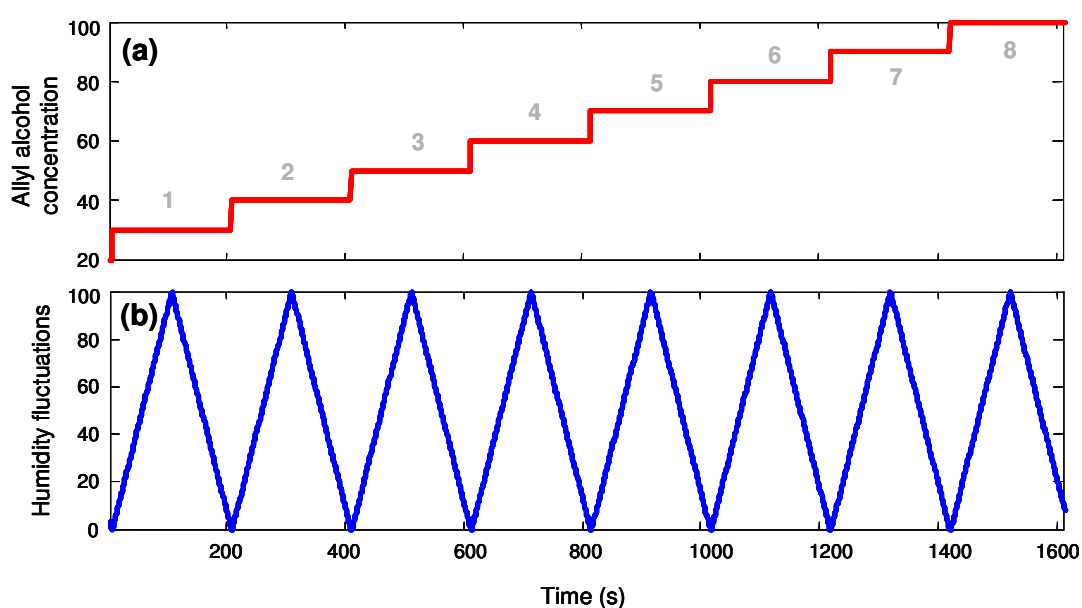


Fig. 98 Variations on humidity and allyl alcohol concentration. (a) Concentration profile of allyl alcohol. (b) Humidity. The concentration of allyl alcohol is increased following a staircase profile from 30% to 100% (denoted by numbers 1-8), whereas the humidity varies from its minimum (0%) to its maximum value (100%) for each level of allyl alcohol concentration.

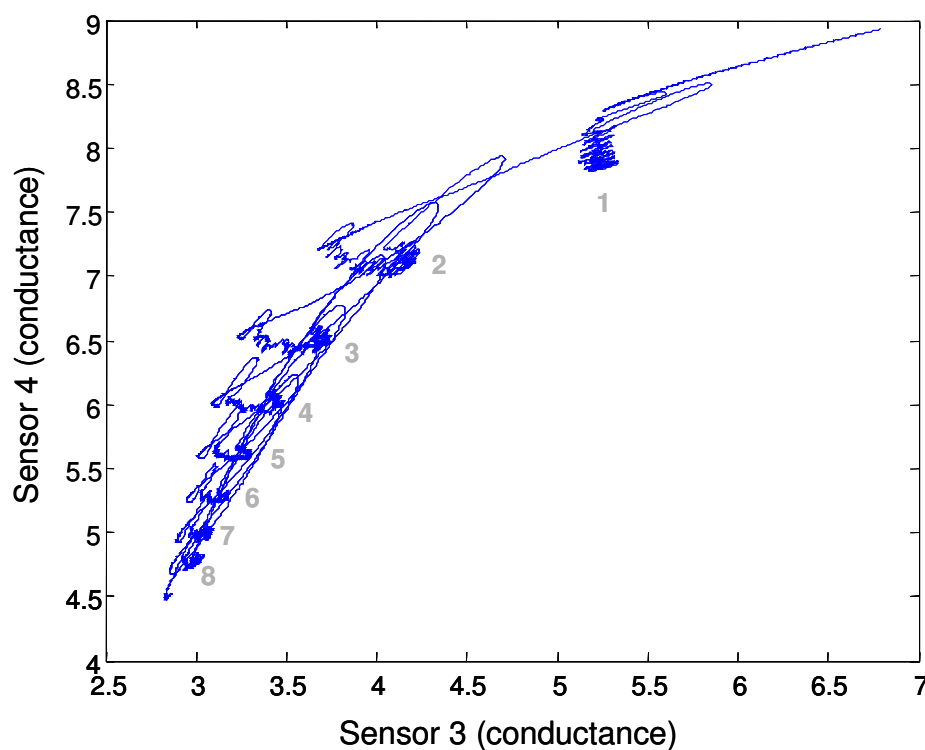


Fig. 99 Response of the MOS sensors to increasing concentrations of allyl alcohol (denoted by numbers 1-8) under fluctuations in humidity.

Fluctuations in the background signals are essential to allow the model to learn the odor-specific hyperplane in which the sensors operate when exposed to the background, as we have just explained. The speed at which the KIII model learns the odor-specific hyperplane depends on the type of the fluctuation. Our experience with the model (not formally reported in this manuscript) indicates that cyclic fluctuations speed up the training process, whereas random fluctuations lead to longer training periods.

It is interesting to note that, in the olfactory system, fluctuations in the odorant stimulus are pervasive due to the respiratory cycles. These fluctuations have been suggested to lead to hierarchical identification of odors (Ambros-Ingerson et al., 1990).

It is worth to notice that the dynamics of the KIII model are not fully exploited by the proposed novelty-detection mechanism, since activity at the periglomerular cell level reflects only the processing performed at that stage. The only influence on the periglomerular cell activity comes in the form of feedback connection anterior olfactory nucleus. This feedback does not seem to play an important role in the computational function: removal of this connection has little impact in the behavior of the novelty detector (not formally reported in this manuscript). One potential approach to engage the complete KIII model, and thus exploit its rich dynamics, would be to detect novelty as a transition between different types of attractors, i.e. from fixed points to limit cycles to strange attractors.

An interesting direction of future work with the KIII novelty detector is to determine the extent to which anti-Hebbian learning can cope with long-term sensor drift. It is known that MOS sensors response drifts over time due to irreversible chemical reactions and poisoning of the sensors. It is possible that the anti-Hebbian learning rule may be able to capture the direction of variance introduced by drift and, therefore, compensate for this effect without losing its ability to detect new odors.

## CHAPTER IX

### CONCLUSIONS

In this dissertation we have taken a dynamical systems approach for processing signals from gas-sensor arrays. We have presented coding and learning mechanisms that have been inspired by processing in the olfactory system. Using this approach, we have tackled the following four computational functions: (i) enhanced memory recall, (ii) contrast enhancement, (iii) background suppression, and (iv) novelty detection.

First, we have proposed a coding scheme that captures temporal information in the KIII model. This scheme is based on the synchrony of oscillations across channels. We have compared this temporal code with the conventional approach based on the amplitude of the oscillations. We have also shown that our approach is more robust in cases with overlapping patterns. These results support a growing body of evidence (Laurent and Davidowich, 1994) indicating that temporal information is key to neural information processing.

Second, we have proposed a Hebbian/anti-Hebbian learning rule that models contrast enhancement in the olfactory bulb. We have shown that the Hebbian/anti-Hebbian rule leads to pattern orthogonalization when used in a linear associative memory. We have also shown that the Hebbian/anti-Hebbian rule provides pattern separability that is

comparable to that obtained with Fisher's Linear Discriminant Analysis (LDA). Considering that LDA is optimal when class-covariances are equal (as is the case in the synthetic problem studied in Chapter VI), it is remarkable that our local learning rule can provide comparable performance. We have shown the contrast-enhancement mechanism to be particularly suitable to process highly collinear patterns, as is the case of MOS gas sensor arrays.

Third, we have combined the local habituation mechanism with the Hebbian/anti-Hebbian rule to achieve background suppression. The Hebbian/anti-Hebbian learning rule reduces the overlap of the stored patterns, thus facilitating the habituation to odors already presented. Using this approach, we have demonstrated background suppression with gas-sensor-array responses to binary and ternary mixtures.

Finally, we have proposed a novelty-detection mechanism based on anti-Hebbian learning of periglomerular lateral connections. This mechanism allows the system to suppress the output activity of the KIII to previous odors, thereby increasing its sensitivity to new ones. Since different odors represent sources of variance along different directions in feature space, anti-Hebbian learning allows the KIII model to reduce its response to inputs along the directions of odor previously presented. This increases the sensitivity of the KIII model to novel odors. We have also demonstrated the ability of our approach to detect novel odors in presence of a strong background.

Three different dynamical behaviors are generated by the KIII model: chaotic, limit cycles, and fixed points. Different parts of the KIII model are responsible for each of these behaviors. Chaotic behavior is due to feedback connections from cortex and anterior olfactory nucleus, whereas limit cycle behavior is generated by the coupled oscillators (KII sets) in the olfactory bulb, and fixed-point behavior is originated at the periglomerular cell layer. By analyzing the role played by the neurodynamics in achieving the computational function, we can determine which components in the KIII model are involved in achieving those functions. In the case of phase coding, odor-discriminatory information is due to the limit-cycle behavior of the model; chaotic activity does not seem to be relevant for this coding scheme. Similarly, oscillatory behavior in the model seems sufficient to perform contrast enhancement and background suppression. In the case of novelty detection, we use the fixed point behavior of the periglomerular cells rather than the limit cycle behavior provided by the olfactory bulb. Thus, it appears that most of the useful dynamics in the KIII have their origin in the oscillatory behavior of the olfactory bulb. The chaotic behavior of the KIII model seems to have little, if any, influence on the computational functions proposed in this dissertation. This should come as no surprise by considering that the phase code and the three learning mechanisms operate when an input is present; in this case, the KIII model displays a near-limit-cycle behavior.

The four mechanisms presented in this dissertation can be grouped according to their computational function:

- temporal coding (Chapter V) and Hebbian/anti-Hebbian learning (Chapter VI) address the issue of *robust recovery of overlapping patterns*;
- habituation (Chapter VII) and anti-Hebbian learning (Chapter VIII) address the problem of *novelty detection*.

The proposed mechanisms have been systematically characterized on synthetic data, and also validated on experimental data from an e-nose prototype built for this purpose. It should be noted that although the mechanisms presented in this dissertation were primarily used for processing of gas-sensor-array signals, their application is not limited to this type of input. For example, the Hebbian/anti-Hebbian rule can be used to improve the separability of any general set of overlapping patterns.

### **IX.1. Future work**

A clear direction of future work is to study other coding and learning mechanisms, or combination of those, to mimic new computational functions for processing gas-sensor-array data. One such learning mechanism is reinforcement learning. Since this type of learning occurs at a higher level rather than at synaptic level, it would complement the learning mechanisms studied in this dissertation. In terms of new coding schemes, our results from Chapter V indicate that those based on temporal aspects of odor information are rather promising. Examples of such codes are latency codes, time to reach the limit cycle; temporal multiplexing, and phase locking (Cariani, 1995). These coding schemes can be studied in conjunction with the proposed learning mechanism to further improve signal processing.

The associative memory function in the KIII model is located in the olfactory bulb. However, it is commonly accepted that memory functions in the olfactory system are located at the olfactory cortex. A possible direction of research, one that would improve the biological realism of the model, is to replace the single KII set that models the prepyriform cortex with a bank of KII sets. Combined with learning mechanisms to establish feed-forward and feedback connection between the olfactory bulb and olfactory cortex, this addition would allow the model to perform odor segmentation and/or hierarchical clustering of odors.

Laurent and Davidowich (1994) have hypothesized that the temporal evolution of the odor code, which increases odor separability, can be thought as a non-linear projection onto a high dimensional space. Principe (2004) has suggested that the temporal evolution of activity of a KII bank can perform a similar projection to improve pattern separability. This represents an additional direction of future work, one that shares parallels with kernel approaches, in which a non-linear projection to a high dimensional space is used to improve pattern separability.

### **IX.1.1. Experimental**

There are several improvements that could be made to the e-nose prototype used for collecting data. Specifically, we suggest the following two additions to provide more precise control of experimental conditions: (1) including a mass-flow controller, and (2)

closed-loop temperature control. We expect the mass-flow controller to provide finer control of the dynamic headspace, thereby further improving the repeatability of the sensor response. The closed-loop temperature control would improve the repeatability of the sensors' operating temperatures, helping compensate for the loss/gain in temperature due to endothermic/exothermic reactions on the sensor surface.

Finally, another direction for future work is optimization of temperature profile to enhance discrimination between different odors at multiple concentrations.

## REFERENCES

- Abe H, Yoshimura T, Kanaya S, Takahashi Y, Miyashita Y, Sasaki SI (1987) Automated odor-sensing system based on plural semiconductor gas sensors and computerized pattern recognition techniques. *Anal Chim Acta* 194:1-9
- Abe H, Kanaya S, Takahashi Y, Sasaki S (1988) Extended studies of the automated odour-sensing system based on plural semiconductor gas sensors with computerized pattern recognition techniques. *Anal Chim Acta* 215:155-168
- Adrian ED (1926) The impulses produced by sensory nerve ending. *J Physiology* 61: 49-72
- Adrian ED (1928) The basis of sensation. WW Norton, New York
- Aishima T (1991a) Aroma discrimination by pattern recognition analysis of responses from semiconductor gas sensor array. *J Agric Food Chem* 39:752-758
- Aishima T (1991b) Discrimination of liquor aromas by pattern recognition analysis of responses from a gas sensor array. *Anal Chim Acta* 243:293-300
- Alligood K, Sauer T, Yorke J (1997) Chaos: an introduction to dynamical systems. Springer-Verlag, New York

- Amamoto T, Yamaguchi T, Matsuura Y, Kajiyama Y (1993) Development of pulse drive semiconductor gas sensor. *Sensors and Actuators B* 13–14:587–588
- Ambros-Ingerson J, Granger R, Lynch G (1990) Simulation of paleocortex performs hierarchical clustering. *Science* 247:1344-1348
- Aonishi T, Kurata K. (1999) Statistical mechanics of an oscillatory associative memory with scattered natural frequencies. *Phys Rev Lett* 82:13-18
- Aoyagi T (1995) Network of neural oscillators for retrieving phase information. *Phys Rev Lett* 74:4075-4082
- Aradi I, Barna G, Érdi P, Gröbner T (1995) Chaos and learning in the olfactory bulb. *International Journal of Intelligent Systems* 10:89-117
- Arbib M, Erdi P, Szentagothai J (1997) *Neural organization: structure, function, and dynamics*. The MIT Press, Cambridge, MA.
- Axel R. (1995). The molecular logic of smell. *Scientific American* 273:154-9
- Ballentine D, Rose-Pehrsson S, Grate J, Wohltjen H (1986). Correlation of surface acoustic wave device coating responses with solubility properties and chemical structure using pattern recognition. *Anal Chem* 58:3058-3066

- Ben-Yishai R, Bar-Or RL, Sompolinsky H (1995) Theory of orientation tuning in visual cortex. *Proc Natl Acad Sci USA* 92:3844-3848
- Bi G, Poo M (2001) Synaptic modification by correlated activity: Hebb's postulate revisited. *Annu Rev Neurosci* 24:139-166
- Bogacz R, Brown MW, Giraud-Carrier C (1999) High capacity neural networks for familiarity discrimination. In: *Proceedings of ICANN'99, Edinburgh, Scotland*, pp 773-778
- Bogacz R, Brown MW, Giraud-Carrier C (2000) Model of familiarity discrimination in the brain – efficiency, speed and robustness. In: *Proceedings Emer. Net Workshop, Celestica, United Kingdom*, pp 23-26
- Brennan PA, Keverne EB (1997) Neural mechanisms of mammalian olfactory learning. *Progress in Neurobiology* 51:457-481
- Buck L, Axel R (1991) A novel multigene family may encode odorant receptors: a molecular basis for odor recognition. *Cell* 65:175-187
- Cariani P (1995) As if time really mattered: temporal strategies for neural coding of sensory information. *Communication and Cognition-Artificial Intelligence* 12:157-219

- Chang H, Freeman W, Burke B (1998a) Local homeostasis stabilizes a model of the olfactory system globally in respect to perturbations by input during pattern classification. *International Journal of Bifurcations and Chaos* 8(11):2107-2123
- Chang H, Freeman W, Burke B (1998b) Biologically modeled noise stabilizing neurodynamics for pattern recognition. *International Journal of Bifurcations and Chaos* 8(2):321-345
- Chang H, Freeman W, Burke B (1998c) Optimization of the olfactory model in software to give  $1/f$  power spectra reveals numerical instabilities in solutions governed by aperiodic (chaotic) attractors. *Neural Networks* 11:449-466
- Chang S, Tamiya E, Karube I, Sato M, Masuda Y (1991) Odorant sensor using lipid-coated SAW resonator oscillator. *Sensors and Actuators B* 5:53-58.
- Clifford P, Tuma D (1983) Characteristic of semiconductor gas sensors part I: steady state gas response. *Sensors and Actuators* 3:233-254
- Clussnitzer U, Quarder S, Otto M (2001) Interpretation of analytical patterns from the output of chaotic dynamical memories. *Fresenius J Anal Chem* 369:298-703.
- Cohen MA, Grossberg S (1983) Absolute stability and global pattern formation and parallel memory storage by competitive neural networks. *IEEE Trans Syst Man Cybern* 13:815-826

- Corcoran P, Lowery P (1995) Neural processing in an electronic odour sensing system. In: Proceedings of the 4th international conference on artificial neural networks, Churchill College, Cambridge, UK, pp 415-120
- Crook P, Hayes G (2001) A robot implementation of a biologically inspired method for novelty detection. In: Proceedings of towards intelligent mobile robots conference, Manchester, UK, pp 52-57
- Dalton P (2000) Psychophysical and behavioral characteristics of olfactory adaptation. *Chemical Senses* 25:487-492
- Davide F, Natale C, D'Amico A (1994) Self-organising multisensor systems for odour classification: Internal categorization, adaptation and drift rejection. *Sensors and Actuators B* 18-19:244-258
- Davis JL, Eichenbaum H (1991) *Olfaction: a model system for computational neuroscience*, MIT Press, Cambridge, MA
- DeCoste MC, Burl A (2001) Support vector machines and kernel fisher discriminants: a case study using electronic nose data. In: Fourth workshop on mining scientific datasets, San Francisco, pp 68-73
- Doty R (1991) Olfactory system. In: *Smell and taste in health and disease*, Raven Press, New York, pp 175-203

- Duda R, Hart P, Stork D (2001) Pattern classification. John Wiley and Sons, New York
- Dutta R, Hines E, Gardner J, Kashwan K, Bhuyan M (2003) Tea quality prediction using a tin oxide-based electronic nose: an artificial intelligence approach. *Sensors and Actuators B* 94:228–237.
- Eckmann J, Ruelle D (1985) Ergodic theory of chaos and strange attractors. *Reviews of Modern Physics* 57(3):617-656.
- Egan D (1975) Signal detection theory and ROC analysis. Academic Press, New York.
- Eisenberg J, Freeman WJ, Burke B (1989). Hardware architecture of a neural network model simulating pattern recognition by the olfactory bulb. *Neural Networks* 2:315-325.
- Ema K, Yokohama M, Nakamoto T, Moriizumi T (1989) Odour-sensing system using a quartz-resonator sensor array and neural network pattern recognition. *Sensors and Actuators* 18:291-296.
- Figaro (1996) Figaro Engineering, Inc., Osaka, Japan.
- Fletcher M, Wilson D (2003) Olfactory bulb mitral-tufted cell plasticity: odorant-specific tuning reflects previous odorant exposure. *J Neurosci* 23:6946-6955

- Freeman W (1975) Mass action in the nervous system: examination of neurophysiological basis of adoptive behavior through the EEG. Academic Press, New York
- Freeman W (1978) Simulation of chaotic EEG patterns with a dynamic model of the olfactory system. *Biological Cybernetics* 56:139-150
- Freeman W (1988) Strange attractors that govern mammalian brain dynamics shown by trajectories of encephalographic (EEG) potential. *IEEE Trans. Circuits and Systems*, 35:781-183.
- Freeman W (1991) The physiology of perception. *Scientific American* 264(2):78-85
- Freeman W (1992) Tutorial on neurobiology: from single neurons to brain chaos. *Int J Bifurc Chaos* 2(3):451-482
- Freeman W (1995) The creation of perceptual meanings in cortex through chaotic itinerancy and sequential state transitions induced by sensory stimuli. In: Kruse P, Stadler M, (Eds), *Ambiguity in mind and nature*. Springer series in synergetics, Springer, New York, pp 421-437
- Freeman W (1999) Olfactory system: odorant detection and classification. In Amit D, Parisi G (Eds.) *Building blocks for intelligent systems: brain components as elements of intelligent function*, chap 3. Academic Press, New York

- Freeman W, Chang H, Burke B, Rose P, Badler J (1997) Taming chaos: stabilization of aperiodic attractors by noise. *IEEE Trans. Circuits and Systems* 44(10):989-996
- Freeman W, Kozma R, Otto M (2000) Biologically motivated pattern recognition using chaotic dynamical memories. Presented at the Research Society for Nonlinear Theory and Its Applications (NOLTA). Dresden, Germany.
- Freeman W, Yao Y, Burke B (1988) Central pattern generating and recognizing in olfactory bulb: a correlation learning rule. *Neural Networks* 1:277-288
- Gardner J (1991) Detection of vapours and odours from a multisensor array using pattern recognition. Part 1: Principal component and cluster analysis. *Sensors and Actuators B* 4:109-115
- Gardner J, Barlett P (1999) *Electronic noses: principles and applications*. Oxford University Press, Oxford, UK
- Gardner J, Hines E, Tang H (1992) Detection of vapours and odours from a multisensor array using pattern recognition techniques. Part 2: Artificial neural networks. *Sensors and Actuators B* 9:9-15
- Gardner J, Hines E, Wilkinson M (1990) Application of artificial neural networks to an electronic olfactory system. *Meas Sci Tech* 1:446-451

- Gardner J, Shurmer H, Tan T (1992) Application of an electronic nose to the discrimination of coffees. *Sensors and Actuators B* 6:71-75
- Grossberg S (1988) Nonlinear neural networks: principles, mechanisms, and architectures. *Neural Networks* 1:17-61
- Gutierrez-Osuna R (2002) Pattern analysis for machine olfaction: a review. *IEEE Sensor Journal* 2(3):189-202
- Gutierrez-Osuna R Gutierrez-Galvez A (2003) Habituation in the KIII olfactory model with chemical sensor arrays. *IEEE Trans Neural Networks* 14(6):1565-1568
- Gutierrez-Osuna R, Gutierrez-Galvez A, Powar N (2003) Transient response analysis for temperature modulated chemoresistors. *Sensors and Actuators B* 93: 57–66
- Gutierrez-Osuna R, Korah S, Perera A (2001) Multi-frequency temperature modulation for metal-oxide gas sensors. In: *Proceedings of the eighth international symposium on olfaction and electronic nose*. Washington, DC, pp 25-30
- Gutierrez-Osuna R, Powar NU (2003) Odor mixtures and chemosensory adaptation in gas sensor arrays. *International Journal on Artificial Intelligence Tools* 12(1):1-16
- Haberly, L. B. (2004) Olfactory cortex. In: G. Shepherd, (Eds.), *The synaptic organization of the brain* (pp. 317-345). Oxford University Press, Oxford

- Harris T (1993) Neural network in machine health monitoring. *Professional Engineering*, July/August, pp 23-28
- Haykin S (1999) *Neural networks: a comprehensive foundation*. Prentice Hall, Upper Saddle River, NJ.
- Hebb DO (1949) *The organization of behavior*. Wiley, New York
- Heilig A, Barsan N, Weimar U, Schweizer-Berberich M, Gardner JW, Gopel W (1997) Gas identification by modulating temperatures of SnO<sub>2</sub>-based thick film sensors. *Sensors and Actuators B* 43:45–51
- Hendin O, Horn D, Hopfield JJ, (1994) Decomposition of a mixture of signals in a model of the olfactory bulb. *Proc. Natl. Acad. Sci.* 91(13):5942-5946
- Hertz J (1995) Computing with attractors. In: Arbib, M.A. (Eds.), *Handbook of brain theory and neural networks*. MIT Press, Cambridge, MA, pp 230-234
- Hildebrand JG, Shepherd GM (1997) Mechanisms of olfactory discrimination: converging evidence for common principles across phyla. *Annu Rev Neurosci* 20:595-631.
- Hiranaka Y, Colbow K, Consadori H (1992) Gas-dependent response in the temperature transient of SnO<sub>2</sub> gas sensors. *Sensors and Actuators B* 9:177–182

- Hirsch M, Baird B (1995) Computing with dynamic attractors in neural networks. *Biosystems* 3:173-195
- Hoffheins B, Lauf R (1988) Gas sensor arrays for olfactory analysis: Issues and opportunities In: *Proc Sensor Expo, Chicago, IL* pp 205-213
- Hoffman JD (1992) *Numerical methods for engineers and scientists*. McGraw-Hill, New York
- Hopfield JJ (1982) Neural networks as physical systems with emergent computational abilities. *Proc Natl Acad Sci USA* 79:2554-5258
- Hopfield JJ (1984) Neurons with graded response have collective computational properties like those of two-state neurons. *Proc Natl Acad Sci USA*, 81:3088-3092
- Hoppensteadt FC, Izhikevich EM (2000) Pattern recognition via synchronization in phase-locked loop neural networks. *IEEE Trans Neural Networks* 11:734-738
- Ide J, Nakamoto T, Moriizumi T (1993) Development of odour-sensing system using an auto-sampling stage. *Sensors and Actuators B* 13-14:351-354
- Ikegami A, Kaneyasu M (1985) Olfactory detection using integrated sensor. In: *Proceedings International Conference on Solid-state Sensors and Actuators, Philadelphia*, pp 136-139

- Ikohura K, Watson J (Eds.) (2000) The stannic oxide gas sensor: principles and applications. CRC Press, Boca Raton, FL
- Iwamoto M (1989) Adsorption and desorption of gases on metal oxides and their sensor. In: Proceedings of 34<sup>th</sup> meeting of Japanese Association of Chemical Engineers, Japan, pp 23-25
- Kaneko K, Tsuda I (2001) Complex systems: chaos and beyond – a constructive approach with applications in life sciences. Springer-Verlag, Berlin
- Kaneyasu M, Ikegami A, Arima H, Iwanaga S (1987) Smell identification using a thick-film hybrid gas sensor. IEEE Com 10:267-273
- Kato Y, Yoshikawa K, Kitora M (1997) Temperature-dependent dynamic response enables the qualification and quantification of gases by a single sensor. Sensors and Actuators B 40:33–37
- Kay L, Lancaster L, Freeman W (1996) Reafference and attractors in the olfactory system during odor recognition. International Journal of Neural Systems 7:489-495
- Kohonen T, Oja E (1976) Fast adaptive formation of orthogonalizing filters and associative memory in recurrent networks of neuron-like elements. Biological Cybernetics 21:85-95

- Kojima K, Ito K (1998) Dynamical learning of neural networks based on chaotic dynamics. In: Proc. IEEE International Conference on Systems, Man, and Cybernetics 4:3674 – 3679
- Kozma R (2003) On the constructive role of noise in stabilizing itinerant trajectories on chaotic dynamical systems. *Chaos* 11(3):1078- 1089
- Kozma R, Ankaraju P (2003) Learning spatial navigation using chaotic neural network model. In: Proc. International Joint Conference on Neural Networks IJCNN'2003, Portland, OR, pp 1476-1479
- Kozma R, Freeman W (2000) Encoding and recall of noisy data as chaotic spatio-temporal memory patterns in the style of the brains. In: Proc. International Joint Conference on Neural Networks, Como, Italy, pp 5033-5036
- Kozma R, Freeman W (2001) Chaotic resonance-methods and applications for robust classification of noisy and variable patterns. *Int J Bifurc Chaos* 11:1607-1629
- Kozma R, Freeman W (2003) Basic principles of the KIV model and its application to the navigation problem. *Journal of Integrative Neuroscience* 2(1):125-145
- Kozma R, Freeman W, Erdi P (2003) The KIV model – nonlinear spatio-temporal dynamics of the primordial vertebrate forebrain. *Neurocomputing* 55-56:819-826

- Kozma R, Kasabov N, Swope J, Williams M (1997) Combining neuro-fuzzy and chaos methods for intelligent time series analysis - Case study of heart rate variability. In: Proc. IEEE Int. Conf. on Systems, Man and Cybernetics. Orlando, FL, pp 3025-3029
- Kozma R, Voicu H, Wong D, Freeman W (2003) A dynamical neural network algorithm for autonomous learning and navigation control in unknown environment. In: Proc. IEEE International Conference on Systems, Man, and Cybernetics. Washington, DC, pp 1232-2137
- Kunt TA (1997) Dynamic modeling and optimization of micro-hotplate chemical gas sensors. Ph.D. dissertation, University of Maryland, College Park, MD.
- Kunt TA, McAvoy TJ, Cavicchi RE, Semancik S (1998) Optimization of temperature programmed sensing for gas identification using micro-hotplate sensors. *Sensors and Actuators B* 53:24–43
- Kuramoto Y (1984) Chemical oscillations, waves, and turbulences. Springer, Berlin.
- Kuzmina M, Manykin E, Surina I (2001) Recurrent associative memory network of nonlinear coupled oscillators. In: Proceedings International Conference on Artificial Neural Networks (ICANN), Vienna, Austria, pp 110-116

- Laurent G, Stopfer M, Friedrich R, Ravinovich M, Volkoskii A, Abarbanel H. (2001) Odor processing as an active dynamical process: experiments, computation and theory. *Annu Rev Neurosci* 2001, 24, 263-297.
- Laurent, G. (1997). Olfactory processing: maps, time and codes. *Current Opinion in Neurobiology*, 7, 547-553.
- Laurent, G. (2002). Olfactory network dynamics and the coding of multidimensional signals. *Nature Reviews Neuroscience*, 3, 884-895.
- Laurent, G. and Davidowich, H. (1994). Encoding of olfactory information with oscillating neural assemblies. *Science*, 265, 1872-1875.
- LeCun Y, Boser B, Denker JS, Henderson D, Howard RE, Hubbard W, Jackel LD (1990) Handwritten digit recognition with a back-propagation network. In: *Proc. Advances in Neural Information Processing Systems*. Denver, CO, pp 396-404
- Lee AP, Reedy BJ (1999) Temperature modulation in semiconductor gas sensing. *Sensors and Actuators B* 60:35–42
- Li H, Kozma R (2003) A dynamical neural network method for time series prediction using the KIII model. In: *International Joint Conference on Neural Networks* Portland, OR, pp 347-352

- Li Z, Hertz J (2000) Odour recognition and segmentation by a model olfactory bulb and cortex. *Network Comput Neural Syst* 11:83–102
- Li Z, Hopfield JJ (1989) Modeling the olfactory bulb and its neural oscillatory processings. *Biol Cybern* 61:379-392
- Liljestrom H (1995) Autonomous learning with complex dynamics. *International Journal of Intelligent Systems* 10:119-153
- Lippmann RP (1987) An introduction to computing with neural nets. *IEEE ASP Magazine* 4:22-61
- Llobet E, Ionescu R, Al-Khalifa S, Brezmes J, Vilanova X, Correig X, Barsan N, Gardner JW (2001) Multi-component gas mixture analysis using a single tin oxide sensor and dynamic pattern recognition. *IEEE Sensors Journal* 1(3):207–213.
- Lourenço C, Babloyantz A, Hougardy M (2000) Pattern segmentation in a binary/analog world: unsupervised learning versus memory storing. *Neural Networks* 13:17-89
- Lundström I, Erlandsson R, Frykman U, Hedborg E, Spetz A, Sundgren H (1991) Artificial 'olfactory' images from a chemical sensor using a light-pulse technique. *Nature* 352:47-50
- Ma M, Shepherd GM (2000) Functional mosaic organization of mouse olfactory receptor neurons. *Proc. Natl. Acad. Sci. USA* 97(93):12869-12874

- MacLeod K, Laurent G (1996) Distinct mechanisms for synchronization and temporal patterning of odor-encoding neural assemblies. *Science* 274:976-979
- Mahowald M, Mead C (1991) The silicon retina. *Scientific American* 264:76-82
- Malnic B, Hirono J, Sato T, Buck L (1999) Combinatorial receptor codes for odors. *Cell* 96:713–723
- Mark J, Allcock H, Lampe F (1990) Contemporary polymer chemistry. Prentice Hall, New York
- Mizokawa Y (1977) ESR study of adsorbed oxygen on tin dioxide. *Japanese Journal of Applied Physics* 46:580-610
- Molter C, Salihoglu U, Bersini H (2005) Learning cycles brings chaos in continuous hopfield networks. In: Proceedings of the IJCNN conference. Montreal, Canada, pp 1550-1556
- Mori K, Nagao H, Yoshihara Y (1999) The olfactory bulb: coding and processing of odor molecule information. *Science* 286:711-715
- Morrison S (1977) The chemical physics of surfaces. 1<sup>st</sup> edition, Plenum Press, New York

- Mosley P, Williams D, Norries O (1988) Electrical conductivity and gas sensitivity of some transition metal tantalates. *Sensors and Actuators* 14:79-85
- Mountcastle V (1998) *The cerebral cortex*. Harvard University Press, Cambridge, MA
- Muramatsu H, Tamiya E, Karube I (1989) Detection of odorants using lipid-coated piezoelectric crystal resonators. *Anal Chim Acta* 225:399-408
- Nagle HT, Schiffman SS, Gutierrez-Osuna R (1998) The how and why of electronic noses. *IEEE Spectrum*, September:22-34.
- Nakamoto T, Fukuda A, Moriizumi T, Asakura Y. (1991) Improvement of identification capability in an odor-sensing system. *Sensors and Actuators B*, 3:221-226
- Nakamoto T, Fukuda A, Moriizumi T (1993) Perfume and flavor identification by odor-sensing system using quartz-resonator sensor array and neural-network pattern recognition. *Sensors and Actuators B* 10:85-91
- Nakamoto T, Fukunishi K, Moriizumi T (1990) Identification capability of odor sensor using quartz-resonator array and neural-network pattern recognition. *Sensors and Actuators B* 1:473-476
- Nakamoto T, Takagi H, Utsumi S, Moriizumi T (1992) Gas/odor identification by semiconductor gas-sensor array and an analog artificial neural-network circuit. *Sensors and Actuators B*, 8:181-186

- Nakata S, Akakabe S, Nakasuji M, Yoshikawa K (1996) Gas sensing based on a non-linear response: discrimination between hydrocarbons and quantification of individual components in a gas mixture. *Anal Chem*, 68:2067–2072
- Nakata S, Kaneda Y, Nakamura H, Yoshikawa K (1991) Detection and quantification of CO gas based on the dynamic response of a ceramic sensor. *Chem Lett* 1505–1508.
- Nakata S, Nakamura H, Yoshikawa K (1992) New strategy for the development of a gas sensor based on the dynamic characteristics: principle and preliminary experiment. *Sensors and Actuators B* 8:187–1892
- Nakata S, Ozaki E, Ojima N (1998) Gas sensing based on the dynamic non-linear responses of a semiconductor gas sensor: dependence on the range and frequency of a cyclic temperature change. *Anal Chim Acta* 361: 93–100
- Nakata S, Yoshikawa K (1996) Non-linear dynamics in chemical assembly. *Trends Chem Phys* 4: 23–58
- Newton I (1999) *The principia : mathematical principles of natural philosophy*, University of California Press, Berkeley, CA
- Nishikawa T, Lai Y, Hoppensteadt F (2004) Capacity of oscillatory associative-memory networks with error-free retrieval. *Phys. Rev. Lett.* 92:10-19

- Ohnishi M, Ishibashi T, Kijima Y, Ishimoto C, Seto J (1992). A molecular recognition system for odorants incorporating biomimetic gas-sensitive devices using Langmuir-Blodgett films. *Sensors and Materials* 1:53-60
- Okahata Y, En-na G, Ebata H (1989) Synthetic chemoreceptive membranes. Sensing bitter or odorous substances on a synthetic lipid multibilayer film by using quartz-crystal microbalances and electric responses. *Anal. Chem.* 62:1431-1438
- Okahata Y, Shimizu O (1987) Olfactory reception on a multilayer-coated piezoelectric crystal in a gas phase. *Langmuir* 3(6):1171-1172
- Otto M, Quarder S, Claußnitzer U, Lerchner J (2000) A nonlinear dynamic system for recognizing chemicals based on chemical sensors and optical spectra. In: *Proceedings of the World Multiconference on Systemics, Cybernetics and Informatics*. Orlando, FL, pp 413-418
- Ozturk MC, Principe JC, Davis B, Erdogmus D (2003) Simulation of the freeman model of the olfactory cortex: a quantitative performance analysis for the DSP approach. In: *Proceedings Intl Joint Conf on Neural Networks*. Portland, OR, pp 332-336
- Pearce TC (1997a) Computational parallels between the biological olfactory pathway and its analogue. The electronic nose: Part I. Biological olfaction. *BioSystems* 41:43-67

- Pearce TC (1997b) Computational parallels between the biological olfactory pathway and its analogue. The electronic nose: Part II. Sensor-based machine olfaction. *BioSystems* 41:69-90
- Pearce TC, Schiffman SS, Nagle HT, Gardner J (eds) (2003) Handbook of machine olfaction. Wiley-VCH, Weinheim, Germany
- Pearce TC, Verschure PF, White J, Kauer JS (2001) Robust stimulus encoding in olfactory processing: hyperacuity and efficient signal transmission. In: S. Wermter, J. Austin and D. Willshaw (eds), Emergent neural computation architectures based on neuroscience, Springer-Verlag, New York, pp 123-147
- Perera A (2003) Smart instrumentation based on gas sensor arrays: Novel hardware concepts and algorithmic issues. Ph. D. dissertation. Universitat de Barcelona, Spain.
- Perera A, Papamichail N, Barsan N, Weimar U, Marco S (2003) On-line event detection by recursive dynamic principal component analysis and gas sensor arrays under drift conditions. *Proceedings of IEEE Sensors*. Toronto, Canada, 2:860-865
- Perez-Lisboa MO, Barriga-Puente de la Vega M, Ramirez-Fernandez FJ (1999) Study of sensitivity and selectiveness of gas sensor array to periodic stimuli. In: *Proceedings of the International Conference on Microelectronics and Packaging*. Campinas, Spain, pp 267–269

- Persaud K, Dodd G (1982) Analysis of discrimination mechanisms in the mammalian olfactory system using a model nose. *Nature* 299:352
- Principe J (2004): personal communication. Symposium on Intentional Dynamical Systems. Memphis, TN
- Principe J, Euliano N, Lefebvre W (1999) *Neural and adaptive systems*. John Wiley and Sons, New York
- Provost F, Fawcet T (1997) Analysis and visualization of classifier performance: comparison under imprecise class and cost distributions. In *Proceedings of the Third International Conference of Knowledge Discovery and Data Mining*, Huntington Beach, CA, pp 79-85
- Quarder S, Claussnitzer U, Otto M (2001) Using singular-value decomposition to classify spatial patterns generated by a nonlinear dynamic model of the olfactory system. *Chemom Int Lab Systems* 59:45-51
- Quoy M (1995) Hebbian learning in chaotic neural networks. In: *Proc. Computation and Neural Systems Meeting (CNS)*. Monterrey, CA, pp 45-51
- Raman B, Gutierrez-Galvez A, Perera-Lluna A, Gutierrez-Osuna R (2004) Sensor-based machine olfaction with a neurodynamic model of the olfactory bulb. In: *Proceedings*

of the 2004 IEEE/RSJ Intl Conference on Intelligent Robots and Systems. Sendai, Japan pp 55-59

Raman B, Gutierrez-Osuna, R (2004) Chemosensory processing in a spiking model of the olfactory bulb: chemotopic convergence and center surround inhibition. In: Proc. NIPS. Vancouver, BC, pp. 13-16

Ratton L, Kunt T, McAvoy T, Fuja T, Cavicchi R, Semancik S (1997) A comparative study of signal processing techniques for clustering microsensor data (a first step towards an artificial nose). *Sensors and Actuators B* 41(1-3):105-120.

Recce M (2001) Encoding information in neuronal activity. In: Mass W, Bishop CM (eds) *Pulsed Neural Networks*. MIT Press, Cambridge, MA, pp. 111-131

Ressler K, Sullivan S, Buck L (1994) Information coding in the olfactory system: evidence for a stereotyped and highly organized epitope map in the olfactory bulb. *Cell* 79:1245-1255

Rodriguez-Mendez ML, Arrieta A, Parra V, Bernal A, Vegas A, Villanueva S, Gutierrez-Osuna R, Saja JA (2004) Fusion of three sensory modalities for the multimodal characterization of red wines. *IEEE Sensors Journal* 4(3):348-354

- Rose-Pehrsson S, Grate J, Ballentine D, Jurs P (1988) Detection of hazardous vapors including mixtures using pattern recognition analysis of responses from surface acoustic wave devices. *Anal. Chem.* 60:2801-2811
- Rose-Pehrsson SL, Grate JW (1993) A surface acoustic wave sensor array for trace organic vapor detection using pattern recognition analysis. In: *Proceedings International Conference on Monitoring of Toxic Chemicals and Biomarkers*. Washington DC, pp 299-311
- Rowe DL (2002) Dynamic neural activity as chaotic itinerancy or heteroclinic cycles? *The Behavioral and Brain Sciences* 24:811-812
- Russell E, Chiang L, Braatz R (2000). *Data driven techniques for fault detection and diagnosis in chemical processes*. Springer, London
- Ryan J, Lin MJ, Mikkilainen R (1998) Intrusion detection with neural networks. In: Jordan M, (eds), *Advances in neural information processing systems* 10:943-949, MIT Press, Cambridge, MA
- Sakuraba Y, Nakamoto T, Moriizumi T (1990). New method of learning vector quantization using fuzzy theory. *Trans Inst Electron Comm Eng*, J73D-II, 11:1863-1871

- Samsonovich A, McNaughton B L (1997) Path integration and cognitive mapping in a continuous attractor neural model. *J Neurosci* 17:5900-5920
- Santos JP, Fernandez MJ, Fontecha JL, Lozano J, Aleixandre M, Garcia M, Gutierrez J, Horrillo MC (2005) SAW sensor array for wine discrimination. *Sensors and Actuators B* 107:291–295
- Sears WM, Colbow K, Consadori F (1989a) General characteristics of thermally cycled tin oxide gas sensors. *Semicond Sci Technol* 4:351–359
- Sears WM, Colbow K, Consadori F (1989b) Algorithms to improve the selectivity of thermally cycled tin oxide gas sensors. *Sensors and Actuators B* 19:333–389
- Seung S (1996) How the brain keeps the eyes still. *Proc Natl Acad Sci USA* 93:13339-44
- Shepherd G (1994) Discrimination of molecular signals by the olfactory receptor. *Neuron* 13:771-790
- Shepherd G, Greer CA (2004) Olfactory bulb. In: Shepherd G (eds), *The synaptic organization of the brain*. Oxford University Press, Oxford, pp. 159-204
- Shepherd GM (1987) A molecular vocabulary for olfaction. *Annals of the New York Academy of Sciences* 510:98-10

- Shurmer H, Gardner J, Chan H (1989) The application of discrimination techniques to alcohols and tobaccos using tin-oxide sensors. *Sensors and Actuators* 18:361-371
- Shurmer H, Gardner J, Corcoran P (1990) Intelligent vapour discrimination using a composite 12-element sensor array. *Sensors and Actuators B* 1;256-260
- Singer W, Gray CM (1995) Visual feature integration and the temporal correlation hypothesis. *Ann Rev Neuroscience* 18:555-586
- Spors H, Grinvald A (2002) Spatio-temporal dynamics of odor representations in the mammalian olfactory bulb. *Neuron* 34(2):301-315
- Stopfer M, Bhagavan S, Smith B, Laurent G (1997) Impaired odor discrimination on desynchronization of odor-encoding neural assemblies. *Nature* 390:70-74
- Strogatz SH.(1994) *Nonlinear dynamics and chaos*. Addison-Wesley, New York.
- Strogatz SH (2000) From Kuramoto to Crawford: Exploring the onset of synchronization in populations of coupled oscillators. *Phys D* 143:1-20
- Thorpe SJ, Delorme A, Van Ruelen R (2001) Spike-based strategies for rapid processing. *Neural Networks* 14:715-725
- Tsuda I (1992) Dynamic link of memory-chaotic memory map in non-equilibrium neural networks. *Neural Networks* 5:313-326

- Tsuda I (1996) A new type of self-organization associated with chaotic dynamics in neural networks. *International Journal of Neural Systems* 7:451-459
- Van Rullen R, Thorpe SJ (2000) Is it a bird? Is it a plane? Ultra-rapid visual categorization of natural and artificial objects. *Perception* 30:655-668
- van Trees HL (1968) *Detection, estimation and modulation theory, Part I*, Wiley, New York
- Vassar R, Chao SK, Sitcheran R, Nuñez JM, Vosshall LB, Axel R (1994) Topographic organization of sensory projections to the olfactory bulb. *Cell* 79:981-991
- Wamsley A, Haswell S, Metcalfe E (1991) Evaluation of chemometric techniques for the identification and quantification of solvent mixtures using thin-film metal oxide sensor array. *Anal. Chem.* 250:257-264
- Wang D (1998) Habituation. In: M.A. Arbib (Eds.), *The handbook of brain theory and neural networks*. MIT Press, Cambridge, MA, pp 441-444
- Wang D (1999) Object selection based on oscillatory correlation. *Neural Networks* 12:579-592
- Wang D, Bumann J, von der Malsburg C (1990) Pattern segmentation in associative memory. *Neural Computation* 2(1):94-106

- Wang L, Chan KL (2002) Learning kernel parameters by using class separability measure. In: 6th Kernel Machine Workshop on Learning (in conjunction with NIPS Conference), Whistler, Canada, pp 122-140
- Wang X, Fang J, Carey, Yee S (1993) Mixture analysis of organic solvents using nonselective and nonlinear gas sensors with artificial neural networks. *Sensors and Actuators B* 13-14:455-477
- Wang X, Yee S, Carey P (1993) An integrated array of multiple thin-film metal oxide sensors for quantification of individual components in organic vapor mixtures. *Sensors and Actuators B* 13-14:458-461
- White J, Dickinson TA, Walt DR, Kauer JS (1998) An olfactory neural network for vapor recognition in an artificial nose. *Biol Cybern* 78:245-251
- White J, Hamilton KA, Neff SR, Kauer JS (1992) Emergent properties of odor information coding in a representational model of the salamander olfactory bulb. *J Neurosci*, 12:1772-1780
- White J, Kauer JS (1999) Odor recognition in an artificial nose by spatio-temporal processing using an olfactory neuronal network. *Neurocomputing* 26-27:919-924
- Wiener N (1958) *Nonlinear problems in random theory*, MIT Press, Cambridge, MA
- Wiener N (1961) *Cybernetics*. 2<sup>nd</sup> edition, MIT Press, Cambridge, MA

- Wijk RA (1989) Temporal factors in human olfactory. Doctoral Dissertation, University of Utrecht, The Netherlands
- Wilson D (2000) Comparison of odor receptive field plasticity in the rat olfactory bulb and anterior piriform cortex. *Journal of Neurophysiology* 84:3036-3042
- Winfree AT (1967) Biological rhythms and the behavior of populations of coupled oscillators. *J Theor Biol* 28:327–374
- Winquist F, Hornsten E, Sundgren H, Lundstron I (1993) Performance of an electronic nose for quality estimation of ground meat. *Meas Sci Technol* 4:1493-1500
- Wlodek S, Colbow K, Consadori F (1991) Signal-shape analysis of a thermally cycled tin oxide gas sensor. *Sensors and Actuators B* 3:63–68
- Wyszynski B, Yamanaka T, Nakamoto T (2005) Recording and reproducing citrus flavors using odor recorder. *Sensors and Actuators B* 106:388–393
- Xu D, Principe J (2004) Dynamical analysis of neural oscillators in an olfactory cortex model. *Trans on Neural Networks* 15(5):1053-1062
- Yamana M, Shiino M, Yoshioka M (1999) Oscillator neural network model with distributed native frequencies. *Journal of Physics A: Mathematical and General* 32(19):3525-3533

- Yamazoe N (1979) Interactions of the tin oxide surface with O<sub>2</sub>, H<sub>2</sub>O and H<sub>2</sub>. *Surf Sci* 86:355
- Yao Y, Freeman W (1989) Pattern recognition in olfactory systems: modeling and simulation. *International Conference on Neural Networks* 1:699-704
- Yao Y, Freeman W (1990) Model of biological pattern recognition with spatially chaotic dynamics. *Neural Networks* 3:153-170
- Yao Y, Freeman W, Burke B, Yang Q (1991) Pattern recognition by a distributed neural network: an industrial application. *Neural Networks* 4:103-121
- Yea B, Osaki T, Sugahara K, Konishi R (1997) The concentration estimation of inflammable gases with a semiconductor gas sensor utilizing neural networks and fuzzy inference. *Sensors and Actuators B* 41:121–129
- Yokohama K, Ebisawa F (1993) Detection and evaluation of fragrances by human reactions using a chemical sensor based on adsorbate detection. *Anal. Chem.* 65:673-677
- Yokoi M, Mori K, Nakanishi S (1995) Refinement of odor molecule tuning by dendrodendritic synaptic inhibition in the olfactory bulb. *Proc. Natl. Acad. Sci.* 92:3371–3375

Zou K, Hall W, Shapiro D (1997) Smooth non-parametric receiver operating characteristic (ROC) curves for continuous diagnostic test. *Statistics in Medicine* 16:2143-2156

## **APPENDIX A**

### **SYNAPTIC PLASTICITY**

The classical Hebbian learning rule postulates that the synaptic connection between two neurons is strengthened if the presynaptic neuron A contributes to the activation of the postsynaptic neuron B (Hebb, 1949). Bi and Poo (2001) extended this postulate by showing that synaptic connections can also be weakened by a lack of causality between the presynaptic and the postsynaptic neuron. Fig. 100 shows the change in the synaptic efficacy between two neurons as a function of their relative activation time. These results indicate that synaptic efficacy is increased if the presynaptic neuron fires before the post-synaptic neuron (i.e., Hebb's postulate). But more important for our purposes, these results also suggest that synaptic efficacy is decreased if the postsynaptic neuron fires after the presynaptic neuron. This represents an extension of Hebb's rule, and is commonly referred to as spike-time dependent plasticity (STDP) Bi and Poo (2001).

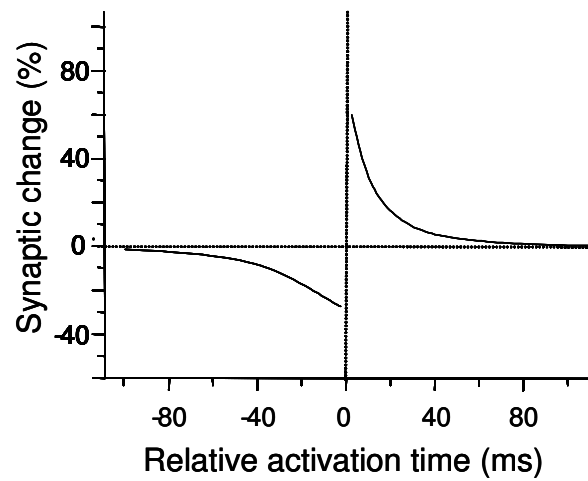


Fig. 100 Spike-time dependent learning rule. Synaptic change as a function of relative activation time between two neurons. Negative values of the activation time, which indicate that the presynaptic spike follows the postsynaptic spike, cause weakening of the connection, whereas positive values of the activation time, which indicate that the postsynaptic spike follows the presynaptic spike, cause a strengthening of the connection.

## APPENDIX B

### FISHER DISCRIMINANT RATIO

Pattern separability in Chapter VI was measured with the Fisher Discriminant Ratio (Duda and Hart, 2001). Assuming a discrimination problem with  $C$  classes the Fisher Discriminant Function is computed following the expression (Wang and Chang, 2002):

$$J = \frac{\text{tr}(S_B)}{\text{tr}(S_W)} \quad (\text{B.1})$$

where  $S_B$  is the between-class scatter and  $S_W$  is the within-class scatter, defined by:

$$S_B = \sum_{i=1}^C (\mu_i - \mu)(\mu_i - \mu)^t \quad (\text{B.2})$$

$$S_W = \sum_{i=1}^C \overbrace{\sum_{y \in C_i} (y - \mu_i)(y - \mu_i)^t}^{S_W^i} \quad (\text{B.3})$$

where  $\mu_i$  is the mean of class  $i$ ,  $\mu$  is the pooled mean, and  $C_i$  is the number of samples from class  $i$ . The between-class scatter is a measure of the distance between the mean of each one of the classes, whereas the within-class scatter is a measure of the spread of

each class. Thus, class separability is directly proportional to  $S_B$  and inversely proportional to  $S_W$ , as captured by the objective function in Eq. B.3.

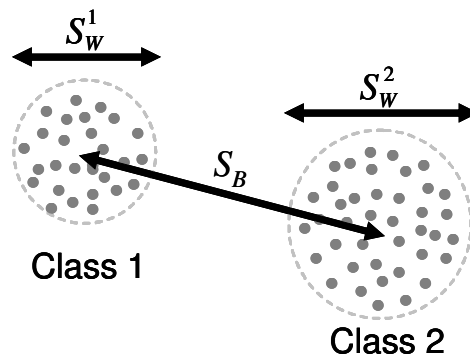


Fig. 101 Illustration of the between class-scatter  $S_B$ , and within class-scatter  $S_W^1$ ,  $S_W^2$  for a two-class problem.

## VITA

Agustin Gutierrez-Galvez received a B.S. in physics and a B.En. in electrical engineering 1995 and 2000, respectively, both from the Universitat de Barcelona. He received his Ph.D. degree in Computer Science at Texas A&M University in May 2006. His research interests are computational models of the olfactory system and pattern recognition applied to odor detection with gas sensor arrays.

Permanent Address:

C/ Calabria 242, 3-3

08029, Barcelona

SPAIN